Quantum degenerate mixtures of ^{23}Na - ^{39}K and coherent transfer paths in NaK molecules

Von der Fakultät für Mathematik und Physik
der Gottfried Wilhelm Leibniz Universität Hannover

zur Erlangung des akademischen Grades

Doktor der Naturwissenschaften
- Dr. rer. nat. -

genehmigte Dissertation von

Dipl.-Phys. Torben Alexander Schulze

2018

Referent:	Prof. Dr. Silke Ospelkaus Institut für Quantenoptik Leibniz Universität Hannover
Korreferent:	apl. Prof. Dr. Carsten Klempt Institut für Quantenoptik Leibniz Universität Hannover
Korreferent:	Prof. Dr. Jan Arlt Department of Physics and Astronomy Aarhus University
Tag der Promotion:	23.05.2018

QUANTUM DEGENERATE MIXTURES OF ^{23}NA-^{39}K AND COHERENT TRANSFER PATHS IN NAK MOLECULES

PHD THESIS

TORBEN ALEXANDER SCHULZE

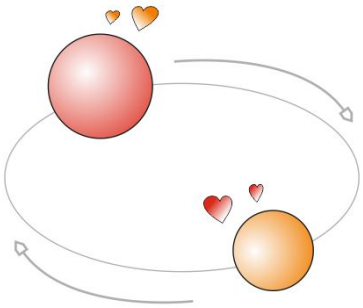

Fakultät für Mathematik und Physik
Leibniz Universität Hannover

April 6, 2018

I may not have gone where I intended to go,
but I think I have ended up where I needed to be.

— Douglas Adams

Dedicated to each reader of this thesis.

ABSTRACT

The discovery and development of methods to cool, trap and manipulate atomic ensembles have generated a revolution in atomic physics, culminating in the ever expanding research field of ultra-cold matter through the realization of Bose-Einstein condensates (BECs). Since the first realization of BEC more than two decades ago, the majority of studies were concerned with systems displaying short-range contact interaction. Following pioneering experiments in ultra-cold KRb, systems involving ultra-cold mixtures have rose to considerable interest through their capability to form diatomic polar molecules. The long-range character of dipolar particle interactions enables the study of a whole new spectrum of quantum many-body phenomena by giving access to the strongly correlated regime.

In this context, NaK is a splendid candidate to investigate dipolar effects due to its large electric dipole moment of 2.72 Debye, its chemical stability and the large history of spectroscopic studies devoted to its ground and excited state manifolds. This thesis reports on the first ever realization of a dual-species degenerate mixture of ^{23}Na and ^{39}K. The experimental apparatus combines two pre-cooled atomic sources into a UHV collection region, where a two-color magneto-optical trap is operated. After transferring both species into an optically plugged quadrupole trap, the ^{23}Na ensemble is cooled by selectively removing the hottest atoms from the trap through microwave transitions, while ^{39}K is sympathetically cooled through its thermal contact to ^{23}Na. Following the transfer into an optical dipole trap, the mixture operation suffers from strong losses as the atomic clouds approach the high-density regime. Interspecies interactions are identified as the system parameter that drives the loss mechanism.

In order to realize a quantum degenerate mixture, the dual-species collisional properties are investigated both theoretically and experimentally. By preparing both optically trapped ensembles in the spin state $|f = 1, m_f = -1\rangle$, atom loss spectroscopy is performed in a magnetic field range from 0 to 1000 G. The observed features include several s-wave poles and a zero crossing of the interspecies scattering length as well as inelastic two-body contributions in the $\mathcal{M} = m_{Na} + m_K = -2$ submanifold. Different magnetic field regions are identified for the purposes of sympathetic cooling of ^{39}K and achieving a quantum degenerate mixture. Forced evaporation creates two Bose-Einstein condensates simultaneously at a magnetic field that provides sizable intra- and interspecies scattering rates needed for fast thermalization. The impact of the differential gravitational sag on the miscibility criterion for the mixture is discussed.

The experimental setup and measurements are complemented by theoretical calculations that form a feasibility study of molecular NaK. Starting from ultra-cold Feshbach molecules, the study demonstrates possible pathways for the creation of ultra-cold polar NaK molecules in their absolute electronic and rovibrational ground state. In particular, a multi-channel analysis of the electronic ground and K(4p)+Na(3s) excited state manifold of NaK is presented. It analyzes the spin character of both the Feshbach molecular state and the electronically excited intermediate states and discusses possible coherent two-photon transfer paths from Feshbach molecules to rovibronic ground state molecules.

The experimental results serve as a promising starting point for the magnetoassociation into quantum degenerate ^{23}Na^{39}K Feshbach molecules. The theoretical analysis assures qualitative understanding as well as quantitative statements for the feasibility of the subsequent ground state conversion. In combination, they fill a critical gap towards the creation of chemically stable ultra-cold molecular Bose-Einstein condensates of NaK.

Keywords: Dipolar systems, Bose-Einstein condensation, Quantum degenerate mixtures, Feshbach resonances, Two-photon transitions

ZUSAMMENFASSUNG

Die Entdeckung und Entwicklung von Methoden zum Kühlen, Fangen und der Manipulation atomarer Ensembles leitete eine Revolution auf dem Gebiet der Atomphysik ein, die in der Realisierung von Bose-Einstein-Kondensaten (BEKs) in dem sich ständig erweiternden Forschungsfeld der ultrakalten Materie gipfelt. Seit der erstmaligen BEK-Realisierung vor mehr als zwei Jahrzehnten beschäftigt sich ein Großteil der experimentell durchgeführten Studien mit kurzreichweitig wechselwirkenden Systemen. Im Zuge zukunftsweisender Experimente an und mit ultrakaltem KRb ist die Erzeugung ultrakalter Mischungen von großem Interesse, da diese Systeme die Erzeugung diatomarer polarer Moleküle ermöglichen. Durch den langreichweitigen Charakter der dipolaren Wechselwirkung lässt sich ein vollkommen neuartiges Spektrum von Quantenvielteilchenphänomenen untersuchen, durch die man sich den experimentellen Zugang zum Regime starker Korrelationen verspricht.

In diesem Zusammenhang ist NaK ein hervorragender Kandidat für die Untersuchung dipolarer Effekte. Es weist ein großes elektrisches Dipolmoment von 2.72 Debye auf, ist chemisch stabil, und seine Molekülzustände sind durch eine Vielzahl von spektroskopischen Studien gut bekannt. In der vorliegenden Arbeit wurde erstmals eine quantenentartete Mischung aus ^{23}Na und ^{39}K erzeugt. In der experimentellen Apparatur werden in einem Ultrahochvakuum zwei vorgekühlte Atomquellen in einer dichroitischen magneto-optischen Falle gesammelt. Nach dem Transfer beider Spezies in eine optisch verschlossene Quadrupolfalle wird das ^{23}Na-Ensemble durch die selektive Entfernung seiner heißesten Atome mittels Mikrowellenstrahlung gekühlt, während ^{39}K durch seinen thermischen Kontakt zu ^{23}Na sympathetisch gekühlt wird. Nach der Überführung in eine optische Dipolfalle erfährt die Mischung starke Verluste im Regime hoher Dichten. Die Interspezieswechselwirkung wird als der Systemparameter identifiziert, der den Verlustmechanismus maßgeblich treibt.

Um eine quantenentartete Mischung realisieren zu können, werden die binären Kollisionseigenschaften des Systems sowohl theoretisch als auch experimentell untersucht. Nach Präparation beider optisch gefangener Ensembles im Spin-Zustand $|f = 1, m_f = -1\rangle$ wird Feshbachspektroskopie in einem Magnetfeldbereich von 0 bis 1000 G durchgeführt. Zu den beobachteten Strukturen gehören mehrere Pole und ein Nulldurchgang der Interspezies-Streulänge sowie inelastische Zweikörperverluste in der Untermannigfaltigkeit $\mathcal{M} = m_{Na} + m_K = -2$. Verschiedene Magnetfeldbereiche werden im Bezug auf ihre Eignung zur sympathischen Kühlung von ^{39}K und zur Erzielung einer quantenentarteten Mischung diskutiert. Optisches Verdampfungskühlen erzeugt zeitgleich zwei Bose-Einstein-Kondensate bei einem Magnetfeld, in dem sowohl Intra- als auch Interspeziesstreuraten günstig sind und für eine schnelle Thermalisierung sorgen. Der Einfluss des differentiellen Gravitationsversatzes auf das *mean-field* Mischbarkeitskriterium wird diskutiert.

Die experimentelle Apparatur und die dazugehörigen Messungen werden durch theoretische Berechnungen ergänzt, die eine Machbarkeitsstudie des molekularen NaK darstellen. Ausgehend von ultrakalten Feshbach-Molekülen zeigt die Studie mögliche Wege zur Erzeugung ultrakalter polarer NaK-Moleküle in ihrem absoluten elektronischen und rovibronischen Grundzustand auf. HierfÃ¼r wird eine Vielkanalanalyse des elektronischen Grundzustandes und der angeregten K(4p)+Na(3s) Mannigfaltigkeit von NaK vorgestellt. Der Spincharakter sowohl des Feshbach-Molekülzustands als auch der elektronisch angeregten Zwischenzustände werden analysiert sowie mögliche kohärente Zwei-Photonen-Transfers zu rovibronischen Grundzustandsmolekülen diskutiert.

Die experimentellen Ergebnisse dienen als vielversprechender Ausgangspunkt für die Magnetoassoziation in quantenentartete ^{23}Na^{39}K Feshbachmoleküle. Die theoretische Analyse sichert sowohl ein qualitatives Verständnis als auch quantitative Aussagen zur

Machbarkeit des Grundzustandstransfers. Kombiniert man theoretische und experimentelle Ergebnisse, so füllen diese eine kritische Lücke zur Bildung von chemisch stabilen, ultrakalten NaK-Molekülen.

Schlagwörter: dipolare Systeme, Bose-Einstein Kondensation, quantenentartete Mischungen, Feshbach-Resonanzen, Zweiphotonenübergänge

PUBLICATIONS

Some ideas and figures have appeared previously in the following publications:

- ⋆ T.A. Schulze, I.I. Temelkov, M.W. Gempel, T. Hartmann, H. Knöckel, S. Ospelkaus and E. Tiemann, *Multichannel modeling and two-photon coherent transfer paths in NaK*, Physical Review A, **88**, 023401 (2013) [1]
- ⋆ F. Richter, D. Becker, C. Bény, T.A. Schulze, S. Ospelkaus and T.J. Osborne, *Ultracold chemistry and its reaction kinetics*, New Journal of Physics **17**, 055005 (2015) [2]
- ⋆ M.W. Gempel, T. Hartmann, T.A. Schulze, K.K. Voges, A. Zenesini and S. Ospelkaus, *Versatile electric fields for the manipulation of ultracold NaK molecules*, New Journal of Physics **18**, 045017 (2016) [3]
- ⋆ T.A. Schulze, T. Hartmann, K.K. Voges, M.W. Gempel, E. Tiemann, A. Zenesini and S. Ospelkaus, *Feshbach spectroscopy and dual-species Bose-Einstein condensation of* ^{23}Na $-^{39}$ K *mixtures*, Physical Review A, **97**, 023623 (2018) [4]

CONTENTS

1 INTRODUCTION

The first experimental realization of Bose-Einstein condensates (BECs) in 1995 [5, 6, 7] paved the way for the research field of *ultracold quantum gases*, that has been ever expanding since then. This unique quantum state of matter draws its appeal through an excellent *theoretical* understanding of the particle properties on a microscopic level, paired with a superb *experimental* degree of control over these properties. The contact-free modification of both their internal and external degrees of freedom by optical and magnetic fields, together with the absence of impurities or thermal excitations render Bose-Einstein condensates nowadays one of the cleanest environments amongst all physical systems. This makes them ideally suited to be operated as a quantum emulation platform for problems that are difficult to tackle in their original context, such as high-temperature superconductivity [8]. The study of ultracold gases therefore contributes not only to research in fundamental atomic and molecular physics, it also enriches the understanding of various scientific fields such as condensed matter physics [9], physical chemistry [10] and metrology [11].

A multitude of the unique and unusual phenomena that can be studied within a BEC can be attributed to its particle interaction, whose nature and strength is given by the sign and magnitude of the underlying scattering length. Through the use of external magnetic fields, these interactions can be freely adjusted, allowing to set them to arbitrary attractive, repulsive or even vanishing values. Together with the also widely shapeable interaction of atoms with light, a variety of exotic quantum phases have been realized in ultracold systems such as the transition from a molecular BEC to a BCS superfluid [12, 13] or the superfluid-to-Mott-insulator transition in an optical lattice [14]. However, the amount of engineerable many-body systems is ultimately limited by the fundamental *short-range* character of the particle interaction, as the underlying Van-der-Waals dispersion scales with r^{-6}, where r is the interatomic distance of the colliding particles. This strongly obstructs the achievable quantum phases. As an example, the spin-spin interaction of short-range systems in optical lattices is governed through second-order effects such as superexchange interaction, which are inherently small.

These limitations motivated the quest to study *long-range* interacting quantum gases, in which neither of these restrictions exist, and where many-body physics on a whole new level can be expected [15]. In an optical lattice environment with long-range interactions, a particularly exciting novel many-body quantum phase can emerge in which the system possesses superfluid properties but the superfluid order parameter displays a periodic modulation. Such a system exhibits long-range off-diagonal order like a superfluid, but also long-range diagonal order like a solid crystal - a *supersolid* is formed [16]. As such a many-body state defies intuition (atoms forming a crystal are localized, whereas delocalized frictionless movement is a key element of superfluidity), initial theoretical studies were cautious to only speculate about the existence of such seemingly paradoxical and elusive state of matter [17]. Nowadays, a theoretical understanding has been established (defects in the solid mediate the superfluid properties), but experimental realization has remained sparse. After stirring the solid-state community for almost a decade,

initial claims of supersolid signatures in Helium-4 [18, 19] have been subsequently disproved [20], with the debate laid to rest by the authors of the initial discovery themselves [21]. The question of how to realize and thoroughly study supersolid systems remained - ultracold *dipolar* gases could be the answer.

1.1 DIPOLAR DREAMS

To the candid reader, studious of the magnetic philosophy:

[...] For after we had, in order to discover the true substance of the earth, seen and examined very many matters taken out of lofty mountains, or the depths of seas, or deepest caverns, or hidden mines, we gave much attention for a long time to the study of ***magnetic*** *forces - wondrous forces they, surpassing the powers of all other bodies around us, though the virtues of all things dug out of the earth where to be brought together. Nor did we find this our labor vain or fruitless, for every day, in our experiments, novel, unheard-of properties came to light: and our Philosophy became so widened, as a result of diligent research, that we have attempted to set forth, according to magnetic principles, the inner constitution of the globe [...] and we have dug them up and demonstrated them with much pains and sleepless nights and great money expense. Enjoy them you, and, if ye can, employ them for better purposes.*

- William Gilbert, *De magnete* (1600), translated from latin [22].

A variety of strategies, all equipped with individual benefits and limitations, are conceivable to introduce long-range interactions in ultracold systems [23, 24, 25], and first signatures of supersolid properties have been shown very recently in atomic ensembles where the long-range nature of the particle interaction is mediated by cavities or synthetic gauge fields [26, 27]. A particularly promising approach is given by using *dipolar quantum gases* interacting through dipole-dipole interaction (DDI). For a system of aligned dipoles, the DDI of two particles takes the form

$$V_{dd}(r) = \frac{C_{dd}}{4\pi}\frac{1-3\cos^2(\vartheta)}{r^3} \tag{1.1}$$

where ϑ is the angle between relative particle position and polarization direction and C_{dd} is a constant that governs the interaction strength. In addition to their $\propto r^{-3}$ long-range character, the anisotropy of their interaction allows for the synthesis of geometrically non-trivial arrangement of structures and a tunability of sign and strength similar to the short-range interacting case. The supersolid phase itself has been predicted to prevail also in dilute systems, where three-body interaction has been identified as a stabilization mechanism [28]. Therefore, a supersolid can be realized in a dipolar quantum gas - **if** the dipole-dipole interaction is strong enough, and **if** the quantum degenerate regime can be reached.

The search for a suitable dipolar quantum gas produced a wide variety of different candidates. To put these different systems into perspective, the dipolar length scale

$$a_{dd} = \frac{C_{dd}\, m}{12\pi\, \hbar^2} \tag{1.2}$$

is defined. This DDI length has to be compared to the typical length scale of the system, e.g. the short-range interaction strength (typically $\sim 100 a_0$ with the Bohr

radius a_0) or the optical lattice spacing (typically 532 nm $\approx 10^4 a_0$) to assess its impact on the physical system.

Magnetic dipole interaction is found in atoms through the non-closed shell electrons, and therefore the magnetic dipole moment will be on the order of the Bohr magneton μ_B. These systems have the great advantage that a handful of them has already been Bose-Einstein condensed [29, 30, 31], thus dipolar phenomena can already be investigated on the quantum degenerate level. Seminal experiments with ^{52}Cr ($\mu_{Cr} = 6\,\mu_B$) demonstrated dipolar effects such as magnetostriction and d-wave collapse [32, 33], yet the comparatively weak dipolar interaction ($a_{dd,Cr} = 16\,a_0$) could only probe the weakly-interacting regime, as the otherwise dominant short-range interaction ($a_{Cr} = 96\,a_0$ [34]) had to be artificially reduced.

In addition to the quadratically scaling magnetic moment, the enumerator in eq. (1.2) also incorporates the mass of the dipole. Current investigations therefore use heavy lanthanide atoms such as ^{168}Er and ^{164}Dy. These possess additional polarizable electrons through their open f-orbital, giving magnetic dipole moments of $\mu_{Er} = 7\,\mu_B$ and $\mu_{Dy} = 10\,\mu_B$, rendering dysprosium (together with terbium) the most magnetic atom in the periodic table. Together with their mass, this results in dipolar lengths comparable to the short-range interaction ($a_{dd,Er} = 67\,a_0$, $a_{dd,Dy} = 133\,a_0$). In these systems, textbook examples of dipolar systems such as the roton quasiparticle spectrum were observed [35], and the dipolar interaction was further used to evaporatively cool a Fermi gas to quantum degeneracy, which is not possible using solely short-range interactions [36]. The generation of *quantum droplets* proved to be particularly interesting [37]. This novel quantum state emanates through careful balance of mean-field and beyond-mean field effects, and its beyond-mean field nature makes it an attractive quantum many-body state to study. It was shown that droplets can align in a self-organized "striped" state, indicating supersolid-like periodic density modulations. However, matter-wave interference experiments probing their long-range off-diagonal order [38] showed that no coherent phase links exist between these droplets - up to now, dipolar supersolids remain uncharted in these systems.

1.2 MOLECULAR NIGHTMARES

A diatomic molecule is one atom too many!

- Arthur Schawlow [39]

The range of accessible dipolar interaction can be hugely enhanced by using heteronuclear molecular systems. Their large *electric* dipole moment is given by the spatial charge separation, which is on the order of the cgs-unit Debye. Compared with magnetic interaction, the ratio of the corresponding coupling constants

$$\frac{C_{dd,elec.}}{C_{dd,mag}} \propto \frac{\text{Debye}^2\,\varepsilon_0^{-1}}{\mu_B^2\,\mu_0} \approx 1.2 \times 10^4 \tag{1.3}$$

is clearly in favor of the molecular systems. This is shown in fig. 1 by comparing the dipolar length in a_0 for magnetic dipoles together with a variety of diatomic molecules. Even the homonuclear molecule Er_2, that features twice the magnetic moment and mass, is inferior to the weakest diatomic alkali combinations LiNa and KRb. As the electric dipole moment has to be induced through an externally applied

electric field with a given polarization direction, the dipolar strength and sign in a 2D dipolar system can be freely adjusted, giving a tunability comparable to that found in short-range systems through Feshbach resonances. Dipolar molecules are therefore the ideal candidate for studying strongly-interacting, long-range systems. Yet the system also has to be sufficiently dense, as otherwise the typical interaction parameter $\sqrt{na_{dd}^3}$ in a gas, where n is the density, would be too low for a significant contribution on reasonable time scales. It is therefore desirable to use systems in which Bose-Einstein condensates with sufficiently large particle numbers can be realized. This is where diatomic molecules face challenges. In contrast to the hyperfine structure of simple atomic systems, their internal states also include vibration and rotation. This makes established methods to reach the ultracold regime, such as laser cooling and evaporative cooling, extremely difficult, and their realization requires sophisticated models and resourceful implementation. Significant progress has been made in recent years, most notably in diatomic systems with one valence electron such as CaF or SrF, in which highly diagonal Franck-Condon factors suppress excessive vibrational branching. After the first successful realization of molecular laser cooling [42] and magneto-optical trapping [43], recent demonstrations include sub-Doppler cooling [44] and optical trapping [45]. Furthermore, the sources are constantly improved, and techniques such as molecular Zeeman slowing were shown in atomic testbeds with molecular analogue level structure [46]. Nevertheless, state-of-the-art phase space densities of direct cooled sources are on the order of 10^{-12} [44] - the quantum degenerate realm is still far, far away.

This experiment therefore uses a "best of both worlds" approach, by selecting two atomic species for which the pathway to quantum degeneracy has been already demonstrated, and using established cooling methods to achieve Bose-Einstein condensation for both species.[1] Subsequently, the atomic samples can be converted into weakly bound molecules using magnetoassociation by Feshbach resonances [47], and the Feshbach molecule can be transformed into a ground state molecule

1 The list of all species that have been Bose-Einstein condensed so far: all stable alkali metals; calcium and strontium; chromium; ytterbium, erbium, dysprosium; hydrogen; metastable helium.

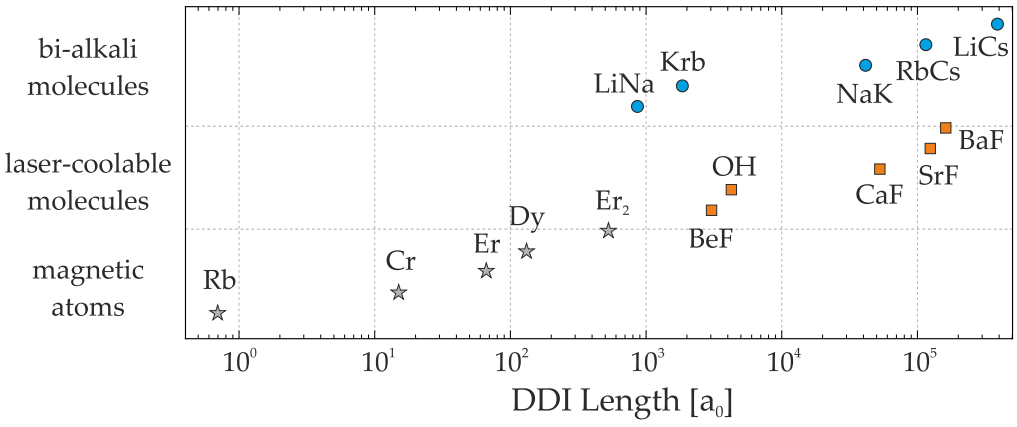

Figure 1: DDI length for magnetic atoms (gray stars), bi-alkali molecules (blue dots) and laser-coolable molecules (orange squares). The electric dipoles are assumed to be fully polarized through an external electric field [40, 41].

by a two-photon STIRAP process [48]. Due to the fully coherent nature of both processes, the phase space density of the initial atomic ensembles is being preserved, resulting in a dense ultracold molecular sample close to quantum degeneracy. This indirect approach is a detour in comparison with direct cooling methods and requires the design and characterization of a quite complex apparatus. Yet since each of the required steps has already been tested many times in atomic systems, a successful experimental realization up to the stage of ground state molecules can be guaranteed, and only technical challenges have to be overcome.

As soon as one enters the world of ultracold molecules, complexing mechanisms can be encountered, and not all of them are fully understood yet. This is shown schematically in fig. 2. While the collision of two condensed neutral atoms is well studied theoretically and experimentally, the collision process of two diatomic molecules can already lead to many different phenomena, since, strictly speaking, this is already a four-body process that takes place on a highly nontrivial potential energy surface. In addition to the usual s-wave scattering, which constitutes the short-range interaction, ultracold chemical reactions can occur in which the heteronuclear dimers are converted into homonuclear ones.[2] Such a process was observed, for example, in the pioneering KRb experiment at JILA [50]. In this species combination, the corresponding chemical reaction is exothermic, which leads to high losses and severely limits the achievable densities.

This is only one loss category, and more are perceivable through the large ro-vibrational density of states that is present in a molecular collision. From a theoretical point of view, these processes are very difficult to model, since many effects play a role here whose interplay is not exactly known. Thus, a recent approach is to describe the underlying dynamics that drive scattering by statistical arguments in order to extract the scattering observables. An essential result of such an analysis is the prediction of extremely long lifetimes of the tetramer produced in a diatomic collision [51, 52], a process that was nicknamed "sticky" collisions and which is sketched as a third result path in fig. 2. However, the entire model is based on the assumption that molecular collisions are ergodic, so that the trajectories

2 The fact that chemical reactions can happen *at all* in an ultracold environment is quite remarkable due to the lack of activation energy. As it is induced by quantum-mechanical threshold effects [49], the corresponding research field has been coined *quantum chemistry*.

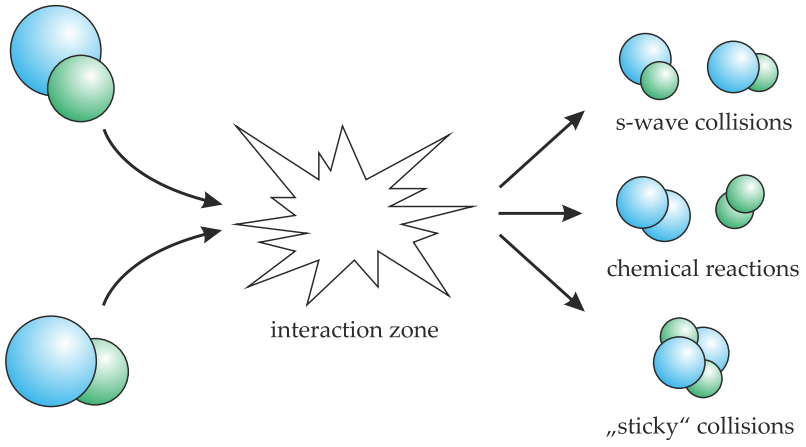

Figure 2: Schematic of the molecular scattering process, with three thinkable outcomes.

of the classical analogue system follow chaotic motion. In the end, it can only be shown experimentally whether and to which extent this assumption holds. For this purpose, two molecules could be loaded into an optical lattice, and their number monitored using high-resolution imaging methods. If tetramers would associate and subsequently dissociate on the predicted millisecond scale, this would lead to a decay and revival of the corresponding diatomic signal. However, this opens up further questions, regarding the dynamic polarizability of such a tetramer in an optical trapping environment *et cetera*. Most of these questions can only be answered experimentally. The incredibly complex field of ultracold molecules is therefore of interest not only for dipolar systems, but also for addressing and resolving fundamental problems of cold collision physics, and can make significant contributions to both nodes.

Initial experiments were concentrating on KRb combinations, which is a convenient choice for tandem operation due to the similar D2 transition lines of both atomic species. In this system, first signatures of optical lattice many-body dynamics could be traced by probing dipolar spin-exchange interactions [53, 54]. As outlined above, the dipole moment of KRb is rather small compared to other available diatomic combinations, and its chemical reactivity constrains the achievable densities. Both together restrict again the gas parameter $\sqrt{na_{dd}^3}$, and therefore other species combinations were pursued. However, all of the fundamental methods, including the association [55], coherent state transfer [56] and hyperfine state control of the ground state molecules [57] were demonstrated in the KRb system at JILA. KRb therefore plays the same role for electric dipolar systems that ^{52}Cr plays for magnetic ones - as a pathbreaking first-generation experiment, in which the basic methodology was introduced, fundamental first questions were answered and typical obstacles unveiled.

Nowadays, a wide variety of combinations is currently under investigation. All above considerations of diatomic molecular properties can be summarized as follows: It is strongly advisable to use a system for which both constituents can be cooled to quantum degeneracy (either individually or using sympathetic cooling), where chemical reactions are endothermic and where both the atomic as well as the molecular system has been investigated as good as possible. Under these conditions, both species have to be alkali-metal atoms, for which cold chemical reactivity calculations are available [58]. These calculations show that chemical stability can only be obtained for five species combinations: NaK, NaRb, NaCs, KCs and RbCs. To screen also further chemical effects, recent proposals showed that a dipolar shielding mechanism can be installed in all five combinations, in which the DDI can be used to adjust the ratio of elastic to inelastic collisions [59]. All five combinations are actively pursued in experiments today [60, 61, 62, 63, 64, 65], which allows cross-species comparison of dipolar phenomena.

1.3 THE TASK OF THIS THESIS

In this experiment, a combination of ^{23}Na and ^{39}K was chosen. NaK is a promising candidate with a large dipole moment of 2.72 Debye, that has been extensively studied by molecular spectroscopy for almost a century [66]. A large number of experimental data and spectroscopic constants are available in the literature, leading to the potential energy curves of the involved electronic states [67, 68, 69, 70, 71], and

are supplemented by sophisticated theoretical studies of molecular properties like radiative lifetimes, dipole moments or static polarizabilities [72, 73]. Furthermore, the natural potassium isotopes ^{39,40,41}K provide the unique possibility to switch between the study of fermionic and bosonic systems. In recent, seminal experiments at the MIT, dual quantum degenerate samples using ^{23}Na and the fermionic ^{40}K have been created, associated into molecules and prepared in their absolute ground states [74, 75]. Both bosonic combinations, ^{23}Na^{39}K and ^{23}Na^{41}K, have been left unexplored in the ultracold regime up to now.

The Hannover NaK experiment has been explicitly designed for the study of NaK ground state molecules and is equipped with state-of-the-art technology that will make this possible. Upon the realization of ground state molecules, an electrode configuration using an Indium tin oxide structure coated directly onto the chamber windows will enable versatile electric manipulation of the dipoles [3]. In the optical lattice environment, a custom microscope objective allows single-site resolution as demonstrated on a testbed environment using gold nanoparticles [76].

Yet the path to ground state molecules was only known on a qualitative level, with many questions on the way. At the time the experiment was planned, the MIT results had not been published and it was not clear whether the methods demonstrated at JILA, namely the magnetoassociation by Feshbach resonances followed by a coherent two-photon transfer, would also be feasible for other species combinations. While both ^{23}Na and ^{39}K had been individually Bose-Einstein condensed, nothing was known regarding their mixture properties in the ultracold regime. While single-species quantum degenerate experiments are nowadays an established routine for alkali-metals, dual-species Bose-Einstein condensates are still not as commonly found.

For this reason, the first objectives of the experiment were the production of a quantum-degenerate ^{23}Na + ^{39}K mixture, the identification of suitable Feshbach resonances, and the precise theoretical understanding of the underlying molecular potentials to propose feasible two-photon pathways. All these objectives were achieved by the time this work was completed. They are presented in this thesis as follows:

- ⋆ The central phenomena, namely Feshbach resonances in molecular spectra and Bose-Einstein condensates in atomic systems, are presented in **Chapter 2**. This provides a clear introduction to the underlying theories and concepts. It further motivates the route that was traversed theoretically and experimentally in order to realize and study these phenomena.

- ⋆ The individual stages of the experimental setup are described in **Chapter 3-6**. It starts with a description of the laser systems and culminates in the realization of single-species quantum degenerate matter. The fundamentals have been layed out and the most relevant measurements are presented, sometimes in a more rigorous or elaborate fashion. This provides future PhD students, regardless whether they work at this apparatus or try to build or fix their own one, with a reference text that tries to be concise yet complete.

- ⋆ **Chapter 7** is devoted to the measurements of the previously unknown Feshbach spectrum of ^{23}Na + ^{39}K in order to achieve the first ever dual-species Bose-Einstein condensate of this species combination. The here presented results are the basis for publication [4].

- ⋆ **Chapter 8** presents the framework of theoretical calculations, in which a detailed analysis of possible two-photon pathways for preparing ultracold NaK in its absolute ground state was performed. The presented results were the basis for publication [1].
- ⋆ The thesis closes with an outlook in **Chapter 9**. It is shown that the achieved experimental progress offers a broad spectrum of further investigations in the direction of quantum degenerate mixtures, Feshbach spectra and molecular gases.

2

FUNDAMENTALS

All following chapters are equipped with the theoretical tools to understand the concepts at work, and the corresponding equations are introduced or derived when they are needed or applied. This chapter provides an additional background of the main phenomena encountered and treated in this thesis, namely *Feshbach resonances* and *Bose-Einstein condensates*. The description featured here follows is not meant as a complete review[1]. It rather tries to string together the thoughts which lead to the conceptual design, theoretical treatment and experimental realization of the individual pieces that form this thesis.

The first section is devoted to the interaction between particles, and therefore introduces fundamental aspects of scattering theory with a focus on *resonant* scattering. This section further gives an introduction to the typical experimental and theoretical techniques that are used to obtain and improve molecular potential energy curves. The second section describes the quantum statistics of Bosons and the implications in the ultra-cold limit, which leads to the emergence of Bose-Einstein condensates (BECs). It further introduces ^{23}Na and ^{39}K as the building blocks of quantum degenerate matter in this thesis. A survey of their optical, magnetic and scattering interaction properties motivates the role allocation that ^{23}Na will be used as a coolant for the ^{39}K cloud throughout most stages of the experiment. The chapter finishes by presenting the route in phase space that has to be traversed in order to realize BECs experimentally, which motivates and links the subsequent chapters of this thesis.

2.1 A MAGNETIC CONTROL KNOB: FESHBACH RESONANCES

Interactions make life interesting [83], motivating the endeavour to achieve absolute control over them. In an ultra-cold setting, this becomes possible by utilizing the unique properties of scattering interaction of bound and continuum states. This section sheds some light on the origin and meaning of the individual scattering observables. Despite the simple appearance, the scattering aspects of a diatomic collision will remain quite complex. A simple yet effective toy model first explains the appearance of poles in the scattering length when the interaction potential is varied. Adding multiple channels then naturally leads to the description of *Feshbach resonances* as a tool to freely tune the scattering interaction and to enable molecular binding. The section closes with a brief review of the available experimental and theoretical methods to obtain high-quality molecular potential energy curves and to predict the corresponding scattering properties.

1 To this end, a mix of textbook examples [77, 78, 79, 80] and extensive review articles [81, 82] is recommended, whose combined reasoning is followed here.

Radial Schroedinger equation

Consider scattering of an incident plane wave with wavevector k on a spherical target, e.g. the atomic interaction potential $V(\boldsymbol{r})$. The time-independent Schroedinger equation for the relative motion reads

$$\left(\frac{\hat{\boldsymbol{p}}^2}{2\mu} + V(\boldsymbol{r})\right)\Psi(\boldsymbol{r}) = E\Psi(\boldsymbol{r}) \tag{2.1}$$

with the reduced mass μ. The scattering problem is typically approached by inspecting the scattering solution at a distance far beyond the potential range. In this case, the outgoing scattered wave can be described as a spherical wave, direction-modulated by a scattering amplitude $f(\vartheta, \phi)$ that carries all the information of the process. Together with the incoming plane wave this gives:

$$\Psi(r, \vartheta, \phi) \underset{r\to\infty}{=} e^{ikr\cos(\vartheta)} + f(\vartheta, \phi)\frac{e^{ikr}}{r}. \tag{2.2}$$

All scattering problems discussed here are radially symmetric ($V(\boldsymbol{r}) = V(r)$) and their solutions can therefore be decomposed into partial waves characterized by the spherical harmonics $Y_{\ell,m}(\vartheta, \phi)$. Through the azimuthal symmetry of plane wave and interaction potential, the angular dependence simplifies to the Legendre polynomials $P_\ell(\cos(\vartheta))$, where the relation $Y_{l,0} = \sqrt{\frac{2\ell+1}{4\pi}}P_\ell(\cos(\vartheta))$ holds.

Upon expanding the scattering wave function into partial waves

$$\Psi(\boldsymbol{r}) = \sum_{\ell=0}^{\infty}\frac{\psi_\ell(r)}{r}P_\ell(\cos(\vartheta)), \tag{2.3}$$

the functions $\psi_\ell(r)$ satisfy the radial Schroedinger equation

$$\frac{-\hbar^2}{2\mu}\frac{d^2\psi_\ell(r)}{dr^2} + \left[V(r) + \frac{\hbar^2\ell(\ell+1)}{2\mu r^2}\right]\psi_\ell(r) = E\psi_\ell(r). \tag{2.4}$$

For larger angular momenta, the centrifugal barrier term $\propto \ell^2$ keeps the particles apart from each other, hence their scattering contribution will decrease with increasing ℓ. In the low-temperature limit ($k \to 0$), the impact parameter needed to gain an angular momentum of $\hbar$ is so large that the interaction potential is essentially zero in the sampled region, and therefore no phase shift can be accumulated.[2] Hence only $\ell = 0$, so called s-wave scattering, will give a noteworthy contribution to the system.[3]. In what follows, all higher partial waves are dropped and $\psi_{l=0}(r) \equiv \psi(r)$ is used. The radial Schroedinger equation describing low-energy scattering then simplifies to

$$\frac{-\hbar^2}{2\mu}\frac{d^2\psi(r)}{dr^2} + (V(r) - E)\psi(r) = 0. \tag{2.5}$$

2 In a semi-classical description, the non-quantized angular momentum is related by $\langle\ell^2\rangle = (b\cdot\hbar k)^2$ to the impact parameter b. For a collision energy of a 1 μK, the de-Broglie wavelength of ^{23}Na is on the order of 1 μm. Hence, the required impact parameter is 160 nm ≈ 70 r_0, where r_0 is the typical Van-der-Waals length scale associated with the Na_2 potential.

3 When dipolar interaction is introduced into the system, this changes dramatically as all ℓ states are coupled through the dipolar anisotropy. As an example, consider the strongly magnetic system of Erbium. Multi-channel analyses of the measured resonance density in this system indicate that the Hilbert space has to be extended up to $\ell = 50(!)$ to account for all relevant couplings and reproduce the correct number of resonances [84]

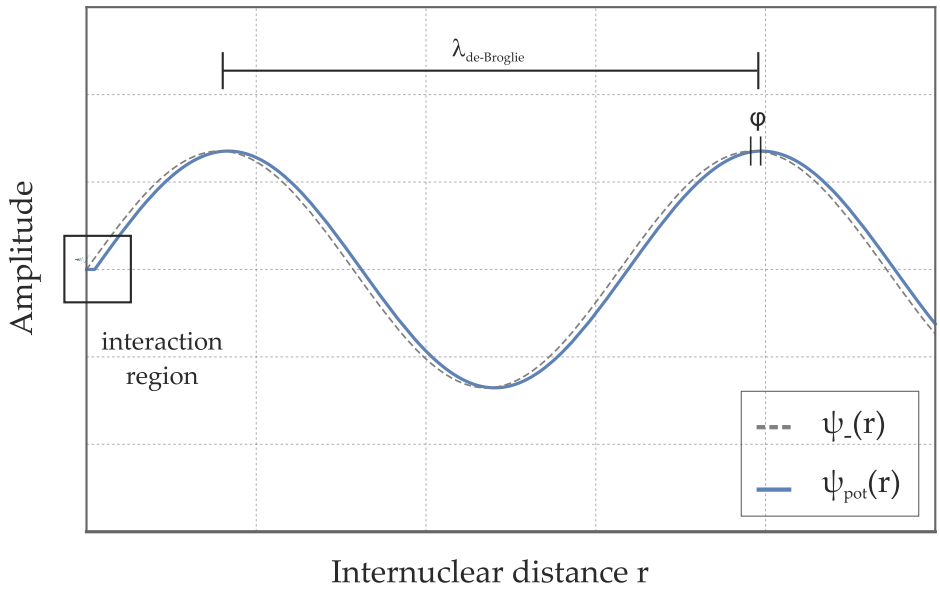

Figure 3: Scattering wave function as a function of internuclear distance for an interacting (solid blue) and interaction-free (dashed gray) system. At low energies, the de-Broglie wavelength is typically much larger than the range of the underlying interaction potential (indicated by boxed region). At large distances, the interaction manifests itself into a scattering phase shift φ.

Low-energy scattering

As a starting point, consider equation (2.5) in absence of an interaction potential. The well known solutions are $\psi_+(r) = \cos(kr)$ and $\psi_-(r) = \sin(kr)$, the subscript denoting their parity, where the latter solution fulfills the boundary condition $\psi_-(0) = 0$. Next, one adds a short-range interaction potential, and examines the scattering wave function $\psi_{\text{pot.}}(r)$ at internuclear distances on the order of the de-Broglie wavelength $\lambda_{\text{de-Broglie}} = 2\pi/k$. With $V(r) = 0$ at this distance, the scattering solution will acquire the same functional form as the interactionless case. Therefore the distortion of the wave function due to the interaction potential will effectively only give rise to a phase shift φ, as seen in fig. 3.

In the long-range limit, the scattering solution can be thus written as

$$\psi_{\text{pot.}}(r) \underset{r\to\infty}{=} \sin(kr + \varphi(k)), \tag{2.6}$$

where the phase shift describes the delay or advance of the spherical wave in comparison to the non-interacting case. The phase shift will also depend on the amount of kinetic energy in the collision, which is accounted for by expressing it as a function $\varphi(k)$ of the matter wave vector k. In the low-energy limit, the *s-wave scattering length* is then defined by

$$\lim_{k\to 0} k\cot(\varphi(k)) = -\frac{1}{a}. \tag{2.7}$$

Therefore the whole effect of the interaction potential can be described by one parameter, namely the scattering length *a* that is obtained out of of the scattering phase shift (in-text written in italics). This implies that for low-energy scattering, the exact shape of the interaction potential is not important as long as it leads

to the same phase shift. This justifies pseudo-potential approaches which will be encountered later in the description of Bose-Einstein condensates.

Using the small-angle approximation in eq. (2.7) gives $\tan(\varphi(k)) \approx \varphi(k) = -k\,a$, and inserting this into eq. (2.6) gives rise to the simple form

$$\psi_{\text{pot.}} \approx \sin(kr - ka) \approx k(r - a) \tag{2.8}$$

for the low-energy scattering wave function in the region where the interatomic potential is zero. By drawing a tangent to this linear part, the intersection with the x-axis gives the scattering length. At first glance, this might not appear as a particularly useful task. By employing a toy model and adiabatically working through some examples, it will turn out to be a helpful feature to understand resonance characteristics later on.

2.1.1 *Toy model*

Since the exact shape of the potential is not necessarily needed, a minimalistic model mimicking hard sphere scattering is employed. The description starts with a box potential of infinite height ($V_0 = \infty$) and an extent r_{box}. Both potential and scattering wave function are graphically presented in fig. 4 (1). With eq. (2.8), the scattering solution becomes very intuitive: It has to be zero inside the box, and linear outside. Therefore the x-axis intersection is at the box radius that defines its boundary conditions, so the scattering length is $a = r_{\text{box}}$. In this picture, low-energy scattering can be seen as billard ball like collisions[4], where each billard ball has a radius given by the scattering length a.

In the next step, the potential height is reduced from infinite to some finite value $V_0 \gg k$ that reflects the repulsive interaction strength. Due to its finite probability amplitude in the box, the scattering wave function acquires a concave shape, being linear outside of the box and exponentially decreasing inside. Most notably, its x-axis intersection and hence the scattering length will be at a point $r < r_{\text{box}}$ ((2) in fig. 4). Keeping in mind the less repulsive barrier, the magnitude of the scattering length therefore reflects the strength of the scattering interaction. If the box extent is kept at r_{box} and its potential height subsequently decreases, so will the intersection with the x-axis and hence the scattering length because of the smaller exponential decay constant in the classically forbidden box region. At vanishing potential, the intersection point is the origin - this is just the small-angle approximation for the sine wave, and the interactionless result $a = 0$ is recovered.

Tuning the interaction strength to attractive is done by setting $V_0 < 0$, which realizes a square well. First, V_0 is chosen small enough that the well does not accomodate any bound state solutions. Because of the attractive nature of the square well interaction, the scattering wave function becomes convex through the increased probability amplitude inside of the well. The scattering wave function solution inside the well will be given by $\sin(\tilde{k}r)$, with a wavevector $\tilde{k}^2 = (2\mu V_0)/\hbar^2$. Plotting a tangent to it then leads to a negative intersection, ergo $a < 0$, which is in line with the attractive interaction of the potential. By increasing the well depth, the tangent becomes parallel to the x-axis. This way the negative value of the scattering length can be increased up to $a \to -\infty$. At this critical potential

4 However, the low-energy quantum billard balls exhibit a larger scattering cross section, $\sigma_0 = 4\pi a^2$. For indistinguishable bosons, $\sigma_0 = 8\pi a^2$ as a result of their symmetrization.

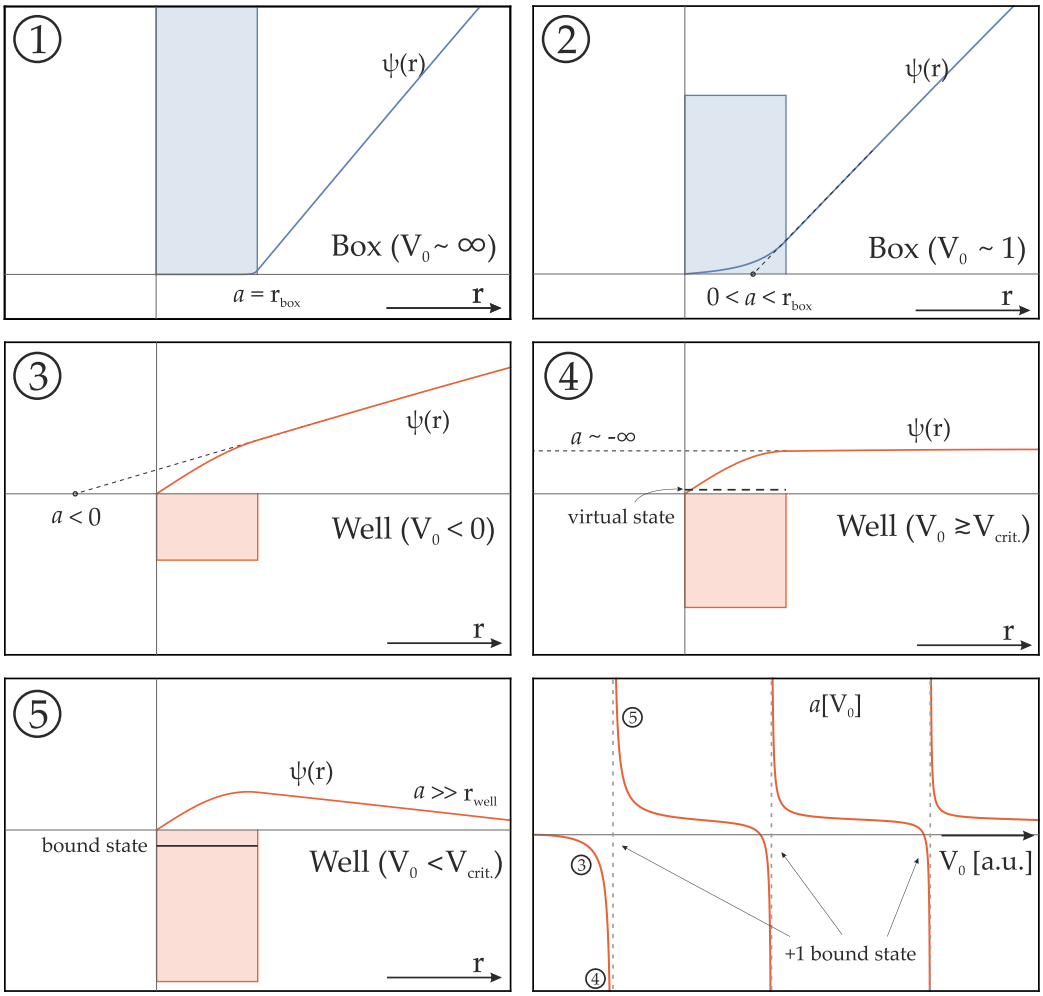

Figure 4: Scattering wave function for a variety of toy model potentials. For repulsive box (blue shaded) potentials, the scattering length is positive (1) and decrases with the box height V_0 (2). For attractive interaction $V_0 < 0$ in a square well (red shaded), the scattering length is negative (3). $a \to -\infty$ is associated with a virtual state just above threshold (4). As this enters as a shallow bound state into the system, the scattering length becomes resonant and turns to the positive side (5). The scattering length then depends on the position of the last bound state, and every new appearing bound state leads to resonant behaviour (6).

depth $V_{crit.}$, the wave function acquires a total phase of $\pi/2$ inside the well, which is equivalent to the statement that the well can accomodate a (shallow) bound state. Increasing the well depth a bit further ($V_0 < V_{crit.}$), the wave function will curve faster inside the well and the intersection becomes positive! See fig. 4 (5). Thus, most remarkably, despite the purely *attractive* nature of the potential, its depth can give rise to exceedingly large *repulsive* interactions when inspected at long distances. With the emergence of a bound state, $a \to \infty$. For such a shallow bound state, the low-energy scattering wave function inside the well is mostly identical to the bound state solution. This links the binding energy ΔE of the weakly bound state to the scattering length such as

$$\Delta E = \frac{\hbar^2 k^2}{2\mu} = \frac{\hbar^2}{2\mu a^2}. \tag{2.9}$$

Through this inverse relationship, every bound state can be seen as a catalyst that resonantly amplifies the scattering length. This also satisfies our intuitive picture of resonant scattering: Being resonant with the bound state, the scattering solution can oscillate many times back and forth in the square well, when it will accomodate much larger phase shifts[5]. This toy-model approach can readily be carried over to more complex-shaped, short-range potentials (it however fails for Coulomb interaction). Regardless of the exact potential form, the general idea is the same: Further increase of the well depth gives a universal behaviour whenever an additional bound state enters the system, leading to a pole in the scattering length. As the newly bound state immerses deeper into the potential, the scattering length value reduces (it therefore can be even zero, turning an interacting system into an effectively non-interacting one at ultra-low energies). A large positive/negative scattering length can therefore be associated with a bound/virtual state situated just below/above threshold.

2.1.2 *Two-channel Feshbach resonances*

The interaction potentials sensed by the scattering atoms follow a Lennard-Jones form, whose exact shape is determined by the equilibration of repulsive Pauli and attractive dispersion forces. This in turn fixes the number and location of the bound states. At first glance, it therefore appears as if the scattering length would be a system constant for the considered diatomic collision through the position of its last bound state. It will now emerge that this is not the case. The Hilbert space of the diatomic collision usually comprises a lot of different state combinations. During the collision, only the total magnetic quantum number is conserved because of the cylindrical symmetry along the collision axis, and the overall effective potential is usually not diagonal in the atomic pair basis. Therefore coupling matrix elements between the state combinations exist, which enables transitions between these states, even though these might be small. Now, each interaction potential can be globally shifted through the state's energy dependence on magnetic fields because of their magnetic moment. When different states display different magnetic moments, they can be shifted with respect to each other. Thereby it is certainly possible to shift a bound state to resonance with a free entrance state using external magnetic fields, such that already a weak coupling can have a drastic effect because of the vanishing energy difference.

The toy model under consideration is now slightly upgraded. Instead of a square well, two realistic Lennard-Jones like potentials energy curves (PECs) are considered, which are both depicted in fig. 5. It is further assumed that there exists a coupling with coupling strength Ω between them, as otherwise their treatment would be completely separable. Taking the coupling into account, it is possible that a probability density current entering through one particular state is fragmented into multiple state outcomes during the collision. A *channel* is then defined as a set of stable fragments that can enter or leave a collision. The system is assumed to be prepared in a certain atomic state, defining the entrance channel of the system. The red and the blue curve can then be assigned asymptotically to two different hyperfine state combinations, e.g. $|\psi_{\text{red}}\rangle = (|1\rangle_{\text{Na}} + |1\rangle_{\text{K}})$ and $|\psi_{\text{blue}}\rangle = (|2\rangle_{\text{Na}} + |1\rangle_{\text{K}})$ with $|f\rangle_i$ denoting the total angular momentum quantum number of species i. In

5 The concept at work is hence similar to the way light resonates in a Fabry-Perot cavity on resonance.

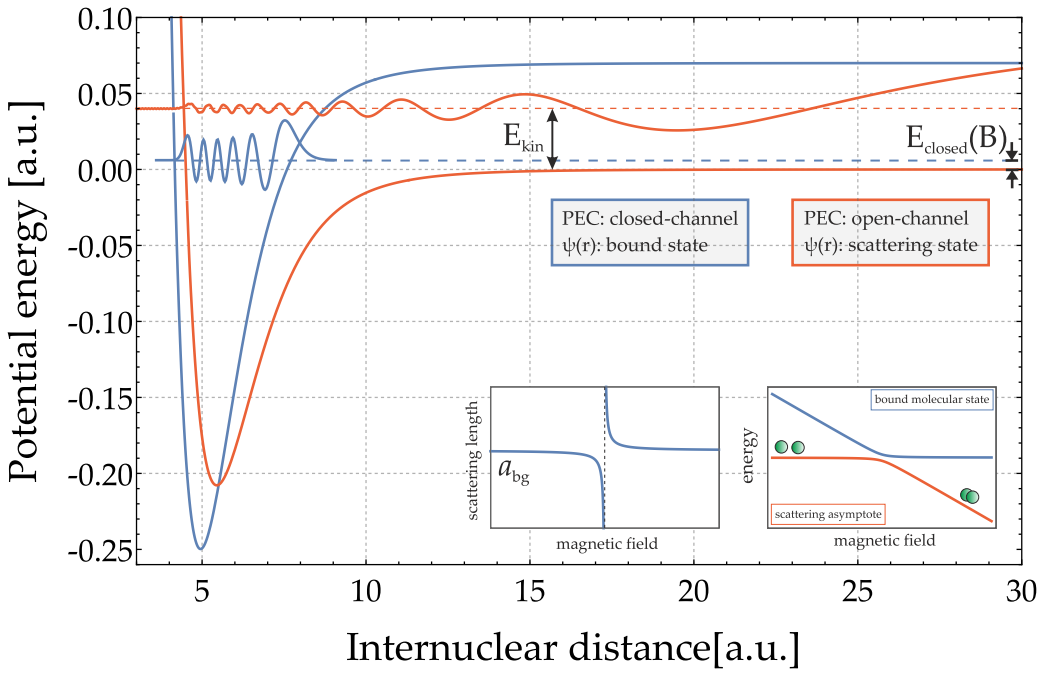

Figure 5: Two-channel model schematic of a Feshbach resonance. The molecular potential curves correspond to the open (red) and the closed (blue) channel, respectively. Tuning $E_{closed}(B)$ to zero with the help of magnetic fields gives rise to a Feshbach resonance that resonantly amplifies the scattering length of the incident channel (right inset). The Feshbach resonance features an avoided crossing of free atomic and bound molecular state (left inset). An adiabatic sweep of the magnetic field transforms one into the other.

this case, their coupling will be given by the hyperfine spin-orbit interaction. In general, their different spin composition leads to different magnetic moments and therefore to a differential Zeeman energy shift. As before, the considered diatomic collision takes place in the ultra-cold limit ($k \to 0$). Even though its kinetic energy E_{kin} is practically zero, the scattering wave function (red curve) is not bound by the molecular PEC, therefore the red PEC represents an *energetically open* channel. The second, blue PEC is chosen such that its dissociation energy is larger than the sum of E_{kin} and the entrance channel dissociation energy. So from the perspective of the entrance channel, the blue PEC represents a closed channel of the system. It further features a molecular bound state at an energy $E_{closed}(B)$ that is close to the zero energy of the entrance channel, and that is magnetically tunable with respect to the entrance channel. On the basis of the extensive discussion using square wells, the concept of a *Feshbach resonance* can now be easily understood as follows: By magnetically tuning $E_{closed}(B)$ to zero (and, similarly, $E_{kin} \to 0$), the scattering solution becomes resonant with the molecular bound state. Its finite coupling Ω then mediates Landau-Zener like transitions between free atomic and bound molecular state, and the scattering length gets resonantly amplified in presence of the bound state. Therefore Feshbach resonances can be seen as the natural *multi-channel* extension of the single-channel zero-energy resonances discussed in the previous toy model.

The insets of fig. 5 further sketches the two powerful features that render Feshbach resonances a standard tool in cold atomic and molecular experiments:

1. If there was no coupling between red and blue curve, the scattering length would be purely determined by the potential depth and shape of the red entrance channel. This is denoted as the background scattering length a_{bg}. In the vicinity of a Feshbach resonance, it can be written as

$$a(B) = a_{bg}\left(1 - \frac{\Delta B}{B - B_0}\right), \tag{2.10}$$

emphasizing its magnetic tunability. Here, B_0 marks the magnetic field location at which the Feshbach resonance occurs. ΔB is the resonance width that is proportional to the coupling strength Ω. The shape of the scattering length pole depends on the energetic direction from which the molecular bound state enters. This is schematically shown in the right inset of fig. 5 for a state entering "from above". Knowledge of the exact location of Feshbach resonances gives thus nearly **absolute control** over the interaction strength by magnetic fields, as sign and magnitude of the scattering length are freely choosable.

2. As can be seen from the energy level diagram in the left inset of fig. 5, the free diatomic scattering state and the molecular bound state show an avoided crossing at the position of the Feshbach resonance, with an energy gap that is given by the resonance width ΔB. Starting with free atoms, a slow sweep of the magnetic field across the resonance is equivalent to an **adiabatic passage** into the bound molecular state, enabling quantum control of the molecular binding process. Therefore, Feshbach resonances can be seen as a portal into the molecular realm.

2.1.3 *Potential energy curves*

This last part gives a description of the correct form of the interaction potentials and outlines how they can be approached experimentally and theoretically. Accurate knowledge about them is imperative, as they keep the secret of the resonance locations. Their description here features the Born-Oppenheimer approximation, which separates the electronic from the nuclear motion as the latter takes place on comparably large time-scales, such that the electron cloud can adapt to each relative movement of the nuclei. This allows to calculate and adiabatically connect the electronic eigenenergies for each internuclear distance. The result is a characteristic curve that follows a Lennard-Jones form as shown in fig. 6.

The description of diatomic potential energy curves can be dissected into three parts (short-range, chemical and long-range region), which are smoothly connected. The short-range part is strongly repulsive because of the Coulomb interaction of the overlapping electron clouds, and can be modeled with the help of an inverse power law giving a sufficiently steep slope. At internuclear distances larger than the LeRoy radius

$$r_{\text{LeRoy}} = 2\left\{\sqrt{\langle r_A^2\rangle} + \sqrt{\langle r_B^2\rangle}\right\}, \tag{2.11}$$

the atoms of the dimer can be considered detached and the long-range description takes over. Here, $\langle r_i\rangle^2$ is the expectation value of the squared radius of the outermost electron on atom i. Beyond this region, the atoms charge distributions are

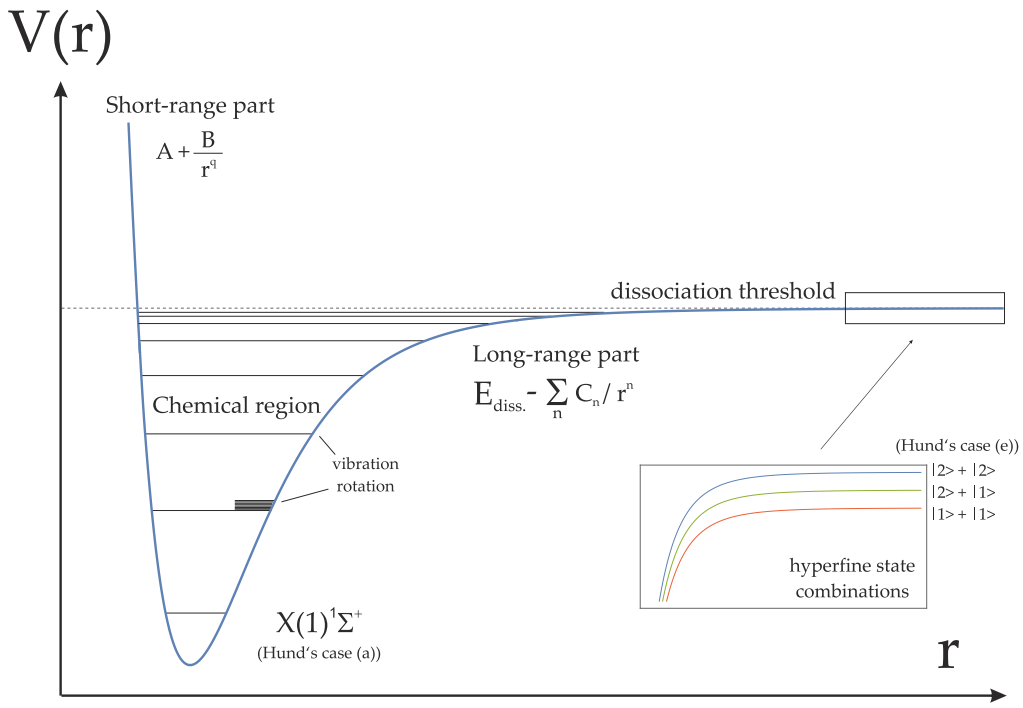

Figure 6: Exemplary potential energy curve, details see text.

separated from each other, and their interaction can be described by Van-der-Waals dispersion forces. The corresponding potential is then given by an inverse power series

$$V_{\textit{Long-range}}(r) = E_{\text{Diss.}} - \sum_n \frac{C_n}{r^n} \tag{2.12}$$

involving the individual dispersion coefficients C_n and the dissociation energy $E_{\text{Diss.}}$. The leading term is given by the properties of the colliding particles, e.g. $r = 6$ for neutral particle collisions such as those discussed here, $r = 4$ for atom-ion interaction *et cetera*. In the fully detached limit ($r \to \infty$), all properties reduce to the atomic ones. As an example, one recovers the hyperfine splitting of the atomic levels (inset in fig. 6). At large internuclear distances, the convenient state representation is therefore given by the individual atomic quantum numbers in an atomic basis set (Hund's case (e)).

In between the short- and long-range regimes, the chemical region is the part in which covalent bonding gives rise to a steep potential minimum and accomodates a number of bound ro-vibrational states. In this region, the correct state nomenclature is given by the "molecular basis" (Hund's case (a)) with ${}^{2S+1}\Lambda^{\pm}_{\Omega}$ symmetry. Here, Λ and Ω are the projections of the electron orbital and total angular momentum along the internuclear axis.

Experimental methods

Experimental efforts to survey potential energy curves can be divided into two type of experiments. In *molecular spectroscopy*, a hot molecular sample is prepared in an atomic beam or a heatpipe, and optically excited using lasers with a large tuning

range (e.g. dye lasers). As there is no selection rule for vibrational levels, the excited molecule decay will branch into the plethora of ground state vibrational levels. Using Fourier-transform spectroscopy (or equivalent methods), the fluorescence spectrum of such a molecule can be recorded and the position of ro-vibrational levels can be determined out of the corresponding transition energies. Given the thermal Boltzmann distribution, this spectroscopic method usually starts at the absolute ground state and allows for an extensive probing of the chemical region, resulting in a map of spectroscopied and assigned vibrational and rotational levels. The long-range region is usually less well explored through the unfavorable Franck-Condon overlap which makes the highest vibrationally excited states difficult to access.

In *Feshbach spectroscopy*, an ultra-cold sample is prepared in a well-defined quantum state. Feshbach resonances are then located by tuning an external magnetic field, equivalent to the two-channel model description employed earlier. The resonantly amplified interaction strength will give rise to typical features, e.g. losses in the atomic population, which makes them traceable as a function of the applied field. Locating resonances for a single specific spin state combination allows predictions for the other ones as they share the same underlying potentials with different admixtures. Predictions can be even made for other isotopic combinations, e.g. ^{23}Na $-^{40}$ K resonances can be used to predict collisions in ^{23}Na $-^{39}$ K and ^{23}Na $-^{41}$ K. As the initial state is given by unbound particles, this method naturally samples the long-range part of the underlying potential and interacts with the least bound states of the potential - therefore molecular and Feshbach spectroscopy can be seen as complementary measurements, which if combined yield the true potential description.

Theoretical methods

The theoretical framework can be roughly divided into the acquisition of bound and scattering solutions, respectively. Bound state solutions are needed if one wants to navigate through molecular spectra, e.g. by searching for an optimal optical transition from one molecular state to the other. The scattering problem has to be solved if one is interested in scattering properties such as the scattering length or the location of Feshbach resonances. In both cases, the simple two-channel approach that was shown for the explanation of Feshbach resonances has to be expanded to the multi-channel system of the diatomic collision.

Because of the cylindrical symmetry, the individual angular momenta are not conserved during the collisions, but the total magnetic quantum number $\mathcal{M}$ is. Therefore, for a given $\mathcal{M}$, the number of channels is given by the number of possible projections of the individual angular momenta onto the space fixed axis that equate to this value $\mathcal{M}$. As a simple example, consider the atomic state labels $(f, m_f)_A$ with the total angular momentum f and its projection m_f for species A, and further set $\ell = 0$. Then, the state combinations

$$|\psi_1\rangle = |1, 0\rangle + |1, -1\rangle \tag{2.13}$$

$$|\psi_2\rangle = |1, -1\rangle + |1, 0\rangle \tag{2.14}$$

$$|\psi_3\rangle = |1, 1\rangle + |2, -2\rangle \tag{2.15}$$

all share the same total magnetic quantum number, $\mathcal{M} = -1$. When the atomic pair corresponding to $|\psi_1\rangle$ is prepared in the experiment, the coupling to $|\psi_2\rangle$ and $|\psi_3\rangle$ (and all other channels equating to $\mathcal{M} = -1$ with nonvanishing coupling matrix element to $|\psi_1\rangle$) has to be accounted for in the theoretical description of the scattering process. In matrix form, the N channels are comprised in a single column vector

$$\boldsymbol{\Psi}(r) = \begin{pmatrix} \psi_1(r) \\ \vdots \\ \psi_N(r) \end{pmatrix} \tag{2.16}$$

The N internal states are then coupled through the matrix elements of the Hamiltonian H of this collisional vector space. The resulting set of coupled differential equations

$$\frac{-\hbar^2}{2\mu}\frac{d^2\boldsymbol{\Psi}(r)}{dr^2} + (\boldsymbol{W}(r) - E \cdot \boldsymbol{I})\,\boldsymbol{\Psi}(r) = 0, \tag{2.17}$$

where $\boldsymbol{I}$ is the identity matrix, are the multi-channel extension of the simple single-channel radial Schroedinger equation (2.5) set up in the beginning of this section. The coupling matrix elements $\boldsymbol{W}_{ij}(r)$ comprise terms such as the hyperfine, magnetic spin-spin and Zeeman interaction as well as the potential energy curves for the electronic levels. They can be implemented using *ab-initio* calculated values, and sometimes have been acquired experimentally. Represented in an atomic basic set and in the long range limit $r \to \infty$, they correspond to the atomic description, e.g. the hyperfine operator will be diagonal and reduces to the hyperfine splitting with a splitting constant α.

The numerical treatment of this problem is straightforward (which should not be confused with easy). Bound state solutions are obtained through diagonalization of a matrix to obtain the eigenenergies and bound state eigenfunctions after the system has been put on a radial grid. Even for a vast Hilbert space and enormous amount of coupling coefficients, fast and efficient spectral methods such as the split-operator [85] or Fourier grid method [86] exist. The treatment of scattering solutions is significantly more demanding. In a typical *coupled-channel calculation*, the N-channel wave function $\boldsymbol{\Psi}(r)$ is propagated numerically and matched to asymptotic functions, similar to the simple sine wave comparison showed at the beginning of the section. In the multi-channel case, the solutions are matched to Bessel functions [87], resulting in the scattering matrix $S(E)$ that comprises all phase shifts φ_n for a given energy:

$$S(E) = \sum_n^N e^{2i\varphi_n} |n\rangle\langle n|. \tag{2.18}$$

Repeating this simulation for a variety of magnetic fields and collision energies unveils the location of resonant structures. This method is straightforward yet computationally expensive, with the computation time scaling as N^3 where N is the number of involved channels [88]. It can therefore reach its limits when a calculation has to be performed on a fine grid of collisional energies and magnetic fields or has to incorporate a large number of rotational angular momenta. This motivated the development of alternative calculational strategies that try to generate

computational shortcuts using approximations. Multi-channel quantum defect theory (MQDT) is used to obtain a matrix $\xi(E, B)$, that encapsulates all short-range dynamics and is rather insensitive towards changes in the collision energy E or magnetic field B. Therefore, this matrix has to be obtained only once, which significantly shortens the number of operations over time [88]. Another, even cruder approximation is done in the asymptotic-bound state (ABM) model. As the location of a bound state near threshold is a core element for the appearance of resonant scattering signatures, the ABM model replaces the kinetic and interatomic part directly by their bound-state energies. The main appeal of this model is that it gets rid of all scattering states. Because only bound states have to be considered, the problem simplifies again to the diagonalization of a matrix, therefore neither the amount of written code nor the computational costs will be obstacles.

These three methods (coupled-channel, MQDT, ABM) strongly vary in complexity, which also defines their application area. If one is interested in a coarse prediction of Feshbach resonance locations and can extract the scattering properties experimentally, the fast and simple yet effective ABM model constitutes an appealing approximative approach to the problem. Therefore it is often employed as a first navigational guide in cold atom labs, after which the experiment itself can be used to pinpoint the resonance location. The appeal of MQDT is that it provides scattering observables such as the scattering length (which the ABM does not) and yet is computationally lighter than a full coupled-channel approach. Nevertheless, the coupled-channel calculation remains the most exact approach as it involves no approximations with the exception of basis truncation. It therefore will give the highest accuracy, which was confirmed by a recent, detailed comparative study employing all three models together and comparing them to experimental data [89].

Putting it together

On the one hand, both of the presented experimental methods, molecular and Feshbach spectroscopy, demand high-quality theoretical models through the assignment of the fluorescence data as well as the prediction and assignment of resonance channels. On the other hand, the accuracy of the theoretical predictions are strongly dependent on the quality of the experimental data. The *diatomic researcher* is faced with the experimental task to acquire spectroscopic data and the theoretical task to reconstruct the corresponding PECs. Upon reviewing these together with *ab-initio* calculations, further improvements can be proposed. In ultra-cold experiments, scattering calculations have to be performed that give access to the collisional properties of the system. Recasting these into experimentally observable quantities, these calculations give the parameter region in which typical scattering signatures can be discovered and further help in interpreting such signatures correctly. In the framework of molecular potentials, the interplay between theory and experiment can thereby be seen as a continuous feedback loop, with collaboration leading to fruitful advances for both nodes.

2.2 THE COLD PLAYGROUND: BOSE-EINSTEIN CONDENSATES

"The sample in our lab is the only chunk of this stuff in the universe, unless it is in a lab in some other solar system."
- E. Cornell [90]

The previous section focused exclusively on the interaction between two particles. Even though the scattering problem was decomposed using the formalism of wave mechanics, the resulting scattering observables can still be assigned to classical trajectories of particles. For non-resonant repulsive interactions, the billard ball analogy perfectly holds.

The following section treats the complementary situation: The particle interactions are neglected, but their quantum nature is emphasized and their number is drastically increased. The latter statement means that methods from statistical mechanics can be applied. These describe the thermodynamic properties of an ensemble that occupies a certain region in the phase space spanned by the conjugate variables position (x, y, z) and momentum (p_x, p_y, p_z). Defining a box with volume given by the Planck constant h,

$$\Delta_x \Delta_y \Delta_z \Delta_{p_x} \Delta_{p_y} \Delta_{p_z} = h^3, \tag{2.19}$$

and asking how many particles are in the box, the answer will be equal to the *phase space density* (PSD) of the ensemble.

An increase in the quantum nature implies that the thermal de Broglie wavelength Λ, i.e. the ensemble average of all single particle matter wavelengths $\lambda = \frac{h}{p}$,

$$\Lambda = \sqrt{\frac{2\pi\hbar^2}{m k_B T}}, \tag{2.20}$$

is significantly large. Here $\hbar = \frac{h}{2\pi}$, k_B is the Boltzmann constant and T the ensemble temperature. Combining eq. (2.19) and (2.20) while denoting the density of the sample as n, the PSD can be written as

$$\mathrm{PSD} = n\Lambda^3. \tag{2.21}$$

When Λ reaches the typical interparticle distance of the ensemble ($\Lambda^3 \sim 1/n$), the wavepackets will start to overlap. What then happens is determined by the quantum statistics of the ensemble, and is quite spectacular for the bosonic case treated here.

2.2.1 *Bose-Einstein statistics*

In the following, a quantum gas of indistinguishable, non-interacting bosonic particles is discussed. Because of the lack of interactions, a good choice for the N-particle state $|\Psi\rangle$ describing the system is given by the direct product of the single-particle states $\psi_{\mathbf{s}_i}$ that are each fully described by a set of quantum numbers $\mathbf{s}_i$. Due to their indistinguishable nature, the state has to be additionally symmetrized by summing over all possible permutations $\mathcal{P}$ of the $(1, \ldots, N)$-tuple:

$$|\Psi\rangle = \mathcal{N} \sum_{\mathcal{P}} (+1)^P \mathcal{P} \left(|\psi_{\mathbf{s}_1}\rangle |\psi_{\mathbf{s}_2}\rangle \ldots |\psi_{\mathbf{s}_{N-1}}\rangle |\psi_{\mathbf{s}_N}\rangle \right), \tag{2.22}$$

with a normalization factor $\mathcal{N}$, and where the plus sign was explicitly written to emphasize the proper symmetric solution needed for describing bosons (a negative sign would appear for fermions that populate the vector space spanned by antisymmetric states).

In the Fock basis $|N; \dots n_i \dots\rangle$, the N-particle state $|\Psi\rangle$ is fully determined by the occupation numbers $n_i (= 0, 1, 2, \dots)$ that indicate how many particles are in a given state $|\psi_{s_i}\rangle$. The mean occupation number can be expressed by a distribution function $\langle n_i \rangle = n(\varepsilon_i)$ that depends on the single-particle energy ε_i of a particle in state $|i\rangle$. For a particle in free space as considered here, $\varepsilon(p) = p^2/2m$, hence $\varepsilon_0 = 0$ for the ground state energy of the system. Under the constraint $N = \sum_i n(\varepsilon_i)$, the occupation distribution can be evaluated via the Landau grand potential [78], which yields the *Bose-Einstein distribution*

$$n(\varepsilon_j) = \frac{1}{e^{\beta(\varepsilon_i - \mu)} - 1}, \tag{2.23}$$

with $\beta = (k_B T)^{-1}$. The chemical potential μ has to satisfy $-\infty < \mu < 0$ as it will lead to negative occupation or divergence otherwise.

For high temperatures ($\beta \to 0$), this expression converges to the classical Boltzmann distribution. In the low-temperature case ($\beta \to \infty$), something remarkable happens. To highlight this, it is used that in statistical mechanics the number of particles *usually* can be written in the density of state formalism that turns energy dependent sums into integrals over the energy,

$$N = \sum_i n(\varepsilon_i) = \int d\varepsilon \, \mathcal{D}(\varepsilon) \, n(\varepsilon), \tag{2.24}$$

with the three-dimensional density of states $\mathcal{D} \propto V T^{3/2} \sqrt{\varepsilon}$ where constants have been omitted for lucidity. Note that in the thermodynamic limit, one has $N \to \infty$, $V \to \infty$, but $N/V = \text{const.}$ Hence

$$\frac{N}{V} = \text{const.} = T^{3/2} \int_0^\infty d\varepsilon \, \frac{\sqrt{\varepsilon}}{e^{\beta(\varepsilon - \mu)} - 1}. \tag{2.25}$$

For $T \to 0$, the value of the integral has to increase, and this compensation can only be done by adjusting its denominator through $\mu \to 0$. As the absolute value of μ is bounded from below, this formalism will break down at some *critical temperature* T_c. Setting $\mu = 0$, the integral at T_c can be evaluated using the geometric series, giving

$$\int_0^\infty d\varepsilon \frac{\sqrt{\varepsilon}}{e^\varepsilon - 1} = \int_0^\infty d\varepsilon \sqrt{\varepsilon} \sum_{n=1}^\infty e^{-n\varepsilon} = \sum_{n=1}^\infty \frac{1}{\sqrt{n^3}} \int_0^\infty d\varepsilon \, \sqrt{\varepsilon} \, e^{-\varepsilon} = \Gamma(3/2) \, \zeta(3/2) \tag{2.26}$$

where the integral has been recast into a product of Gamma and Riemann Zeta functions:

$$\Gamma(3/2) = \sqrt{\pi}/2; \quad \zeta(3/2) = 2.612 \tag{2.27}$$

Beyond this point, the formalism above has to be re-evaluated. Note that as $\mu \to 0$, the relative population of the ground state should increase massively according to eq. (2.23). On the other hand, the density of states scales as $\sqrt{\varepsilon}$, so the ground state has a relative weight of zero. This apparent contradiction is resolved by applying the density of states formalism starting from the first excited state and treating the ground state population N_0 separately:

$$\frac{N}{V} = \frac{1}{V} [N_0(T) + N_{\text{exc.}}(T)] = \frac{N_0(T)}{V} + \frac{\zeta(3/2)}{\Lambda^3(T)}, \tag{2.28}$$

where the integral (2.26) has been evaluated for the excited state part and the temperature dependence of Λ is explicitly written. As N/V is the density, the phase-space density can be identified in the equation. It can be shown that the selective treatment of the ground state is not necessary for the first or further excited states [78], which makes sense since the energy difference between ground and first excited state already forms a huge gap as the temperature goes to zero. At temperatures $T < T_c$, $\Lambda(T)$ increases and the excited states can accomodate less particles, which in turn will start to *condense* in the ground state. It then follows that

$$\frac{N_{exc.}(T)}{V} = \frac{\zeta(3/2)}{\Lambda^{-3}(T)} = \frac{\left(N\Lambda^3(T_c)\right)}{\Lambda^3(T)} = N\left(\frac{T}{T_c}\right)^{3/2} \tag{2.29}$$

and the ground state population can be expressed as

$$\frac{N_0(T)}{N} = 1 - \left(\frac{T}{T_c}\right)^{3/2}. \tag{2.30}$$

Therefore at T_c, a phase transition occurs, characterized by a macroscopic population of the ground state. This is the process of Bose-Einstein condensation. It is a truly remarkable result if one takes into account that bosons do not have to evade each other (therefore their occupation numbers are not restricted, which is the case for fermions), and no direct interaction has been imposed between them.

The treatment up to here involved a free bosonic part and the thermodynamic limit. In a real experiment, the bosons are usually confined in a trap and their atom number is large, but finite ($N \sim 10^5$). The treatment for a 3D harmonic trap with trap frequencies $\omega_{x,y,z}$ is analogous to the one above and only involves a slightly different density of states. The result of eq. (2.30) is the same up to a different exponent, i.e.

$$\left(\frac{N_0(T)}{N}\right)_{\text{harm.}} = 1 - \left(\frac{T}{T_c}\right)^3 \tag{2.31}$$

The critical temperature T_c can then be expressed by the experimental parameters through

$$k_B T_c \simeq 0.94\hbar\left(\omega_x\omega_y\omega_z N\right)^{1/3}. \tag{2.32}$$

Through finite size effects, this number will be slightly shifted. As an example, for an atom number $N = 1000$, the real transition temperature is lowered by about 7% [91].

2.2.2 *Gross-Pitaevskii equation*

In this part, the quantum mechanical framework of the condensed bosonic cloud is presented. By using some well-tested approximations, the problem reduces to a non-linear Schroedinger equation. Starting from there, the experimentally relevant density distribution is discussed in combination with the sign and magnitude of the interaction strength.

In light of the large densities prevailing in a condensed gas compared to a thermal cloud, interactions can no longer be neglected. Writing the single-particle Hamiltonian as

$$H_0 = -\frac{\hbar^2}{2m}\nabla^2 + V(\mathbf{r}, t), \tag{2.33}$$

the Hamilton operator in second quantization is given by

$$\hat{H} = \int d^3r\, \hat{\psi}^\dagger\, H_0\, \hat{\psi} + \frac{1}{2}\int d^3r \int d^3r'\, \hat{\psi}^\dagger(\mathbf{r})\hat{\psi}^\dagger(\mathbf{r}')\, V_{\text{int}}(\mathbf{r}-\mathbf{r}')\, \hat{\psi}(\mathbf{r}')\hat{\psi}(\mathbf{r}), \quad (2.34)$$

where $\hat{\psi}^{(\dagger)}$ are the corresponding bosonic annihilation (creation) operators. The time dependence for the field operators is obtained in the Heisenberg picture

$$i\hbar\partial_t\hat{\psi}(\mathbf{r},t) = \left[\hat{\psi}(\mathbf{r},t), H\right] = \left\{H_0(t) + \int d^3r'\, \hat{\psi}^\dagger(\mathbf{r},t)\, V_{\text{int}}(\mathbf{r}-\mathbf{r}')\, \hat{\psi}(\mathbf{r},t)\right\}\hat{\psi}(\mathbf{r},t). \quad (2.35)$$

This equation can be simplified using some approximations. First and foremost, the extensive discussion of the last section on ultra-cold scattering showed that the exact interaction potential is not important as long as it gives rise to the same scattering length. Therefore, the true interaction potential is replaced by a pseudo-potential

$$V_{\text{int}}(\mathbf{r}-\mathbf{r}') \to \frac{4\pi\hbar^2}{m}\, a\, \delta(\mathbf{r}-\mathbf{r}') \equiv g\delta(\mathbf{r}-\mathbf{r}'), \quad (2.36)$$

where the interaction strength g was introduced. The field operator is expressed by the system's single-particle eigenfunctions and their corresponding annihilation and creation operators

$$\hat{\psi}(\mathbf{r}) = \sum_i \phi_i(\mathbf{r})\hat{a}_i = \varphi_0(\mathbf{r})\hat{a}_0 + \sum_{i\neq 0}\phi_i(\mathbf{r})\hat{a}_i, \quad (2.37)$$

where the ground state has been explicitly separated. The creation and annihilation operators satisfy the bosonic commutation relations

$$\left[\hat{a}_i, \hat{a}_j^\dagger\right] = \delta_{ij}; \quad \left[\hat{a}_i, \hat{a}_j\right] = \left[\hat{a}_i^\dagger, \hat{a}_j^\dagger\right] = 0. \quad (2.38)$$

As $T \to 0$, more and more particles assemble in the ground state. For a macroscopic occupation N_0, adding or removing one particle should not change the physical picture significantly. This justifies the replacement of the ground state operators by complex numbers through

$$\hat{a}_0^\dagger \approx \hat{a}_0 \approx \sqrt{N_0}, \quad (2.39)$$

which is refered to as a part of the Bogoliubov approximation. The complete Bogoliubov approximation also neglects additional anharmonic terms involving multiple creation and annihilation operators. These are on the order of $N - N_0$ and neglecting them is reasonable for $N_0 \approx N$. In such a *mean-field* description of the sytem, the condensed part is described by a single complex number $\psi_0(\mathbf{r})$ that is called the condensate wave function. The total field operator (2.37) then acquires the form

$$\hat{\psi}(\mathbf{r}) = \underbrace{\psi_0(\mathbf{r})}_{\text{condensate}} + \underbrace{\delta\hat{\psi}}_{\text{fluctuations}}. \quad (2.40)$$

Neglecting the excited state fluctuations $\delta\hat{\psi}$ and using the pseudo-potential approach realizes the *Gross-Pitaevskii equation* (GPE)

$$i\hbar\,\partial_t\psi_0(\mathbf{r},t) = \left\{-\frac{\hbar^2}{2m}\nabla^2 + V_{\text{ex}}(\mathbf{r},t) + g|\psi_0(\mathbf{r},t)|^2\right\}\psi_0(\mathbf{r},t), \quad (2.41)$$

which is a nonlinear Schroedinger equation that features an interaction induced nonlinearity $g|\psi_0(\mathbf{r},t)|^2$.

BEC density distribution

It is now shown how the condensate interactions modify the density distribution of the ensemble. For this, the confinement is assumed to be harmonic and separable in all directions, which reflects the commonly used trapping environment in cold atoms experiments:

$$V(\mathbf{r}) = \sum_{i}^{3} \frac{1}{2} m \omega_i^2 x_i^2, \qquad (i = x, y, z). \tag{2.42}$$

By integrating the phase space density distribution over all momentum coordinates, the density profile in configuration space is obtained (the momentum distribution can be obtained analogously). Remember that in the high-temperature limit, the Bose-Einstein distribution converges to the Maxwell-Boltzmann distribution, so its density profile will reduce to the well-known Gaussian:

$$n_{\text{Thermal}}(\boldsymbol{r}) = \exp\left[-\sum_{i}^{3} \frac{x_i^2}{2\sigma_i^2}\right], \tag{2.43}$$

with the characteristic spatial extent $\sigma_i = \omega_i^{-1}\sqrt{k_B T/m}$ and the peak density normalized to one. When the temperature and therefore the PSD approaches its critical value, the Bose-Einstein distribution has to be used. Using (2.23), this becomes

$$n_{\text{Bose}}(\boldsymbol{r}) = \frac{1}{g_{3/2}(1)} g_{3/2}\left\{\exp\left[-\sum_{i}^{3} \frac{x_i^2}{2\sigma_i^2}\right]\right\}, \tag{2.44}$$

with the polylogarithmic function

$$g_{3/2}(z) = \sum_{n=1}^{\infty} \frac{z^n}{n^{3/2}}; \qquad g_{3/2}(1) = \zeta(3/2) = 2.612 \tag{2.45}$$

that leads to a *Bose-enhanced Gaussian* distribution. It is noted that the higher order terms in this series vanish quickly not only for increasing temperature, but also for a large distance to the clouds peak density. This motivates the often used approach to analyze primarily the wings of the non-condensed distribution, when (2.44) again reduces to (2.43). It is now shown that the density profile of a condensed cloud has a significantly different functional form than both of the two descriptions above.

Using the ansatz $\psi_0(\mathbf{r}, t) \stackrel{!}{=} f(t)\psi_0(\mathbf{r})$, the GPE can be written in its stationary form

$$\mu\, \psi_0(\mathbf{r}) = \left\{-\frac{\hbar^2}{2m}\nabla^2 + V_{\text{ex}}(\mathbf{r}) + g|\psi_0(\mathbf{r})|^2\right\}\psi_0(\mathbf{r}). \tag{2.46}$$

The chemical potential $\mu = (E(n) - E(n-1))/\hbar$ describes the energy of a particle in presence of all the other ones, and therefore can be seen as a manifestation of the mean-field approximation used earlier. Through the interaction term, the density distribution appears in the description of the problem (because $|\psi_0(\mathbf{r})|^2 = n_0(\boldsymbol{r})$) and will affect the energy of the system according to the sign of g. As shown in the last section discussing scattering theory, the sign of the scattering length

dictates whether the interacting particles experience effective repulsion ($a > 0$) or attraction ($a < 0$). An attractive interaction will contract the cloud and increase the density, which in turn increases the strength of this attraction. Through this mutually reinforcing mechanism, the cloud becomes mechanically instable and collapses into a high-density region before it is scattered all over the place (Bosenova [92]). Therefore, only tiny condensates on the order of a thousand atoms can be maintained with attractive interaction, when their collapse is counteracted by the kinetic energy of the trapped system [93]. Being interested in stable condensates with large atom numbers, only repulsive interactions are considered.

With $g > 0$, the interaction energy minimizes if the wave function is spread as uniformly as possible, which then depends on the trapping environment. When the product of particle number and scattering length is large compared to the typical trapping length scale (e.g. the oscillator length $\overline{a}_i = \sqrt{\hbar/m\omega_i}$), the kinetic term is outmatched by the interaction term and can be neglected (Thomas-Fermi approximation). The stationary GPE in this case simplifies to

$$\mu\,\psi_0(\mathbf{r}) = \left\{V_{ex}(\mathbf{r}) + g|\psi_0(\mathbf{r})|^2\right\}\psi_0(\mathbf{r}) \tag{2.47}$$

which is analytically solvable:

$$|\psi_0(\mathbf{r})|^2 = \begin{cases} \frac{\mu - V(\mathbf{r})}{g} & \mu \geqslant V(\mathbf{r}) \\ 0 & \text{else} \end{cases} \tag{2.48}$$

Therefore the density profile acquires the inverted form of the trapping potential and can be seen to fill up the trap in a similar fashion in which a liquid starts filling a container. The chemical potential can be written in terms of the experimentally accessible parameters atom number and trap frequencies as

$$\mu = \frac{15^{2/5}}{2}\frac{N\,a}{\overline{a}}^{2/5}\hbar(\omega_x\omega_y\omega_z)^{1/3} \tag{2.49}$$

For the harmonic trap, the density profile is given by an inverted parabole in every direction that fills the interior of an ellipsoid:

$$n_{BEC}(\boldsymbol{r}) = \left(1 - \sum_i^3 \frac{x_i^2}{R_i^2}\right)\theta\left(1 - \sum_i^3 \frac{x_i^2}{R_i^2}\right) \tag{2.50}$$

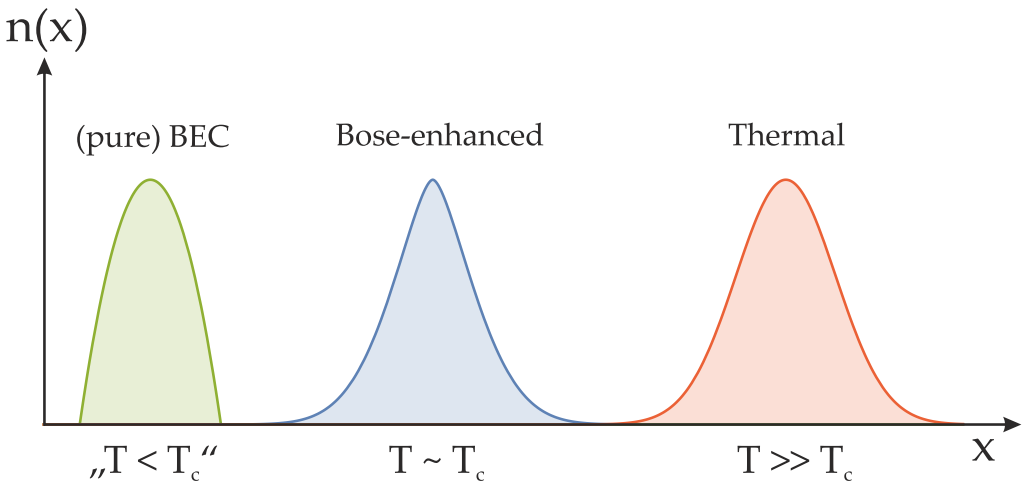

Figure 7: Density profiles for a condensed, Bose-enhanced and thermal cloud.

with the Heaviside theta θ and where the peak density is again normalized to one. Its radial extent in one of the directions x_i is called the Thomas-Fermi radius

$$R_i = \sqrt{\frac{2\mu}{m\omega_i^2}}. \tag{2.51}$$

The onset of Bose-Einstein condensation is therefore directly observable through analysis of the ensemble's density distribution. All three density profiles are shown next to each other in fig. 7. The notion "$T < T_c$" that is featured there has to be used with care - as a BEC does not follow a Maxwell-Boltzmann distribution, a temperature in the thermodynamic sense cannot be assigned to it. In the following, it will always be assumed that a residual non-condensed ("thermal") part is still present in the trap, for which temperature is a well-defined quantity, and that both condensed and thermal part are in thermal equilibrium with each other.

Mixture phases in the two-component GPE

Quantum gas mixtures are realized by encoding different components either in the spin degree of freedom (spinor BECs) or by using different atomic species. The generalization of the GPE framework to a multiple-component version is rather straightforward [94]. In the case of a two-component mixture, both components are represented through their own condensate wave function, and an additional non-linear term $\sim g_{12}$ describes their interspecies interaction. The following discussion of possible mixture quantum phases follows [95] and [96]. In the stationary case, the system is described by the coupled two-component GPE:

$$\mu_1\psi_1(r) = \left\{\frac{-\hbar^2}{2m_1}\nabla^2 + V_1(r) + g_{11}|\psi_1(r)|^2 + g_{12}|\psi_2(r)|^2\right\}\psi_1(r), \tag{2.52}$$

$$\mu_2\psi_2(r) = \left\{\frac{-\hbar^2}{2m_2}\nabla^2 + V_1(r) + g_{22}|\psi_2(r)|^2 + g_{12}|\psi_1(r)|^2\right\}\psi_2(r), \tag{2.53}$$

where the chemical potentials μ_i for component i are given by the normalization condition $\int d\boldsymbol{r}|\psi_i(\boldsymbol{r})|^2 \stackrel{!}{=} N_i$. Because $g_{11} < 0$ or $g_{22} < 0$ leads already to collapse of the single-component wave function, both intraspecies interactions are assumed to be positive. Then, depending on the sign and magnitude of the interspecies interaction strength, the clouds will try to coalesce or evade each other, realizing a set of different mean-field quantum phases. In the simplest case of a homogeneous environment, the energy of a fully phase separated and the energy of a miscible system is given by

$$E_{sep} = \frac{g_{11}N_1^2}{2V_1} + \frac{g_{22}N_2^2}{2V_2}, \tag{2.54}$$

$$E_{mis} = \frac{g_{11}N_1^2}{2V} + \frac{g_{22}N_2^2}{2V} + \frac{g_{12}N_1N_2}{V}. \tag{2.55}$$

Note that the subscript of the volumes is different, i.e. $V = V_1 + V_2$ is the total volume occupied of both species together. The two separated phases in E_{sep} can be linked through the mechanical equilibrium criterion $\partial_{V_1}E_{sep} \stackrel{!}{=} \partial_{V_2}E_{sep}$, when the energy of the separated system can be rewritten in terms of the total volume as

$$E_{sep} = \frac{g_{11}N_1^2}{2V} + \frac{g_{22}N_2^2}{2V} + \frac{\sqrt{g_{11}g_{22}}N_1N_2}{V} \tag{2.56}$$

Comparing equations (2.55) and (2.56), the question which of these two state configurations minimize the energy of the system is answered by the interplay of intra- and interspecies interaction through the *miscibility criterion* $g_{12} < \sqrt{g_{11} g_{22}}$, which gives $E_{sep} > E_{mis}$ and therefore miscibility. A similar analysis can be performed for negative values of g_{12} and asking when energetic instabilities will make the system collapse in a similar way to the Bosenova phenomenon outlined earlier. The general result is:

$$\text{miscible:} \quad |g_{12}| < \sqrt{g_{11} g_{22}} \tag{2.57}$$

$$\text{immiscible:} \quad |g_{12}| > \sqrt{g_{11} g_{22}} \quad \text{and } g_{12} > 0 \tag{2.58}$$

$$\text{collapse:} \quad |g_{12}| > \sqrt{g_{11} g_{22}} \quad \text{and } g_{12} < 0 \tag{2.59}$$

As all three interactions parameters g_{11}, g_{12}, g_{22} are dependent on the respective scattering lengths, they are magnetically tunable and phase transitions can be studied [97, 98, 62].

Recent theoretical and experimental studies have focused on the region in which attractive interspecies interaction is balanced out by the repulsive intraspecies interaction [96, 99]. It is perceivable that when the mean-field effects cancel each other, beyond-mean-field effects can start to play a role. For a single-component gas, the next higher-order quantum corrections to the mean-field description can be written as

$$\frac{E}{V} = \frac{1}{2} g\, n^2 \left[1 + \frac{128}{15\sqrt{\pi}} \sqrt{n\, a^3} \right], \tag{2.60}$$

i.e. the energy density functional is supplemented by an additional, perturbative term called the Lee-Huang-Yang correction [100]. This term is usually much smaller than the mean-field term. Following the seminal work of Petrov [96], the main implication for competing interactions is quickly repeated here in a simplified form. For this, the system is assumed to be composed of equal densities and equal individual intraspecies interactions:

$$g_{11} = g_{22} = g > 0, \tag{2.61}$$

$$n_1 = n_2 = n/2. \tag{2.62}$$

while the interspecies interaction is negative and *a little bit* larger than the intraspecies interaction:

$$\delta g = g_{12} + g < 0 \tag{2.63}$$

It is important to note that while δg will be small, g can be quite sizable. As outlined above, for $\delta g < 0$, the system will be mean-field instable and should collapse. The corresponding chemical potential μ can be written as

$$\mu \propto \delta g\, n + g\, n \sqrt{n\, a^3}. \tag{2.64}$$

Where the first term accounts for the residual mean field shift through the counteracting interaction strengths depending on δg, and the second term denotes the Lee-Huang-Yang correction. Quite importantly, this second term depends on g, not δg!. If δg is sufficiently small, these two terms can therefore become comparable. Moreover, the density dependence of both terms follow a different power. When the system now becomes mean-field instable, the beyond-mean-field term grows

faster with the density, which leads to an equilibration of the two terms at a certain critical density n_0. This *quantum stabilization* mechanism leads to the formation of a *quantum droplet* in the system. This novel quantum state of matter combines some unique characteristics, and their experimental study is currently of high interest [101, 99, 37, 102].

2.3 THE BUILDING BLOCKS: SODIUM AND POTASSIUM

This section outlines the most relevant properties of the chosen atomic species. An extensive selection of atomic properties for the used atoms can be found for sodium in [103] and for potassium in [104].

Strictly speaking, the only species selection criterion for studying Bose-Einstein condensates is that it should be a boson. Yet the process of condensation demands phase space densities on the order of one, and not all species are equally suited for this task. In order to achieve efficient phase space compression, three atomic properties are of importance:

1. The atom should possess a sizable magnetic moment in order to be trappable by magnetic fields.
2. The internal energy structure should comprise isolated optical transitions for efficient laser cooling, and different g-factors in order to be able to achieve magneto-optical trapping.
3. The scattering properties should ensure good thermalization properties for evaporative cooling. Ideally, Feshbach resonances at accessible magnetic field windows should be available.

Alkali atoms excel in all three of these aspects. Their magnetic moment is reasonably large through the unpaired electron. As all other electrons occupy closed-shells, alkali spectra are quite simple, and strong optical transitions are found at convenient wavelengths in the visible-to-infrared-region. At good last, scattering properties can be expressed through the long-range Van-der-Waals dispersion of the atomic pair. The leading term there is the C_6 coefficient, that can be approximately written as $C_6 \approx \frac{3}{4}(\Delta E)^{-3}$, where ΔE is the D line for Alkali systems [105]. As these are in the visible to infra-red regime, the corresponding C_6 coefficient are larger than 10^3, when evaporative cooling can become feasible through the achievable thermalization rates. The alkalis are therefore a splendid choice for the realization of ultra-cold matter. Still, each species exhibits its own pecularities.

The only stable isotope configuration for sodium is ^{23}Na. Together with ^{87}Rb, it is considered as one of the workhorses for bosonic systems, as they share strongly favorable properties for laser cooling and evaporation [106], and it can be condensed by following a "Ketterle-approved" recipe [82]. Potassium possesses three stable[6] isotopes, ^{39}K,^{40}K and ^{41}K, with a natural abundance of 93.26%, 0.01% and 6.73%, respectively. Along the alkalis, it provides the unique feature that both bosonic (^{39}K,^{41}K) as well as fermionic (^{40}K) isotopic combinations can be studied, a feature otherwise only shared by Lithium.

6 strictly speaking, ^{40}K is a radioactive β^- emitter, and its decay channel into argon is used for radiometric dating. Its half-life of 1.28×10^9 years renders it quasi-stable for all ultra-cold purposes.

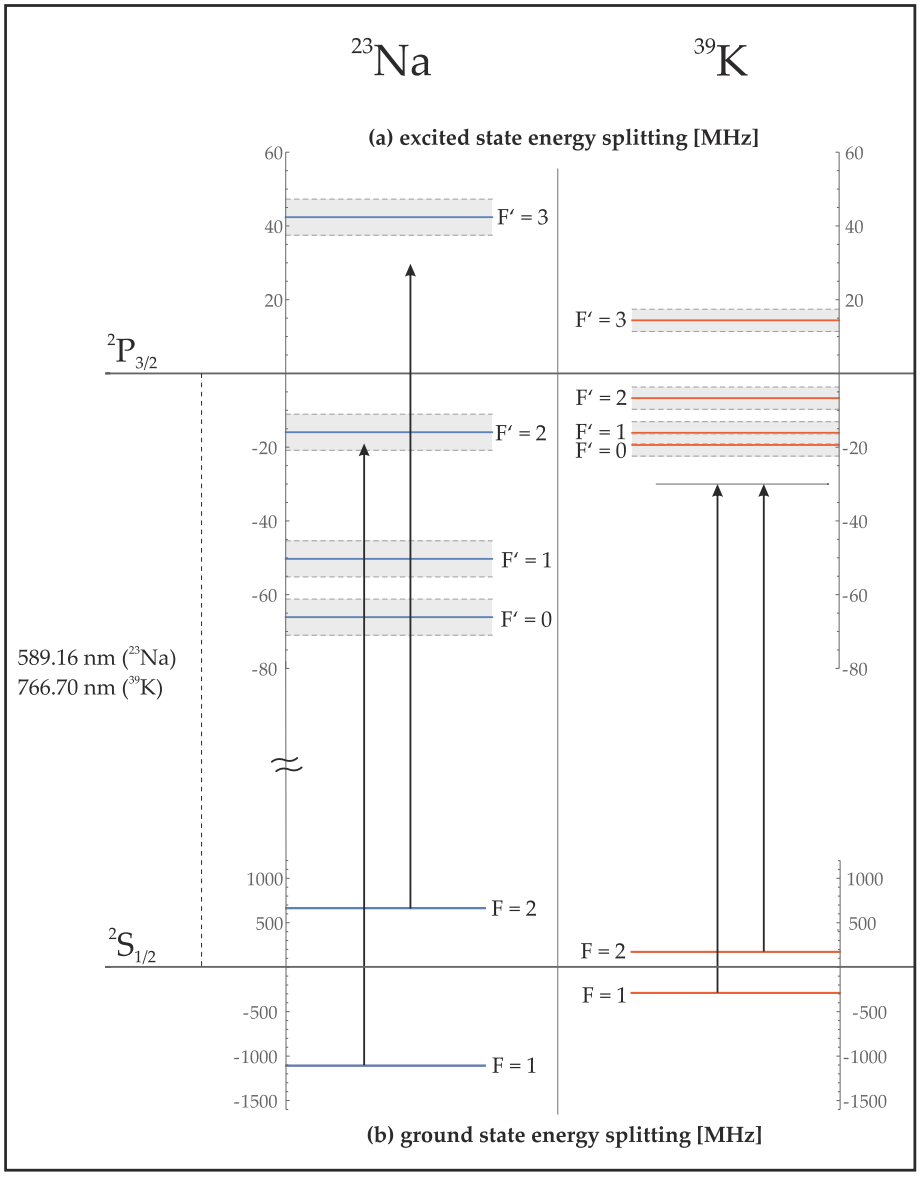

Figure 8: Energy diagrams and ultra-cold collisional properties of both ^{23}Na and ^{39}K for the relevant internal states utilized throughout this thesis.

Owing to their same nuclear spin of $i = 3/2$, the atomic level structure of both atoms is qualitatively identical, with the same quantum numbers and projections and the same linear Zeeman shifts.[7]. Quantitatively, ^{39}K has some distinct atomic and spectral features, rendering the route towards Bose-Einstein condensation more challenging. These can be found in fig. 8, in which the D2 line energy diagram and the magnetic-field dependent scattering interaction (for collisions in the spin channel $|1,-1\rangle + |1,-1\rangle$) is depicted for both species. Due to its small nuclear magnetic moment [107], the hyperfine splitting of ^{39}K is much smaller compared to ^{23}Na. In fact, the hyperfine spacing of the excited state manifold does not outweigh the linewidth of the individual lines, $\Gamma_K = 2\pi \times 6.035$ MHz. Hence, it becomes difficult to isolate cooling transitions from each other, when the notion of a 'cyclic' transition will be less pronounced than for ^{23}Na. If one employs conventional laser cooling by red-detuning a few linewidths (indicated in fig. 8 by arrows representing cooling and repumping beams, respectively), the whole multiplet will be excited instead. This induces interference effects between the sublevels, ultimatively affecting the laser-cooling forces [108]. Therefore, every optical manipulation involves nontrivial optical pumping effects as well as trade-offs between cooling and heating forces, which have to be accounted for if one wants to either estimate the number of trapped atoms or cool them below the Doppler temperature. In a nutshell, compared with the trailblazing bosonic systems ^{23}Na and ^{87}Rb, large cold samples of ^{39}K are harder to achieve.

The collisional properties of both species are given by its respective singlet and triplet scattering length. In a cold atom system, one is typically interested in the scattering length of a specific spin state instead, which can be obtained by angular momentum recoupling. In this thesis, the spin state combination of interest is $|1,-1\rangle+|1,-1\rangle$, for which ^{23}Na features no resonant structures below 1000 G, and displays a feasible scattering length of $a_{Na} = 52\, a_0$, where a_0 is the bohr radius. The situation for ^{39}K is again unfavorable. By constructing the full two-atom Hamiltonian out of the singlet and triplet potential curves, Bohn and co-workers estimated all Zeeman combinations to exhibit a negative scattering length [109]. The drawbacks of negative scattering are twofold: For negative scattering lengths, the k-dependent s-wave scattering cross section is known to display a steep minimum as k is decreased before it reaches its $k \to 0$ limit value of $\sigma = 4\pi a^2$. This basically disables rethermalization at a given temperature, in this case around $\sim 320\mu$K, hence single-species evaporation will not be efficient. Moreover, once a condensate is formed, its attractive self-interaction renders it mean-field instable. These points make ^{39}K a less desirable choice for cooling as well as condensing, yet solutions to the presented challenges exist and have been succesfully met. In this thesis, ^{39}K is cooled sympathetically, using ^{23}Na as an evaporative refrigerant. Once a condensate is about to form, mean-field stability can be ensured by the presence of an external magnetic field that tunes the scattering properties to a desired value, using one of the three Feshbach resonances that have been tabulated in the literature for this spin state [110].

7 Note that throughout this thesis, small letters are used to denote quantum numbers corresponding to an atom, whereas capital letters are used to describe coupled diatomic quantum numbers such as $F = f_{Na} + f_K$

3 LASER SYSTEMS

The creation of cold atoms demands a variety of laser sources for the purpose of cooling, trapping, internal state manipulation and detection of the atomic ensembles. With the exception of the repulsive blue plug barrier and the optical dipole trap (see section 5.3 and chapter 6), all of these are nearly resonant with the individual D2 line of the corresponding atomic species. Most characteristics of the laser systems will therefore have their roots in the two different fundamental frequencies that have to be provided.

With a wavelength of 767 nm, the D2 transition of ^{39}K lies in the near-infrared region where laser diodes are the laser source of choice. By assembling them in an external-cavity diode laser (ECDL) configuration, the target wavelength can be realized with a small laser linewidth in a simple and reliable setup. Their straight conversion of electric to optical power, the low number of needed components and the moderate costs highlight them as a popular choice in laser laboratories working with ultra-cold atoms.

In the case of ^{23}Na, the D2 transition at 589 nm has posed an experimental challenge in the past, as laser diodes cannot operate in this spectral region. Optical frequencies in the yellow and orange spectral range had to be generated using dye lasers that suffer quick chemical degradation and employ dyes which are poisonous or even carcinogenic. Salvation was brought in 2009 by the astronomers community, in which ^{23}Na fluorescence is utilized to form laser guide stars at an altitude of 100 km. The development of high-power narrowband fiber lasers at 589 nm [111] made this experimental task significantly easier, rendering ^{23}Na nowadays as a highly fashionable laser cooling atom source. The following chapter describes the generation and alteration of the light sources for both atomic species. Both systems are set up and boxed in on an optical table adjacent to the main experimental table. Together with a set of curtains, this separation avoids unwanted stray light in the experiment chamber. An optical fiber distribution network connects the individual laser light ports to the main experiment.

3.1 ^{23}Na LASER SYSTEM

The ^{23}Na laser system was designed and set up in this thesis. A simplified sketch of it involving the most notable optical components is depicted in figure 9. At its heart lies a Visible Raman Fiber Amplifier (VRFA-P-1800-589-SF, MPB communications), that amplifies and frequency-doubles an infrared laser seed source, giving 1.8 W of 589.158 nm single-mode light at a fundamental frequency ω_0.

A variety of seed sources have been built and tested regarding single-mode stability and long-term reliability.[1] In the end, the most reliable performance was

1 Most notable, these included a range of custom Littrow laser designs starring a batch of Innolume laser diodes (*GC-1178-TO-200*). After testing multiple grating lengths, transversal mode suppressions and longitudinal mode restriction methods for different batch items without completely satisfying results, and after communication with the group of G. Ferrari at the INO-CNR (Trento, Italy) revealing similar experiences, the author strongly advises against using the aforementioned laser diode model.

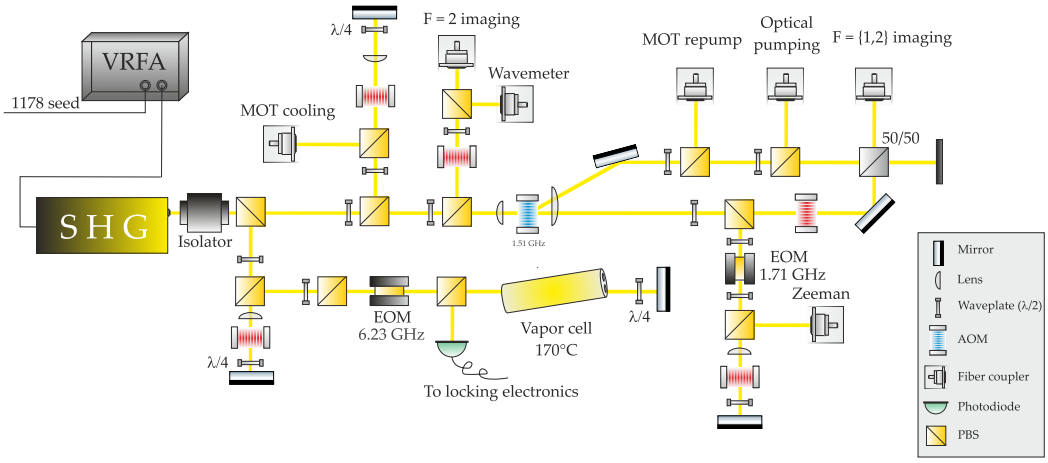

Figure 9: Simplified illustration of the ^{23}Na laser system. Blue (red) color coding of the AOMs illustrate positive (negative) frequency shifts with respect to the incident beam.

achieved by a laser system using a Toptica DFB laser diode (LD-1178-0030-DFB-1). It can emit up to 30 mW in a wavelength window of $1177.5 - 1179.5$ nm that is coarsely tunable via the operating temperature with a tuning coefficient of 0.09 nm/K. By stabilizing the diode housing temperature to 38 °C, the DFB diode emits at a central wavelength of 1178 nm which is fine-tuned by the applied laser diode current. Feeding $\geqslant 10$ mW into the VRFA via an optical fiber, this gets amplified to up to 10 W of infrared power at 1178 nm by fiber laser amplifiers pumped at 1120 nm. Gradual degrading of the fiber amplifier's pump diodes made it necessary to steadily increase the amount of seed light over the years, with the current status being 20 mW, which is also the nominal injection maximum specified by the VRFA distributor.

Upon exiting the VRFA, the fundamental beam is branched into multiple paths using $\lambda/2$ waveplates and polarizing beam-splitters (PBS), spectrally modified using acusto- and electro-optic modulators (AOMs, EOMs), and finally coupled into optical fibers so it can be sent to the main table. Every branch element contains a PBS in front of the fiber as well as an externally controllable blade shutter, both not depicted in Fig. 9.

A spectroscopy branch is devoted to the stabilization of the 1178 nm seed source. Its frequency-doubled laser frequency ω_0 is locked to the doppler-free crossover signal of the ^{23}Na D2 line. The spectroscopy part exhibits an aluminum container that comprises a 75 mm long sodium vapor cell. The capton covered surface of the container is wound with a high-resistance wire (10 Ω/m Konstantan), where counterpropagated double-winding avoids unwanted solenoid effects. Applying 26 V (current 1 A) to the wire heats the cell up to 170 °C, corresponding to a vapor pressure of 3.6×10^{-5} mbar. A spectroscopy laser beam passes through the cell, serving as a pump beam causing saturated absorption. It then gets reflected at a zero degree mirror and passes the cell a second time, where it acts as the probe beam. The doppler-free absorption spectroscopy signal is then obtained by collecting the passed probe beam on a photodiode. Using the frequency modulation spectroscopy technique [112] via an EOM, this is transformed into an error signal that is fed forward to the DFB diode current control of the infrared laser seed. An AOM situated upstream of the cell in double-pass configuration allows to

freely shift the fundamental frequency ω_0 with respect to the crossover transition, $\omega_0 - 2 \cdot \Delta_{AOM} = \omega_{Crossover}$.

The locking point of ω_0 is set about 200 MHz blue-detuned with respect to the cyclic $|f = 2, m_f = 2\rangle \rightarrow |f = 3, m_f = 3\rangle$ transition frequency on the D2 line. The value of ω_0 is continuously coarsely monitored by a wavelength meter (HighFinesse WS/6, absolute accuracy 100 MHz) and exactly deduced by performing absorption imaging of a cold atomic cloud (see also sec. 4.3). A frequency scan of the detection beam AOM gives rise to a Lorentzian line shape of the detected atom number, which is shown in Fig. 10 (a). A fit gives the locking point $w_0 = 207.5$ MHz. The extracted full width half maximum (FWHM) $\Gamma/2\pi = 10.2(\pm 0.4)$ MHz slightly overestimates the natural linewidth $\Gamma_{Na}/2\pi = 9.795$ MHz by about 4%, possibly due to saturation effects.

All other needed frequencies are generated by individual modulators from laser beams operating at the locking point ω_0. The choice of optical components as well as their implementation reflects the amount of spectral versatility needed for each port. For example, the MOT cooling beam has to be adjusted to the capture velocity in the MOT, and high tunability is an experimental relief for the simultaneous optimization of the Zeeman coil, MOT coil and laser detuning parameters. It further has to be independently tunable for the optical molasses stage. Its spectral tunability is therefore realized in a cat-eye double-pass configuration [113], where downstream of the AOM a lens with focal length f and a 0° mirror are inserted at distances f and 2f, respectively. This greatly amplifies the frequency range that is efficiently injected into the optical fiber compared to an ordinary AOM double-pass in absence of this lens (see Fig. 10 (b)).

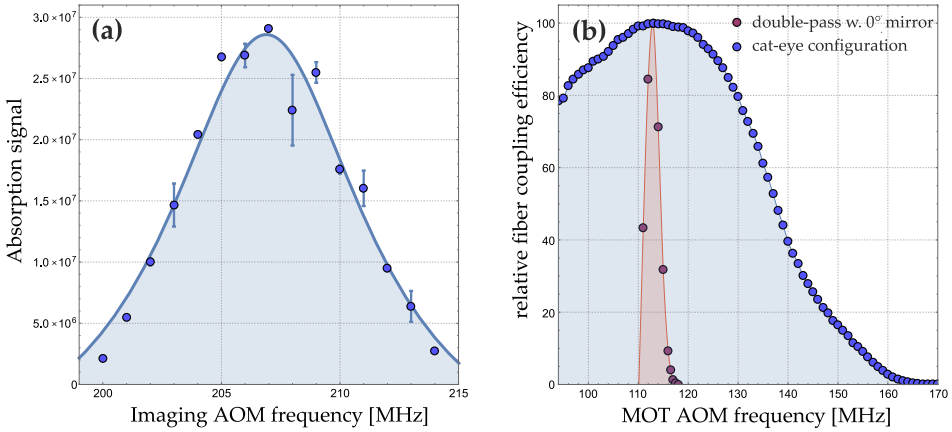

Figure 10: Assorted details regarding the ^{23}Na laser system. (a): Absorption imaging signal of cold atoms as a function of imaging frequency. The locking point ω_0 is obtained by shifting the imaging frequency to resonance, where the signal is largest. A Lorentz function fit (solid line) is used to extract the width and maximum position. The vertical axis assumes the on-resonance scattering cross section for each detuning and therefore corresponds to the real atom number only on resonance. (b): Relative fiber coupling efficiency as a function of the AOM frequency shift for an AOM situated upstream of the fiber in double-pass configuration. A cat-eye configuration (blue curve) strongly enhances the bandwidth compared to a double-pass using only a 0° mirror (red curve).

A counterexample demanding no spectral versatility is given by the Zeeman repumping beam. It has to bridge exactly 1.7133 GHz compared to the Zeeman cooling beam, and is therefore implemented by generating sidebands via an EOM on the Zeeman cooling before the latter is itself shifted using an AOM. Table 1 gives an overview of the individual ports including their purpose, detuning Δ to the relevant transition and the amount of power available on the main table, while Fig. 11 shows the system in operation.

Purpose	$\|f\rangle \rightarrow \|f'\rangle$	Δ in MHz / in Γ	Power in mW
Zeeman slowing	$\|2\rangle \rightarrow \|3\rangle$	-400 / -40.8	80 (combined)
Zeeman repumping	$\|1\rangle \rightarrow \|2\rangle$	-400 / -40.8	
MOT cooling	$\|2\rangle \rightarrow \|3\rangle$	-18.5 / -1.9	120
MOT repumping	$\|1\rangle \rightarrow \|2\rangle$	0	12
F = 2 imaging	$\|2\rangle \rightarrow \|3\rangle$	0	0.2
F = 1 imaging	$\|1\rangle \rightarrow \|1\rangle$	0	0.2
Spin polarizing	$\|1\rangle \rightarrow \|1\rangle$	0	0.05

Table 1: Overview of the used laser ports. The detuning Δ is given with respect to the corresponding relevant transition. The power refers to the fiber output power on the main table.

Figure 11: Sodium laser system in operation.

3.2 ^{39}K LASER SYSTEM

The ^{39}K laser system used in this experiment was designed and built in a previous PhD thesis [76] and subsequently upgraded. A detailed description of the used lasers including explosion drawings and an assembly tutorial is given in [114], whereas the used electronics are described in [76]. Its main features are briefly repeated and all modifications are mentioned.

Compared with the ^{23}Na laser system, the main difference is governed by the number of individual lasers employed in the setup. With only one Raman fiber amplifier, the ^{23}Na system provides exactly one fundamental frequency, and the spectral flexibility is ultimately limited by the bandwidth of the components used for modulation. Due to the low costs of ECDLs, the ^{39}K system instead provides the possibility to manufacture a set of individual lasers with different fundamental frequencies, which are then stabilized onto each other via offset locks. In particular, a total of three different fundamental frequencies are in operation: A master laser that is stabilized onto the crossover transition of the potassium D2 line provides the atomic reference frequency, whereas two slave lasers provide the fundamental frequencies for cooling and repumping. The advantage of a master-slave setup manifests itself in almost freely selectable set frequencies only limited by the offset lock electronics. As an example, fermionic and bosonic potassium MOTs demand quite different cooling strategies and therefore drastically different sets of detunings. The versatility regarding the laser locks allows to switch between operating a fermionic or bosonic MOT by simply changing the offset lock parameters and adapting the intensities in the beams. This has been demonstrated in our setup [76]. The additional use of AOMs allows for fast switching of the individual ports.

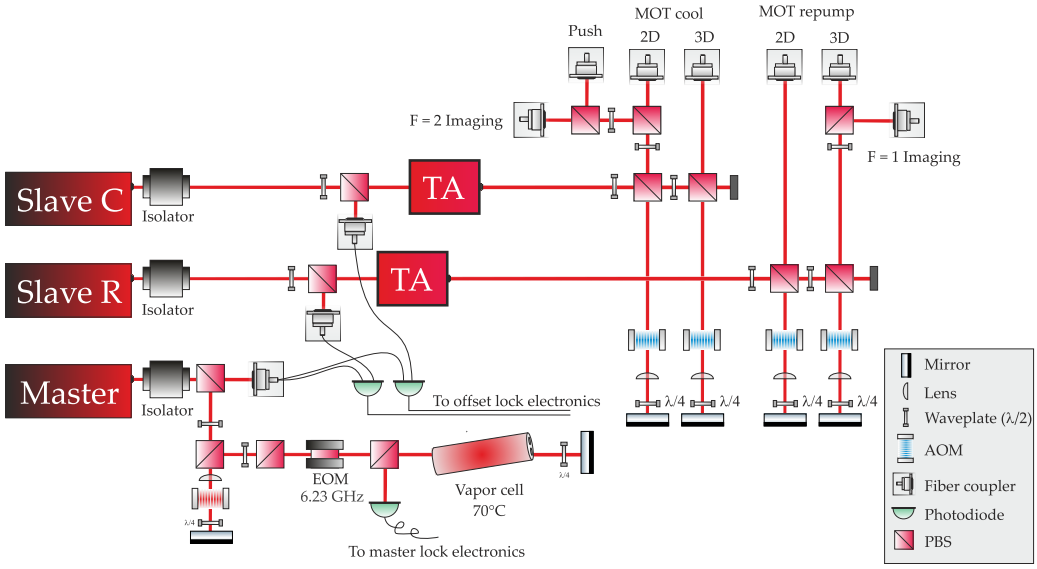

Figure 12: Simplified illustration of the ^{39}K laser system. Blue (red) color coding of the AOMs illustrate positive (negative) frequency shifts.

Figure 12 shows a brief sketch of the laser system employed in this thesis. The system can be briefly divided in three subregions, which are used for locking, laser power amplification and frequency modulation respectively. Both master and slave lasers are built using interference filters as frequency-selective elements, based on the so-called Paris design [115]. The lasing wavelength is coarsely set by the incident

angle of the interference filter and the laser diode temperature, whereas fast and fine spectral variations are achievable via a Piezoelectric transducer as well as the applied diode current. The master laser locking region is inherently identical to the one of the ^{23}Na setup, using a potassium vapor cell heated to 70 °C. The locking point (205 MHz blue-detuned with respect to the cyclic transition) is determined using absorption imaging similar to Fig. 10 (a), which is cross-checked by probing the velocity distribution of a ^{39}K atom beam in a neighbouring lab. The master beam is further split into two beams being sent to two separate photodiodes, where they interfere with the individual slave laser beams. The resulting beat frequencies are used for the offset lock as described in [76].

The major part (> 40 mW each) of both slave lasers is sent to the amplifying region, where both beams are individually amplified using Tapered Amplifiers (TA), providing $\approx$ 1 W (cooling path) and $\approx$ 750 mW (repumping path) at 2 A TA current. In the frequency modulation region, each beam is split up twice and sent to a unique AOM port, where they receive additional frequency shifts. In the initial setup of [76], where only Doppler cooling was demonstrated, the AOM ports were set up in a conventional double-pass configuration using just a 0° mirror. This proved to be limiting the performance of the system when sub-Doppler cooling strategies were implemented. The laser system was then modified [116] to provide a higher frequency tunability by using cat-eye configurations, enhancing the frequency tunability similar to the one shown in the ^{23}Na setup (see Fig. 10). The frequency shifted beams are then sent via optical fibers to the experiment table. The used frequencies and intensities of the individual experimental ports are summarized in table 2.

Purpose	$\|f\rangle \rightarrow \|f'\rangle$	Δ in MHz / in Γ	Power in mW
2D MOT cooling	$\|2\rangle \rightarrow \|3\rangle$	-8.7 / -1.4	60
2D MOT repumping	$\|1\rangle \rightarrow \|1\rangle$	-20.4 / -3.4	35
2D Pusher	$\|2\rangle \rightarrow \|3\rangle$	0	0.1
3D MOT cooling	$\|2\rangle \rightarrow \|3\rangle$	-41 / -6.8	135
3D MOT repumping	$\|1\rangle \rightarrow \|2\rangle$	-22 / -3.6	105
F = 2 imaging	$\|2\rangle \rightarrow \|3\rangle$	0	0.2
F = 1 imaging	$\|1\rangle \rightarrow \|2\rangle$	0	0.2

Table 2: Overview of the used laser ports. The detuning Δ is given with respect to the corresponding relevant transition. The power refers to the fiber output power on the main table.

4

THE TWO-COLOR 3D MOT

The following chapter introduces the main vacuum chamber in which all experiments performed in this thesis - from the first MOT fluorescence up to the demonstration of quantum degenerate matter - have been conducted. It further features the cornerstone of each cold atomic system, the magneto-optical trap (MOT). After a quick introduction to the concept of laser cooling, all the needed ingredients are layed out and piecewise discussed. Once all constituents are gathered, the system parameters have to be adjusted for optimal performance and orchestrated into one experimental sequence, whose description closes this chapter.

MOT operating principle

In this thesis, the most popular type-I MOT[1] is used, whose operating principle demands the atomic structure to fulfill $f' = f + 1$. Therefore the natural type-I MOT habitat for ^{23}Na and ^{39}K is governed by their D2 lines involving the hyperfine transition $|f = 2\rangle \rightarrow |f' = 3\rangle$.

A MOT utilizes the mechanical effects of light on atoms in order to restrict their trajectories simultaneously in configuration space (which traps them) as well as in momentum space (which cools them). For every dimension, this is achieved by using two counter-propagating, red-detuned and σ-polarized light sources together with a quadrupole magnetic field. Then both laser detunings, and hence the differential force that acts on the atoms, acquire spatial and momentum dependence through the Zeeman and Doppler effect, respectively. After numerous cycles of absorption and spontaneous emission, the resulting restoring force pushes the atoms to the origin given be the magnetic field zero. A friction force leads to dissipation of energy (i.e. cooling), and the omnidirectional spontaneous emission is time-averaged out. The cooling is eventually equilibrated by diffusive heating linked to fluctuations in the atomic momentum that appear in the spontaneous emission process. By equating both contributions, the steady-state Doppler temperature

$$T_D = \frac{\hbar\Gamma}{2k_B}; \quad T_{D,Na} = 235\,\mu K, \quad T_{D,K} = 145\,\mu K \tag{4.1}$$

with the Boltzmann and reduced Planck constant k_B and $\hbar$, and the respective natural linewidth Γ, is defined as the natural temperature limit that appears in a MOT. It can be undercut by pure optical post-cooling mechanisms such as polarization-gradient cooling [118]. In atomic systems that continuously interact with laser light characterized by a wavenumber k_L, the fundamental optical cooling limit is the recoil temperature at which the atomic momentum equals the photon momentum of its interacting light field:

$$T_R = \frac{\hbar^2 k_L^2}{m k_B}; \quad T_{R,Na} = 2.40\,\mu K, \quad T_{R,K} = 0.42\,\mu K, \tag{4.2}$$

where m is the respective atomic mass.

1 Other MOT types are possible, with the type-II MOT being of special interest for studies devoted to direct laser cooling of molecules, as they avoid rotational branching [117].

4.1 EXPERIMENTAL SETUP

The magneto-optical trapping zone is provided by a set of six laser beams and a magnetic field coil pair in anti-Helmholtz configuration that realize a quadrupole field

$$B(x, y, z) = B' \sqrt{x^2/4 + y^2/4 + z^2}. \tag{4.3}$$

The beams drive the cyclic transition $|f = 2, m_f = 2\rangle \rightarrow |f = 3, m_f = 3\rangle$, yet residual coupling to $f' = 2$ and subsequent decay into the $f = 1$ manifold gives rise to a loss channel for the cooling cycle. This is counteracted by installing a second, repumping frequency that continuously drives the $|f = 1\rangle \rightarrow |f' = 2\rangle$ transition. Apart from this, the ingredients needed to realize a MOT can be summarized as follows:

1. Connections to two atomic reservoirs delivering a high flux of preferably pre-cooled atoms.
2. An ultra-high vacuum (UHV) environment in order to minimize collisions with hot background atoms, maximizing the ensemble lifetime.
3. Diagnostics to acquire the relevant parameters atom number and ensemble temperature.

At first glance, the first two points seem to be antonymous to each other, as UHV implies a scarce amount of atoms, whereas source reservoirs indicate an ample amount instead. They are both satisfied by the experimental setup which is shown in fig. 13, that features an UHV main chamber separated via differential pumping stages from the individual atomic sources. The following sections outline how these ingredients have been realized and put together in the experimental apparatus.

4.1.1 *Pre-cooled atomic sources*

This section gives a brief overview regarding the infrastructure of the used atomic sources. Their typical operation performance is presented in section 4.4 together with the 3D-MOT.

Potassium

^{39}K atoms are provided using commercial dispensers (Alvatec Alkali Vacuum Technologies) as a metal vapour source. These consist of small tubes made from stainless steel that contain potassium either as an alloy or in chloride form. Resistive heating of the tube will lead to sublimation of pure potassium. The used dispensers are artificially enriched, i.e. they contain a ^{40}K abundance of 5.5% compared to the natural abundance of 0.01%. This enables the use of the atomic source for either fermionic or bosonic operation. The hot potassium is distributed into a custom made vacuum chamber [76] which is connected to the main chamber through a bellow and a differential pumping stage pointing along $\vec{e}_y$. A magneto-optical interaction zone in this chamber realizes a two-dimensional (2D) MOT that pre-cools the hot ensemble in the $x - z$ plane. Its magnetic part is given by a horizontal and vertical coil pair, realizing an Anti-Helmholtz magnetic field in the chamber. All coils are

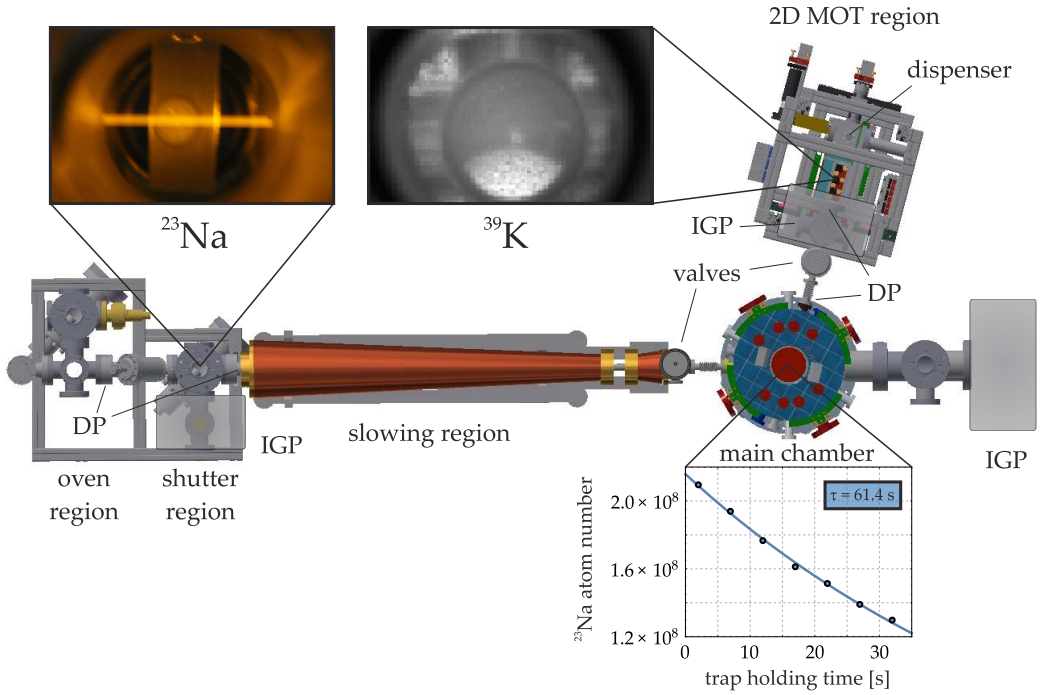

Figure 13: Sketch of the experimental setup without optics, showing the atomic sources and the UHV main chamber. Hot ^{23}Na and ^{39}K are distributed using an oven and dispensers, as seen by their respective fluorescence (upper left inset). After pre-cooling utilizing a ^{23}Na Zeeman slower and a ^{39}K 2D MOT respectively, both species are fed through differential pumping stages (= DP) into the main chamber. The chamber provides UHV conditions as shown through ensemble lifetimes on the order of a minute (lower right inset). The region connections can be interrupted using valves, and each vacuum region is maintained by locally installed ion getter pumps (opaque rectangles).

individually addressable by current supplies in order to freely move the atoms along the horizontal (x) and vertical (z) direction. The optical forces are generated by an array of red-detuned, σ^+ polarized, counterpropagating vertical and horizontal beams spanning parallel $x-z$ planes. The two-dimensional confinement creates a tube of transversally cold atoms, which are longitudinally guided towards the 3D MOT chamber by a low-intensity 'pushing' beam propagating along y.

The bellow connection to the main chamber gives mechanical flexibility upon connecting the vacuum components, but can lead to misalignment of the precooled atomic beams. Hence upon first assembly, the vacuum structure itself has to be geometrically aligned to the main chamber center. Afterwards, coarse optimization of the 'unpushed' 2D MOT was performed by observing and increasing the fluorescence signal directly in the 2D MOT chamber with a camera placed along the axial direction (therefore removing the pushing beam), as seen in fig. 13. With help of the camera, the 2D MOT position is aligned with the flange leading to the 3D MOT using the four coil controlling power supplies. The starting point of the used 2D MOT frequencies are based on those published in [108]. Fine optimization of the 2D MOT system was then conducted iteratively by using the 3D MOT loading rate as a figure of merit (see sec. 4.4).

Sodium

^{23}Na atoms are provided using a reflux oven currently operating at 330°C that emits gaseous sodium with a mean speed of approx. 750 m/s through a nozzle ($\varnothing = 2$ mm). The consumption of ^{23}Na depends on the applied temperature, with a rule of thumb in this experiment being that for $T = 350$°C, 10 g are depleted after about 3000 hours of operation. The main oven region is heated in a constant time interval from 8 AM to midnight via a time switch. To avoid clogging of the nozzle, a second heating control keeps the front flange connection constantly above sodiums melting point of 97.8°.

Upon exiting the nozzle, the collimated atomic beam passes two differential pumping stages and a waypoint in which a TTL signal driven pneumatic shutter toggles the atomic flow. Downstream of the shutter, the atoms enter a 1 m long magneto-optical interaction zone known as a *Zeeman slower*.

Here, the atoms are illuminated by a single, counterpropagating σ^+ polarized laser beam as they are moving through a CF-16 brass pipe. The beam comprises two fundamental frequencies that are both strongly red-detuned by 400 MHz compared to the cooling and repumping transition respectively. By applying a magnetic field created by a coil wound around the pipe, the resulting Zeeman effect together with the Doppler effect shift these laser beams to resonance with a certain velocity class of the atomic distribution. Following a cascade of absorption-emission processes similar to the Doppler cooling mechanism utilized in a MOT, the atoms are then slowed longitudinally. Furthermore, the Zeeman laser beam is focused onto the oven nozzle, which creates a cone of slowing light that counteracts the transversal spread of the atom beam. As the atomic velocity decreases, the lower Doppler shift detunes the laser beam spatially, which is accounted for by reducing the number of coil winding layers (starting from 24), generating an inhomogeneous magnetic field that decreases downstream. As the magnetic field has to be adapted to the Doppler shift, the current providing optimal trapping conditions for this first decreasing-field coil is directly linked to the initial chosen oven temperature. A second, increasing-field coil (up to 6 layers), appended to the first one, realizes a spin-flip Zeeman slower, where the current set to this coil sets the final velocity of the slowing process. The initial values of Zeeman beam detuning, power and Zeeman coil currents were based on calculations performed in [119]. This source also contains all details regarding its design and construction. Similar to the potassium system, optimization of coil currents and slowing beam parameters has been performed by using the 3D MOT loading rate as a figure of merit, see section 4.4.

4.1.2 *Science chamber*

Both pre-cooled atomic sources are collected in a cylindrical UHV region called the *main chamber*. In addition to its connections to the atomic sources and an in-vacuum microwave antenna, the chamber features optical access through twelve viewports in the horizontal plane that are occupied by various diagnostic items and the cooling/trapping beams as labeled in fig. 14. Two video cameras at an inclined angle of 90° are used for by-eye-surveillance, while two imaging systems and ANDOR cameras as well as a photodiode detector are used to infer the ensemble observables such as its atom number. MOT and optical dipole trap use the same viewports, and their operation is toggled by externally controllable flippable mirrors.

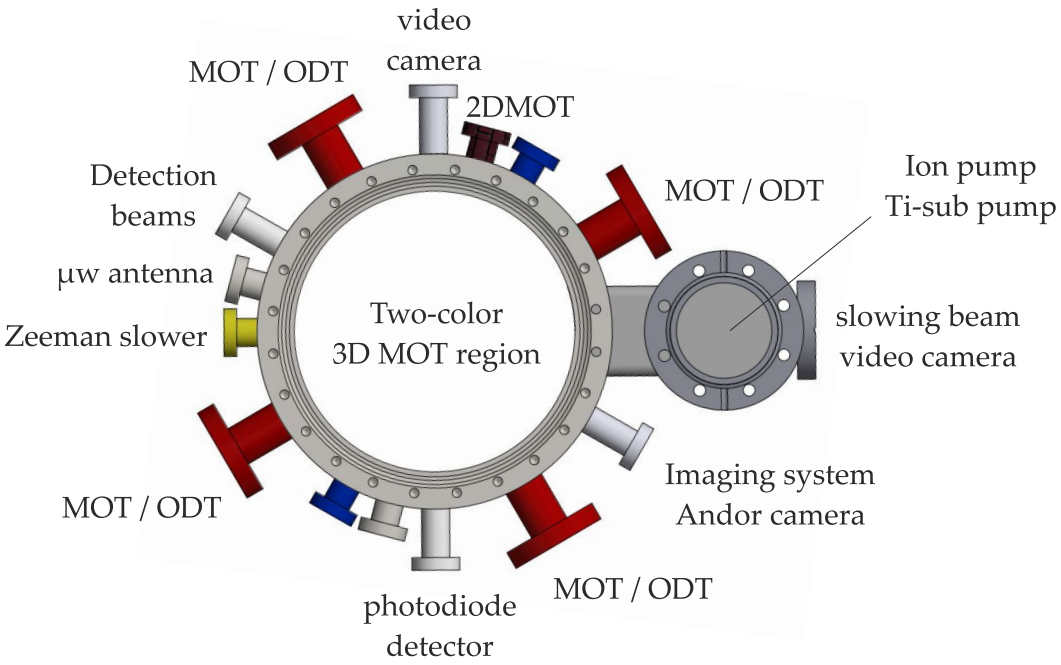

Figure 14: Viewport overview of the science chamber that houses the two-color 3D MOT. Each flange connection is labeled by its purpose. Upstream of the red colored ports, flippable mirrors allow to switch between 3D MOT and ODT operation.

Further optical access is granted along the vertical axis through two vertical CF-200 vacuum windows. These are coated with an indium tin oxide mask that enables the application of large ($\sim 10\,\mathrm{kV/cm}$), tunable electric fields in order to polarize the molecules [3]. The cooling and repumping light for both species is distributed via optical fibers onto the main optical table. There, they are split into five beam paths whose diameters are expanded to 11 mm each. The optics are mounted either on the optical table or several breadboards that surround the chamber and are themselves fixed on marked points to the optical table. These breadboards are made out of fiber reinforced plastic and liftable by 2 persons. This design gives a significant advantage if one has to directly access the main chamber for maintenance reasons. As an example, at some point the magnetic field coils were exchanged due to a shortcut connection translating into the loss of about a winding in one of the coils. In this case, most of the optics can be removed and reinstated without severely changing the beam alignment simply by carrying the breadboards away and back.

A network of dichroic mirrors sends all five beams into the chamber, realizing four horizontal and one vertical trapping beam whose intensity ratios are freely adjustable for both species using $\lambda/2$ waveplates, and whose polarization is set to circular just before entering the chamber using dichroic $\lambda/4$ waveplates. The vertical beams are retroreflected using an externally controllable flipping mirror, which completes the desired six-beam MOT configuration and allows for vertical absorption imaging by flipping the mirror out of the beam path. All beams are quickly switchable and frequency tunable via AOMs on the laser optical table.

Magnetic fields are provided by a coil pair and a compensation cage cube spanning a volume of approx. $1.73\,\mathrm{m}^3$. The coil pair comprises 24 windings each that realize a quadrupole field with a conversion ratio of $B' = 0.8\,(\mathrm{G/cm})/\mathrm{A}$ between field gradient and applied electric current along the (vertical) symmetry

axis. Electric current is provided by two power supplies (*DELTA SM-30 200*) in master-slave configuration that deliver up to 200 A each. Insulated-gate bipolar transistors (*Mitsubishi CM300DY-24NF*) enable fast on/off switching. A water cooling system in the coil holders allows safe operation at a total current of at least 300 A. The compensation coils are controlled through six power supplies, which allows to set magnetic bias fields on the order of a few Gauss in an arbitrary direction.

4.1.3 *UHV conditions*

The main chamber grants UHV conditions needed for disturbance-free operation of the cold atomic system through the use of Ion getter pumps. Contaminations through outgassing of chamber parts and impurities in the atomic sources[2] form a background of gas atoms whose room temperature strongly exceeds the $\sim 1\,\mathrm{K}$ binding energy of the MOT. Hence every collision of a background atom with a trapped cold atom causes a loss of the latter from the trap. The resulting "one-body" atom loss dynamics of the cold cloud

$$\frac{dN}{dt} = -\Gamma_{bg} N(t) \tag{4.4}$$

follow an exponential decay with the loss coefficient Γ_{bg}, that is usually expressed by the *lifetime* $\tau = (\Gamma_{bg})^{-1}$ of the sample. Later through the thesis, non-exponential losses due to higher-order terms (Majorana, two-body and three-body losses) will be encountered. Even though it will be not the correct solution to the underlying differential equation, it is still possible to fit a simple exponential decay to these combined higher-order phenomena and call it an *effective 1/e lifetime*, which is the convention followed throughout this thesis.

For a given background gas species, the loss coefficient Γ_{bg} can be formally expressed as $\Gamma_{bg} = n\langle\sigma v\rangle$, with the density n and the thermally averaged product of loss cross section σ and velocity v. For large enough trap depths, the loss cross section can be evaluated classically, giving [120]

$$\Gamma_{bg} \approx 6.8 \frac{P}{(k_B T)^{3/2}} \left(\frac{C_6}{m_{bg}}\right) (U_0 m_0)^{-1/6} \tag{4.5}$$

with the partial pressure P and mass m_{bg} of the corresponding background gas species, trap depth U_0 and mass m_0 of the trapped cold atom species and the van-der-Waals dispersion coefficient C_6 describing the interaction between both. The contamination of the chamber is mostly given by hydrogen molecules. Using the corresponding C_6 coefficients for $Na - H_2$ and $K - H_2$ collisions, the loss rate coefficients are roughly equal, reading

$$\Gamma_{bg-Na} \approx \Gamma_{bg-K} \approx 4 \times 10^{10}\,\mathrm{bar}^{-1}\,\mathrm{s}^{-1} \tag{4.6}$$

for a trap depth of 1 K. The relation eq. (4.6) implies that the atoms themselves can be used as an adequate sensor of the vacuum conditions to cross-check the readout of the installed ion pump controllers. The ion pump controller on the main chamber displays a current of 4 nA, translating into vacuum conditions better than 10^{-11} mbar [76]. Using here a result of the working environment presented in the

2 SAES potassium dispensers are famous for containing non-negligible amounts of rubidium.

following chapter 5, the lifetime of the atomic ensembles is typically evaluated in a pure quadrupole trap in absence of trapping light. The inset of fig. 13 shows a typical measurement, in which the ^{23}Na atom number is measured for variable holding times. The ensemble temperature is set to a few hundred μK, where non-linear losses are negligible (see fig. 24 for a discussion of those). The exponential decay fit gives a lifetime of $\tau = 61.4 \pm 1.3\,\mathrm{s}$, when (4.6) implies a vacuum quality better than 10^{-12} mbar. Over the course of a few months, increasing pollution (that mainly stems from the 2D MOT region) can steadily worsen the vacuum conditions. A titan sublimation pump is installed next to the ion getter pump, and 'firing' titan restores the conditions to the one of the inset in fig. 13.

4.2 EXPERIMENT CONTROL HIERARCHY

This section describes how each experimental sequence in this thesis was orchestrated, monitored and evaluated. For the purpose of this section, the experiment can be treated as a black box that generates a set of output observables $f(x)$ from a set of input parameters x during an experimental sequence. Such a sequence consists of a list of input parameter shaping commands, such as *close the shutter* or *set the AOM frequency to 200 MHz*, which are executed with exact relative timing. The command hierarchy of an experimental sequence is depicted in fig. 15. A sequence protocol is built and executed using the LabVIEW based graphical user interface *Unicorn*. Executing a manual prompt processes the sequence to its end. Every protocol is represented as a $(M + K + 1) \times N$ matrix as depicted in the top of the figure. The N columns denote consecutive time slots during which the respective commands are executed, where the dwell time is set in integer multiples of 10 μs. The commands are assigned to M different digital and K different analog of an ADwin Pro II board (Jaeger Messtechnik GmbH) constituting the matrix rows. Furthermore, a virtual interface (VISA) channel is employed, that can be used to process communication protocols via lines of code with a number of devices such as tunable frequency generators. The ADwin board distributes the digital (analog) commands to the experiment black box using TTL (±10 V) signals. This completes the experimental input. The output observables $f(x)$ are twofold. For once, a set of diagnostic elements is used to continuously monitor the key components of the black box (magnetic fields, optical fields, MOT population) during operation, in order to be able to trace possible irregularities back to their origin. Second, an array of camera pictures is taken during the course of the sequence. These are handled and combined by the LabVIEW analysis program *Narwhal* to infer details regarding the underlying atomic distribution such as peak density and width using automated fitting. The protocol file, picture files and atom distribution fit files for each ran sequence are combined and stored together in a SQLITE database using the xml2db library.

The experiment is only operated with at least one experimentalist present in the laboratory. After $\sim 1-2\,\mathrm{h}$ warming up of the individual system components and daily maintenance tasks, sensible data is usually acquired starting at 10 AM. In this experiment, a typical experimental sequence is $30-45\,\mathrm{s}$ long, with the main contribution being the evaporation time. Therefore, the amount of accumulated data over time can be vast. Figure 16 shows a histogram of the number of saved sequences over the course of a day. A python based data analysis program has been developed that allows quick initial processing of the data and features a set

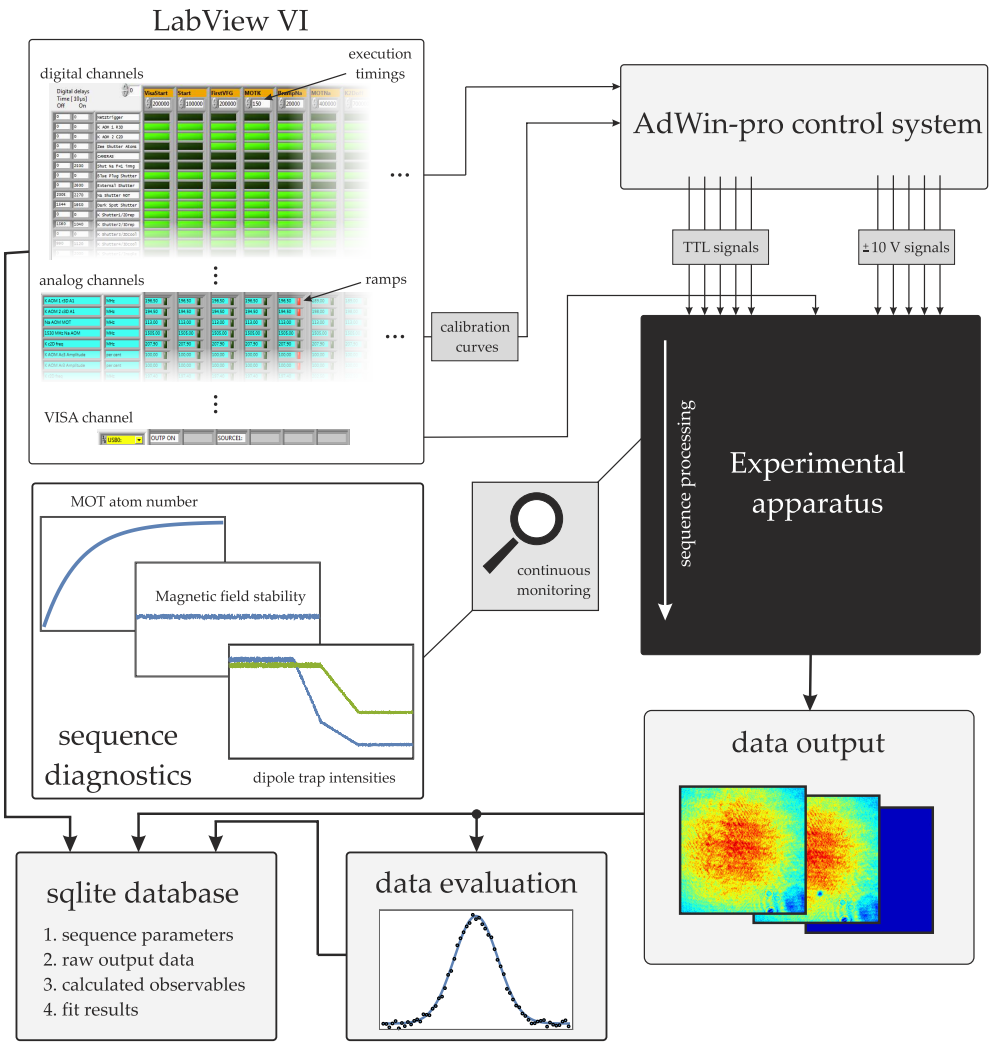

Figure 15: Experiment control hierarchy (details see text).

of customizable fitting routines [121]. Rigorous further analysis of usable data is handled using a *Mathematica* notebook library that has been developed in the group.

4.3 ATOM DETECTION

When near-resonant laser light passes through an atomic cloud, it will be absorbed and re-emitted. Both processes can be used to count the number of illuminated atoms and to infer their spatial distribution. In this experiment, fluorescence detection is mainly used to monitor the atom number of rather hot ensembles such as those found in MOTs, whereas absorption detection is used for optically thick samples such as BECs. By using both methods independently for the intermediate regime (~ 100 µK cold ensembles), the resulting atom number measurements are used to calibrate each other and cross-check for discrepancies. The remaining systematic uncertainties are estimated to be around 20%.

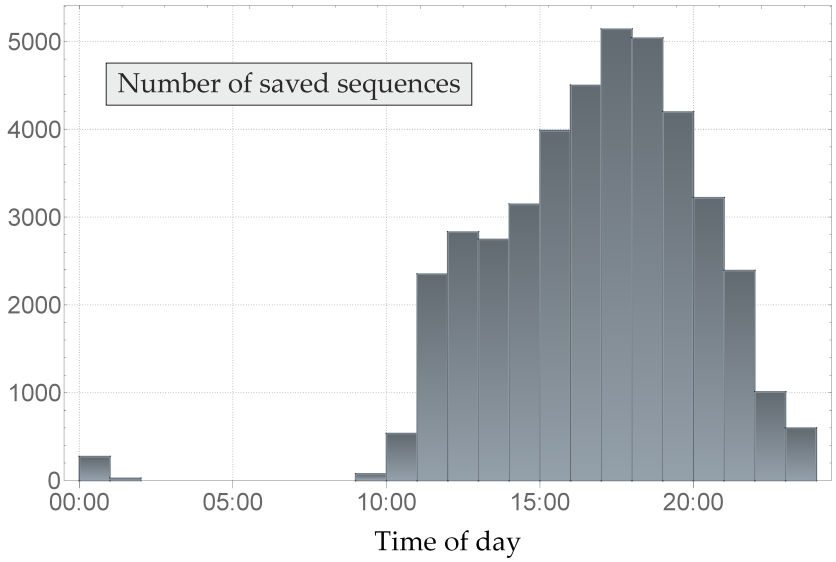

Figure 16: Histogram showing the number of saved sequences, binned by the hour in which they were taken, for 100 consecutive experimental working days.

4.3.1 *Fluorescence imaging*

Fluorescence detection uses the fact that the total photon scattering rate will be proportional to the excited state population p_e, i.e.

$$\gamma_{\text{scatt.}} = \Gamma p_e \tag{4.7}$$

with the natural linewidth Γ of the excited state. Hence the photons scattered through constant illumination by the slightly detuned MOT beams can be used to obtain the atom number while operating the MOT. As the photons are isotropically scattered, they can be detected by placing a collecting lens at a distance r that cuts out a fraction of the spherical surface area $4\pi r^2$ and deflects the corresponding light onto a switchable gain photodiode detector. Every detected photon carries an energy $\hbar\omega$ contributing to the deposited optical power. The latter is converted into a photodiode current using the respective radiant sensitivity R of the detector and ultimately read out as a voltage signal $U[V]$ through the switchable gain G. To account for residual background light scattering, this signal is substracted from a signal $U_{bg}[V]$ that uses the same MOT beam configuration with the magnetic field coils turned off. The atom number is then determined by

$$N_{\text{Fluo.}} = (U - U_{bg}) \, \frac{4\pi}{\Omega} \, \frac{1}{(\gamma_{\text{scatt.}})\,(\hbar\omega)\,(R)\,(G)} \tag{4.8}$$

where Ω is the solid angle of the collection lens surface area.

For ^{23}Na, the hyperfine splitting outweighs the linewidth of the individual lines, and the cooling transition is sufficiently isolated. Therefore only a weak amount of repumping light ($P_{Na,r}/P_{Na,c} \sim 10\%$) is needed. In this case, both the cooling and repumping transition can be treated as two separate two-level systems whose scattering contributions can be added up. For a two-level system, the steady state scattering rate acquires the form

$$\gamma_{\text{scatt.,Na}} = \Gamma \sum_{i}^{2} \frac{1}{2} \frac{I_i/I_{\text{sat.},i}}{1 + I_i/I_{\text{sat.},i} + (2\delta_i/\Gamma_{Na})^2} \tag{4.9}$$

with total and saturation intensity I_i and $I_{sat.,i}$ and respective detuning δ_i for the individual contributions of cooling $(i = 1)$ and repumping $(i = 2)$ beam.

For ^{39}K, the situation is more complex, rendering it as a special case among the alkali metal atoms. Due to its comparatively small ground and excited state hyperfine splitting, the transitions can not be isolated from each other, when the notion of a 'cyclic' transition will be less pronounced than for ^{23}Na, demanding $P_{K,r} \sim P_{K,c}$. Consequently, any description involving the two-level approximation featured in eq. (4.9) is flawed as it disregards optical pumping effects. Instead one has to take into account both hyperfine ground and all four excited hyperfine levels as well as the combined cooling and repumping laser powers, when one arrives at optical bloch equations for the population dynamics of the full six-level model. As continous illumination by the MOT beams gives a constant photodiode signal in the fully loaded MOT, it can be assumed that the steady state population is reached. The photon scattering rate will again be proportional to the excited state population and the natural linewidth, and the former can be generally expressed as a sum over the individual hyperfine components:

$$\gamma_{K,\text{scatt.}} = \Gamma_K p_e = \Gamma_K \sum_{f'=0}^{3} p_{f'} \tag{4.10}$$

The exact dynamics are by no means trivial, but simplify significantly if one disregards coherences induced between the levels and instead sets up a rate-equation model, which for ^{39}K has first been done by Williamson *et al.* [122] whose reasoning is followed here. In particular, denoting $\Gamma_{f,f'}$ as the $f \leftrightarrow f'$ branching ratio weighted linewidth and $\xi_{f,f'}$ as the corresponding absorption oscillator strength, the individual excitation rates $\varrho_{f,f'}$ are

$$\varrho_{f,f'} = \frac{\xi_{f,f'}\,\Gamma_{f,f'}}{2} \frac{I_f/I_{sat.}}{1 + (2\delta_f/\Gamma_K)^2} \tag{4.11}$$

where I_f is the intensity of the beam driving the transition from the corresponding f ground state. The steady-state solution is then obtained by using the sublevel-averaged oscillator strengths to calculate the individual absorption and emission rates, and then equating these, giving

$$p_f = \frac{\sum_{f'}(\varrho_{f,f'} + \Gamma_{f,f'})p_{f'}}{\sum_{f'} \varrho_{f,f'}} \tag{4.12}$$

$$p_{f'} = \frac{\varrho_{1,f'}\, p_1 + \varrho_{2,f'}\, p_2}{\varrho_{1,f'} + \varrho_{2,f'} + \Gamma} \tag{4.13}$$

for all f and f' states. By combining (4.12) and (4.13) the relative ground state population is

$$p_{(f=2)} \times \sum_{f'} \varrho_{2,f'} \frac{\varrho_{1,f'} + \Gamma_{1,f'}}{\varrho_{1,f'} + \varrho_{2,f'} + \Gamma} = p_{(f=1)} \times \sum_{f'} \varrho_{1,f'} \frac{\varrho_{2,f'} + \Gamma_{2,f'}}{\varrho_{1,f'} + \varrho_{2,f'} + \Gamma} \tag{4.14}$$

This expression can be explicitly evaluated by setting $p_{f=1} = 1$ without loss of generality. With both p_f obtained, all $p_{f'}$ can then be acquired out of eq. (4.13). Together with the normalization condition $\sum_f p_f + \sum_{f'} p_{f'} \stackrel{!}{=} 1$, this directly gives the desired population ratio for each f' state, which are then summed up, resulting in p_e.

Fluorescence detection is an appealing method for monitoring the atom number, as the here presented minimal version employs few and cheap optical elements that can be implemented at arbitrary spherical angles into the experiment. The downside is given by the relatively large number of parameters which have to be accurately known and whose uncertainties add up. Through reflections of scattered photons by the atomic cloud on the chamber surface, the photodiode might catch a higher-than-assumed solid angle. The Gaussian beam nature of the MOT beams further give an inhomogeneous intensity distribution that is spatially averaged in the description above. These effects can be accounted for by pursuing fluorescence detection using systems of different size, position and illumination methods, e.g. by comparing the six-beam generated photodiode signal with a one-beam signal catched by a CCD camera at a different position in a subsequent experimental run. For MOT operation, one is mainly interested in the order of magnitude in the atom number, hence the remaining uncertainties of the hereby used minimal version are tolerable. When these effects are well controlled and disturbances suppressed, the method of fluorescence detection particularly excels in systems intending the study of few-atom systems. Single atom detection has been demonstrated in optical lattices [123, 124] studying Mott-insulators, while exact particle counting of mesoscopic ensembles has been demonstrated in bulk systems intending to study entanglement on the few-atom level [125, 126].

4.3.2 *Absorption imaging*

Absorption imaging is the most prevalent imaging technique in cold atom systems, providing high signal to noise while being dependent on only a low number of parameters. It uses the fact that the absorbed photons were directed, whereas the emitted fluorescence is omnidirectional, therefore the absorbing effect of an optically thick cloud can be observed on the illuminating beam itself. By sending a single, low-intensity resonant light pulse through the cloud and onto a CCD camera, the thereby casted atomic shadow can be imaged on the camera when the shadow position and extent unveils the atomic distribution through inversion. Denoting the beam propagation axis as e_y, the undistorted (i.e. in absence of the cloud) light beam intensity on each (x, z) tuple of the CCD chip is denoted as $I_0(x, z)$. Traversing the atomic cloud modifies this according to the Lambert-Beer law:

$$I(x, z) = I_0(x, z)\, e^{-OD(x,z)} \tag{4.15}$$

where the optical column density OD

$$OD(x, z) = \frac{\sigma^\star}{\alpha} \int dy\, n(x, y, z) \tag{4.16}$$

denotes the thickness of the absorptive medium and is given by the effective absorption cross section $\sigma^\star$ and the column density $\tilde{n}$, which is the onefold integrated density distribution of the atomic cloud. $\sigma^\star$ is related to the resonant cross section $(\sigma_0 = \hbar\omega_{atom}\Gamma/2I_{sat.})$ through

$$\sigma^\star = \frac{\sigma_0}{\alpha} \frac{1}{1 + I(x, z)/\alpha I_{sat.}} \tag{4.17}$$

where the dimensionless reduction factor $\alpha > 1$ incorporates imperfections in the polarization and different magnetic field orientations, but also accounts for hyperfine state peculiarities such as those described earlier for ^{39}K in the fluorescence section.

In an experimental sequence, the atomic cloud is released from the trap and the picture containing the atoms, $I_A(x,z)$, is taken after a variable time of flight. Following a waiting time after which the remaining atoms have dropped out of the camera's field of view, the second, reference image $I_R(x,z)$, is taken with the same exposure time and laser parameters. A third, so-called dark image $I_{Dark}(x,z)$, is acquired independently that contains neither light nor atoms but only the camera background noise. Out of this three pictures, the optical column density is obtained in the low-intensity limit as:

$$OD(x,z) = \log\left[\frac{I_A(x,z) - I_{Dark}(x,z)}{I_R(x,z) - I_{Dark}(x,z)}\right], \tag{4.18}$$

which is schematically shown in fig. 17. For large illuminating intensities, saturation effects are no longer negligible. This gives rise to another, linear term in eq. (4.18) in addition to the logarithmic one. In this setup, the validity of eq. (4.18) has been cross-checked using a calibration method similar to the one described in [127], in which the probe intensity is varied by more than one order of magnitude.

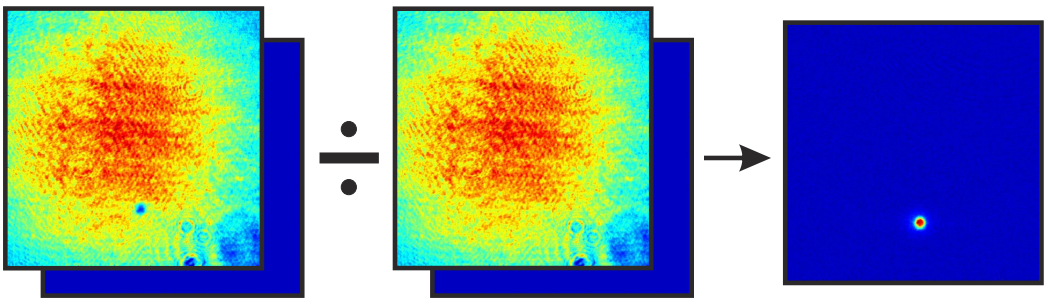

Figure 17: Absorption detection using the horizontal imaging system. Shown are cutouts of the pictures imaged on the CCD chip during an experimental run, with the atomic shadow clearly visible on the left picture. Division of the picture with and without atoms yields the optical density. Beforehand, a 'dark' background picture is substracted from both pictures. The division process eliminates fringes and systematic errors in the detection beam intensity.

The detection beams for both species are delivered onto the main table using single-mode fibers to ensure a clean transverse mode profile. There, they are expanded to a beam diameter of about 12 mm using a telescope and polarized using a dichroic $\lambda/4$ waveplate. All beams operate on resonance. For both species, the pulse durations are typically 60 µs. The laser intensities are adjusted so that the CCD chip is almost saturated, which is fulfilled by intensities considerably below the respective saturation intensities. For most of the experiments carried out in this thesis, both atomic species are initially prepared in the $|f = 1, m_f = -1\rangle$ state, and a set of detection beams allows their direct imaging. Alternatively, they are pumped into the $f = 2$ manifold by an optical pumping flash. A second set of detection beams then makes use of the cyclic transition $m_f = 2 \rightarrow m_{f'} = 3$ that usually gives a higher contrast. For ^{39}K with its close level spacing, a high-magnetic-field imaging was set up by dynamically tuning the frequency generator in the master-slave offset

lock after the MOT phase. Operating in the Paschen-Back regime then allows to drive $|m_i, m_j\rangle_K \rightarrow |m_i, m_{j'}\rangle_K$ transitions. These are instrinsically cyclic owing to the selection rule $\Delta m_i = 0$.

Time of flight measurements

Through eq. (4.16) and (4.18), the atom number can be obtained by integrating the optical column density over the x-z plane, which is equivalent to summing all pixel values:

$$N = \frac{\Delta_x \Delta_z}{\sigma^\star} \sum_i \sum_j OD(x_i, z_j), \tag{4.19}$$

where $\Delta_x \Delta_z$ gives the area which is imaged onto a single pixel. For this, the magnification of the imaging system has to be determined. A reliable calibration method is given by releasing a quantum degenerate gas from an optical trap and observing its free falling trajectory as depicted in 18. A BEC is best suited for this task because of the large signal-to-noise ratio even at a large time of flight. By fitting the vertical center of mass displacement (in pixels) to the well known equation $z_{BEC}(t) = z_{BEC}(0) + M' \times \frac{1}{2} g_0 t^2$ with the local gravity $g_0 = 9.8126\,m/s^2$ [128], one obtains the fitting parameter M' that incorporates the magnification as well as the true pixel size on the chip. In the case of the horizontal imaging readout, which is shown in fig. 18 (a), the conversion is $14.02\,\mu m$/pixel.

As the absorption technique naturally integrates the profile along the beam propagation direction, two-dimensional column density distributions are obtained. A combination of vertical and horizontal imaging using two imaging systems and cameras (*Andor iXon3* for horizontal, *Andor iXon Ultra 888* for vertical imaging) grants access to the full three-dimensional density distribution. The horizontal imaging beams are the ones outlined above. For vertical imaging, frequency and intensity adapted MOT beams are used whose retroreflection is halted by flipping away a mirror. Using two cameras further allows to set vastly different magnifications. The low-magnifying ($M = 0.57$) horizontal imaging is well-suited for the analysis of cold and ultra-cold clouds, whereas the high-magnifying ($M = 10.33$) vertical imaging allows for fine-tuning of the blue plug or optical dipole trap beams on the μm level (see chapter 5 and 6) and will be capable of resolving intra-trap structures such as quantum droplets.

To obtain the temperature of the ensemble, the cloud is again released from the trap and its expansion dynamics is monitored. Assuming a harmonic confinement in all directions, the equation of motion is separable in all three dimensions. For each dimension, the initial density distribution will be Gaussian, characterized by a width $\sigma(t = 0) \equiv \sigma_0$. After release, the cloud will keep its Gaussian functional form, but expand according to its momentum distribution which will imprint itself on the width through

$$\sigma(t) = \sqrt{\sigma_0^2 + \frac{k_B T}{m} t^2}, \tag{4.20}$$

with the species mass m and the expansion time t. Therefore the temperature can be obtained by letting the atoms expand for a set of TOF times and perform Gaussian fit routines to their integrated column density, which gives their width.

Such a measurement is shown in fig. 18 (b) for both species at the end of the optical molasses phase. A fit of (4.20) to the measurement gives (53 ± 0.4) µK for the sodium and (106 ± 4.0) µK for the potassium cloud, respectively.

4.4 3D MOT CHARACTERIZATION AND COOLING SEQUENCE

To operate the 3D MOT, all geometrical, optical, thermal and magnetic parameters have to synergize. This implies heavy sampling of the large parameter space in order to maximize the atomic signal in the MOT. Moreover, the two-color MOT houses two species whose parameter spaces are not separable. As an example, they experience the same magnetic field gradient but might favor different values, when trade-off solutions for a set of *joint parameters* seem unavoidable. Yet this already poses the main question regarding the MOT sequence assembly: what is a suitable figure of merit in a coupled two-species experiment that defines the "optimal" parameter configuration?

The experimental sequence described in this section is based on the following reasoning: In subsequent stages of the experiment, ^{23}Na will be used as a coolant for ^{39}K, which is a very costly process in terms of the sodium atom number. Therefore the complete experimental sequence was first arranged and optimized for the operation of a single-species sodium MOT, defining an operating point $\mathcal{P}_0$ in parameter space in terms of MOT beam alignment, molasses timing *et cetera*. This parameter space point was subsequently fine-tuned using a figure of merit obtained in later stages of the experiment, most notably the phase space density of an almost condensed cloud. Moreover, the joint parameters of both species, such as the molasses time, were varied. By observing the atom number of a just condensed cloud, information regarding the sensitivity to these parameters was obtained. This gave a good understanding which parameters are largely fixed and which can be adjusted if they turn out to be unfavorable for ^{39}K.

In the initial MOT realization procedure, the horizontal MOT beams were first aligned to the geometric center of the chamber using marked flange caps and irises that reduce the beam diameters to a few mm. The retroreflected vertical beam was

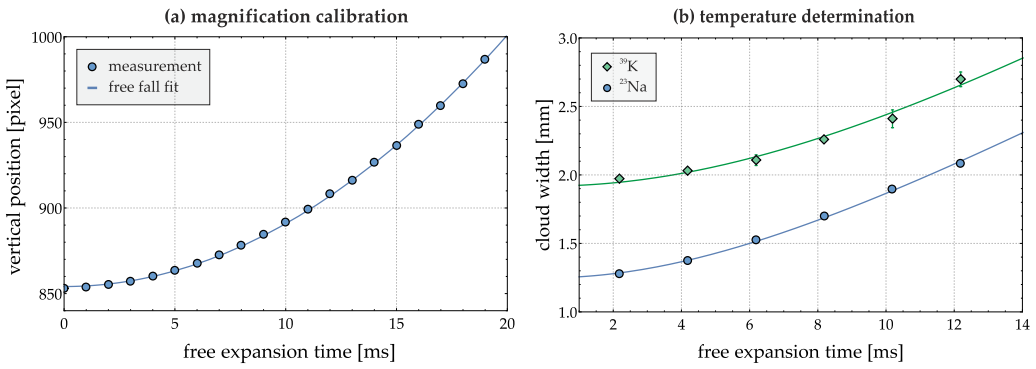

Figure 18: (a) Camera calibration measurement using the vertical center of mass for a free falling BEC after release from an optical trap. A quadratic fit gives the conversion ratio between pixel size and spatial extent.
(b) Temperature determination by using time of flight measurements for both atomic species. A fit of eq. (4.20) to the expanded width gives the temperature of each cloud, in this case after the molasses phase.

aligned onto these by realizing and maintaining a MOT while the iris apertures were subsequently reduced to their minimum. The power in each beam was first set roughly equal. The repump beam was superimposed with the cooling beam using two mirrors and a beam splitter, and their superposition ensured by observing their far-field intensity patterns at the end of the room using a periscope technique. The Zeeman light beam was focused and aligned directly onto the oven nozzle, using the fluorescence in the oven region. The starting parameters of the Zeeman slower (coil values, frequencies, intensity) were chosen according to the ones calculated in its design study [119].

^{23}Na

Once a MOT is formed, all MOT parameters are scanned and their ratios varied in an iterative fashion in order to localize beneficial parameter regions. Being a nowadays standard element invariably featured in cold neutral atom experiments, the whole MOT characterization strategy follows an established process [129, 106, 130, 131].

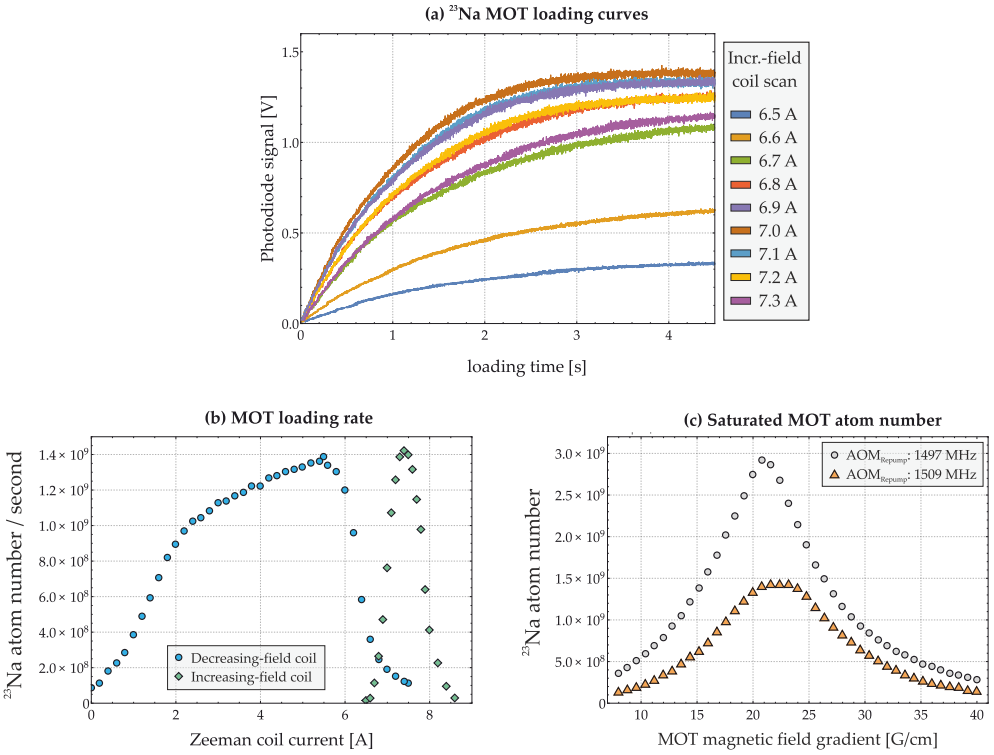

Figure 19: Selected curves of the ^{23}Na MOT characterization. (a) Exemplary loading curve set acquired in the optimization process, in this case for a scan of the increasing-coil field value. (b) MOT loading rate as a function of applied Zeeman coil current and an oven temperature of 333° C, once for a scan of the decreasing-field (blue dots) and increasing-field coil (green diamonds). (c) Saturated MOT atom number as a function of applied magnetic field gradient. The mutual dependence of the parameter set is exemplarily shown by mistuning a single parameter (repumping frequency, orange triangles). This already gives a distinctively different functional form and a shifted maximum compared to the optimized scenario (gray dots).

The only parameters that are not externally addressable are the laser beam intensity ratios and their alignment. Note that bad power balancing in a MOT can be canceled out by geometric misalignment. This can be fine for a MOT but is detrimental for the optical molasses stage that is about to follow. To prevent beam-walking in the wrong direction, the quality of power balancing is monitored by strongly reducing the magnetic field gradient to a few G/cm and observing the 3D expansion behaviour of the cloud using surveillance cameras from two axes. The more isotropic, the better. For ^{23}Na, there are additional $\lambda/2$ plates in the horizontal beam paths. Their orientation is adjustable by micrometer screws that allow for fine and reliable equalization of the beam intensities.

Exemplary ^{23}Na MOT loading curves taken during the optimization procedure are shown in fig. 19 (a), where the increasing-field coil current is varied and all other parameters are kept constant. For the Zeeman slower optimization, the component responsible for non-optimal behaviour (e.g. one can be slowing limited through the transversal spread or too high final slowing velocity) can be usually identified by studying the loading curve shape. Typical are kinks that appear in a trapping limited scenario when the loading is fast but suddenly capped. For a MOT, the two main figures of merit are the saturated atom number and the loading rate (or flux), the latter being defined as the initial slope of the loading curve. The optimal Zeeman coil values were obtained by evaluating the loading rate as shown in fig. 19 (b). The decreasing-field coil optimum of 5.5 A is in agreement with the optimum of 5.03 A that was calculated in [119] for a starting capture velocity of the slower of 900 m/s. A significant deviation exists between the experimentally found increasing-field optimum (7.4 A) and the calculated one (9.03 A). This is explained by the transversal momentum imposed on the particles through slowing. As the increasing-field coil finalizes the slower, its magnetic field value determines the amount of final slowing and defines the final velocity as the atoms leave the slowing region. Larger coil currents lead to smaller final velocities, but also increase the transversal spread over a given distance. The distance between Zeeman slower and science chamber, given by the amount of vacuum components inbetween, is approx. 22 cm for this setup. This is quite large compared to other setups (e.g. $\geqslant$ 12 cm featured in [129]), and the corresponding transversal spread significantly reduces the flux into the main chamber. In order to reach the calculated ideal slowing parameters in the future, a six-way flange cross, situated between slower and bellow connection, can be used to realize a transversal cooling stage [132] that guides the atoms and allows further longitudinal slowing.

For these slowing parameters, the optimal magnetic field gradient was found to be $B'_{Na} = 20.8\,G/cm$ (see fig. 19 (c)). In summary, for the ^{23}Na system, loading rates of 1.4×10^9 atoms/s and saturated atom numbers of 3×10^9 atoms after about 2.5 seconds of loading were realized.

^{39}K

After characterization of the ^{23}Na 3D MOT, the species operation was swapped and a similar optimization routine was started for ^{39}K without touching the geometric alignment. The starting conditions in terms of laser power ratios and frequencies are based on those featured in [131] and [133]. For ^{39}K, the narrow hyperfine splitting naturally splits the detuning space in several regions. Doppler cooling can only be employed either very close to resonance ($|\delta| \sim \Gamma_K$) in the low-intensity

limit, or below the whole excited state manifold ($|\delta| \sim 5.6\Gamma_K$) in the high-intensity limit. The latter is favorable as its velocity capture range is about one order of magnitude larger. Cooling and repumping intensities are branched from the laser table in a way that operates the 2D MOT in the low-intensity, near-resonant and the 3D MOT in the high-intensity, far-detuned limit. In contrast to ^{23}Na, the ^{39}K beams are distributed on the main table to their individual beam paths by using additional fused fiber optic couplers, which leads to losses of $20-40\%$ of the light power tabulated in the laser system chapter (tab. 2). In the 2D and 3D chamber, this gives total MOT laser intensities of $(I_{c.}, I_{r.})_{2D} = (1.82, 1.36) I_{Sat.}$ per beam and $(I_{c.}, I_{r.})_{3D} = (12, 10.8) I_{Sat.}$ per beam, respectively. For the 2D MOT values, this matches exactly the values given in [133].

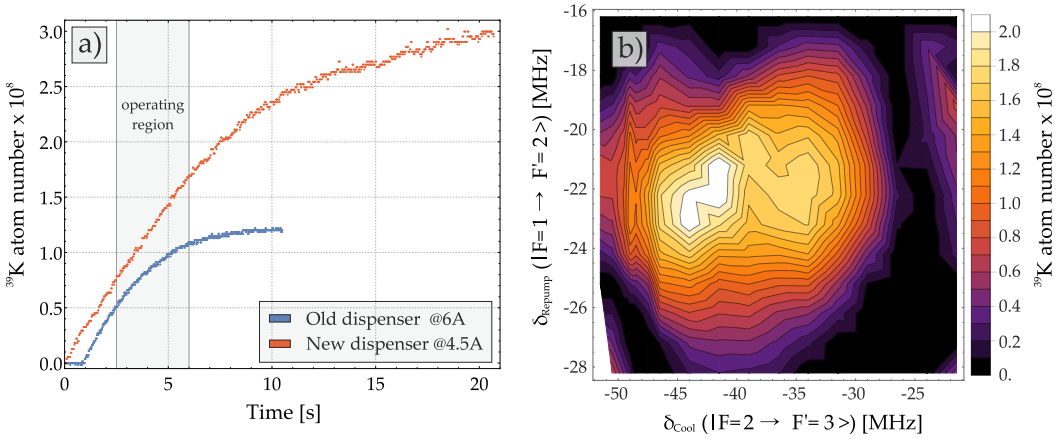

Figure 20: Typical ^{39}K MOT loading curves (without pushing beam) for the old and new dispenser. For the dual-species BECs, only the first 2-4 seconds are used. (b) MOT atom number after 10 s of loading as a function of both cooling and repumping laser detuning.

Typical MOT loading curves for the potassium MOT can be seen in fig. 20. For both curves, the pushing beam was off. All measurements shown in this thesis have been conducted with a dispenser that was signaling progressing depletion and hence had to be operated at a rather high current of 6 A (blue curve). The large resistive heating also sublimated other materials, worsening the vacuum and, together with the lesser amount of ^{39}K, limited the achievable MOT sizes. During the process of writing up this thesis, the then empty dispensers were replaced by ones from the SAES group that behave mostly identical, but are not enriched. For the new SAES dispenser, the needed vapor pressure is already reached at 4.5 A. The iterative optimization has then be carried out in a similar fashion as for the sodium cloud. The optimal magnetic field gradient for operating the ^{39}K MOT was found to be $B'_K = 6.4\,\mathrm{G/cm}$. To complement the magnetic field parameter scans shown for the sodium MOT, fig. 20 (b) shows a typical optical field parameter scan, namely in laser detuning space for the 3D MOT beams. Similar to sodium, all potassium parameters were later fine-tuned, in this case by using the phase space density of a 50 µK cold cloud in the magnetic trap as a figure of merit. Even though the saturated atom numbers are much larger for the new dispenser, it is mentioned here that the ^{39}K MOT is usually never fully loaded. This can be traced back to the sympathetic cooling mechanism that only remotely affects the potassium atom number. In fact, dual-species condensates are usually achieved in this setup by

loading an unpushed MOT for about two seconds. This is indicated by a shaded region in 20 (a) that outlines the typical MOT loading duration. For such short loading times, the loading rate, which is similar for both dispensers, becomes more important than the actual MOT saturation value. The pushing beam increases both loading rate and saturation value. Yet the dual-species condensates were found to be quite sensitive to the exact atom number ratio. Having a slower potassium loading curve was then actually beneficial as it allowed easier fine tuning of the exact amount of loaded atoms. Hence especially for the later shown measurements, the pushing beam has been deactivated.

Experimental sequence

The used laser cooling sequence is shown in fig. 21. It is processed as follows: The sequence starts by loading ^{39}K at its optimized magnetic field gradient B'_K, while ^{23}Na is withhold via the pneumatic shutter. This first, single-species operation is mainly used as a surveillance mechanism to verify stable potassium conditions, without having its signal overshadowed by the sodium cloud on the photodiode detector or the video cameras. After two seconds, the atom shutter is triggered. The two-color 3D MOT is still operated at the potassium favoring gradient B'_K until a sufficient amount of ^{39}K is loaded. The presence of ^{23}Na atoms was not found to significantly obstruct the ^{39}K cloud. Following this, the magnetic field coils are quickly ramped up to the sodium-favored gradient B'_{Na} and the ^{39}K laser frequencies are adapted to minimize losses. After about two seconds the sodium MOT is saturated, finishing the MOT phase.

After the MOT, an optical molasses is prepared and held, cooling both samples through polarization-gradient cooling using the MOT beams. The molasses transition features a steady reduction of both repumping lasers while the magnetic field

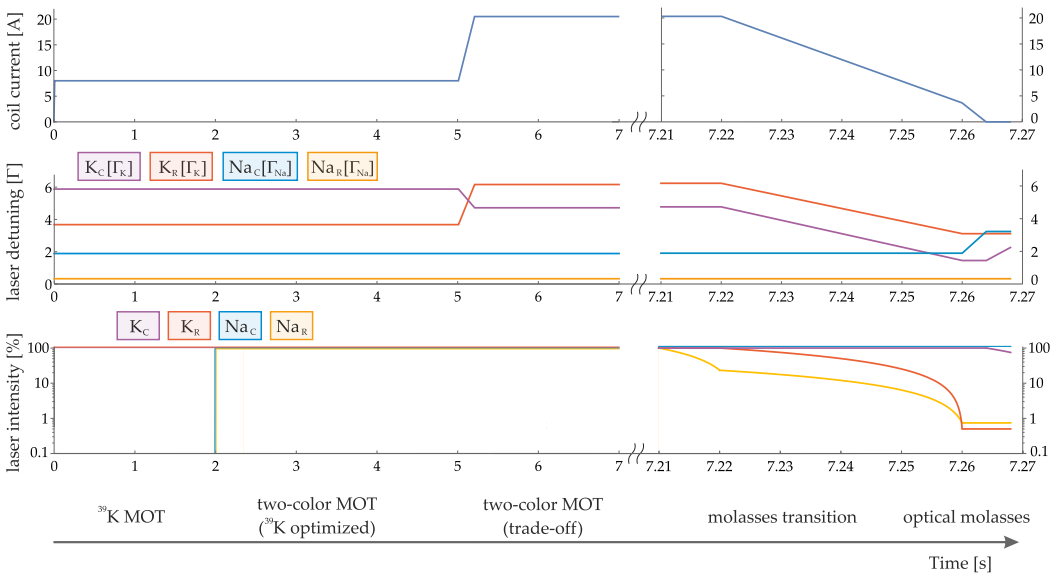

Figure 21: Experimental cooling sequence. The subscripts denote c = cool, r = repump. The detuning is given in absolute values of the frequency difference to the transition $|f = 2\rangle \rightarrow |f' = 3\rangle$ transition (cooling) and $|f = 1\rangle \rightarrow |f' = 2\rangle$transition (repumping). For further details, see text.

gradient is lowered in 40 ms. In contrast, the usual molasses initialization method, i.e. switching the magnetic field abruptly, gave lower accessible temperatures yet inferior capture efficiencies, which in this configuration are nearly unity for both clouds. In dual-species operation, tuning of the individual timings and parameters to a trade-off configuration was necessary. In the case where no common optimum was found for both species, leaning towards the sodium-favored configuration was usually beneficial in view of the later sympathetic cooling mechanism. In the end, this gave dual-species sub-Doppler temperatures $T_{Na} = 53\,\mu K$ and $T_K = 106\,\mu K$ as probed by TOF expansion. Together with the 3×10^9 ^{23}Na and the typical loading of 1×10^8 ^{39}K atoms, these parameters constitute the normal operating conditions in the dual-color MOT system.

5

MAGNETIC TRAPPING

Magneto-optical cooling and trapping of alkali-metal atoms is limited in terms of achievable temperatures as well as densities, hence different cooling strategies are required to exceed phase space densities beyond $\approx 10^{-5}$. After the molasses phase, the MOT beams are switched off and the coil currents ramped up, creating a pure *magnetic trap* which provides a tight confining repository for the atoms. The trapping mechanism hereby relies on the Zeeman interaction for weak magnetic fields. Assuming that an atom's magnetic moment $\boldsymbol{\mu}$ is aligned with the local magnetic field $\boldsymbol{B}$, the magnetic energy shift will be given by

$$\Delta E = -\langle \boldsymbol{\mu} \cdot \boldsymbol{B} \rangle = \mu_B m_f g_f |\boldsymbol{B}| \tag{5.1}$$

with the Bohr magneton $\mu_B/k_B \approx 67\,\mu K/G$, the total spin projection m_f and the Landé factor g_f. The inclined reader will remember that for the coil configuration used in this experiment the energy shift of (5.1) obtains its spatial dependence in quadrupolar form, $B(x, y, z) = B'\sqrt{x^2/4 + y^2/4 + z^2}$. Multiple things are notable:

1. For each internal atomic state, higher magnetic field amplitudes will either attract or repel the corresponding atom, depending on the combined signs of Landé factor and spin projection. As Maxwell's equations allow the formation of local minima yet forbid local maxima in $|\boldsymbol{B}|$, only the atoms feeling repulsion (commonly referred to as low-field seekers) can be magnetically trapped. State-selective trapping demands a reconfiguration of the state population present in a MOT in order to minimize transfer losses. This is briefly discussed in section 5.1 together with the initial transfer.

2. Equation (5.1) is a scalar quantity, and therefore the energy shift depends only on the magnetic field amplitude and not on its orientation. This is due to the postulate that the magnetic moment orientation will always be parallel to the local magnetic field. The limitations of such an assumption and the consequences (Majorana losses) are discussed in section 5.3.

3. The generated magnetic trapping potential is conservative, and therefore does not induce any sort of cooling by itself. Cooling will be provided externally using microwave radiation, which is presented in sec. 5.4.

Using the above techniques for subsequent phase space compression, quantum degenerate samples of ^{23}Na can be generated in a magnetic trap [5, 129]. For ^{23}Na, the corresponding cooling efficiency has been mapped out down to the condensation threshold ($\sim 1\,\mu K$ for densities $\sim 10^{13} cm^{-3}$) and the already presented MOT and molasses parameters have been fine-tuned to optimize the atom number at this temperature. The negative scattering length of ^{39}K however dictates the use of Feshbach fields in order to generate a ^{39}K condensate, and the additional interspecies interaction gives rise to stronger losses as the densities are increased. Therefore, it is emphasized that the experimental task in this chapter is not necessarily to reach the coldest temperatures or highest densities. As condensates can be generated

in magnetic as well as in optical traps, the quadrupole trap merely serves as an intermediate step to increase the dipole trap loading efficiency, which will take place before reaching the BEC threshold. It is further pointed out that because ^{39}K will be sympathetically cooled, only a low amount on the order of $10^6 - 10^7$ atoms have to be loaded in the magnetic trap. Hence the requirements regarding efficient ^{39}K trap transfer are comparably lax, and for most magnetic trapping properties the focus lies on the ^{23}Na performance.

5.1 MAGNETIC TRAP TRANSFER

Initial temperature

Once a magnetically trapped atomic cloud has thermalized, adiabatic changes of the trapping gradient B′ will leave its phase space density unchanged. The initial field gradient however will impose a diabatic change due to the sudden switch-on of the coils. The stiffer the gradient, the more Zeeman energy is imposed upon the atoms. On the other hand, the initial gradient has to be strong enough to hold the atoms against gravity and has to minimize the vertical mode matching offset caused by the gravitational sag. Using the virial theorem [134], the temperature of a thermalized sample in the magnetic trap can be expressed as

$$T_{MT} = T_i/3 + 16(\mu K/G)\sigma_i m_f B' \tag{5.2}$$

with T_i being the initial MOT or molasses temperature and σ_i its root mean square width. The experimentally determined magnetic trap temperature is usually larger than this calculated value, because the magnetic trap origin will be close to but not identical to the molasses position. This spatial mismatch will inflict further heating beyond the scope of eq. (5.2), and the temperature of the clouds after the magnetic trap transfer can easily exceed several hundred μK. In the early stage of this experiment as well as in a competing ^{23}Na-^{40}K group employing a similar setup, $T \simeq 1$ mK were reported [76, 135]. To hold the heating due to displacement minimal, a prealignment scheme involving multiple-axes imaging was used: The position of each molasses cloud was first compared and superimposed with that of strongly magnetically compressed MOTs, as the latter indicate the magnetic trap origin. Following this prealignment procedure, and using the molasses scheme of section 4.4 ($T_{Na} = 53\,\mu K$, $T_K = 106\,\mu K$), a sudden switch on to 80 G/cm appeared optimal for the dual-species operation. For this gradient and the measured rms width after the molasses stage, eq. (5.2) predicts $T_{MT,Na} = 99.5\,\mu K$ and $T_{MT,K} = 159.7\,\mu K$. The experimentally determined temperatures $T_{Na} \approx 100\,\mu K$ and $T_K \approx 240\,\mu K$ hint at residual imperfections in the positioning of the potassium cloud but show excellent agreement otherwise. It is mentioned that the estimation of initial temperatures in a quadrupole trap is usually slightly vague. The high initial kinetic energy and the finite magnetic coil switch-off time result in a rather small available time of flight window for both species (see also section 5.2 for a discussion of alternative methods used for cross-checking). Moreover, as the trap cannot be disabled instantaneously, adiabatic cooling effects may persist. Following this initial trapping, the quadrupole trap is ramped adiabatically to its final gradient value B'_0. When one (both) DELTA power supply is (are) in operation, usually $B'_0 = 156\,G/cm$, ($B'_0 = 216\,G/cm$).

Optical pumping: $f = 1$ *or* $f = 2$*?*

For the ground state of ^{23}Na and ^{39}K, the Landé factors are $g_{f=1} = -g_{f=2} = -1/2$. Hence the set $|f, m_f\rangle$ of magnetically trappable states is given by the low-field seekers $|2,2\rangle$,$|2,1\rangle$ and $|1,-1\rangle$, and the magnetic trap transfer efficiency depends on the population distribution over these internal states. It is further essential that trapped atoms do not change their internal state by spin-changing collisions. Due to the different signs of their Landé factors, the magnetic moment orientation of the $f = 1$ and $f = 2$ trappable substates is flipped with respect to each other, and collisions between these atoms can transfer both to untrapped states (e.g. via $|1,-1\rangle + |2,1\rangle \rightarrow |1,0\rangle + |2,0\rangle$). The first task of magnetic trapping therefore consists in choosing a hyperfine submanifold to work in and removing all atoms in other states. The concept of redistributing the atomic population by flashes of laser light is called *optical pumping*. Using resonant σ^+-polarized light, one continuously drives transitions $|f, m_f\rangle \leftrightarrow |f', m_f + 1\rangle$. Any spontaneous decay back to the ground state will be arbitrarily polarized and therefore the set of magnetic quantum number decay channels is $\{m_f, m_f + 1, m_f + 2\}$. Repeating this process hence gives a net preference to higher m_f states, magnetizing the sample. The generation of negative net magnetization is analogous.

As the magnetic field gradient scales with m_f, the $|f = 2, m_f = 2\rangle$ state experiences the largest magnetic potential of all trappable states. In systems like ^{87}Rb, where all scattering cross sections are about equal, this state has beneficial properties regarding elastic collisional rates for the later cooling process and is therefore the usual state of choice. In contrast to ^{87}Rb, the scattering cross sections of $f = 1$ and $f = 2$ are quite different in ^{23}Na. In particular, $|f = 2, m_f = 2\rangle$ displays a more unfavorable inelastic scattering rate, limiting the $1/e$ lifetime in a condensate to a few seconds [136]. The common approach therefore is to prepare the sample in the $f = 1$ manifold, which is also followed here. It has further been shown [129] that optical pumping is usually much less effective compared to systems like ^{87}Rb, the main reason being stronger depolarizing mechanisms due to the smaller hyperfine splitting. High conversion efficiencies of 0.75 were only realized in the presence of large magnetic bias fields of $80 - 100\,\mathrm{G}$ [137, 138], an option that is not available in the setup of this thesis. In this setup, a first pumping flash using a former MOT cooling beam transfers all atoms into the $f = 1$ manifold, which is traced using state-selective absorption imaging. Having made sure that the sample is cleaned of $f = 2$ atoms, the capture efficiency is evaluated by retrapping the atoms in their initial MOT configuration. The corresponding photodiode signal ratio gives transfer efficiencies in the range of $26 - 31\%$ for this pure $|f\rangle$ pumping scheme. m_f selective pumping demands a well-defined quantization axis along the propagation of the pumping beam. Using bias fields on the order of a few Gauss induced by the compensation cage, a second pumping flash increases the transfer efficiency by a factor of $1.5 - 1.6$. The low switching time of the bias fields as well as residual jittering in the beam shutter switching time made this second pumping constantly interfere with the optimal molasses and magnetic trap capture parameters. Evaluating the gain of optical pumping at later stages of the experiment, this lead to slightly higher average atom numbers, yet at the cost of higher shot-to-shot fluctuations. The m_f selective pumping was therefore eventually discontinued and only the first pumping flash is currently in use.

5.2 MEASURING *in-situ*

In situ (latin), measuring a phenomenon at the place of its occurence, without isolating or removing it from its original environment.

For the evaluation of the phase space density, only the static [82] parameters atom number and temperature have to be determined. Both can be inferred after a TOF measurement as outlined in sec. 4.3. However, the instant deactivation of the quadrupole coil fields and the associated eddy currents generate parasitic transient magnetic fields, and the corresponding Zeeman interaction detunes the atoms with respect to the detection beam. For the experiment at hand, eddy currents were found to persist for up to 3.4 ms, giving a lower limit for achievable reliable TOF as well as uncertainties regarding the initial width of the expanding cloud. Moreover, at high temperatures the released cloud quickly disperses, leading to rapidly decreasing contrast. Both effects together constrain the available analysis window and the deduction of the temperature can be error-prone. Lastly, the limited switch-off time of the magnetic trap does work on the atoms and can lead to a small amount of adiabatic cooling which is difficult to characterize. A convenient alternative consists in the acquisition of *in situ* absorption pictures of the still trapped cloud, when the relevant parameters can be extracted out of the density distribution. This has to be done with care, as the presence of the linear trapping potential leads to anharmonic mixing between the spatial coordinates, so that the standard procedure of integrating over all but one coordinate and then obtaining a width has to be applied and interpreted correctly. The total trapped atom number can be written as

$$N/n_0 = \int_V n(x,y,z) = \iiint \exp\left[-\frac{g_f m_f \mu_B B'}{k_B T}\sqrt{x^2/4 + y^2/4 + z^2}\right] dx\,dy\,dz, \quad (5.3)$$

with the peak density $n_0 = n(0,0,0)$, and the in-trap density distribution $n(x,y,z)$ being given by a Boltzmann factor with $1/e$ length that is the ratio of magnetic force and thermal energy. Any non-tomographic measurement method integrates along the detection axis here chosen to be y, yielding the column density $n_{\int_y}(x,z) = \int_{-\infty}^{\infty} n(x,y,z)dy$. Considering a cut through the vertical direction, the functional form of the density distribution can be expressed as

$$n_{\int_y}(x,0) \propto 2|x|\,\mathcal{K}_1\left(\frac{g_f m_f \mu_B B'}{k_B T}|x|\right), \quad (5.4)$$

with $\mathcal{K}_1$ being the modified bessel function of second kind and first order. The temperature is then evaluated as [130]

$$T = \frac{2}{5}\frac{g_f m_f \mu_B B'}{k_B}\Delta_{\int} \quad (5.5)$$

where $\Delta_{\int}$ is the full width half maximum of $n_{\int_y}(x,0)$, and the $\int$-subscript signals the onefold integration. For a gradient of 216 G/cm along the vertical direction and atoms in $|f = 1, m_f = -1\rangle$, this gives a conversion factor of $0.145\,(\mu K/\mu m)$ between temperature and horizontal cloud extent. Experimentally, it is common to integrate the column density also over the other (in this case vertical z-) direction to suppress systematic noise. However, as the magnetic trapping potential is not separable along the cartesian coordinates, the functional form and therefore also the FWHM value of the column density along x will be a function of z, and for the problem at hand, the subsequent integration along z will broaden the obtained signal. This is depicted in the inset of Fig. 22 for a 40 μK hot cloud. By denoting

the integrated column density as $n_{\int\int_{y,z}}(x)$ and its FWHM as $\Delta_{\int\int}$, eq. (5.5) has to be complemented by a correction factor $\epsilon_1 = \Delta_{\int}/\Delta_{\int\int}$ in order to give the correct temperature estimate, and will lead to an overestimation otherwise. In the limit of complete integration over z, the integrated column density is

$$n_{\int\int_{y,z}}(x) = 4\pi \left(\frac{k_B T}{g_f m_f \mu_B B'}\right)^2 \left(1 + \frac{g_f m_f \mu_B B'}{2k_B T}|x|\right) \exp\left[-\frac{g_f m_f \mu_B B'}{2k_B T}|x|\right]. \quad (5.6)$$

For calculational convenience, it is much simpler to perform a Gaussian fit with standard deviation σ_{Gauss} to $n_{\int\int_{y,z}}(x)$ and approximate the integrated FWHM by the fitted one using $\Delta_{\text{Gauss}} = 2\sqrt{2\log(2)}\sigma_{\text{Gauss}}$ for a Gaussian FWHM. This commonly used [139, 130, 140] Gaussian approximation introduces a second correction factor $\epsilon_2 = \Delta_{\int\int}/\Delta_{\text{Gauss}}$ that one has to account for. Due to the limited integration bounds, both functional form mappings will be inherently nonlinear. The correction factors are determined by first calculating the integrated column density for ensemble temperatures between 10 µK and 300 µK using numerical integration. The estimated temperature is extracted using eq. (5.5), once using the corresponding FWHM of the exact functional form and once for a Gaussian fit of said form. To highlight the susceptibility of the correction factors to the integration bounds, the integration is performed completely along y and in a fixed 20 mm^2 area in the xz plane. The result is depicted in fig. 22 for a temperature range up to 205 µK, together with the FWHM of the column density for which eq. (5.5) is exact. The broadening due to integration along the vertical direction corresponds to a correction $\epsilon_1 \approx \frac{3}{4}$ that can also be obtained by comparing eq. (5.4) and (5.6). Shrinking the vertical integration window in an experimental sequence then gives values between $\frac{3}{4}$

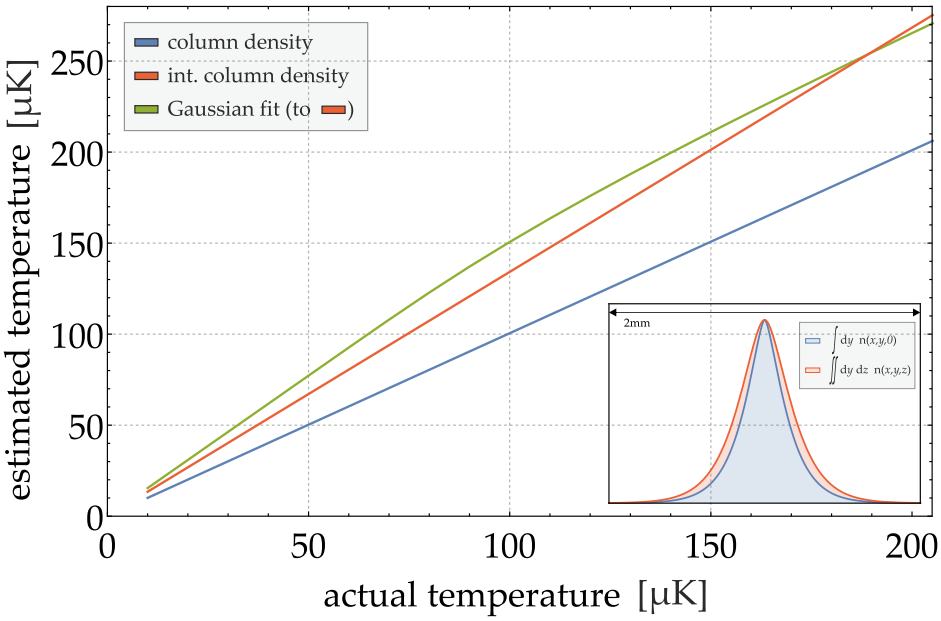

Figure 22: Estimated temperature using eq. (5.5) for the FWHM of the column density (blue curve), integrated column density (red curve) and a Gaussian fit to the latter (green curve). Out of the different slopes, the correction factors ϵ_1 and ϵ_2 can be evaluated. The inset shows the broadening of the integrated column density (red curve) compared to a column density cut through the $z = 0$ plane (blue curve) for a 40 µK hot cloud and a gradient of 216 G/cm.

(for the whole cloud) and 1 (for the central slice). The Gaussian approximation gives a nonlinear overestimation, being 15% for temperatures up to 60 μK and then bending over to smaller overestimations, which can be attributed to the changing ratio between cloud width and integration bounds. In total, both correction factor functions appear benign. The last complication arises due to the effect of Zeeman shifts on the absorption technique. The presence of the inhomogeneous magnetic trapping potential changes the interaction of the detection beam with the atomic distribution with respect to local polarization and detuning, which in turn leads to different local scattering cross sections. For a probe beam on the cyclic transition $|2,2\rangle \rightarrow |3,3\rangle$, the differential Zeeman shift between the trap center and the cloud density FWHM $\Delta_{\int}$ is

$$\delta(\Delta_{\int}) = 6.95\,(\mathrm{MHz/G})\frac{k_B}{\mu_B}T = 100\,\mathrm{kHz/\mu K} \times T \tag{5.7}$$

The actual field gradient drops out of the calculation, as the cloud adapts its extent according to eq. (5.5). Hence the spatial distortion is mainly governed by a comparison of the atom species linewidth to the thermal spread. These effects appear strongly pronounced for ^{39}K, as its smaller natural linewidth reacts more sensitive to the inhomogeneous Zeeman shifts, and its small hyperfine spacing more sensitive to local optical pumping. No globally monotonic scaling between in-situ and real atom number could be obtained here, rendering even qualitative statements futile. In order to obtain better estimations for this species, the probe frequency would have to be detuned several linewidths to decrease the impact of the differential Zeeman shifts on the absorption cross section [7][1].

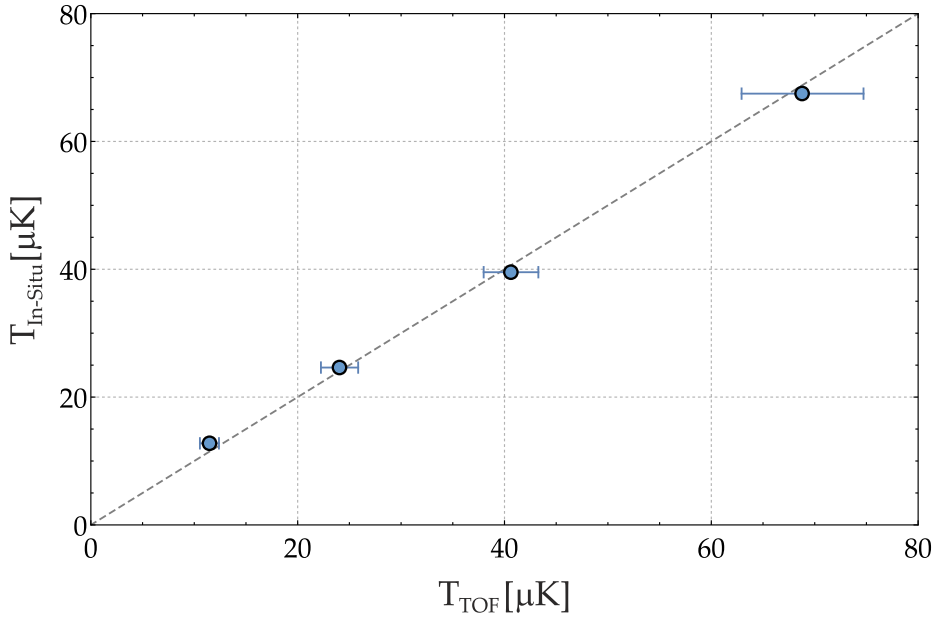

Figure 23: Experimental temperature determination using the in-situ and TOF method for the ^{23}Na system. Both methods are in agreement with each other, as indicated by the unity slope line (dashed gray curve). The vertical error bars, given by the standard deviation using the estimate along horizontal and vertical direction, are smaller than the plot markers.

1 An exact in-situ atom number determination will only be possible by fitting a convolution of all the spatially dependent parameters with the unknown density distribution to the acquired signal [141].

For ^{23}Na with its comparatively large linewidth, a much better agreement is found. At temperatures between 10 and 100μK acquired via TOF, atom number scaling factors between 3 and 3.7 are observed. Figure 23 shows a comparison of TOF and in-situ temperature estimations for given evaporation depths and ^{23}Na, using eq. (4.20) and (5.5) together with the appropriate correction factors ϵ_1, ϵ_2. The temperature estimates agree with each other in a window given by a standard error of ±7% and therefore lie well in each other error bars. This result proved to be very valuable during the optimization stage of the dual-species operation. By approximating the ^{23}Na parameters using in-situ imaging and measuring the ^{39}K atom number in a subsequent TOF, the static parameters for both species can be obtained in one single shot. In experiments with a cycle time on the order of a minute, this approach allows expeditious qualitative optimization on a finely sampled parameter grid. Once the optimal working point has been narrowed down in parameter space, this method can be complemented by the more time-devouring approach of separate TOF measurements for each species in order to cross-check the determined temperatures and reassess whether the species are in thermal equilibrium with each other.

5.3 MAJORANA LOSSES AND OPTICAL PLUGGING

In a semi-classical picture, the atom's magnetic moment precesses around the quantization axis set by the magnetic field. In order to maintain this precessing motion when the field is subject to changes, the atom has to adiabatically realign to the magnetic field orientation on a timescale given by the inverse Larmor frequency of its precession, $(\omega_L)^{-1} = (\mu B/\hbar)^{-1}$. Every faster change will be diabatic and can lead to spin flipping excitations in the local eigenbasis. At the origin, the magnetic field approaches zero and $(\omega_L)^{-1}$ diverges. Consequently, an atomic spin passing the center cannot follow the field direction fast enough and will 'lose' its quantization axis. It is then possible that the magnetic moment of the atom is reversed relative to the local direction of the magnetic field and therefore spin-flipped into an untrapped state, and thus leaves the trap. This loss mechanism is famously known as *Majorana losses*[2][144]. This phenomenon obstructs the cooling efficiency $\propto N/T$ twofold, as it increases T while decreasing N. As the probability distribution of vibrational wave functions maximize at the semiclassical turning points, hot atoms spend only a short time at the trap center, and their loss rate is dominated by collisions with the background gas. As the system gets colder and denser, Majorana losses become therefore more pronounced. Intuitively, one might expect the loss rate to scale as $\Gamma \propto n \propto \frac{1}{\sigma_x \sigma_y \sigma_z} \propto T^{-3}$. This is partially compensated by the fact that slower atoms have more time to adapt to the magnetic zero, which results in an inverse quadratic instead of cubic scaling $\Gamma \propto T^{-2}$ [145]. To quantify this effect, a simple loss model can be employed [146], treating the magnetic center as an ellipsoid with absorbing boundary conditions. The flux of atoms entering this ellipsoid then directly gives the Majorana loss rate

$$\Gamma_M = \chi \frac{\hbar}{m} \left(\frac{\mu_B g_f m_f B'}{k_B T} \right)^2 \tag{5.8}$$

2 Cynically, Ettore Majorana himself got lost during a short ship trip from Naples to Palermo. His mysterious disappearance has been the subject of debate and exhaustively covered in literature, with vast speculations regarding his motives and fate [142, 143].

where χ is a geometrical prefactor defined by the ellipsoid volume. It can be calculated either by approximating it with the spherically symmetric solution giving $\chi_{\text{symm.}} = \frac{24^{1/3}}{32} \approx 0.09$ [145], where the field gradient B′ has to be replaced by its geometric average over all dimensions, or directly evaluated by numerical integration of the atomic velocity distribution [147]. For a given experimental setup, magnetic field strength noise, fluctuations and drifts affect the loss region. These perturbations are not easy traceable and differ from setup to setup. The most sensible option therefore is to use χ as a free fitting parameter to given data so that it incorporates the averaged perturbations of the given experimental situation. The latter method gives typical values between 0.1 and 1 [146, 148, 149]. Fig. 24 shows measurements of the ^{23}Na effective 1/e lifetime at varying temperatures and a magnetic field gradient of 216 G/cm. Each loss rate has been recorded by monitoring the remaining atom fraction at given trap holding times and extracting the respective time constants out of exponential decay fitting. The high-temperature limit of pure background collision induced losses can be prepared by disabling the molasses stage, when the magnetic trap transfer significantly worsens. In the probed temperature region, the densities are sufficiently low and three-body losses can be neglected. The temperature dependent lifetime loss rate is then given by the inverse overall loss rate

$$\Gamma(T)^{-1} = \left[\Gamma_M(T) + \Gamma_{bg}\right]^{-1} = \left[\chi \frac{\hbar}{m}\left(\frac{\mu_B g_f m_f B'}{k_B T}\right)^2 + \frac{1}{\tau}\right]^{-1} . \tag{5.9}$$

Using χ and the background lifetime τ as fitting parameters yields $\tau = 46.5\,\text{s}$ and $\chi = 0.196$. This is in accordance with other ^{23}Na systems [149], in which $\chi = 0.14$ was measured.

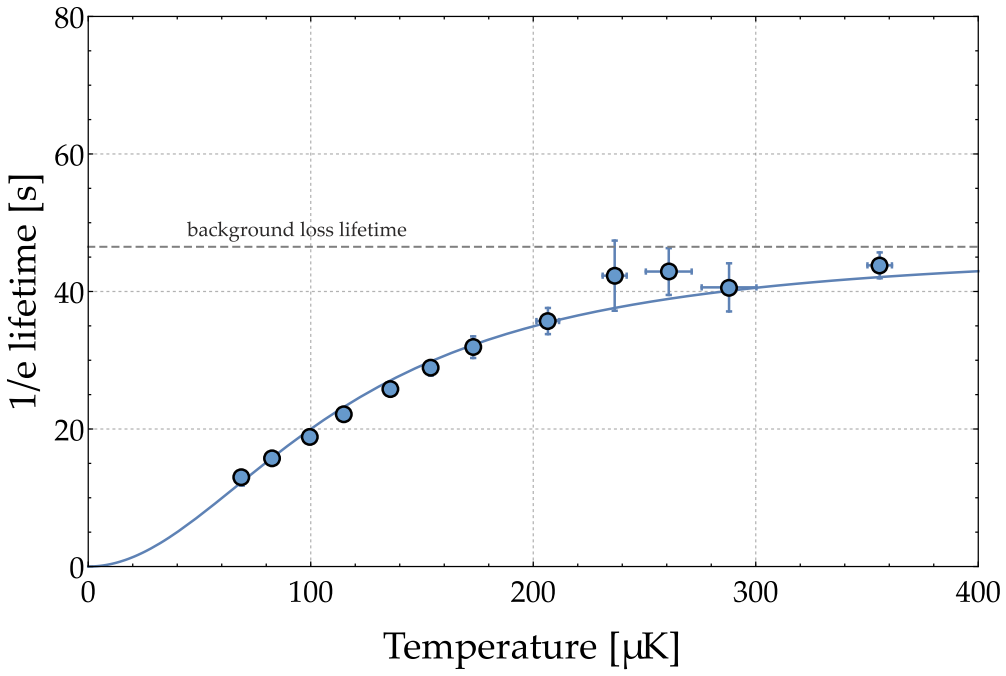

Figure 24: Measured effective 1/e lifetime as a function of temperature. A fit (solid line) using the Majorana loss rate equation gives the geometric prefactor χ.

5.3.1 *Plugging the trap*

A multitude of options exist to suppress this loss mechanism inherent to quadrupole traps. All of them employ additional mechanisms of magnetic or optical origin that superimposes the quadrupole potential. Purely magnetic solutions rely on time-averaging (TOP trap [150]) or on shifts of the magnetic zero (Ioffe-Pritchard trap [151]) using an additional bias field coil. In this thesis, an optical solution is utilized by focusing a blue-detuned laser beam into the magnetic center. There it erects a repulsive potential barrier for the atoms, serving as an *optical plug* of the magnetic trap bottom. For the discussion of optical forces, see chapter 6 and references therein. It is only stated here that $V_{\mathrm{Plug}} \propto I_{\mathrm{Plug}}$ for a blue-detuned beam. The atomic ensemble will then reside in the newly formed minima of the combined magneto-optical hybrid potential, avoiding the loss ellipsoid at the center. The resulting trap geometry depends on the inclined angle between beam propagation and coil symmetry axis. In a horizontal beam configuration, always two minima will be generated, as the beam slices perpendicular through the magnetic field symmetry axis. For the used experiment chamber, such a configuration gives easier optical access, yet is prone to instabilities e.g. due to drifts or vibration induced fluctuations of the magnetic trap position, which appear most strongly pronounced along the axial direction of the trap. The plug is therefore used in a vertical beam configuration, which is immune to vertical drifts smaller than the Rayleigh length. If the beam traverses exactly along the coil symmetry axis, the combined trap generates an infinite amount of degenerate minima at a given radial distance, which is depicted in fig. 25 (a). In experiments that pursue Bose-Einstein condensation already in the plugged trap, this is usually unwanted as an infinite ground state degeneracy will lead to fragmentation rather than condensation. This holds true also for this experiment, as a ring-shaped cloud is less useful for the later transfer into the optical dipole trap. The plug is therefore radially displaced by about half a beam waist, thereby generating one localized absolute minimum (see fig. 25 (b)).

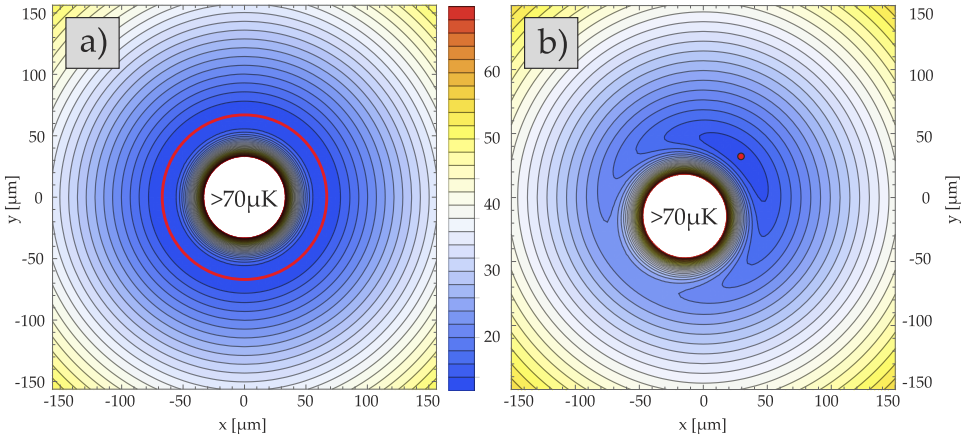

Figure 25: Combined potential (in μK) in a vertical plug configuration for the experimental parameters used in this thesis and a cut along $z = 0$. A plug propagating along the symmetry axis (a) creates a ring of minima (red circle), whereas a deliberate offset from the symmetry axis (b) generates one well defined minimum (red dot). The potential value at the plug center is on the order of 250 μK.

The presence of the plugging potential deforms the density distribution of the cloud, when amongst others the in-situ determination of temperatures (see 5.2) becomes critical. To quantify this, the density distributions for the combined potential with the used experimental parameters were obtained by numerical integration. The resulting integrated column densities $n_{\iint_{y,z}}(x)$ are depicted in fig. 26 together with a cut of the combined potential through the yz-plane. At temperatures above 60 µK, the effect of the plugged hole is less pronounced and gets almost averaged out, when the in-situ temperature determination is still reliable using an appropriate correction factor depending on the plug intensity. At lower temperatures, the density first develops an asymmetry which turns into a skewed Gaussian at temperatures in the low µK regime. Determining the temperature at these parameters would demand a deconvolution of the obtained integrated distribution, which is beyond the treatment introduced in sec. 5.2. In the temperature region $T < 10\mu K$, the accessible expansion times are significantly enlarged, when a TOF analysis becomes the most reliable tool.

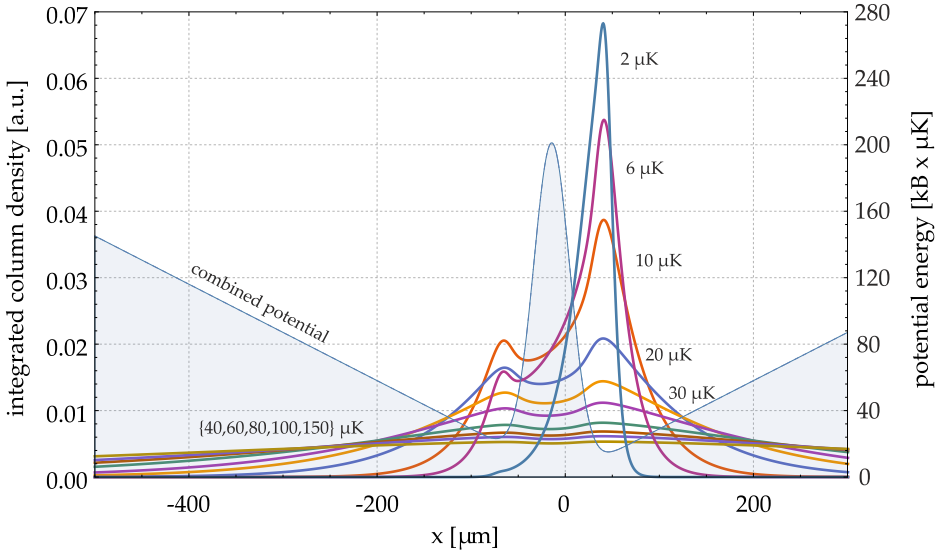

Figure 26: ^{23}Na integrated column density distributions (in arbitrary units) for a plugged trap and temperatures between 2 and 150 µK. The parameters of the combined trap are $B' = 216\,G/cm$, $P_{Plug} = 3.7\,W$, $\lambda_{Plug} = 532\,nm$, $w_0 = 39\,\mu m$ and a radial displacement by $w_0/2$ into the third quadrant of the xy-plane.

5.3.2 *Experimental implementation*

In this experiment, the generating source of the repulsive potential is a single-mode diode laser pumped solid state laser system (*VERDI-V5*) that generates up to 5 W of power in the green part of the optical spectrum ($\lambda_{BP} = 532\,nm$). The experimental setup is depicted together with the initial alignment procedure in figure 27. Despite its apparent simplicity, the optical setup imposes some strict boundary conditions regarding its initial alignment, daily usage and weekly maintenance. It had been previously reported [149] that it is imperative to distribute the beam using an optical fiber to ensure high enough pointing stability. For this task, the experiment uses a large mode area photonic crystal fiber (NKT Photonics), whose fiber coupler connector is embedded in a copper housing. With 5 W of low-wavelength light, the

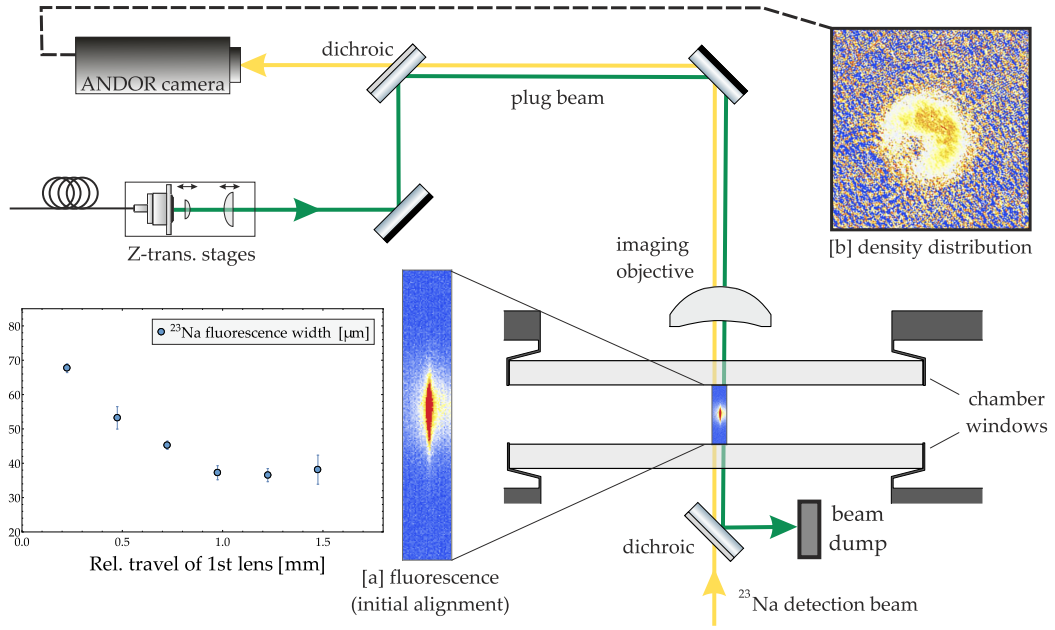

Figure 27: Experimental setup. The initial alignment procedure uses resonant light instead of the plug beam to induce fluorescence in the ^{23}Na cloud [a]. Switching back to the plug beam unveils the plugging effect [b].

power handling of the fiber turns out to play a vital role. Dissipating laser power in the fiber cladding leads to heating and slight deformation of the copper, which in turn squeezes the fiber, slightly changes its orientation and hence again changes the power dissipated into the fiber, generating a closed feedback loop. This also discouraged the use of higher amount of power: Using a different VERDI with nominal output power of 10 W, coupling 8 W into the fiber lead to temperatures of 52°C in the housing. For the 5 W VERDI, stable operating conditions could only be achieved if the fiber is kept in constant thermal equilibrium, which forces to install the plugs on/off switch *after* the fiber. Switching is achieved by using a shutter tandem, of which one is designed to withstand high thermal load, while the other ensures quick and reliable switching [152]. Under these conditions, $3.5 - 3.7$ W of light can be delivered through the fiber, which is monitored by a pickoff photodiode next to the fiber output. As the beam enters the chamber from the top, the plug beam is superimposed with the vertical imaging path using a dichroic mirror. Thus it will pass through the imaging objective, which has to be accounted for when setting the beam spot size and divergence. After the beam has passed the chamber, it is deflected onto a beam dump using a dichroic mirror so not to interfere with the MOT optics. In the initial setup procedure, the beam path is first aligned onto the atomic ensemble position by injecting light resonant with both the cooling and repumping transition of the sodium D2 line into the NKT fiber and maximizing the fluorescence signal on the horizontal detection system (see fig. 27). A two-lens system after the outcoupler sets the focus position and beam waist, both being preset using sodium fluorescence as shown in the inset of fig. 27. For the tested waists between 13 and 50 μm, the corresponding Rayleigh lengths are between 1 and 14.76 mm, rendering the exact focus position largely irrelevant. With a decently aligned beam, absorption imaging along the vertical axis unveils the effect of the blue plug piercing a hole into the atomic distribution. At sufficiently low temperatures, the effect of a decently aligned plug

is stunning, as it greatly increases the observed atom number compared to the plugless configuration. Fine adjustment of the plugging performance as a function of waist size fixes the latter to 39 µm, extracted by a two-dimensional Gaussian fit to the pierced density distribution. For 3.5 W of power, this results in a plug height of 246 µK at its maximum, whereas the optical potential at the magnetic trap center is $V_{p,o} = V_{plug}(0,0,0) \approx 150\,\mu K$. The plug position is monitored daily during the experimental routine check-up and has to be slightly adjusted on a weekly to monthly basis.

Having installed the plug, the Majorana losses are revisited by performing lifetime measurements in the now plugged magnetic trap, as shown in fig. 28. Compared to fig. 24, the vacuum conditions had been improved by applying Titan sublimation pumping, giving lifetimes due to background collisions of over a minute. For $T < 100\,\mu K$, the expected Majorana loss rate (dashed line) translates into lifetimes of below 30 s. Instead, the observed lifetimes are about 35 s larger, signaling the desired suppression. Due to the finite plug height, the Majorana loss mechanism is not completely disabled, as atoms with enough kinetic energy can tunnel through the optical barrier. The increasing density near the trap center reduces the lifetime to its minimum of 28.5 s at $T \approx 10\,\mu K$. At even lower temperatures, the underlying Boltzmann distribution supports less atoms with enough kinetic energy, and the lifetime again increases. Assuming a Boltzmann like exponential loss reduction [149] gives $\Gamma_{M,supp.} \propto \Gamma_M \times \exp\left[-V_{p,o}/k_B T\right]$ for the suppressed Majorana rate. A fit to the data represents the observed behaviour well down to $T \geqslant 4\,\mu K$ (solid line). At even lower temperatures, the deviation from the expected curve indicates the regime from which on 3-body losses, which are not included in the model above, have to be taken into account. Summarizing, the plugged trap supports sufficient lifetimes at all observed temperatures. With the Majorana losses out of the way, the stage is set for performing phase-space compression, which is discussed next.

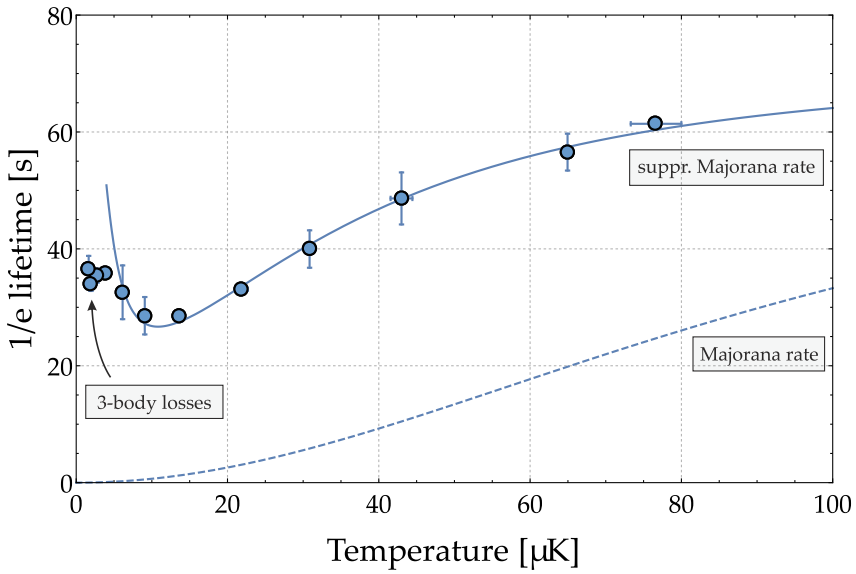

Figure 28: 1/e lifetime as a function of temperature for the plugged trap and $B' = 156\,G/cm$. The expected Majorana loss mechanism (dashed line) appears strongly reduced. Below $T = 4\,\mu K$, the data deviates from the suppressed Majorana rate model (straight line), indicating the region of non-negligible three-body losses.

5.4 EVAPORATIVE COOLING

The total energy of a gas with temperature T in a 3D linear trap is given by $E = \frac{9}{2} N k_B T$. Fixing the binding energy of the system to a certain value $\tilde{U} = \eta k_B T$ will result in an energy-selective removal of atoms carrying thermal energies $\geqslant \tilde{U}$. As this resembles the mechanism in which the hottest parts of a liquid disperse as vapor, this process is widely known as *evaporation*. Encompassing descriptions of evaporative cooling theory can be found in [153, 154, 155], and only the core idea is laid out here. The amount of energy that is removed per particle is given by

$$\frac{dE}{dN} = \tilde{U} + \kappa k_B T = k_B T(\eta + \kappa) \tag{5.10}$$

where $\kappa \sim 1$ denotes the average energy per particle that is removed beyond η. For a thermalized ensemble, this is equivalent to a reduction of temperature if $dT > 0$:

$$(E - dE) = \frac{9}{2}(N - dN)k_B(T - dT) \quad \xrightarrow[dT \ll T]{dN \ll N} \quad \frac{dT}{T} = \frac{\eta + \kappa - 9/2}{9/2}\frac{dN}{N}. \tag{5.11}$$

Hence $\eta + \kappa > \frac{9}{2}$ and therefore $\eta \gtrsim \frac{7}{2}$ as an approximate lowest bound for efficient evaporation using the above Taylor approximation. The remaining atoms are not in thermal equlibrium anymore, as the high-energy tail of their underlying Boltzmann distribution is missing. Thermalizing is achieved by atomic collisions that redistribute the respective atomic velocities and replenish the high-energy tail, forming a new Boltzmann distribution with $T' = T - dT$. The atoms will equilibrate after $\sim 2-4$ collisions with each other, the almost exclusively cited value being 2.7 collisions measured in [156]. The elastic collision rate $\Gamma_{el.} = n_0 \bar{v} \sigma$, given by the equilibrated peak density n_0, mean velocity $\bar{v}$ and elastic scattering cross section σ, therefore plays an important role by ensuring constant thermalization ("thermal adiabaticity" [157]) throughout evaporation. Through the thermal dependence of the mean velocity, cooling the sample will lower $\Gamma_{el.} \sim \sqrt{T}$, which has to be compensated by sufficient density increase in order to maintain thermalization. Expressed in atom number change, this demands that the power law

$$\frac{dN(t)}{dt}\frac{1}{N(t)} = \left(\frac{dT(t)}{dt}\frac{1}{T(t)}\right)^{\alpha}, \qquad \alpha \overset{!}{<} 5/2 \tag{5.12}$$

is fulfilled at all times. A more sophisticated model than the Taylor expansion applied in (5.11) and (5.12) gives $\eta > 3.17$ as the lower bound for the truncation parameter in a 3D linear trap from which on $\Gamma_{el.}$ is at least constant [153], signaling *runaway evaporation*.

For $\eta \gg 1$, only particles carrying enormous relative amount of thermal energy are removed, which happens on a timescale $\sim e^{\eta}$. Thus evaporation becomes less costly in terms of atom number, yet also less efficient regarding the speed of the evaporation process. In an otherwise loss-free environment, the cooling efficiency would then be freely choosable and the upper bound for η determined by the patience of the respective experimentalist. In a real experimental environment, it is given by the timescale set by the ensemble lifetime, in the sense that η has to be low enough so that the elastic collision rate exceeds the overall loss rate Γ_{loss} by at least two orders of magnitude. In experiments with low lifetimes on the order of a few seconds (e.g. atom chip traps [151]), one aims for $\eta \approx 7$. [158]. With magnetic trap lifetimes on the order of a minute such as those found in this experiment, η can be easily set beyond 10.

Evaporation dynamics

If the atomic ensemble behaves sufficiently ergodic (usually satisfied through fast interparticle collisions), any spatial pecularities drop out of the description, when the evaporation dynamics are reduced to pure energy dependent terms. One can further assume that the sample is neither too hot, so that all collisions take place with zero relative angular momentum (s-wave), nor too cold, so that classical statistics is still applicable. Approximating the out-of-equilibrium dynamics by a series of truncate-and-thermalize events [159] characterized by the time scale $(\Gamma'_{el.})^{-1} = (\Gamma_{el.}/2.7)^{-1}$, the time evolution of the two essential parameters temperature and atom number is given by:

$$\frac{dN(t)}{dt} = \left\{ +\Gamma'_{el.}(t) \left(\frac{\gamma_i(\zeta + 3/2, \eta)}{\gamma(\zeta + 3/2)} - 1 \right) - \Gamma_{loss}(t) \left(\frac{\gamma_i(\zeta + 3/2, \eta)}{\gamma(\zeta + 3/2)} \right) \right\} \times N(t), \tag{5.13}$$

$$\frac{dT(t)}{dt} = \left\{ +\Gamma'_{el.}(t) \left(\left(\frac{\gamma_i(\zeta + 5/2, \eta)}{\gamma_i(\zeta + 3/2, \eta)} \middle/ \frac{\gamma(\zeta + 5/2)}{\gamma_(\zeta + 3/2)} \right) - 1 \right) \right\} \times T(t). \tag{5.14}$$

These differential equations are coupled with each other through the elastic collision rate scaling with $\sim N/T$. Taylor approximating for small relative changes in N and T gives a commonly stated description [155, 76], but throughout this thesis the exact version is preferred. The incomplete Gamma function

$$\gamma_i(x, \eta) = \int_0^\eta dt^{x-1} e^{-t} \tag{5.15}$$

denotes the integrated density of states and therefore describes quite intuitively the truncation of the underlying Boltzmann distribution at η. Hence the denominator and numerator of eq. (5.14) denote the average energy (and therefore the temperature) before and after truncation. γ_i converges to the usual Gamma function in the limit of infinite integration, $\gamma(x) = \gamma_i(x, \infty)$. ζ describes the combined power law of the underlying trap (e.g. $\zeta = 3$ for a 3D linear trap), which affects the density of states and therefore enters through the calculation of γ_i. The overall loss rate $\Gamma_{loss} = 1/\tau + \Gamma_M + \Gamma_3$ acquires its time dependence indirectly through both the temperature dependent Majorana term $\Gamma_M \sim T^{-1/2}$ and the density dependent three-body losses $\Gamma_3 \sim n_0^2$. The evaporation dynamics are then fully defined by the chosen η, the resulting $\Gamma_{el.}$ and the system inherent Γ_{loss}.

5.4.1 *Microwave evaporation*

In this experiment, the trap depth of the used magnetic trap is modified using microwave (MW) radiation as shown in Fig. 29. For ^{23}Na, a microwave field with an energy $\hbar\omega_{MW}$ on the order of the hyperfine splitting $E_{HFS} = 1771.626\,\text{MHz}$ couples the initial atomic state $|f = 1, m_f = -1\rangle$ to the set $|f = 2, \{m_f = -2, -1, 0\}\rangle$ via magnetic dipole interaction. The corresponding detuning will acquire spatial dependence through the differential atomic Zeeman-shift, $\delta_{MW}(\boldsymbol{r}) = \hbar\omega_{MW} - (E_{HFS} + \Delta E_{Zee.}(\boldsymbol{r}))$, which forms the key to realize trap depth control. As ω_{MW} does not couple to the f = 2 manifold of ^{39}K, it leaves the potassium trap depth unaffected and therefore is a species-selective process. This is distinctly different to RF evaporation, in which transitions $|f, m_f\rangle \rightarrow |f, m'_f\rangle$ are driven, and where

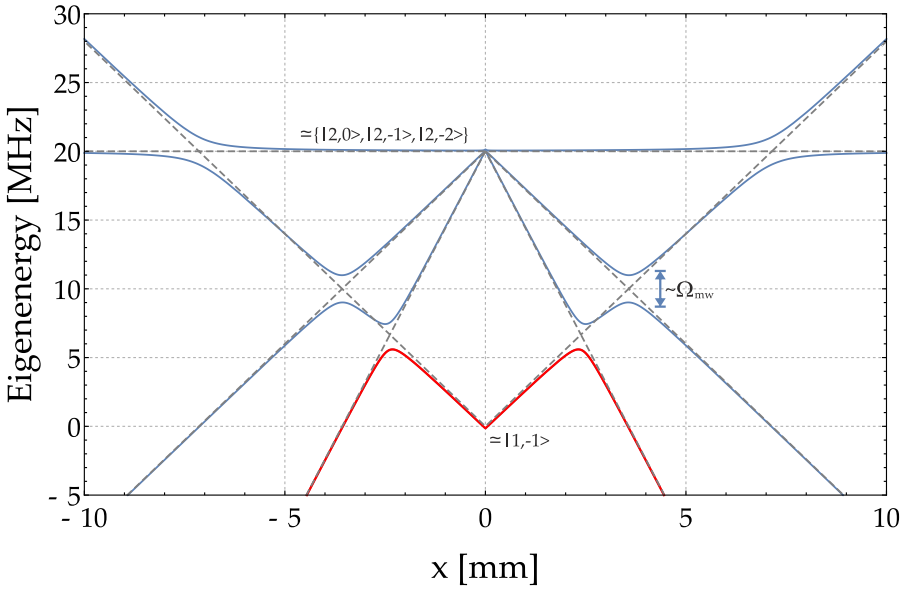

Figure 29: Eigenenergies of bare (dashed gray) and dressed (blue) states for a MW detuning of -20 MHz at the trap center and identical MW Rabi frequencies.

simultaneous evaporation of both species cannot be prevented due to the same g-factors of ^{23}Na and ^{39}K.

Each coupling strength is given by the respective complex Rabi frequency $\Omega_{MW,-2,-1,0}$, which in this simplified notation also contain the respective polarization component and in this example are all set equal. Diagonalizing the resulting rotating frame Hamiltonian gives the spatially dependent eigenenergies as depicted in Fig. 29 for a 1D cut along x. At the bare states' crossing points (dashed gray curves), the Zeeman interaction shifts the MW field into resonance with the hyperfine separation, resulting in avoided crossings of the dressed states (solid blue lines). As the width is given by the Rabi frequency, the corresponding microwave power has to be chosen large enough that diabatic Landau-Zener transitions across the avoided crossings are negligible. Consequently, any atom in the lowest eigenstate (red line) that moves adiabatically beyond the energetically lowest crossing becomes untrapped. In the bare states' picture, this crossing can be associated with transitions $|1,-1\rangle \rightarrow |2,-2\rangle$ and is therefore driven with the π component of the radiation field.[3] Over the course of evaporation, the atoms' spatial extent shrinks with decreasing temperature, which is equivalent to an increase in η if the microwave frequency is kept constant. Thus $\omega_{MW}(t)$ has to be continuously swept to lower values, which slowly shrinks the 3D surface of avoided crossings defined by the resonance condition, thereby keeping η constant.

The *trap bottom* is usually defined as the resonance frequency at the trap minimum, which for a linear trap is given by E_{HFS} at the trap center. Through the blue plug potential, the combined trap minimum V_0 is shifted towards a position (x_0, y_0, z_0).

3 Watch out! The polarization of an electromagnetic field is defined by its electric field component. As magnetic and electric field unit vectors are orthogonal to each other, π-polarised light drives transitions obeying the selection rule $\Delta m_f = \pm 1$, **not** $\Delta m_f = 0$ [160].

For a given temperature and microwave frequency, it therefore appears reasonable to define the truncation parameter by

$$\eta(\omega_{MW}, T) = \frac{|\hbar\omega_{MW} - (E_{HFS} - V_0)|}{f(T)}, \tag{5.16}$$

where

$$f(T) = 3 \times 0.7\,\mathrm{MHz/G} \times \frac{2k_B T}{\mu_B} \tag{5.17}$$

gives the differential Zeeman shift in MHz for a cloud with spatial extent specified by T and the transition considered above. It is however pointed out that this convention is slightly ill-defined. The optical potential is to a great extent identical for all considered $|f, m_f\rangle$ states, and therefore does not affect the resonance condition! So even at detunings smaller than V_0, (hot) atoms exist that are resonant with ω_{MW}. Consequently, the convention used in this thesis is to use only the magnetic part of V_0 for the detuning and hence for η. For the used trap parameters and a radial plug displacement of half a beam waist, $B_0(x_0, y_0, z_0) \approx 330\,\mathrm{mG}$, when the differential Zeeman shift corresponds to a trap bottom of $\approx 700\,\mathrm{kHz}$.

Optimization

As optimization is a process comparing relative numbers, every function that maps monotonically on the exact PSD is sufficient as a figure of merit. The optimization carried out in this thesis therefore uses the in-situ methods described in 5.2 to maximize the peak optical density as well as a "pseudo-PSD" approach obtained out of a single TOF measurement [161]. Out of sec. 5.2 it follows that in a Gaussian approximation the peak density can be expressed as $n_0 \propto N\,T^{-3/2}$. Moreover, for a given TOF time t_0, eq. (4.20) gives that the temperature follows the relation

$$T = \frac{\sigma^2(t_0)}{k_B\,(f(B_0) + g(t_0))} \tag{5.18}$$

where f and g are functions depending on the magnetic field gradient B_0 and t_0 that for the purpose of qualitative optimization do not have to be evaluated as long as they are kept constant. Hence out of the atom number and spatial extent at a large TOF time, the thereby obtained relative density and relative temperature construct a quantity similar to the original PSD which is maximized. After qualitative optimization, the actual phase space density is obtained for the optimized parameter settings.

5.4.2 *Evaporation protocol*

The microwave field ω_{MW} is delivered using a frequency generator [*R&S SMB100A*, $0.1\,\mathrm{MHz} - 12.75\,\mathrm{GHz}$] whose signal is amplified to up to 45 dBm. A first switch decides whether the generator is used for the MW evaporation or for RF state transfer not shown in this thesis (see [162] instead). A second switch interrupts the transmission from the generator, e.g. if only a cutout of a programmed ramp shall be used. A circulator after the switch prevents backreflections of the amplified signal.

At the start of an experimental sequence, a set of ω_{MW} grid points are fed into the generator. Upon receival of a digital trigger signal, the generator processes these with a dwell time of 24 ms. The discrete ramp sampling (opposed to the desired continuous ramp outlined above) is not an issue as long as the dwell time is small compared to the ramps characteristic time constant. The generated signal is emitted into the experiment using a double loop wound copper antenna glued to one of the Feshbach coil holders. To make sure that no self-resonant frequency is present near ω_{MW}, the antenna transfer function has been measured in the region around E_{HFS} using pickup antennas [162].

The evaporation process has been optimized by decomposing the total frequency sweep into a set of seven linearly interpolated ramp stages characterized by their eight start/end points labeled A-H. The first stage (A-B) has been designed to provide robustness against detoriation of one of the earlier experimental stages (molasses, MT transfer). As shown in sec. 5.1, the initial temperature is on the order of 100μK, when $\eta = 10$ would be satisfied by $\omega_{MW} = 2\pi \times 63\,\mathrm{MHz}$. The ramp instead starts at $A = 2\pi \times 100\,\mathrm{MHz} - V_0/\hbar$. In the case the initial temperature doubles (quadruples), this corresponds to $\eta = 8\,(4)$, which still ensures runaway evaporation. The (A-B) ramp length of three seconds leads to a tolerable background collision atom loss of about 5%, whereas the end frequency of $B = 2\pi \times 60\,\mathrm{MHz} - V_0/\hbar$ fixes the temperature to $\lesssim 100\,\mu\mathrm{K}$ which provides similar temperature starting conditions for the ramps that follow. The subsequent ramps (B-G) are optimized using a strategy similar to the one described in [130]. For a given segment, e.g. (B-C), the time constant and MW power are scanned, whereas the following (C-D) ramp is unchanged. Next the stage (D-E) is appended and (C-D) optimized in similar fashion. To avoid getting stuck in a local optimum, it is constantly checked that a global change, e.g. by multiplying all time constants by the same factor, does not significantly improve the result.

The result of this iterative optimization is a ramp where the detuning resembles the functional form of an exponential with a quadratically decreasing time constant, i.e.

$$\delta_{\mathrm{Ramp}}(t) \propto \exp\left[\frac{-t}{6\,\mathrm{s} - 1.6 \times 10^{-3}\,\mathrm{s}^2}\right]. \tag{5.19}$$

This reflects the fact that as the evaporation progresses, the elastic collisions increase over time so that the evaporation time constant can be shortened. The last ramp (G-H) is simply appended using the previous time constant for 4 s. The full ramp duration is 24 s, ending at a final frequency $H = 2\pi \times 1.56\,\mathrm{MHz} - V_0/\hbar$.

5.4.3 *Single-species performance of* ^{23}Na

With ^{23}Na being the workhorse of this procedure, the evaporation was first characterized in single-species operation, and ^{39}K subsequently added. Figure 30 shows the evolution of the ^{23}Na atom number and temperature during the evaporation ramp, once for the plugged case (green triangles) and for a pure quadrupole trap (blue diamonds) with equal starting conditions, a magnetic field gradient of 156 G/cm and a plug characterized by a plug height $U_0 = 246\mu\mathrm{K}$ and beam waist 39 μm.

Comparing points belonging to equal evaporation times, it is clear that in absence of the plug, the Majorana losses and accompanied heating render evaporation

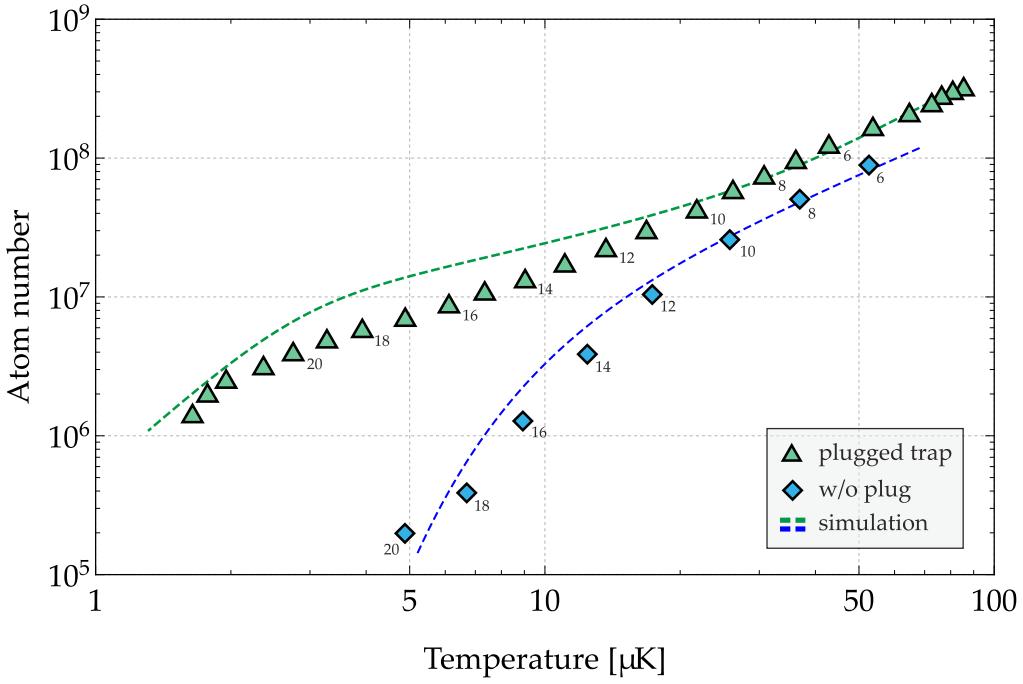

Figure 30: Time evolution of atom number as a function of temperature during evaporation. Points of equal evaporation are marked by their evaporation time in seconds. The pure quadrupole trap (blue diamonds) features strong Majorana losses and accompanied heating compared to the plugged case (green triangles). The dashed lines are simulations of the evaporation dynamics according to (5.13) and (5.14) for the region of interest.

largely inefficient. At temperatures below 20μK, the power law exponent given by the slope in double logarithmic representation rises above 3, when the runaway evaporation criterion (5.12) breaks down. In contrast, the plugged potential operates safely in the runaway regime, with an average slope $\bar{\alpha} = 1.43$. For the stages (B-G) of the evaporation trajectory, the average value for η according to eq. (5.16) is on the order of $\eta = 12$. This is a rather high value compared with other experiments employing RF evaporation [130, 149]. In order to certify it, simulations of the evaporation dynamics were performed that solve the differential equations (5.13) and (5.14) by propagation on a discrete variable time grid defined by $(\Gamma'_{el.})^{-1}$. All other simulation parameters have been fixed by experimentally measured values, where the Majorana and background losses are interpolated using the measurements presented in fig. 28. Lastly, the three-body loss rate coefficient is estimated using measurements in the optical dipole trap (see also section 6.4). Using only the initial conditions as free fitting parameters and setting $\eta = 12$, the simulated evaporation trajectory (dashed lines in 30) decently reproduces the experimental one. The smaller experimental efficiency at lower temperatures compared to the simulation can be attributed to a combination of a possible plug displacement discrepancy between the measurements presented in fig. 28 and fig. 30, and most probable the underestimation of three body losses especially near the end of the ramp.

Peak density and cooling efficiency

Having obtained the quantities atom number N and temperature T, the peak density n_0 and consequently the peak PSD ($= n_0 \Lambda^3$) have to be evaluated. For a plugged potential with large plug Rayleigh length, a plug displacement (x_p, y_p) and including gravity, the peak density is related to the atom number via

$$N = n_0 \iiint_V dx\, dy\, dz \exp\left(-\frac{1}{k_B T}\left\{V_{\text{Mag.}}(x,y,z) + V_{\text{Opt.}}(x,y) + V_{\text{Grav.}}(z)\right\}\right) \tag{5.20}$$

$$V_{\text{Mag.}}(x,y,z) = g_f m_f \mu_B B' \sqrt{x^2/4 + y^2/4 + z^2} \tag{5.21}$$

$$V_{\text{Opt.}}(x,y) = U_0 \exp\left[-2\frac{(x-x_p)^2 + (y-y_p)^2}{w_0^2}\right] \tag{5.22}$$

$$V_{\text{Grav.}}(z) = m\, g\, z \tag{5.23}$$

This integral can be tackled by different approaches in order to access n_0:

1. Explicit numerical integration of eq. (5.20), yielding the "correct" result n_0.

2. Neglecting the plug potential: This appealing approximation makes eq. (5.20) analytically solvable as long as $g_f m_f \mu_B B' > mg$, i.e. as long as the trap holds against gravity. Using $g_f m_f = \frac{1}{2}$ as in this setup, the resulting density $n_{0,\text{lin.}}$ for a linear potential is given by

$$n_{0,\text{lin.}} = \frac{N\left(\left(\frac{1}{2}\mu_B B'\right)^2 - (mg)^2\right)^2}{32\pi\left(\frac{1}{2}\mu_B B'\right)(k_B T)^3} \xrightarrow{2mg \ll \mu_B B'} \frac{N}{32\pi}\left(\frac{\mu_B B'}{2 k_B T}\right)^3 \tag{5.24}$$

   For $B' = 156\,\text{G/cm}$ as used in the measurement shown in fig. 30, the gravitational correction term is on the order of 1%, but has to be accounted for if one decreases the magnetic field gradient at later stages of evaporation to counterfeit losses. This approximation works quite well at high temperatures, but a quick glance at fig. 26 indicates that it will definitely overestimate the density near the trap bottom and therefore at low temperatures.

3. Harmonic approximation: In the vicinity of the combined trap minimum, the slope behaves quadratically rather than linearly. Assume a plug displacement into the third quadrant, when the trap minimum (x_0, y_0, z_0) is situated in the first one as depicted in fig. 25 (b). After a transformation on the principal axes (u, v, z), with $e_{u,v} = \frac{1}{\sqrt{2}}(e_x \pm e_y)$, the potential $V(u,v,z)$ is expanded in second order around the trap minimum $(u_0, 0, z_0)$. Dropping all anharmonicities, this gives

$$V(u,v,z) \approx \frac{1}{2} m\left(\omega_u (u-u_0)^2 + \omega_v v^2 + \omega_z (z-z_0)^2\right). \tag{5.25}$$

   $\omega_{u,v,z}$ then give the radial, angular and vertical trap frequency as seen from the origin, and for the used parameters in fig. 30, $(\omega_u, \omega_v, \omega_z) = 2\pi \times (593, 133, 475)$ Hz. Naturally ω_v is the smallest, vanishing for the rotational

symmetric case $x_p = y_p = 0$. The density $n_{0,\text{harm.}}$ for this approximation is then given by

$$n_{0,\text{harm.}} = N \times \omega_u \omega_v \omega_z \left(\frac{m}{2\pi k_B T} \right)^{3/2}. \tag{5.26}$$

Compared with $n_{0,\text{lin.}}$, the harmonic expansion reproduces the correct density at low temperatures on the order of a few µK, but of course fails in the high temperature limit.

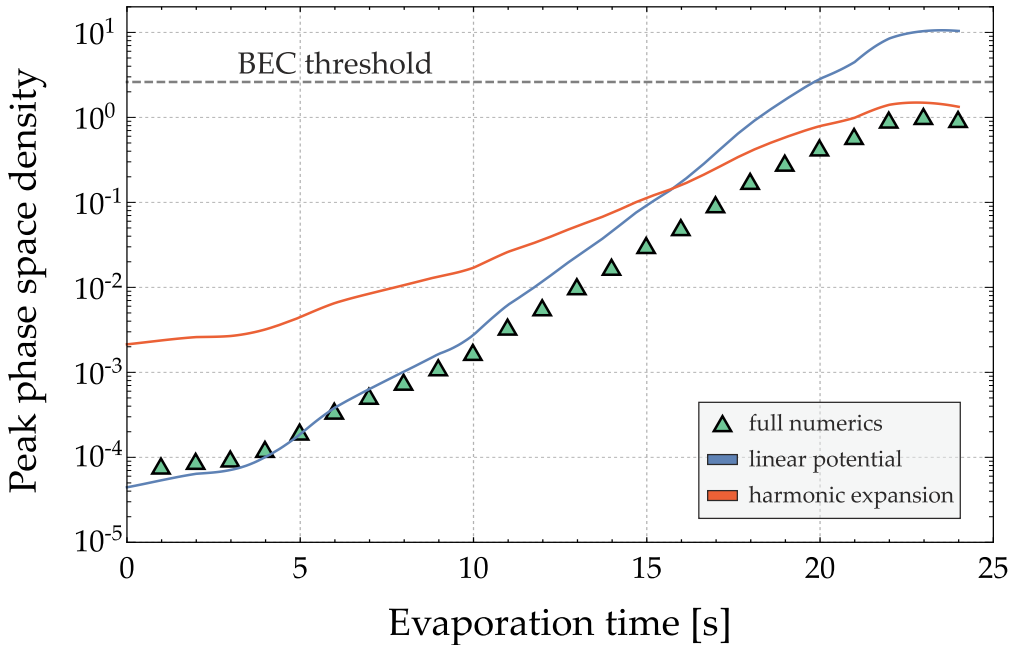

Figure 31: Peak PSD as a function of evaporation time. The blue line corresponds to the analytical solution disregarding the plugging potential, while the red line corresponds to the harmonic expansion around the combined trap minimum. The green triangles are obtained by numerical integration of the exact potential. A gray dashed line indicates the border to the quantum degenerate realm.

Figure 31 shows the peak PSD as a function of evaporation time using all three methods outlined above to obtain the peak density n_0 for the used ramp. As explained above, the linear approximation reproduces the numerical solution particularly well at high temperatures, but overestimates the density at the late stage of evaporation, giving a false peak PSD on the order of 10 after the final evaporation stage. If the above approximations are used, the turning point in which the linear description should be replaced by the harmonic one is at approx. 6 µK, as indicated by the crossing of both lines at approx. 16 s of evaporation.

The explicit numerical integration (green triangles) is now analyzed regarding the phase space compression efficiency. As the usual goal is to enlarge the phase space density at low atom cost, a cooling efficiency $\mathcal{D}$ can be quantified by the power law relation

$$\mathcal{D}(t) = -\frac{d\log(\text{PSD}(t))}{d\log(N(t))}. \tag{5.27}$$

As explained in the evaporation protocol, the first three seconds of the chosen ramp correspond to the "safety net" ramp (A-B). This part therefore leads only to

negligible phase space increase, with a cooling efficiency $D(0-3s) = 1.41$. For the ramp (B-G) corresponding to the interval between 3 and 20 seconds, the average cooling efficiency is found to be $D(3s-20s) = 2$. This is lower than the 2.7 that was given in a comparable experiment [149]. However, that article featured the linear approximation neglecting the plug potential, and as outlined above, this nonlinearly overestimates the density as the evaporation progresses. Applying the same approximation to the ramp interval (B-G) gives the much larger value $D_{lin.}(3s-20s) = 2.57$ that is comparable to [149]. The final evaporation stage (G-H) indicates saturation at a PSD on the order of 1, just below the onset of Bose-Einstein condensation (dashed gray line). In this high density regime, the impact of three body losses becomes sizable, hampering the evaporation efficiency. The usual remedy applied in such a situation is to decompress the magnetic trap by lowering the magnetic field gradient, when further phase space compression is achievable. Yet as outlined in the introduction to this chapter, reaching BEC in the magnetic trap is rather detrimental for the dual-species operation. Hence pushing the pure sodium operation beyond PSDs of 1 was not pursued.

5.4.4 *Sympathetic cooling of ^{39}K*

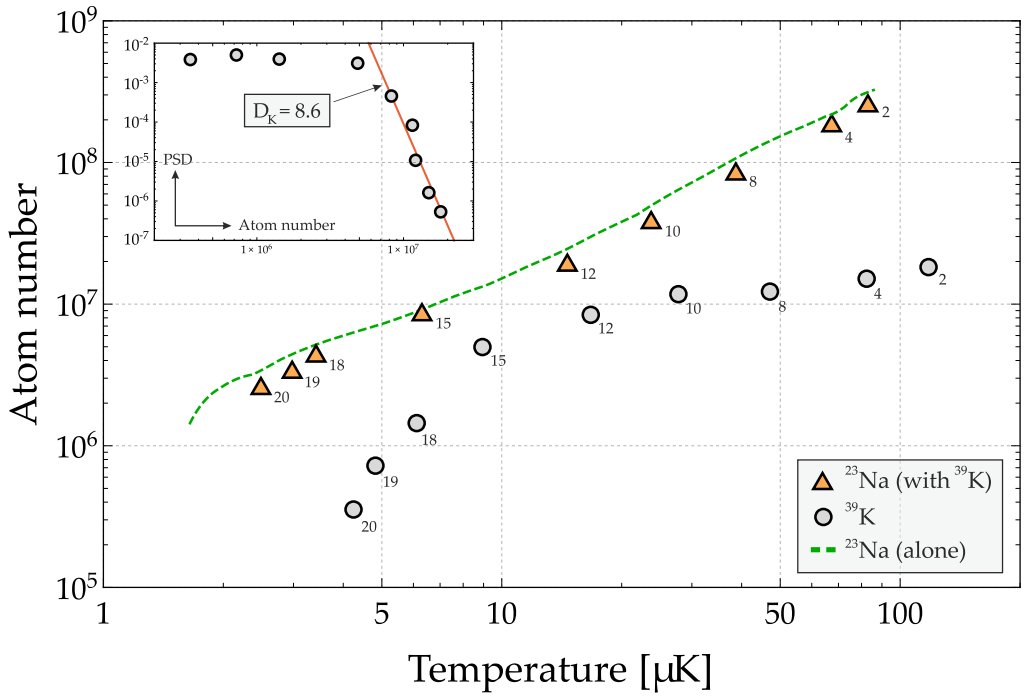

Figure 32: Time evolution N(T) of ^{23}Na (orange triangles) and ^{39}K (gray dots) in dual-species operation. Points are marked by their evaporation time in seconds. Sympathetic cooling of ^{39}K is highly efficient at temperatures $\geqslant 10\mu K$, whereas the time evolution of ^{23}Na is almost unchanged compared to the single-species case (green dashed line). Inset: PSD(N) for ^{39}K during evaporation.

In dual-species operation, both ^{23}Na and ^{39}K are loaded into the plugged trap. The initial trapped atom number ratio N_K/N_{Na} is chosen by adjusting the individual MOT loading times and is set between 10^{-4} and 10^{-1} for the experiments presented throughout this thesis. As stated in section 5.1, the initial potassium temperature

is $T_{i,K} = 240\mu K$. As soon as both species reside in the trap, ^{23}Na is subsequently evaporated and act as a coolant for the ^{39}K cloud mediated by interspecies collisions. Figure 32 shows the time evolution of both N_K (gray dots) and N_{Na} (orange triangles) as a function of their respective temperatures using the evaporation protocol presented earlier. The temperature and atom number of both species have been obtained by TOF analysis. As the evaporation progresses, the ^{39}K temperature is steadily reduced, whereas the cooling efficiency of ^{23}Na is barely affected compared to the single-species evaporation (green dashed line).

Down to temperatures $T \geqslant 10\mu K$, sympathetic cooling is found to be largely efficient, giving rise to cooling efficiency of $D_K = 8.6$ (red line in the inset in fig. 32). This value is smaller than in some other combinations (e.g. $D = 12$ for sympathetic cooling of ^6Li by ^{41}K [163]), but found to be significantly higher than $D = 4.6$ that has been realized for the fermionic counterpart $^{23}Na +^{40} K$ [65]. Up to this point, both clouds are roughly in thermal equilibrium, and the measured ^{39}K temperatures are slightly higher by about $\sim 15\%$. This might hint at unwanted heating during the imaging process, but is in line with deviations found in other experiments [164].

At temperatures below $10\,\mu K$, a rapid decrease in atom number is observed for the ^{39}K cloud, and the cooling efficiency becomes largely ineffective. The source for this is twofold: First, as the blue plug strength is given by its detuning to the respective atomic species D line (see also chapter 6), the repulsive potential is significantly weaker for potassium, ($V_{plug,K} = 0.43\, V_{plug,Na}$). Therefore it will suffer from a higher amount of Majorana losses at lower temperatures. To get an estimate of the expected losses, the supressed Majorana loss rate used in fig. 28 is employed, rescaling the atomic mass and plug strength. For the temperatures measured at evaporation times of $18 - 20\,s$, the estimated loss rate would correspond to about 9% atom number loss per second, which is far below the observed drop of about 50% per second, therefore the Majorana loss contribution appears secondary.

Primarily, the large density region below $10\,\mu K$ exhibits large interspecies three-body losses (Na+Na+K) and (Na+K+K), that appear more pronounced for the smaller potassium cloud. The exact quantification of these loss channels is postponed to the next chapter. They will be revisited in the optical dipole trap (see sec. 6.4) as the absence of Majorana losses simplifies the estimation of three-body losses in such an environment. Yet the main result can be stated as follows: In the face of the high losses prevailing in the high density region of the plugged trap, the temperature region $T \approx 10 - 20\mu K$, reached after $12 - 15\,s$ of evaporation, indicates the optimal loading point for the ODT transfer in dual-species operation. Both major loss contributions will be vanquished there: the interspecies losses can be eliminated by using Feshbach fields, and Majorana losses simply do not appear in optical traps.

6

OPTICAL TRAPPING AND QUANTUM DEGENERACY

For an experiment designed to study ultra-cold molecules, a purely magnetic trap cannot provide the final working environment. $^1\Sigma^+$ ground state molecules are not magnetically trappable as they only possess a nuclear but no electronic magnetic moment. The creation of Feshbach molecules further demands specific magnetic fields in order to magnetoassociate the atom pair. Last but not least, Feshbach resonances enable control of the scattering interaction for the mixture experiment, and the magnetic trap results already indicated these to be of crucial importance. By transferring the atoms into an *optical dipole trap* (ODT), the magnetic field strength becomes again a freely tunable parameter.

Most excellent sources regarding the fundamentals and possible applications of ODTs are [165, 166]. The main ingredients can be summarized as follows: Similar to the magnetic trap (where $\mathcal{H}_{\text{Mag.}} = -\boldsymbol{\mu} \cdot \boldsymbol{B}$ was utilized), the working principle of optical dipole traps relies on energy shifts due to the interaction of internal atomic states with an applied field, in this case laser light. The main difference is that opposed to the *permanent* magnetic moment, the electric dipole moment is *induced* by the external electromagnetic field. The same field couples the ground state $|g\rangle$ to a set of excited states, usually the D line of the respective alkali atom. For a coupling $|g\rangle \leftrightarrow |e\rangle$, the atom-light interaction in the rotating frame is given by the Hamiltonian

$$\mathcal{H}_{\text{A-L}} = \frac{\hbar}{2}\begin{pmatrix} \delta & \Omega(\boldsymbol{r}) \\ \Omega^*(\boldsymbol{r}) & -\delta \end{pmatrix}, \tag{6.1}$$

with the detuning δ and the complex Rabi frequency $\Omega(\boldsymbol{r})$. The eigenenergies

$$E_\pm(\boldsymbol{r}) = \pm\frac{\hbar}{2}\sqrt{\delta^2 + \Omega(\boldsymbol{r})^2}. \tag{6.2}$$

comprise a light shift, with the spatial dependence imprinted via the intensity distribution of the laser beam, $I(\boldsymbol{r}) \propto \Omega(\boldsymbol{r})^2$. The Gaussian shape of a TEM_{00} laser mode then naturally provides an energetic hill (valley) in configuration space for the $|+\rangle$ ($|-\rangle$) state, respectively. Assuming far off detuned laser light and low saturation ($|\delta| \gg |\Omega|$), the problem acquires perturbative characteristics and the corresponding eigenstates $|+\rangle, |-\rangle$ almost coincide with the bare atomic basis $|g\rangle, |e\rangle$. Quite importantly, their assignment is given by δ. When an atom initially in the state $|g\rangle$ traverses a laser region $\Omega \neq 0$, the sign of δ decides whether it will adiabatically evolve into the low-field seeking $|+\rangle$ ($\delta > 0$) or high-field seeking $|-\rangle$ ($\delta < 0$) state. In the latter case, the potential felt by the atoms is given by the energy difference between unperturbed and local eigenstate:

$$\Delta E = E_{(g)} - E_{(-)} = -\frac{\hbar\delta}{2} - \left(-\frac{\hbar}{2}\sqrt{\delta^2 + \Omega(\boldsymbol{r})^2}\right) \tag{6.3}$$

$$= -\frac{\hbar\delta}{2}\left(1 - \sqrt{1 + \left(\frac{\Omega(\boldsymbol{r})^2}{\delta^2}\right)}\right) \tag{6.4}$$

$$\approx \frac{\hbar\Omega(\boldsymbol{r})^2}{4\delta} \propto \frac{I(\boldsymbol{r})}{\delta}, \tag{6.5}$$

where the Taylor series expansion $\sqrt{x^2+1}_{|x=0} \approx 1 + x^2/2 + \mathcal{O}(x^3)$ has been applied. This light-induced energy shift, usually referred to as the *AC Stark shift*, gives rise to the conservative optical trapping potential $V_{\text{opt.}}(\boldsymbol{r})$. Due to the finite admixture of $|e\rangle$ in $|-\rangle$, spontaneous emission naturally appears in the description of the process through decay of the excited state population $p_{|e\rangle} = |\langle -|e\rangle|^2$. In the far-detuned perturbative limit discussed above, perturbation theory dictates that the first-order state correction of $|g\rangle$ by $|e\rangle$ is given by

$$\frac{\langle e|\mathcal{H}_{A-L}|g\rangle}{(E_e - E_g)}|e\rangle = \frac{\Omega(\boldsymbol{r})}{\delta}|e\rangle \tag{6.6}$$

and hence the rate of spontaneous emission $\gamma = \Gamma\, p_{|e\rangle}$ is on the order of

$$|\langle -|e\rangle|^2 \approx \frac{\Omega(\boldsymbol{r})^2}{\delta^2} \propto \frac{I(\boldsymbol{r})}{\delta^2}. \tag{6.7}$$

Comparing eq. (6.5) and (6.7), it is clear that by increasing $I(\boldsymbol{r})$ as well as δ while keeping their ratio constant, spontaneous scattering can be suppressed without affecting the light shift potential. Feasible detunings on the order of several 100 nm with $10-100\,\mu$m foci then demand powers on the order of several Watt to constitute sizable optical trap depths. The easiest way to produce a trapping potential is realized using red-detuned light, as any focused laser beam automatically generates a trapping potential with the trap bottom at its focal point. In particular, the intensity profile of a Gaussian beam propagating along the x axis, with laser power P, beam waist w_0 and spot size parameter $w(x)$

$$I(\boldsymbol{r}) = I(r,x) = \frac{2P}{\pi w_0^2} \times \left(\frac{w_0}{w(x)}\right)^2 \exp\left[\frac{-2r^2}{w(x)^2}\right] \tag{6.8}$$

generates a tight, Gaussian shaped confinement perpendicular to and a loose, Lorentzian shaped confinement along the beam direction.

Essential trap parameters

The optical trapping potential $V_{\text{opt.}}$ is typically expressed using one of the following two forms:

$$V_{\text{opt.}}(x,y,z) = -\frac{\text{Re}\,[\alpha(\lambda)]}{2\epsilon_0 c} I(x,y,z) \approx \sum_i \frac{1}{2} m\omega_i^2 r_i^2, (i = x,y,z). \tag{6.9}$$

The first expression features the complex dynamic polarizability $\alpha(\lambda)$ as a measure of effective (i.e. detuning dependent) coupling strength between atomic structure and interaction field. Formulas involving its real (imaginary) part conform to the exact form of the qualitative descriptions (6.5) ((6.7)). At a given wavelength and set of beam parameters, the overall trapping strength is characterized by the trap depth $V_0 = |V(0,0,0)|$ that is commonly given in multiples of $k_B\,\mu$K. With the finite trap depth, it automatically follows that forced evaporation can be implemented in an ODT simply by reducing the laser beam power.

The second expression in eq. (6.9) approximates the well of the Gaussian potential as harmonic, which is sensible as long as the mean thermal energy of the sample is well below the trap depth. For a single beam propagating along x, the axial and radial trap frequencies are given by

$$\omega_x^2 = \frac{2V_0}{m x_R^2}; \quad \omega_r^2 = \frac{4V_0}{m w_0^2}. \tag{6.10}$$

The Rayleigh length $x_R = \pi w_0^2/\lambda$ is typically large compared to the atomic extent, which implies small spatial variations and hence weak trapping properties on the order of a few Hertz along the beam direction. Adding a second beam along y results in a *crossed optical dipole trap* (cODT) that modifies the trap frequencies according to

$$\omega_i = \sqrt{\omega_{i,1}^2 + \omega_{i,2}^2}, (i = x, y, z) \tag{6.11}$$

for all directions. In such a configuration, tight trapping conditions can be obtained in all three dimensions. Along the vertical axis, the additional gravitational potential shifts the trap minimum, an effect that becomes more pronounced as the laser intensities are reduced, e.g. during forced optical evaporation. The displaced minimum z_0

$$V_z = V_{opt.}(0,0,z) + V_{grav.} \approx \frac{1}{2} m\omega_z^2 z^2 - m\,g\,z \tag{6.12}$$

$$\partial_z V_z = m\left(\omega_z^2 z - g\right) \stackrel{!}{=} 0 \quad \curvearrowright z_0 = -\frac{g}{\omega_z^2} \tag{6.13}$$

is called the *gravitational sag*. In order to counteract the differential gravitational pull between both atomic species, the laser beam wavevectors are usually chosen to be both in the horizontal plane in order to provide the strongest confinement along the vertical direction. Optical potential landscapes starring the essential parameters V_0, ω_i and z_0 are depicted in fig. 33.

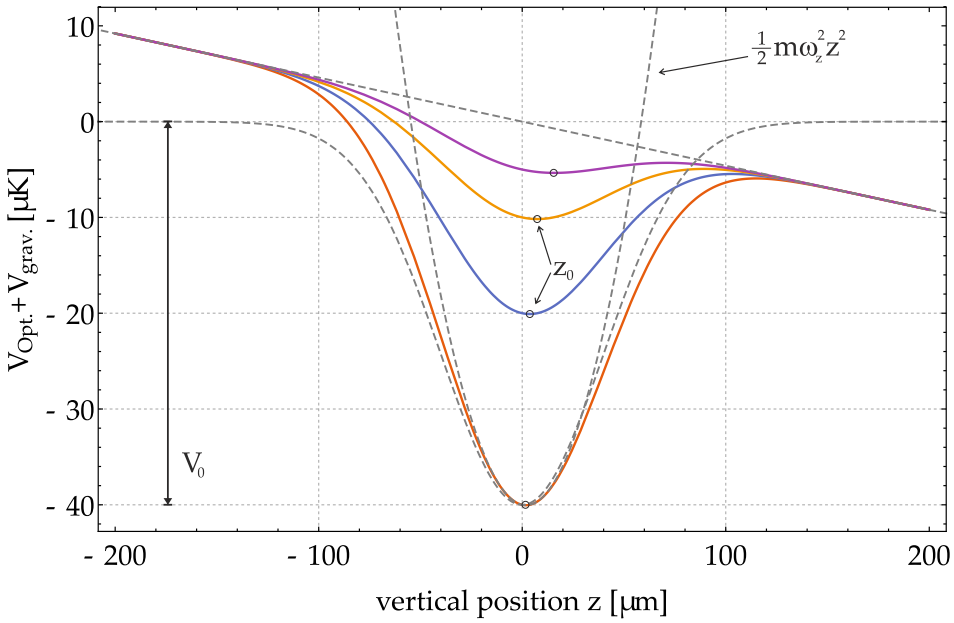

Figure 33: Combined potential $V_{opt.}(0,0,z) + V_{grav.}$ seen by ^{39}K with the essential parameters V_0, ω_i, z_0 highlighted. The optical trap corresponds to a single $\lambda_{ODT} = 1064\,\text{nm}$ beam propagating in the xy-plane with beam waist of $40\,\mu\text{m}$ and powers $\{750, 375, 250, 187.5\}$ mW leading to trap depths of $\{40, 20, 10, 5\}$ μK. The dashed lines depict $V_{opt.}(0,0,z)$, $V_{grav.}$ and the harmonic approximation to the optical potential.

6.1 TWO-SPECIES CONSIDERATIONS

The trapping potentials felt by ^{23}Na and ^{39}K will differ by their respective dynamic polarizabilities according to eq. (6.9) and (6.10), i.e. $V_{0,K}/V_{0,Na} = \alpha_K/\alpha_{Na}$ and

$$\frac{\omega_{i,K}}{\omega_{i,Na}} = \sqrt{\frac{V_{0,K}}{V_{0,Na}} \times \frac{m_{Na}}{m_K}}. \tag{6.14}$$

For selected wavelengths, *ab initio* calculations of $\mathrm{Re}[\alpha]$ are tabulated in the literature [167]. For $\lambda = 1064\,\mathrm{nm}$, they read[1] 597.5 a_0^3 (^{39}K) and 233.6 a_0^3 (^{23}Na). The resulting trap depth ratio of $V_{0,K}/V_{0,Na} \approx 2.5$ unveils two distinct benefits for operating this particular mixture. First of all, the unequal dynamic polarizabilities almost balance the mass ratio 23/39 in eq. (6.14), leading to rather similar trapping frequencies ($\omega_K/\omega_{Na} \approx 1.2$). Second, having a much deeper trap for ^{39}K, forced optical evaporation by reducing the trap intensities leads to a preferred ejection of ^{23}Na. Hence sodium will still serve as the coolant for sympathetic cooling of potassium, keeping the desired role allocation intact. The unequal trap frequencies will however lead to a spatial mismatch of both clouds that worsens the interspecies thermalization rates, and eq. (6.13) dictates that this appears most prominently along the vertical direction through differential displacement of their trap minima. Using the trap frequency ratio obtained above, the differential gravitational sag between both species is evaluated as

$$\delta z_0(\omega_z) = |z_{0,Na} - z_{0,K}| \approx \frac{3.19}{\omega_z^2}\,\mathrm{Hz^2 m}. \tag{6.15}$$

For low vertical trapping frequencies on the order of $2\pi \times 50\,\mathrm{Hz}$, the differential sag of 32 µm can already lead to an effective decoupling of both species, which is typically unwanted in mixture experiments as well as for molecular association. The differential sag can be eliminated by operating the trap at a "magic" wavelength in which the trap frequencies for both species are identical [167, 168]. As *ab initio* calculations are not available for each wavelength, the polarizability $\alpha_i(\lambda) \equiv \alpha_i(\omega)$ for species i is calculated for each trapping frequency ω using a classical oscillator model [165],

$$\mathrm{Re}[\alpha_i(\omega)] = \frac{3\pi\epsilon_0 c^3}{\omega_{D,i}^3}\left(\frac{\Gamma_i}{\omega_{D,i} - \omega} + \frac{\Gamma_i}{\omega_{D,i} - \omega}\right), \tag{6.16}$$

where the detuning is assumed to be large enough that no atomic sub-structure has to be accounted for and the fast oscillating terms are explicitly kept[2]. $\omega_{D,i}$ then describes the individual D line centroid and Γ_i the individual linewidth of each species. Applying this model to ^{23}Na and ^{39}K, a magic wavelength was not found. It can however be synthesized by combining a set of wavelengths to an optical multi-color trap. For an initial trap operating at a wavelength of 1064 nm with power P_1, the stronger confinement of ^{39}K can be equilibrated by adding a second beam whose wavelength λ_2 is situated between the D transition lines of both species and therefore acts deconfining on ^{39}K with a certain strength given

1 This atomic unit description can be converted into SI units using $(\alpha_{SI}/\hbar) = 1.56346 \times 10^{-7}\,\alpha_{a.u.}$.

2 For a wavelength of 1064 nm and the sodium D line, the classical oscillator model agrees with the *ab initio* value below the percent level. If the faster oscillating terms are omitted, the polarizability is underestimated by about 30%

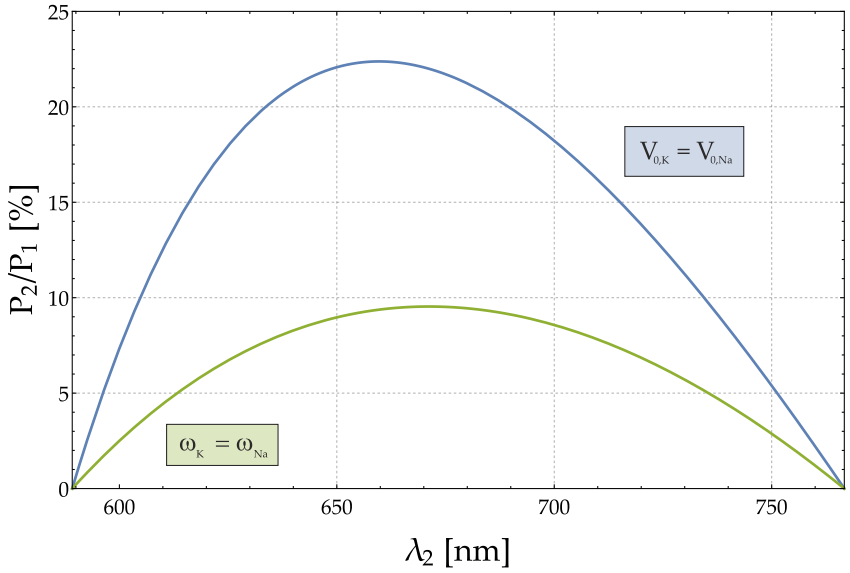

Figure 34: Power ratio P_2/P_1 that fulfils "magic" trapping conditions in an optical two-color trap with $\lambda_1 = 1064\,\text{nm}$ as a function of λ_2. The alkali D lines of the mixture serve as natural roots in the power ratio as the coupling strength diverges at these points.

by its power P_2 and beam waist. Assuming equal spot size of both beams, Fig. 34 shows the power ratio P_2/P_1 needed in the equilibrating beam to fulfill the condition

$$\frac{V_{0,\text{Na}}}{V_{0,\text{K}}} \stackrel{!}{=} \frac{m_{\text{Na}}}{m_{\text{K}}} \tag{6.17}$$

that governs equal trap frequencies, as a function of λ_2. For completeness, also the solution to $V_{0,\text{Na}} \stackrel{!}{=} V_{0,\text{K}}$ is given. The amount of power needed for the second beam never exceeds 10% of the incident beam, e.g. it reads 7.6% at the famous He-Ne wavelength of 632.8 nm. The differential sag only becomes sizable at low trapping frequencies, which is equivalent to laser powers $P_1 \leqslant 100\,\text{mW}$. Hence even a moderate amount on the order of a few mW of additional light is sufficient to achieve equal trapping conditions. A completely different ansatz consists in adding a vertical magnetic field gradient that cancels out the gravitational force [169]. This particular case of *magnetic levitation* requires a magnetic moment ratio $|\boldsymbol{\mu}_{\text{K}}|/|\boldsymbol{\mu}_{\text{Na}}| \stackrel{!}{=} m_{\text{K}}/m_{\text{Na}}$ and can therefore only be implemented in the vicinity of bias fields fulfilling this condition. This however disagrees with the initial statement of this chapter, namely that the magnetic field is needed as a free parameter, and therefore would require an additional coil pair. Even though it might be an appealing solution for differently designed experiments, further discussion on this approach is discarded here.

6.2 EXPERIMENTAL REALIZATION

This experiment operates a crossed ODT as described in the previous section, with an inclined angle of approx. 90°. Both beams are generated out of the same laser source (*Mephisto* solid state laser system, $\lambda_{\text{ODT}} = 1064\text{nm}$, 42 W nominal output power) and distributed to the experiment table using high-power optical fibers

Beam	Power	$w_{\text{Horiz.}}$	$w_{\text{Vert.}}$	$V_{0,\text{Na}}$	$V_{0,\text{K}}$	$\frac{1}{2\pi}(\omega_x, \omega_y, \omega_z)_{\text{Na}}$
along $\vec{e}_y$	4.7 W	46 µm	46 µm	74 µK	188 µK	(1130, 6, 1130) Hz
along $\vec{e}_x$	3.8 W	143 µm	40 µm	22 µK	56 µK	(4, 199, 710) Hz
cODT				96 µK	245 µK	(1130, 199, 1334) Hz

Table 3: Optical dipole trap parameters used in the experiment.

(OzOptics *PMJ-A3AHPC-1064-6/125-3AS-7.5-1*) situated downstream of two AOMs whose first diffracted order is injected. Before they enter the chamber, the beams are shaped to create one radially symmetric beam that ensures a high overall optical trap depth, and an elliptically shaped beam that enlarges the horizontal trap volume while keeping the gravitational sag minimal. The waists have been estimated by mapping out the spot size parameter and independently by measuring trap frequencies (see fig. 37). The used beam parameters are summarized in table 3.
After passing the experimental chamber, a fraction of both beams is directed onto two separate photodiodes whose signal is fed back to the RF input of the AOMs, enabling stabilization and dynamic control of the intensities in the experiment via a PI control loop [170]. A modulation frequency offset on the order of 100 MHz between the AOMs is used to time-average out spatial interferences of the beams as they are crossed. The initial coarse alignment was carried out by looking for characteristic stripe signatures when a cold cloud trespasses the trapping beam during time of flight. For such a procedure, it is advised to deliberately align the ODT below the magnetic trap release position, as longer time of flights increase the search volume. After a first dipole trap signal has been identified, this can be easily beam walked towards the trap minimum using two-axis imaging from the side and the top. Two typical pictures of this positioning procedure are shown in fig. 35.

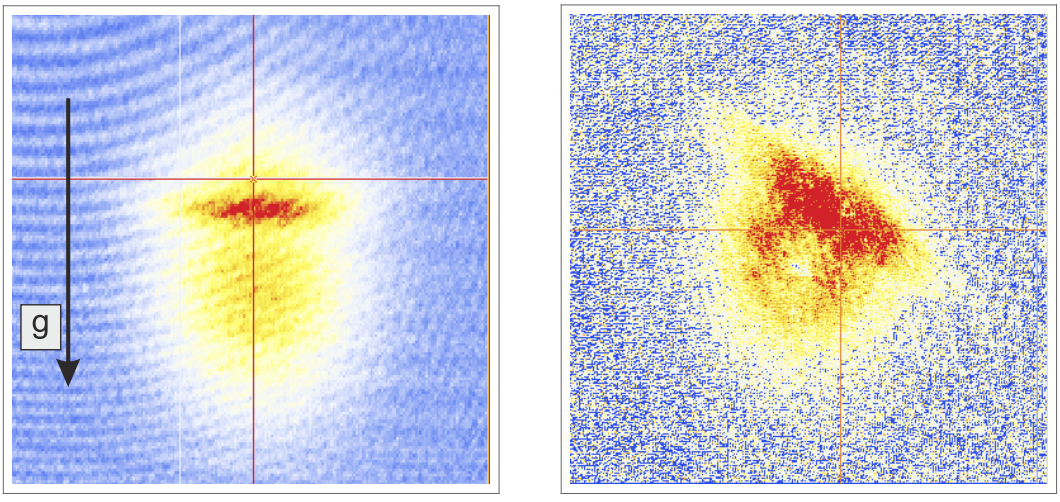

(a) ODT stripe signature in time of flight, imaged horizontally.

(b) ODT together with the plugged quadrupole trap, imaged vertically.

Figure 35: ODT signatures obtained via two-axis imaging. Horizontal imaging is used for vertical alignment and vice versa. The red crosses indicate the potential minimum of the plugged quadrupole trap.

This coarse adjustment method is performed for both trapping beams individually. When sufficient overlap is reached, they are fine-tuned with respect to each other. As the relative vertical offset of the crossed beams to each other changes the combined potential, accurate, reliable and reproducible alignment of both beams with respect to each other is needed. This is realized by equipping both beam paths with two picomotor piezo mirror mounts (Newport *New Focus 8821*) each. In combination with a picomotor controller (Newport *New Focus 8742*), the picomotor angular resolution of 0.7 µrad allows precise relative alignment on the single-pixel level of the used imaging system. The atom transfer from the plugged quadrupole to the optical trap is performed by ramping up both ODT beam intensities in half a second after a certain MW evaporation time, followed by down ramping of the quadrupole field in 0.2 s and sudden shuttering of the blue plug. A residual guiding field $B_{res} = 2.49\,G$, applied along the vertical direction using the compensation coil, preserves the individual spin projection of the atoms, $|m_{f,Na}\rangle = |m_{f,K}\rangle = -1$. If only the AOMs are used for switching the ODT, the combined heating effects on AOM and fiber interfere with the desired intensity regulation speed. Therefore the AOMs are kept in constant thermal equilibrium and switching is achieved by an AOM-shutter tandem. When the ODTs are not operated, the AOMs are kept on continuously and two flag shutters downstream of the AOMs deflect the beams on high-power beam dumps using 1/4 inch mirrors. Just before switching the ODTs into operation, the AOMs are turned off, the shutters opened a millisecond later, and the AOMs turned on again after 100 ms. This way any spurious shutter jittering as well as heating effects are eliminated.

Transfer into the cODT

As outlined at the beginning of this chapter, especially the dual-species operation benefits from the loading of rather hot samples ($T \approx 10\,\mu K$ at evaporation times of approx. 15 seconds) in order to enable tuning of interactions as early as possible. Because both the quadrupole and the dipole trap can be used for phase-space compression, and both of them will display different cooling efficiencies, deeper MW evaporation will not necessarily lead to much larger final phase space densities. The cODT loading conditions were therefore determined in a double evaporation scheme: for a given MW evaporation time, the cODT is loaded, followed by a reduction of the beam intensities in a 3 s long ramp that realizes a second evaporation stage. The beams are always ramped to the same values and kept there for a short thermalization period, after which the cODT is switched off and the atoms undergo a TOF. The final beam intensity after the second evaporation stage fixes the final trap depth, therefore the temperature can be assumed to be comparable. As it further sets the trapping volume, this leaves the atom number as an easily tracable figure of merit as the first evaporation stage time is scanned. Fig. 36 shows the atom number of such doubly evaporated ^{23}Na samples as a function of the MW evaporation time in the quadrupole trap. The chosen final trap depth gives $T = 700 - 800\,nK$ for this measurement (see inset). The result shows a rather small sensitivity of the ^{23}Na system to the pre-evaporation, with similar combined efficiencies over a range of a few seconds.

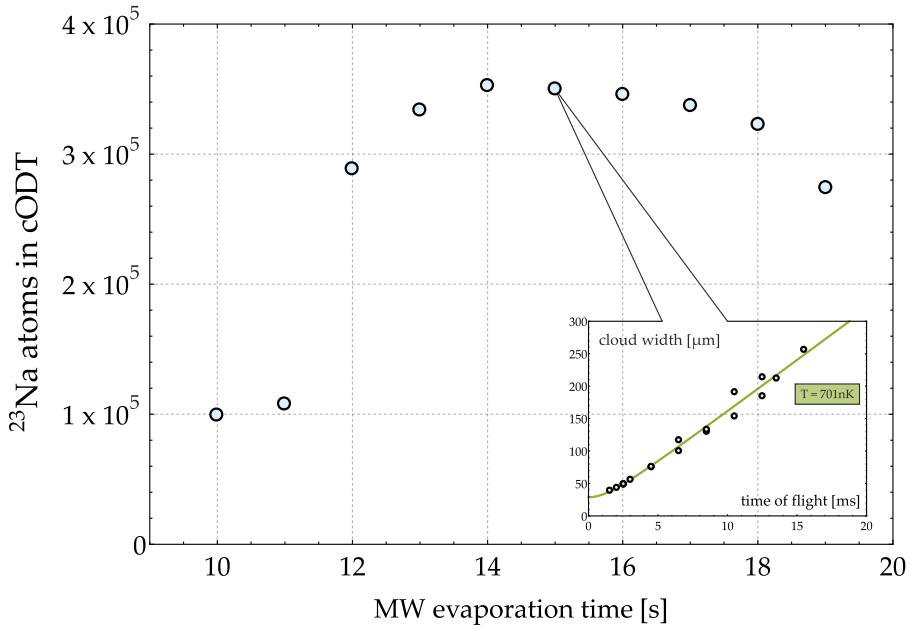

Figure 36: ^{23}Na atom number in the cODT as a function of pre-evaporation time in the quadrupole trap. After the transfer, the cODT intensities were reduced to obtain comparable conditions for each pre-evaporated point (see inset and text).

6.2.1 *Trap frequencies*

In theory, the trap frequencies are completely fixed through the power and waist of each beam. Yet both quantities, especially the spot size, are not exactly known at the position of the atoms. Moreover, as the real trap frequencies can differ from day to day through imperfect relative alignment of the beams, they have to be remeasured on a regular basis. In this thesis, two well-known methods were used to extract the trap frequencies, namely by observing *dipole oscillations* following a directed external force, as well as *parametric heating* as a reaction to a parametric drive. Both phenomena are common in classical mechanical systems and follow rather intuitive reasoning - every child knows how to parametrically drive a swing. By comparing the measured trap frequencies with a numerical ab-initio model for a set of beam powers, both beam spot sizes at the position of the atoms can be exactly deduced, giving the values in table 3.

If one assumes the harmonic approximation (eq. (6.9)) to be exact, the principal axes dynamics are completely decoupled from each other. By adiabatic application of an external force (e.g. ramping up a magnetic field gradient) along one of the principal axes, the cloud will be displaced from its incident trap minimum. Following a sudden switch-off of this external force, the cloud's center-of-mass will perform dipole oscillations along the chosen axis similar to a deflected pendulum, with its oscillation frequency being identical to the trap frequency of the excited principal axis. This behaviour is sometimes referred to as the excitation of Kohn modes.[3]. If the mean energy of the atomic ensemble becomes comparable to the trap

3 The fact that the center-of-mass motion decouples from all internal dynamics, and therefore is independent of the number of atoms, their temperature and their interaction strength, is quite

depth, anharmonicities will lead to dephasing of the oscillation through additional excitation of the other trap frequencies.

The simplest (albeit diabatic) realization of this method is to measure the vertical Kohn mode ω_z by a release-and-recapture procedure. After a sudden ODT switch-off, the cold cloud falls down along z and is recaptured after 500 µs, corresponding to a vertical displacement of 1.2 µm. Following a variable holding time, the atoms are released from the trap and imaged after a fixed TOF time. By sampling the holding time after the recapture, the vertical center-of-mass position in TOF reveals the in-trap oscillation as depicted in fig. 37 (a), when the trap frequency can be extracted by a damped sinusoidal fit.

Along the horizontal direction, the atom cloud can be set into motion using one of the compensation coils, where the applied force vector is not aligned with the

remarkable. It has it's roots in Kohn's theorem [171] which is exact for true harmonic confinement [172].

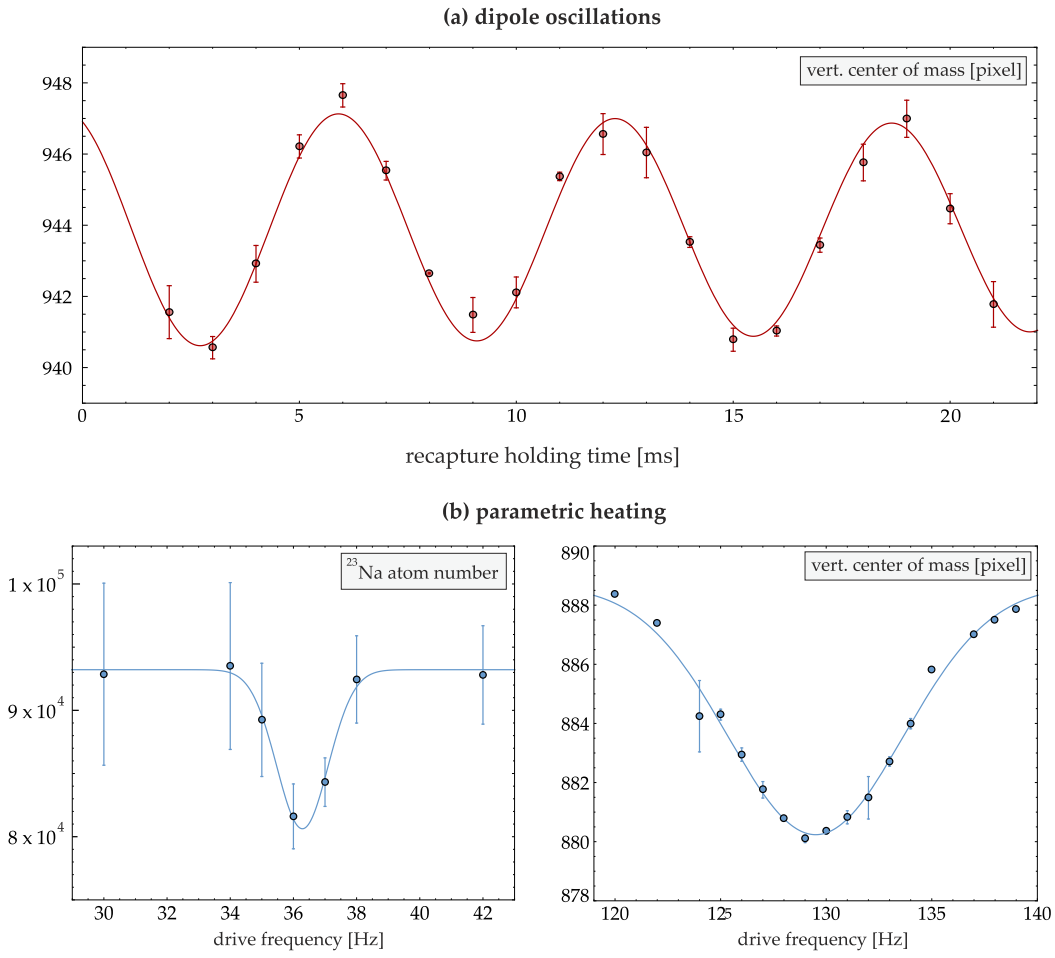

Figure 37: Trap frequency measurement. (a) Dipole oscillations of a ^{23}Na BEC. A sinosoidal fit gives the trap frequency, in this case $\omega_z = 2\pi \times 157$ Hz. (b) Parametric heating of a ^{23}Na BEC. The parametric resonance (or a subharmonic) can be inferred by monitoring the number of particles that have been heated out of the trap (left). Alternatively, the energy pumped into the system gives a breakdown of the harmonic approximation, and the resonance can be observed by probing anharmonicities, such as vertical movements following a horizontal drive (right).

principal axes. In the general case of exciting both horizontal Kohn modes, the periodic oscillation in the xy-plane is given by

$$f(t) = e^{-t/\tau}\{(\cos(\alpha)\, A_x)\sin(\omega_x t + \phi_x) + (\sin(\alpha)\, A_y)\sin(\omega_z t + \phi_z)\}. \quad (6.18)$$

The exponential decay models the dephasing of the oscillation amplitudes A_x and A_y that are given by the incident angle between applied force and trap axis, whereas α denotes the incident angle and therefore the sensitivity of the camera system to the respective principal axis. In systems where equal horizontal trap frequencies are desired, this results in a beat signal $f(t)$ that can complicate the assignment of the trap frequencies [173]. Such geometric requirements do not exist in this setup. For the majority of cases that follow, both beam intensities were set to provide a nearly equal trap depth per beam. Due to their different trapping volumes, the trap frequency of the large volume trapping beam then usually is a factor ~ 3 smaller, rendering the assignment of the oscillation frequencies straightforward. It is also possible to create a perturbation that is automatically aligned with one of the principal axes: First, one of the traps is adiabatically reduced, which displaces the minimum of the remaining trap to its focal point. Afterwards, the reduced trap is diabatically restored to its initial value, when the atoms will display oscillations that probe the radial frequency of the restored trap. Due to the large Rayleigh lengths the differential force felt by the atoms is rather small, but the oscillations can be successfully traced when the time-of-flight time is chosen to be sufficiently large (~ 20 ms).

At good last, the trap frequencies have also been measured by parametrically driving the system. This is done by a modulation pulse that modulates the intensity of one of the trapping beams as

$$I(t) = I_0(1 + \alpha \sin(\omega_{\text{Mod.}} t)), \quad \alpha \ll 1 \quad (6.19)$$

using a frequency generator together with a voltage-controlled amplifier connected to the corresponding intensity-regulating AOM of the trapping beam. Here the modulation amplitude and frequency are denoted as α and $\omega_{\text{Mod.}}$ respectively. When the modulation frequency equals twice the trapping frequency, $\omega_{\text{Mod.}} \approx 2\omega$ (or $\frac{2\omega}{n}$ with an integer n, when the corresponding higher harmonics become resonant), the corresponding parametric resonance leads to an exponential buildup of the atomic oscillation amplitude over time, i.e. particles heat up and leave the trap. A scan of the modulation frequency unveils a typical drop in the atom number (see fig. 37 (b)) at the parametric resonance condition, and the trap frequency can be estimated by a phenomenological Gaussian fit. It is noted that through the steady increase of kinetic energy, the parametric resonance can be observed in almost all of the typically probed observables, e.g. heating leads to an increase in the cloud width and stronger anharmonicities evoke oscillations along the axes perpendicular to the parametrically driven one. This allows to find an observable that gives rise to the smallest uncertainty in the fit, e.g. again the vertical center of mass displacement (see fig. 37 (c)) following a horizontal drive.

All methods outlined above have their advantages as well as technical challenges, e.g. the parametric drive can be applied to each beam individually which purifies the trap frequency assignment. The main benefit of using both of them is that they can be calibrated onto each other.

6.3 BOSE-EINSTEIN CONDENSATION OF ^{23}Na

The choice of distribution is somewhat arbitrary.
-W. Ketterle [82]

To furnish proof that Bose-Einstein condensation has occured, one utilizes the unique properties of this state of matter. Out of the Gross-Pitaevskii equation, it follows that the density distribution of a harmonically trapped BEC in the Thomas-Fermi regime is given by inverted parabolae, characterized by their three Thomas-Fermi Radii $R_i (i = x, y, z)$. This functional form differs significantly from that of an equally trapped thermal, Gaussian-shaped cloud characterized by its three widths σ_i. Yet probing the density distribution *in situ* is challenging due to the rather small size and enormous optical density of a trapped BEC. The trap is therefore switched off and the images are taken after a sufficiently long expansion time. Quite fortunately, it has been shown that the time-evolution of a BEC upon free expansion from a trap obeys analytical scaling solutions, i.e.

$$R_i(t) = R_i(0) b_i(t) = \sqrt{\frac{2\mu}{m\omega_i^2}} b_i(t). \tag{6.20}$$

The introduced scaling factors b_i follow a set of coupled classical equations of motion:

$$\frac{d^2 b_i(t)}{dt^2} = \frac{\omega_i^2}{b_i(t) b_x(t) b_y(t) b_z(t)}. \tag{6.21}$$

This relation was first shown by Castin and Dum [174] and independently by Kagan *et al.* [175]. A treatment based on superfluid hydrodynamic equations that was published shortly later leads to the same result [176]. Therefore, the functional form of the condensate density is conserved in a TOF. Pictures of the ensemble distribution are acquired and analyzed using absorption imaging, yielding the condensates column density

$$\tilde{n}_{BEC}(x, z) = \tilde{n}_{BEC,0} \left(1 - \frac{x^2}{R_x^2} - \frac{y^2}{R_z^2}\right)^{3/2} \theta\left(1 - \frac{x^2}{R_x^2} - \frac{y^2}{R_z^2}\right) \tag{6.22}$$

with the peak column density $\tilde{n}_{BEC,0}$ and the Heaviside function θ. As the thermal cloud also retains its Gaussian shape after expansion, the popular evidence for the process of Bose-Einstein condensation is given by the appearance of a *bimodal distribution* of thermal and condensed cloud as the condensation threshold is crossed.[4]

The quantum degenerate regime is reached through optical evaporation by lowering the trap beam intensities. Due to the unequal beam waists, the radially symmetric beam imposes a more than three times stronger trapping strength on the atoms (see table 3). In the initial evaporation step, this beam is linearly ramped down in 1.5 s to a power of 1 W which provides nearly equal trap depths per beam. In a subsequent evaporation step, both beams are ramped linearly to variable combined trap depths, with roughly equal trap depth per beam. For the deepest evaporation shown here, the final beam powers are 60 mW for the tight-confining and 126 mW for the loose-confining beam after a 2.5 s long ramp.

4 The probably second most popular evidence is the aspect ratio inversion of a condensed cloud in time of flight. It could also be clearly observed in this setup and will be presented in another forthcoming thesis [162].

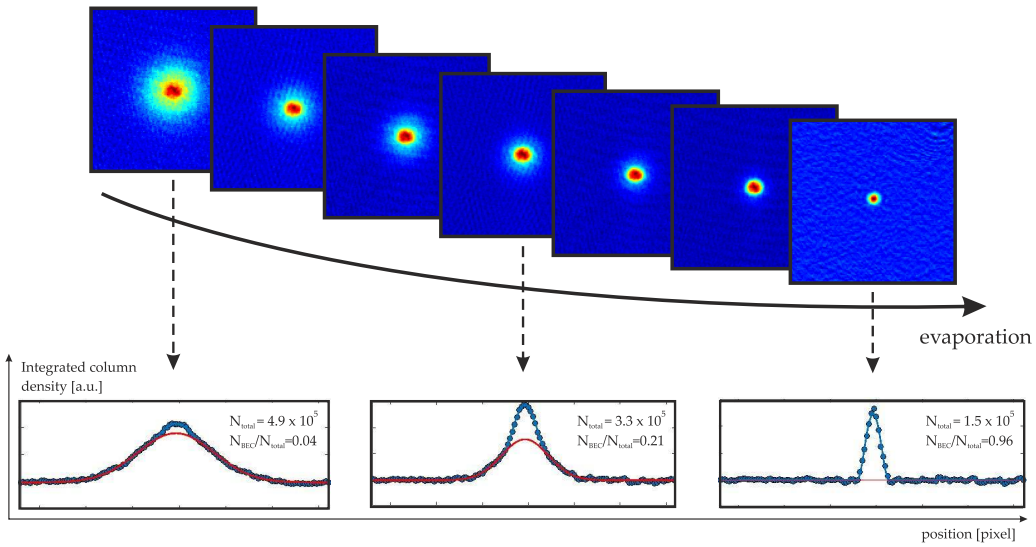

Figure 38: BEC phase transition from a thermal cloud (left) to a pure BEC (right). The bimodal distribution is clearly visible in the intermediate regime.

Figure 38 shows recorded absorption images for a selection of evaporation depths. The color coding of each picture has been normalized onto its peak column density. Starting with an almost pure thermal ensemble (upper left), The onset of condensation is clearly visible by the relative growth of the central part of the cloud, which is identified with the condensed part. In the intermediate regime, two distinct distributions are discernable. As the evaporation progresses, the thermal cloud is not longer discernable and an almost pure BEC is obtained (lower right). To estimate the condensed fraction, a bimodal distribution is fitted to the acquired data. As given by the quote above, any fit method that contains bimodality will in general be able to reflect this property. If one wants to fit the whole data set at once, the most accurate result is obtained by a 2D surface fit *a la* $\tilde{n}_{\text{bimod.}} = \tilde{n}_{\text{therm.}} + \tilde{n}_{\text{BEC}}$, where the BEC part is given by eq. (6.22) and the thermal cloud is modeled by a Bose-enhanced Gaussian

$$\tilde{n}_{\text{therm.}}(x,z) = \frac{\tilde{n}_{\text{therm.},0}}{g_2(1)} g_2\left[\text{Exp}\left(-\frac{x^2}{2\sigma_x^2} - \frac{z^2}{2\sigma_z^2}\right)\right]. \tag{6.23}$$

with $g_2(z) = \sum_{n=1}^{\infty} z^n/n^2$. This description can give rise to interpretational problems in the region where condensate and thermal part overlap. A sensible way of analyzing bimodal distributions therefore first cuts out the central part of the acquired data, when only the thermal cloud wings remain. At sufficient distance from the peak density, the higher order terms in the Bose-enhancement series are negligible and the density distribution converges to the normal Gaussian distribution. Through simulation and subsequent analysis of typical absorption images, it was shown [177] that a simple Gaussian fit gives largely the same result if only the wings are used. Having acquired the thermal part, it is substracted from the whole dataset and the remnants are fitted to eq. (6.22). The thermal fit can further be used to extract the steady-state temperature of the system. As a BEC does not follow a Maxwell-Boltzmann distribution, its expansion properties cannot be used to gain information of the system temperature. It is however in thermal

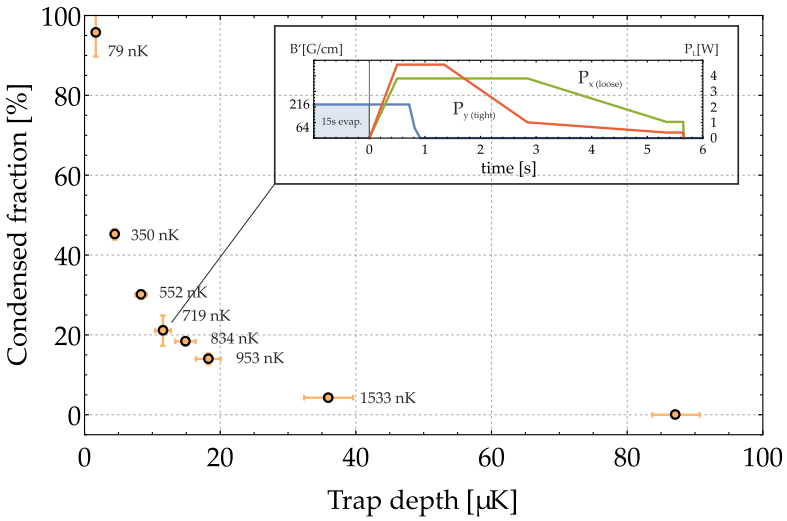

Figure 39: Condensed fraction as a function of final evaporation trap depth. Inset: Exemplary experimental sequence that lead to a bimodal distribution.

equilibrium with the thermal cloud, so the latter one can be used as a thermometer. Performing the cut-and-fit procedure for a set of time of flight images then yields the system temperature.

Figure 39 shows the estimated condensate fraction $N_{BEC}/(N_{BEC} + N_{therm.})$ in percent as a function of the final evaporation trap depth in the cODT. Each data point is the mean value out of $5-10$ realizations under the same experimental conditions, an exemplary experimental sequence is shown as a figure inset. By plotting an atom number ratio, the systematic errors in the individual atom number determination drop out (up to small nonlinearities), hence the vertical error bars are mainly governed by statistics. As the condensate fraction approaches unity, the thermal wings are only vaguely discernable, giving rise to higher uncertainties regarding the actual amount of residual thermal cloud. This also shows that the notion of a "pure" BEC, that is commonly featured in colloquial speech, is a bit loosely defined. With only a few percent of thermal background, thermometry becomes increasingly difficult in this region. Using time of flight and temperature estimations out of condensate fraction and final trap frequencies, the temperature of the "pure" BEC is estimated to be 79 nK. To probe this region with sufficient accuracy, more elaborate diagnostics such as magnon thermometry are required [178].

The "pure" BEC shown in fig. 38 gave an atom number of 1.5×10^5 at a thermal background of a few percent. Following the initial demonstration of BEC, the sequence shown in the inset of fig. 39 was optimized e.g. in terms of ramp speed, and most parameters of the previous experimental stages fine-tuned using the number of condensed atoms as a figure of merit. Only the microwave evaporation was untouched and kept at 15 seconds to ensure formidable dual-species operation later on. Moreover, the removal of spurious noise sources (e.g. damping of vibrations induced by the coil water cooling circuit using *sorbothane*) in the experimental apparatus had a significant effect. In the end, stable, reproducible and "pure" ^{23}Na BECs with a total atom number of 1.1×10^6 were realized in this setup.

6.4 THREE-BODY LOSSES IN THE $^{23}Na^{39}K$ MIXTURE

Having created the ideal coolant, one might expect dual-species condensation to be a straightforward task. This section shows that one first has to overcome an obstacle: interspecies losses. Due to the high densities prevailing in the crossed dipole trap, higher-order effects in the density are no longer negligible. Both atomic clouds can experience sizable three-body recombination effects that scale with the fourth power of the appropiate scattering length [179]. In the following, first the single-species case is discussed and the used formalism and approximations directly adapted to the more complicated case of mixture operation. The whole description assumes non-condensed, i.e. thermal clouds.

Up to third order, the density loss dynamics for the density n_i of species i in single-species operation is described by the rate equation

$$\left(\frac{dn_i(r,t)}{dt}\right)_i = -L_1^i n_i(r,t) - L_2^i n_i^2(r,t) - L_3^i n_i^3(r,t), \tag{6.24}$$

where $L_1(L_2)[L_3]$ denotes the respective one(two)[three]-body coefficient and the $(^i)$ superscript reflects their homonuclear origin. To avoid redundancy, the one-body loss coefficients are replaced by the respective background lifetimes used earlier in this thesis, $L_1^i \equiv 1/\tau_i$. In presence of species j, interrecombination (e.g. i-i-j) gives rise to additional loss terms:

$$\left(\frac{dn_i(r,t)}{dt}\right)_{ij} = -\frac{1}{2}L_2^{ij} n_i(r,t) n_j(r,t) - \frac{1}{3}L_3^{ijj} n_i(r,t) n_j^2(r,t) - \frac{2}{3}L_3^{iij} n_i^2(r,t) n_j(r,t). \tag{6.25}$$

The nomenclature of the respective coefficients can differ from article to article. Some groups include the total number of particles lost in the particular process into their coefficient, which is also the convention used above and throughout the rest of this thesis. The fractional prefactors then account for the contribution of each species to the heteronuclear loss processes.[5] The above equations are quite cumbersome, but can be quickly simplified when adapted to the actual experimental situation. It is recalled that the initially prepared atomic spin state is maintained in the ODT via a 2.5 G magnetic guiding field. With both ensembles being polarized in the state $|F = 1, m_F = -1\rangle$, two-body collisions will be strictly elastic, hence $L_2^{ii} = L_2^{ij} = L_2^{jj} = 0$. Despite the reduction, there will be still 6 fitting parameters $(\tau_{Na}, \tau_K, L_3^K, L_3^{Na}, L_3^{Na,K,K}, L_3^{Na,Na,K})$ left to describe the system. Furthermore, as the loss coefficient of the potassium density depends nonlinearly on the sodium one (and vice versa), the central coldest part of the clouds can be the highest loss region, which can lead to recombinational heating [179] and non-trivial temporal deformation of the individual Gaussian densities (anti-evaporation).

Single-species measurements

To reduce the number of the fitting parameters, it is noted that the single-species collisional loss properties can be first, which fixes the parameters $L_{1,2,3}^i$ in Eq. (6.24). For that, it is assumed that the density distributions are homogeneously reduced, i.e.

5 Other groups prefer to give the rate K_i describing the recombination event, therefore writing $2 \times K_2$, $3 \times K_3$ etc. [180, 181].

$dn_i(r,t)/dN_i(t) = 0$ with the atom number N_i, and heating processes are neglected. This then allows to express the rate equations in terms of atom number loss by spatially integrating the respective densities:

$$\frac{dN_{Na}(t)}{dt} = -\frac{N_{Na}(t)}{\tau_{Na}} - L_3^{Na}\,\xi_{Na}\,N_{Na}^3(t) \tag{6.26}$$

$$\frac{dN_K(t)}{dt}_K = -\frac{N_K(t)}{\tau_K} - L_3^K\,\xi_K\,N_K^3(t) \tag{6.27}$$

ξ_i are geometric factors that incorporate the spatial distribution of the trapped clouds, $\xi_i = \frac{1}{N_i^3(t=0)}\int_V dr^3 n_i^3(r,0)$. For the single-species thermal clouds, analytic solutions for ξ_i can be explicitly written down, but they are kept general here to conform to the two-species case that will follow. The atom loss rate notation has the advantage that instead of continuously tracing it, the density distribution has to be inferred only once using the readily accessible experimental observables atom number, trap frequency and temperature. The danger of this method is that it cleverly conceals the systematic errors of the setup. The geometric prefactors ξ_i are subject to daily changes, most notably due to realignment of the crossed dipole trap beams which changes the jointly generated trap frequencies. Therefore care has to be taken when evaluating data using outdated values of ξ. For the loss measurements that follow here and in the next chapter, the trap frequency values have been regularly updated and are usually acquired immediately after the loss data set has been measured.

By recording single-species loss measurements, the loss coefficients of eq. (6.26) can be determined numerically by fitting the loss rate equations solution to the acquired data.[6] Two single-species sequences are prepared in which the potassium (sodium) atom number is monitored as a function of the holding time t_H in the dipole trap. For the ^{39}K sequence, the ^{23}Na cloud is removed via a resonant light pulse before ^{39}K is transferred into the dipole trap. For the ^{23}Na run, ^{39}K is simply not loaded. Being interested in the high-density region, the microwave evaporation is proceeded up to the region where already the plugged magnetic trap starts to show considerably losses in the ^{39}K signal (compare with fig. 32). After loading the sample into the ODT, the trap frequencies are set to $(\omega_x,\omega_y,\omega_z)_{Na} = 2\pi\times(532,190,865)\,\text{Hz}$ and $(\omega_x,\omega_y,\omega_z)_K = 2\pi\times(647,231,1053)_K\,\text{Hz}$. After the samples have thermalized, their temperatures are measured independently by time of flight measurements, yielding 2.66 µK for ^{39}K and 3 µK for ^{23}Na at atom numbers on the order of $\leqslant 1\times10^5$ (^{39}K) and 5×10^5 (^{23}Na).

The acquired atom number decay curves for holding times up to 41 seconds are depicted in Fig. 41. A considerable amount of three-body losses is observed for neither species. For ^{23}Na in the $|f=1,m_f=-1\rangle$ state, this agrees with calculations by Moerdijk [182] and BEC measurements [136] that determined the L_3 parameter to be on the order of $2\times10^{-30}\,\text{cm}^6\,\text{s}^{-1}$. Even taking into account $3! = 6$ stronger

6 The single-species version with $L_2 = 0$ can be analytically solved, the same is true for $L_3 = 0 \neq L_2$. The solution is given here as it appears quite useful, but is rarely written down:

$$\frac{N_i(t)}{N_i(0)} = \left[\left(1+N(0)^2\xi L_3\tau\right)\left(e^{\frac{2t}{\tau}} - \frac{N(0)^2\xi L_3\tau}{1+N(0)^2\xi L_3\tau}\right)\right]^{-1/2}, \tag{6.28}$$

where the species sub- and superscripts have been dropped. In all other cases, the solutions are obtained using numerics.

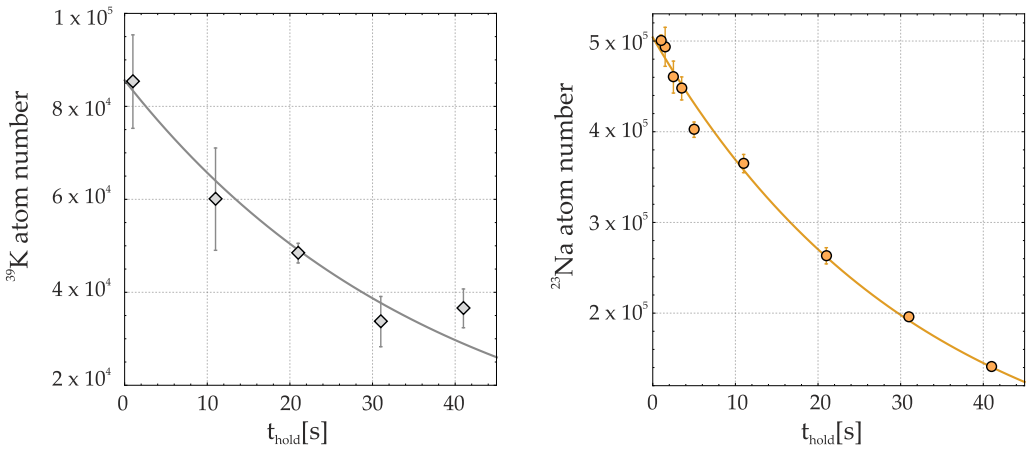

Figure 40: Atom number as a function of their holding time in the dipole trap in single-species operation. Three-body losses appear negligible for both individual species. Two exponential fits (solid lines) govern the individual dipole trap lifetimes (see text).

loss rates due to a bunching factor[7], the three-body decay rate for the experimental parameters would only amount to $4 \times 10^3\,s^{-1}$. The situation for ^{39}K is similar. What remains is the extraction of the $1/e$ lifetime of the samples, which are found to be $\tau_K = 37.8\,s$ and $\tau_{Na} = 31.7\,s$.

Mixture measurements

Having acquired the single-species parameters, the experiment is repeated by preparing a mixture at a temperature of $2.6\,\mu K$ and an imbalanced atom number ratio $N_{Na}/N_K \approx 4$. This simplifies the ensuing analysis, as the losses will primarily affect the minority potassium cloud whereas the sodium majority serves as a collisional bath. The atom number as a function of the holding time for both species is depicted in fig. 41. Rapid losses are observed in the ^{39}K signal, with an effective $1/e$ lifetime of about 240 ms, whereas ^{23}Na, being the majority cloud, shows only a slight decrease over time. This validates the previous findings in the plugged magnetic trap, and pinpoints interspecies losses as the main antagonist of the high-density dual-species operation.

For the loss analysis, it is clear that the one- and three-body losses obtained earlier are negligible on the relevant timescale of the experiment. For completeness, they are put in the analysis as constants, but omitted in the written down description to provide a more lucid notation. Clearly, the loss mechanism is driven by interspecies losses. To model these, one now also has to account for the geometric mismatch of the two cloud densities in the trap due to their different trapping potentials and

7 The probability of finding three bosonic atoms together is enhanced similar to photon bunching in thermal radiation fields. Atom-bunching vanishes in a condensate like photon bunching vanishes in a laser field [183].

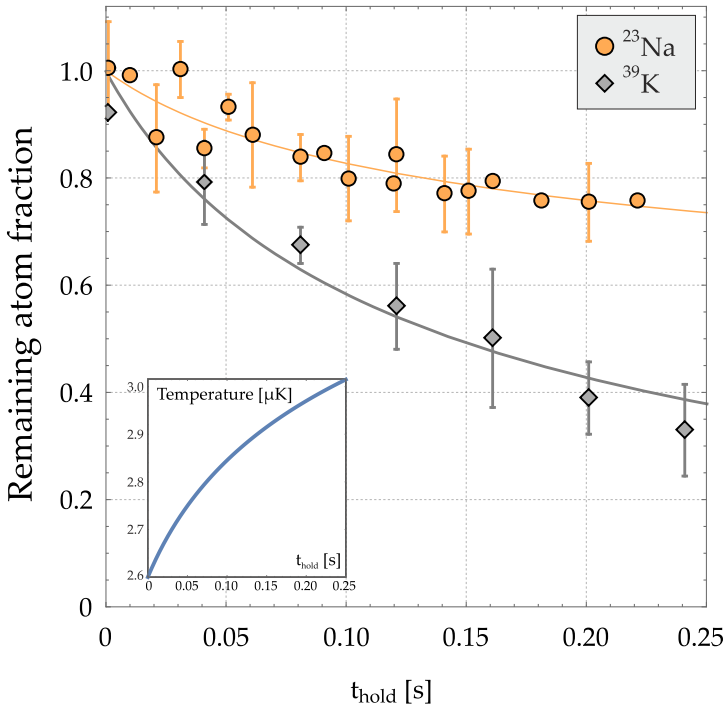

Figure 41: Remaining fraction of ^{23}Na (orange circles) and ^{39}K (gray diamonds) atoms as a function of the holding time in the dipole trap for the mixture experiment. Three-body losses lead to a rapid atom number decay of the minority component ^{39}K. The solid line is a fit of the coupled-system loss rate equations solution to the acquired data. Both atom numbers are normalized to their fitted value at t = 0, being 3.8×10^5 for ^{23}Na and 1.1×10^5 for ^{39}K. Inset: Calculated temperature evolution according to the solution of the presented coupled differential equations. The calculated increase in temperature is on the order of 15%.

differential gravitational sag. For a given experimental parameter set, these are obtained by numerical integration. Then

$$\left\langle N_A^i N_B^j \right\rangle_V = \int_V n_A^i n_B^j d^3r \tag{6.29}$$

is the spatially averaged, temperature-dependent three-body density in a given volume V, where A and B denote the species and i and j the loss exponent. The temperature dependence is explicitly kept, as the rapid depletion might signal strong heating, but the densities are assumed to maintain their Gaussian form through rapid thermalization.

The three-body loss coefficients $L_{Na,Na,K}$ and $L_{Na,K,K}$ are then extracted by fitting the experimental data to the solutions of three coupled differential equations governing the sodium and potassium atom number loss dynamics as well as the temperature time evolution [184, 179]:

$$\begin{aligned}
\frac{dN_{Na}}{dt} &= -\frac{2}{3} L_{Na,Na,K} \left\langle N_{Na}^2 N_K \right\rangle_V - \frac{1}{3} L_{Na,K,K} \left\langle N_{Na} N_K^2 \right\rangle_V \\
\frac{dN_K}{dt} &= -\frac{1}{3} L_{Na,Na,K} \left\langle N_{Na}^2 N_K \right\rangle_V - \frac{2}{3} L_{Na,K,K} \left\langle N_{Na} N_K^2 \right\rangle_V ,
\end{aligned}$$

$$3k_B \frac{dT}{dt} \times (N_K + N_{Na}) = \beta_{Na,Na,K} L_{Na,Na,K} \left\langle N_{Na}^2 N_K \right\rangle_V + \beta_{Na,K,K} L_{Na,K,K} \left\langle N_{Na} N_K^2 \right\rangle_V ,$$

where the third differential equation accounts for the effect of anti-evaporation induced heating. The notation here follows [184]. The quantity β

$$\beta_{Na,Na,K} = \frac{3}{2}k_B T - \frac{2}{3}\frac{\int_V U_{Na} n_{Na}^2 n_K d^3r}{\int_V n_{Na}^2 n_K d^3r} - \frac{1}{3}\frac{\int_V U_K n_{Na} n_K^2 d^3r}{\int_V n_{Na} n_K^2 d^3r}. \tag{6.30}$$

(and similarly $\beta_{Na,K,K}$) accounts for the mean potential energy of the lost atoms, with U being the potential energy [184, 179]. Note that also the second and third term of β are temperature dependent through the temperature dependence of n.

The high loss rate either stems from (Na+Na+K) recombinations, from (Na+K+K) ones, or from a combination of both. One can get initial insight about the physical process by setting either one of the coefficients to zero and assume that the sodium depletion as well as the temperature increase is negligible. Both cases, pure (Na+Na+K) and pure (Na+K+K) losses, are then analytically solvable and can be compared to each other. For this 'poor man's differential equation', It became visible that the (Na+Na+K) solution gives a higher agreement than the (Na+K+K) one, which seems sensible due to the density imbalance in our system. Following the qualitative understanding of the underlying processes, the whole system is solved. As fitting routines can be error-prone to its starting conditions, the sum of squared residuals was first explicitly evaluated on a $\{L_{Na,Na,K}, L_{Na,K,K}\}$ parameter grid. After manually selecting the global minimum region, the numerical fitting routine was executed.

The obtained loss coefficent are $L_{Na,Na,K} = 1.03(62) \times 10^{-25}$ cm^{6}s^{-1} and $L_{Na,K,K} = 0.50(30) \times 10^{-25}$ cm^{6}s^{-1}, where the uncertainties include the statistical error on the fit as well as systematic uncertainties in the evaluation of the experimental quantities: temperature, atom number and trap frequencies for both species. The calculated temperature increase is on the order of 15%, which is about equal to the systematic uncertainties with which the temperature can be determined. The heated cloud temperature is still well below the trap depth, hence the relatively small heating rates will not lead to additional terms such as heating-induced evaporation that might compete with the three-body loss rates. For the observed timescale, this validates the approximative treatment that lead to eq. (6.29) .

In principle, three-body loss measurements allow to draw conclusions about the sign and magnitude of the underlying scattering length through the relation [179]

$$L_3 = \mathcal{C}(a)\frac{\hbar}{m}a^4 \tag{6.31}$$

which is a result out of dimensional analysis (see sec. 7.2.1 for the derivation). However, this relation depends on non-trivial Efimov physics encapsulated in the coefficient $\mathcal{C}(a)$, and the Efimov effect is known to lead to resonances in the three-body coefficient. Without detailed knowledge about the presence or absence of resonant structures for the studied mixture, a conclusive statement cannot be given. Comparison with extensive analysis on other alkali mixture indicates that the loss rate coefficients are on the order of the ones observed in ^{39}K^{87}Rb and ^{41}K^{87}Rb [184], ^{40}K^{87}Rb [185] and ^{6}Li^{133}Cs [89, 186] for scattering lengths of few hundred a_0. This will be revisited in the following chapter, when theoretical predictions of the interspecies scattering length are presented and discussed. Although a clean assignment between losses and scattering interaction remains challenging, this thesis chapter concludes with an important result: With the high amount of

undesirable losses, $B = 0\,G$ does not provide a suitable environment for operating the dual-species apparatus, at least not beyond a low-density region. In order to impede three-body losses, the interspecies scattering has to be reduced, for example by using magnetic fields. This is tackled in the following chapter of this thesis.

7

FESHBACH SPECTROSCOPY AND QUANTUM DEGENERATE MIXTURES

The previous chapters described the experimental apparatus and demonstrated its capability to produce quantum degenerate matter of ^{23}Na. While the dual-species operation appeared largely unproblematic in the initial stages of the experiment, it was shown that the mixture suffers from large losses when the high-density region is reached. As the losses are caused by interspecies interaction, the following chapter is devoted to their study by theoretical and experimental means in order to obtain control over them. The primary objective of the ensuing investigation is to gain the ability to condense both species simultaneously by using Feshbach resonances. Its main results have been published in [4], figures appearing identically in that publication are marked correspondingly. The taken course of action can be summarized as follows:

1. The required magnetic bias fields must be provided and calibrated. Furthermore, the homonuclear Feshbach spectrum has to be recorded, in order to be able to discern homonuclear and heteronuclear effects. This is presented in section 7.1 and section 7.2.

2. The investigation of the heteronuclear system then starts with the theoretical framework, which is presented in section 7.3. To its end, coupled-channel calculations are performed using subroutines developed in the Tiemann group. The results are phrased in terms of experimentally accessible parameters, which unveils distinct signatures in the Feshbach spectrum that are accessible by applying an external magnetic bias field. The results are further compared with another, independently performed study by Viel and Simoni that was published recently [187].

3. The measurements of the Feshbach spectrum for the incident channel of interest ($|1,-1\rangle_{\mathrm{Na}} + |1,-1\rangle_{\mathrm{K}}$) are shown in section 7.4. This includes the exact positions and widths of the predicted signatures in the experimentally accessible region from 0 to 1000 G.

4. The thereby acquired heteronuclear resonance spectrum is combined in section 7.5 with the independently measured homonuclear one. Expressed in terms of the individual scattering lengths, this gives rise to interaction domains characterized by the mean-field stability criterion. These domains are discussed in terms of their suitability for the purposes of sympathetic cooling and achieving a quantum degenerate mixture.

5. Having identified a suitable domain, this chapter closes with the culmination of all combined theoretical and experimental efforts featured so far - the emergence of dual-species degeneracy.

7.1 MAGNETIC FIELD CALIBRATION

Bias fields are generated by using the same coil pair that produces the field gradients in the MOT and quadrupole trap. After the transfer to the dipole trap, the quadrupole field is quickly ramped down to zero. It is then switched from Anti-Helmholtz to Helmholtz configuration using a H-bridge. Using the Biot-Savart law for the coil parameters, 3.25 G/A is obtained as a first estimate regarding the translation between applied electric current and generated magnetic field strength [76]. With the knowledge gained using the quadrupole trap it follows that magnetic fields of about 1000 G can be generated before the thermal load might inflict damage onto the coil environment. The exact calibration is done by using the cold atoms as a magnetic field strength sensor. At a given field strength B, the atomic ground state internal state energies shift according to the well-known Breit-Rabi formula:

$$E(B)_{|j=1/2,m_j,i,m_i\rangle} = -\frac{\Delta E_{HFS}}{2(2i+1)} + m g_i \mu_B B \pm \frac{\Delta E_{HFS}}{2}\sqrt{1+\frac{4mx}{2i+1}+x^2} \tag{7.1}$$

$$\Delta E_{HFS} = a_{hfs}(i+1/2) \tag{7.2}$$

$$x = \frac{(g_j - g_i)\,\mu_B B}{\Delta E_{HFS}} \tag{7.3}$$

$$m = m_i \pm 1/2 \tag{7.4}$$

Here, i and $j = 1/2$ are the nuclear spin and total orbital angular momentum respectively, with g-factors g_i and g_j and projections m_i, m_j, and a_{hfs} is the hyperfine coupling constant. Microwave spectroscopy is then performed by matching a differential energy shift at a given electric current to the frequency of a microwave field. The used probe is a ^{23}Na cloud at temperatures of $700 - 800$ nK to avoid thermal broadening of the spectral lines. The small vertical guiding field, that kept the spins aligned in the ODT, is always kept on. Depending on the magnetic field strength, different basis sets have to be employed in order to return good quantum numbers. For simplicity, two eigenstates are defined by

$$|\beta_1\rangle(B=0) = |f=1, m_f=-1\rangle, \tag{7.5}$$

$$|\beta_2\rangle(B=0) = |f=2, m_f=0\rangle. \tag{7.6}$$

Then $|\beta_1\rangle(B)$ and $|\beta_2\rangle(B)$ denote the states whose eigenenergies at a given field B are adiabatically connectable. Then it can be said that the driven microwave transitions correspond to $|\beta_1(B)\rangle \rightarrow |\beta_2(B)\rangle$, which is schematically shown in fig. 42. After the microwave pulse, the magnetic field is ramped down to zero and the local eigenstate will coincide again with the $|f, m_f\rangle$ basis. The irradiation time of the microwave is chosen to be long (~ 100 ms) compared to typical Rabi periods, so that the number of removed atoms from the $f = 1$ manifold will just follow a Lorentzian lineshape. By scanning the microwave frequency and exclusively imaging the $f = 1$ fraction, a drop in the atom number signals the corresponding microwave resonance.

Figure 42 further depicts an exemplary measurement for an applied current value of $I = 64$ A. The microwave resonance location is obtained using a Lorentzian fit. By classifying the resonance frequency in the Breit-Rabi diagram, the applied current is assigned to a magnetic field value. Repeating such a measurement for a series of current values gives a calibration curve that can be written by the simple

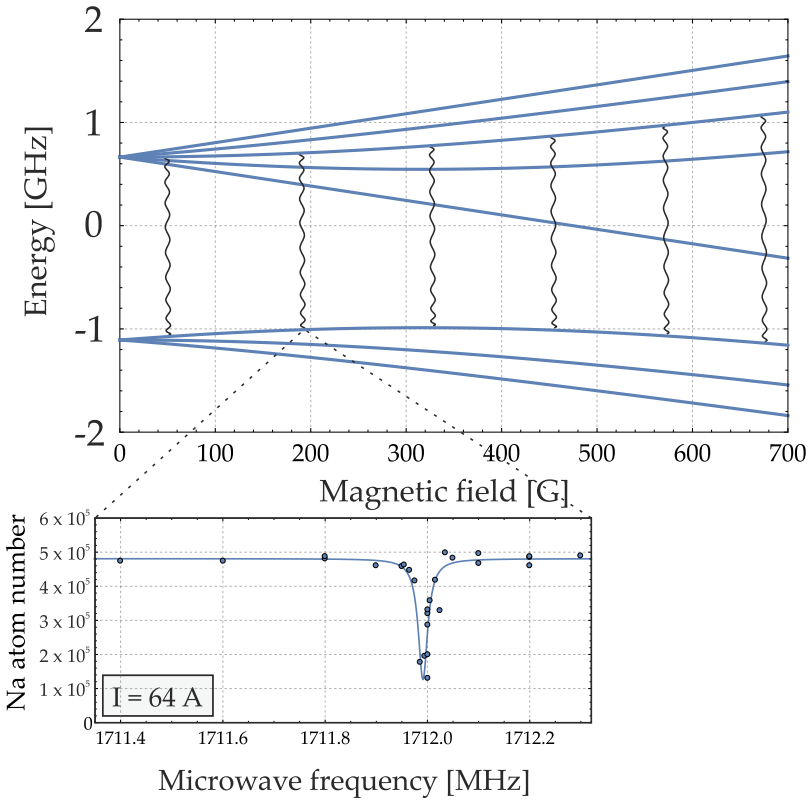

Figure 42: Microwave spectroscopy using ^{23}Na. The upper graph shows the Breit-Rabi diagram and sketches the relevant states for the microwave transitions. The lower graph shows the number of detected ^{23}Na atoms in $f = 1$ as a function of microwave frequency. A dip unveils the resonance location, whose position is determined by a Lorentzian fit (solid line).

linear relationship $B_I = B_0 + B_1 I$. The value B_0 is determined by the strength of the guiding field, the earth's magnetic field and residual magnetizations of experimental apparatus components. Therefore, also the case $I = 0\,A$ is spectroscopied and the guiding field strength varied. This allows the determination of all B_0 contributions, and provides information whether the guiding field is properly aligned with the Helmholtz field[1]. Using this method, the usually applied guiding field strength was determined to be 2.49 G. Since the background magnetic field can vary from day to day, regular re-evaluation of the magnetic field calibration is indispensable. Typically, selected values for the applied current are remeasured after a measurement campaign has been completed, and daily drifts are recorded. In addition, every time a distinctive signature (resonances, zero crossings, etc.) is recorded, the magnetic field strength value of the signature's extremal points is spectroscopied.

The microwave dip positions are determined with a statistical uncertainty on the order of 10 kHz. For a given bias field of 100 G, this translates into a magnetic field uncertainty of 34 mG. Further sytematics will be given by the ripple level, i.e. periodic AC fluctuations and random noise, of the used power supply regulation. For the power supplies used here, the specified peak-to-peak [rms] ripple at full load is equivalent to a peak-to-peak [rms] magnetic field ripple of 180 mG [60 mG].

1 It is.

This is far below the typical width of all signatures that will be encountered in the Feshbach spectrum, which renders further magnetic field stabilization unnecessary.

7.2 HOMONUCLEAR FESHBACH SPECTROSCOPY

In order to distinguish between homonuclear and heteronuclear signatures, the single-species Feshbach spectrum of ^{39}K was recorded separately. As fig. 8 shows, this only has to be done for potassium, since sodium in the spin state under consideration does not possess Feshbach resonances in the experimentally relevant magnetic field range. Strictly speaking, the measurement of the potassium resonances is not necessary, since they have already been located and analyzed 2007 in experiments conducted at LENS [188]. For ^{39}K in $|1,-1\rangle + |1,-1\rangle$, three s-wave resonances are known to exist in the magnetic field window $0 - 1000\,\mathrm{G}$. For this very reason, however, an independent measurement is very well suited for cross-checking the magnetic field calibration[2]. Furthermore, this measurement serves as a testbed for the experimental measurement protocol: Since the result is already known, the orchestrated experimental sequence can be scanned for possible artifacts. This section therefore also serves as an introduction to the Feshbach resonance measurement method, as all subsequent measurements will follow the same patterns of state preparation, field ramps and data evaluation.

7.2.1 *Two-body effects, three-body observables and lineshapes*

As shown in chapter 2, the Feshbach resonance phenomenon is characterized by a pole of the scattering length at the resonance location B_0 as a function of magnetic field:

$$a(B) = a_{bg}\left(1 - \frac{\Delta B}{B - B_0}\right) \tag{7.7}$$

Although this is a two-body effect, it can affect other observables as well. The detection of Feshbach resonances is typically achieved by performing atom loss spectroscopy, which makes use of the fact that the three-body loss rate can be represented as a function of the scattering length. This can be shown by naive dimensional analysis: At the end of the last chapter, the three-body loss rate was introduced through

$$\left(\frac{d}{dt}n(t)\right)_{3\text{-body}} = -L_3 \times n^3(t). \tag{7.8}$$

Therefore, the dimension of the three-body loss coefficient is

$$[L_3] = \frac{(1/\text{length})^3\,/\text{time}}{(1/\text{length})^9} = \frac{\text{length}^6}{\text{time}} \tag{7.9}$$

In the ultra-cold limit, it can be assumed that the scattering length is the only relevant length scale. To generate the dimension time, the reduced Planck constant

2 As with the measurement of temperature (*in-situ* and in time of flight) and atom number (via absorption and fluorescence detection), the benefits of different calibration methods for mutual adjustment is emphasized here.

is employed in combination with the mass of the particle ($\hbar/m = [\mathrm{J\,s/kg}] = [\mathrm{m^2/s}]$). Hence, the three-body loss rate can be expressed as

$$L_3(a) = \mathcal{C}(a)\frac{\hbar}{m}a^4, \tag{7.10}$$

with a dimensionless prefactor $\mathcal{C}(a)$ that can also depend on a, but whose value cannot be determined through this analysis. As a result, an increase in the scattering length is noticeable in a significant increase of the corresponding three-body losses, which can be easily traced by observing the atom number while the magnetic field is scanned. Figure 43 depicts the solution of eq. (7.8) for a constant holding time and $\mathcal{C}(a) = \mathcal{C}$, in which the three-body coefficient has been replaced by the scattering length which in turn can be expressed through the magnetic field. The resulting lineshape (solid line) is well described by either a Gaussian (dashed line) or a Lorentzian (not shown), with a minimum at the resonance location. The FWHM of such fitting curves should not be confused with the width ΔB of a Feshbach resonance, which is defined by the value where the scattering length crosses zero. To avoid confusion, the FWHM value is always denoted as σ.

Taking into account the complete physical description, the exact functional form of the loss curve is not entirely trivial. Two points are given here at a glance:

1. Due to the finite collision energy, the resonance does not occur exactly at the atomic asymptote but in the continuum, and the presence of the continuum states can not be neglected. The coupling of evanescent bound states embedded into the continuum leads to an asymmetric line shape known as the Fano profile, that deviates from the ideal symmetric case outlined above.

2. The coefficient $\mathcal{C}(a)$ is a log-periodic function of the scattering length, with two different functional representations depending on the sign of a, therefore giving also an asymmetric contribution. This can be understood as follows: Three body losses are a loss channel involving three atoms, which are usually described by saying that two of them enter a bound molecular state and the third carries away the excess energy. The probability that such a dimer is formed must depend on the bound state distribution of the underlying

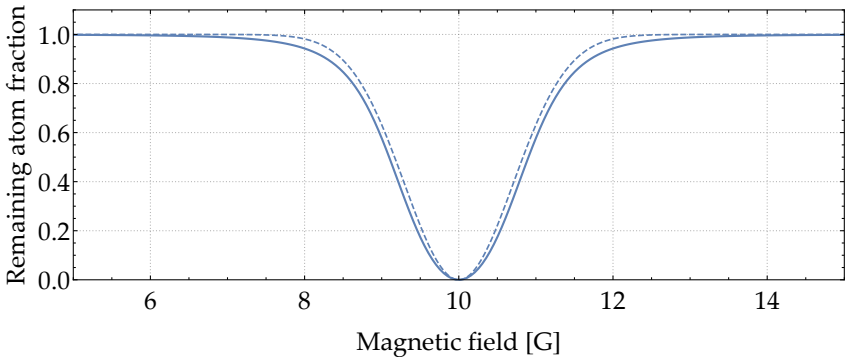

Figure 43: Expected ideal lineshape across a resonance at $B_{res} = 10\,G$ and unity width. The solid line is the solution of the differential equation (7.8) at a constant holding time using the relation (7.10) together with (7.7), which expresses the loss rate coefficient by the magnetic field. The resulting lineshape is not far from a standard Gaussian (dashed line, not a fit).

potential. From the discussion in chapter 2 it is clear that shallow bound states with binding energies $\propto 1/a^2$ exist only at positive scattering length. For negative scattering length, these dimers must therefore either decay into very deeply bound states or form an Efimov trimer state. The physical situation at $a < 0$ and $a > 0$ is described by two entirely different models, which explains their asymmetry with respect to the sign of the scattering length. Typically, periodic dips occur for positive and periodic peaks for negative scattering length. For an in-depth explanation of the origin and extent of Efimov physics, it is referred to [189].

In order to be able to construct the physically correct line profile, one would now have to fold all these effects and implement corresponding fitting parameters. It is clear that this is not a sensible approach when compared to the typical quality and availability of data and the lack of knowledge regarding e.g. the Efimov specifics for this particular mixture. It would further distract from the main purpose of the three-body measurement for this thesis - the detection of Feshbach resonance locations. It is much more advisable to use a function with as few fit parameters as possible. Thus, ultra-cold Feshbach resonances are usually fitted using either gaussian [190, 191] or lorentzian [192, 193] functions, which is also utilized here.

Yet the deviations from the idealized representation in equation (7.10) can be summarized as follows: The position of the resonance determined by three-body measurements will be slightly *detuned* from the real two-body resonance location. The detuning can be considered small when no large asymmetries are observed, but its exact value is difficult to assess and would demand detailed measurements of the Efimov scenario. For an overview, it is referred here to the extensive measurement campaign carried out by the Arlt group [184]. If one is only interested in the exact resonance location, it can be further pinpointed by measuring the binding energy through photoassociation [74].

7.2.2 *Experimental sequence*

After microwave evaporation, the sodium atoms are removed by a resonant light pulse and the potassium cloud is transferred into the optical dipole trap. The quadrupole field is ramped down and subsequently switched to Helmholtz mode. A time of flight measurement of the thermalized cloud gives a temperature of 8.64 µK. In atom loss spectroscopy, it is searched for spectral features as a function of the applied magnetic bias field strength. The magnetic field is ramped in a few milliseconds to a given value B_f and held there for a holding time $t_{hold} \geqslant 100\,\text{ms}$. At the end of each cycle, the cloud is released from the cODT, all magnetic fields are switched off, and the atom number is obtained by performing absorption imaging. As soon as a spectral variation in the atom number is found, the holding time is adjusted in order to obtain a clearly visible drop in the signal without completely depleting the atomic sample. A magnetic field scan using this fixed holding time then recovers the corresponding spectral feature. In order to account for experimental drifts, the magnetic field grid is sampled randomly.

The results are depicted in fig. 44. As a navigational aid, the upper graph shows the scattering length as a function of magnetic field, as calculated by the LENS group [188]. Below that, three cutouts show the measured atom signals in the magnetic field regions where the resonances are expected. Their positions B_i and

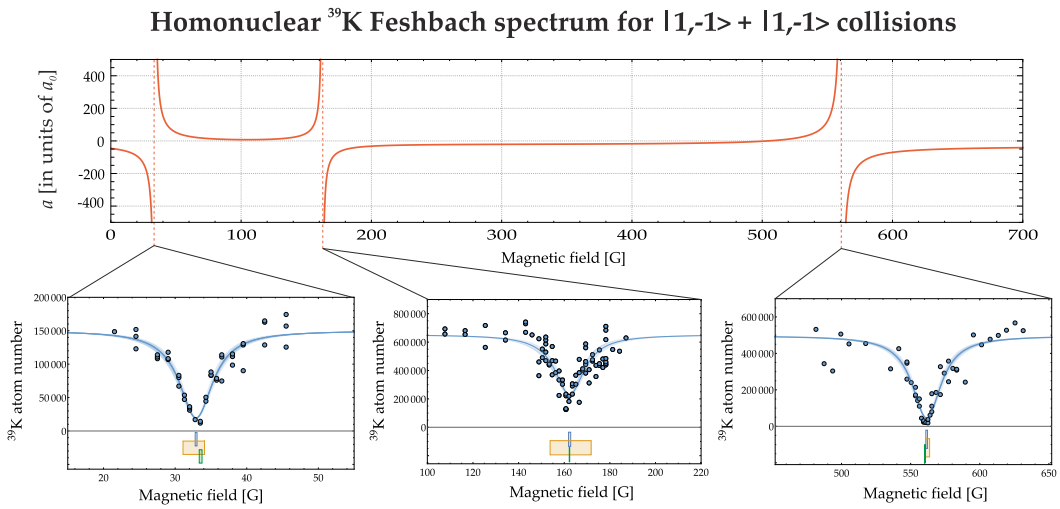

Figure 44: Homonuclear ^{39}K Feshbach spectroscopy. Upper graph: Scattering length for potassium collisions in the spin state under consideration. Lower graph: Atom loss spectroscopy of the three s-wave resonances. A Lorentzian fit of the data set gives the resonance location and FWHM, the shaded region indicates the combined statistical error in resonance location and FWHM. The colored boxes below the resonances denote the standard deviation of this work (blue), [188] (orange) and [194] (green), respectively.

FWHM widths σ_i $(i = 1, 2, 3)$ are extracted using Lorentzian fits. The error with which the resonance position can be determined is then given by the quadratic sum of magnetic-field accuracy and the statistical error obtained out of the fit. The latter is usually the dominant contribution here, but typically far smaller than the characteristic width of each resonance. The obtained resonances, fitted by a symmetric profile, are compared once with a similar measurement campaign done at LENS [188], and further with a second, more detailed campaign also done at LENS [194], in which Efimov structures have been analyzed and a more complex model was applied. The reported resonance locations are given in table 4, and their locations and respective errors are additionally stated graphically through blue, orange and green boxes in fig. 44. Comparison with the values and uncertainties stated in [188], all locations measured here are well inside their error bars. Comparing the data with [194], the measurements are slightly outside each others 1σ error bars. This can be interpreted as the expected error that appears through the simplified fitting model used in this thesis, where Efimov induced asymmetries are not explicitly modeled.

i-th FR	B_i (this work)	σ_i	B_i (D'errico *et al.* [188])	B_i (Roy *et al.* [194])
1	32.9 (0.1)	5.7 (0.7)	32.6 (1.5)	33.64 (0.15)
2	162.4 (0.5)	15.3 (0.5)	162.8 (9)	162.35 (0.18)
3	561.6 (0.6)	25.4 (2.8)	562.2 (1.5)	560.72 (0.2)

Table 4: Experimental magnetic field positions B_i, FWHM widths σ_i and respective errors $(\pm)$ of the located Feshbach resonances, together with the data acquired in [188, 194].

7.3 THEORETICAL MODEL AND EXPECTED SIGNATURES

In this section, the theoretical study is presented that models the diatomic collision process for the spin states under consideration. This will clarify whether scattering phenomena are expected, and if yes, in which magnetic field region one has to search for them. The numerical results are expressed by magnetic field dependent scattering rates, which outlines the form and width of the expected signatures and provides landmarks for the following Feshbach spectroscopy.

The Hamiltonian $\mathcal{H}$ for the diatomic collision is given by

$$\mathcal{H} = T + V(r) + H_{hf}(r) + H_{dd}(r) + H_{Zee}. \tag{7.11}$$

Here, $T = -\hbar^2\nabla^2/(2\mu)$ is the relative kinetic energy operator, whereas $H_{hf,(dd),[Zee]}$ are the hyperfine (magnetic dipole-dipole) [Zeeman] interaction, respectively:

$$H_{hf}(r) = \frac{a_A(r)}{\hbar^2}\left(\boldsymbol{s}_A \cdot \boldsymbol{i}_A\right) + \frac{a_B(r)}{\hbar^2}\left(\boldsymbol{s}_B \cdot \boldsymbol{i}_B\right), \tag{7.12}$$

$$H_{dd}(r) = \frac{2}{3}\lambda(r)\left[3S_z^2 - S^2\right], \tag{7.13}$$

$$H_{Zee}(B) = \frac{\mu_B B}{\hbar}\left[\left(g_s s_z + g_i i_z\right)_A + \left(g_s s_z + g_i i_z\right)_B\right]. \tag{7.14}$$

The hyperfine interaction is mainly given by Fermi contact interaction, and is identical to the atomic hyperfine constant a_i at large distances, $a_i\ r \overset{=}{\rightarrow} \infty = a_i$. At small distances, it acquires radial dependence through electronic distortion of the considered atom by the other one. The dipole-dipole interaction term describes spin-spin interaction through the total molecular spin S and its projection to the molecule fixed axis S_z, whereas the parameter $\lambda(r)$ incorporates the usual r^{-3} dipolar term and second-order spin-orbit interaction. The potential energy $V(r)$ is given by the singlet ($S = 0$) and triplet ($S = 1$) potential energy curves (PECs) and corresponding projectors, $V(r) = P_0 V_0(r) + P_1 V_1(r)$.

To obtain the Feshbach molecular wave function and its binding energy, coupled-channel calculations of the ground state levels are performed. For this, the multi-channel Schroedinger equation is solved numerically by propagating the logarithmic derivative of the multi-channel wave function $\Psi(r)$ in discrete steps with an optimized step mapping function that accounts for the local oscillating frequency of the wave function.[3] The propagation starts at a point r_{start} in a classically forbidden region, $r_{start} < r_{in}$, where r_{in} is the inner turning point in the corresponding classical scattering trajectory. Typically, the value of r_{start} can be set using WKB theory. Through the starting conditions $\Psi_{r_{start}} = 0$ and $\partial_r \Psi_i = 1$, the scattering wave functions will exponentially increase in the classically forbidden region and start oscillating when they reach the allowed region. As outlined in the fundamental chapter, the phase shift is obtained by comparing the resulting scattering solution with asymptotic solutions. In the fundamental single-channel approach, this was done by a simple sine wave, whereas in the general case it is done using spherical Bessel functions to account for centrifugal terms. For a more extensive review of the computational methods employed here, the sources [196, 197, 198, 199, 200] and especially [201] are recommended.

3 Propagating the log-derivative instead of the wave function itself increases the numerical stability.[195].

The predictive quality that this model can accomplish depends on the accuracy to which the above system-dependent parameters (a_i, λ, V_0, V_1) are known. For the diatomic system, hyperfine parameters and electronic and nuclear g factor are tabulated in [107] and the atomic masses in [202]. Crucial for the modeling of cold collisions is the reliability of the $X^1\Sigma^+$and $a^3\Sigma^+$potential energy curves. Very recently, the amount and quality of spectroscopic data for the NaK system has been considerably increased [203, 204], which changes the treatment of the individual terms in the Hamiltonian. The impact of these changes can be traced by comparing the results acquired here with another, independently performed study by Viel and Simoni that was published shortly before [187] but in which evaluation by new data has not been taken into account[4]. Both datasets are briefly reviewed in the following.

The first step consists in the acquisition of the most up-to-date $X^1\Sigma^+$ and $a^3\Sigma^+$ potential energy curves. In most of recent theoretical studies [51, 205, 206], the spectroscopic data from the Tiemann group published in 2008 [207] is employed. Viel and Simoni rely on the same dataset. In their approach, they further replace the hyperfine and spin-spin parameters by the corresponding atomic expressions, setting $a_i(r) \to a_i$ and $\lambda(r) \to \alpha^2 r^{-3}$, where a_i is the hyperfine coupling constant of species i and α is the fine-structure constant.

In a collaborative effort with the Ospelkaus group, the Tiemann group performed a molecular beam study, taking into account the specific needs of a cold collision experiment. In this measurement campaign, the rovibrational ladder of the $a^3\Sigma^+$ potential was investigated up to the last bound state in order to improve the accuracy in the triplet part. The high-resolution hyperfine spectra obtained at various rovibrational levels further allowed to study the radial dependence of the hyperfine and magnetic dipole-dipole parameters $a_i(r)$ and $\lambda(r)$. The details of the used model can be found in the article [203]. As a result, a set of molecular parameters were derived that reproduce the correct radial form of the interaction terms, and these parameters are used here.

Once the potential energy curves have been acquired, they are subsequently modified by using already known Feshbach resonances that provide a complementary, ultra-cold dataset probing the long-range region of the potential. The refinement procedure is done by defining some fitting parameters (e.g. the C_6 coefficient in the long-range dispersion term) and perform coupled-channel calculations. The resulting theoretical resonance locations are then fitted to the experimental data until sufficient convergence is reached. The study of Viel and Simoni employs three s-wave resonances and a p-wave multiplet from the $^{23}Na + ^{40}K$ MIT data set presented in [65]. These resonances are however strongly related to bound states with predominant triplet character (see also fig. 59 in chapter 8 for the magnetic field dependent evaluation of spin expectation values). For the used resonances, the triplet character can be evaluated to be about 98%. It can therefore be expected that the refinement study of Viel and Simoni will give an accurate description of the $a^3\Sigma^+$ triplet potential, while artifacts in the $X^1\Sigma^+$ description might survive. In this study, the PECs were additionaly refined by a recent dataset obtained in the Shanghai group of Pan. This new evaluation gave a significant change for the singlet potential, because their observed resonances (s and d) involve bound states with significant singlet character, with typical spin expectation values of 0.76 [204].

4 The data of [204], in this thesis acquired through priv. communication, was not publicly available at the time the study of Viel and Simoni was conducted.

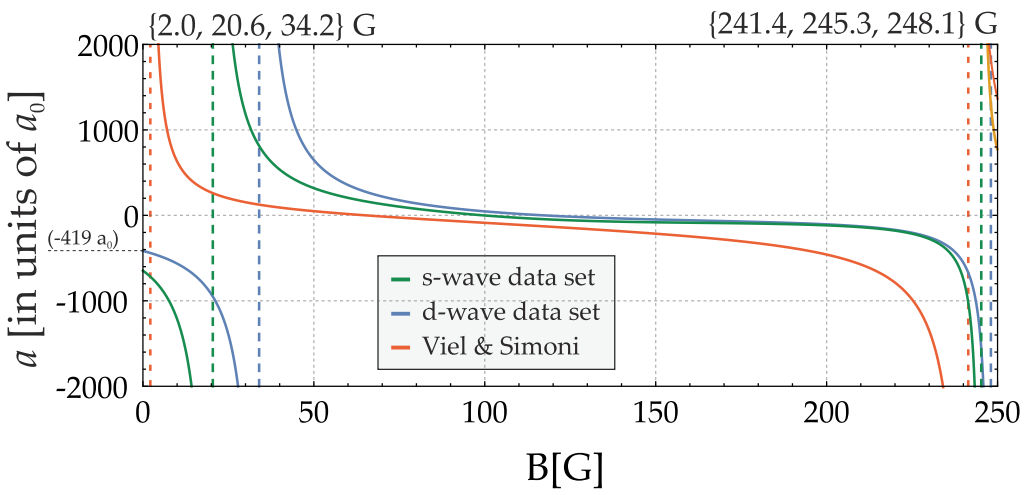

Figure 45: Calculated scattering length as a function of magnetic field using different models and data. Both this and the model used in [187] predict two Feshbach resonances in the magnetic field region below 250 G. The importance of additional d-wave resonances is visible through strong magnetic shifts of the low-field resonance.

Using the refined PECs, isotopic rescaling from ^{23}Na $+^{40}$ K to ^{23}Na $+^{39}$ K is performed by changing the reduced mass μ in T of eq. (7.11) as well as appropriate hyperfine parameters and g-factors for ^{39}K. The corresponding coupled-channel Schroedinger equation is then solved numerically using the methods described earlier. For a given collisional energy, the resonance-dependent collisional properties such as scattering lengths and rates are obtained out of the scattering phase shift. The scattering channels are written as $(|f, m_f\rangle_{Na} |f, m_f\rangle_K |\ell, m_\ell\rangle)$, where f is given by the total angular momentum of the respective atom, ℓ by their relative angular momentum and m_f, m_ℓ denote their projection onto the quantization axis. In the experiment, the pair $|1,-1\rangle_{Na} + |1,-1\rangle_K$ is prepared at temperatures where the $\ell = 0$ contribution will be dominant because of the low temperature. The entrance channel is therefore defined as

$$\alpha = |1,-1\rangle_{Na} |1,-1\rangle_K |0,0\rangle \tag{7.15}$$

Similarly, the Hilbert space is restricted to $\ell = 0$, and therefore does not include the appearance of d-wave resonances or inelastic collisions due to dipole-dipole interaction. The collisional space is then fully defined by $M = m_{Na} + m_K = -2$.

To show the sensibility of the prediction to the model and dataset, the resulting scattering lengths are compared. For this, the calculations in [187] are represented using the formula describing overlapping resonances [208]

$$a(B) = a_{bg} (1 + \varepsilon B) \prod_i^2 \left(1 - \frac{\Delta_i}{B - B_{0,i}}\right). \tag{7.16}$$

Here, $B_{0,i}$ and Δ_i are the resonance location and width for resonance $i\,(= 1, 2)$, whereas a_{bg} is the background scattering length that varies linearly through ε.[5]

5 Inbetween the resonances, the used equation (7.16) shows slight deviations from the numerical result obtained in [187], which is also stated in the corresponding article, where the exact form can be found. As this simplified version does correctly reproduce the widths and locations, it will not have any shortage to the conclusions drawn here.

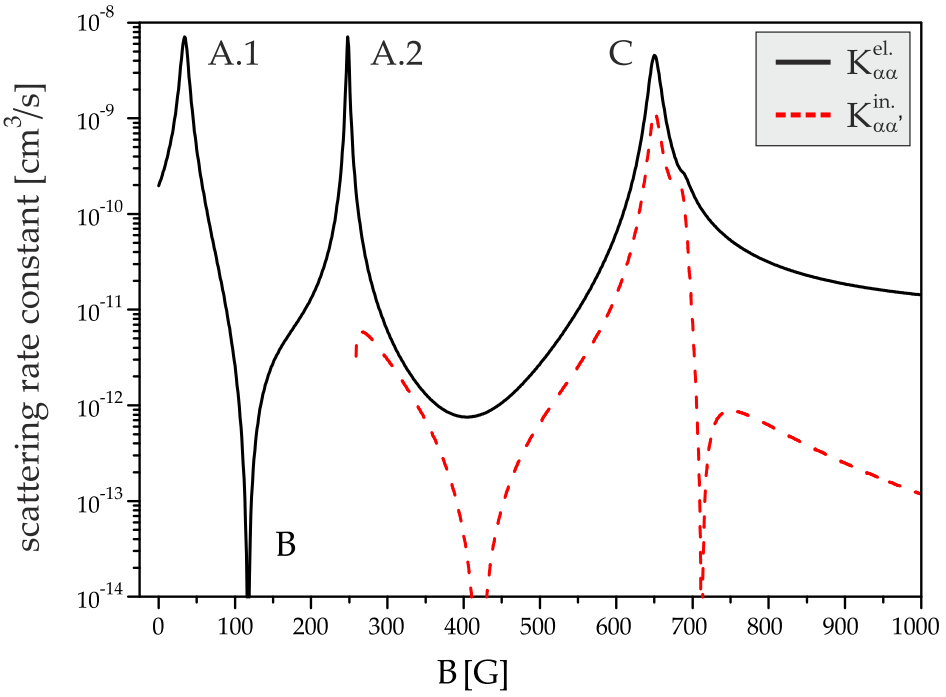

Figure 46: Elastic (straight black) and inelastic (dashed red) two-body scattering rate constants as a function of the magnetic field for the incident channel α. The labels A, B and C denote Feshbach resonances, interaction zeroes and channel mixing, respectively. [4]

The result is shown in fig. 45 for a magnetic field region from 0 to 250 G. The calculations in this study have been done once with the pure MIT set and once by taking into account the additional d-wave data. The model used by Viel & Simoni and in this work agree on a qualitative level, predicting two Feshbach resonances, while quantitative discrepancies persist. This is apparent for the low-field resonance that differs by about 30 G from the one predicted in [187]. It can be seen that the refinement procedure from the work of [204] shifts the calculated low-field resonance significantly to higher fields. Measuring the exact location of this resonance will therefore be imperative, as it gives direct insight into the singlet component. It further dictates the exact value of the interspecies scattering length a_{NaK} in absence of magnetic fields. From the calculations using all refinements, $a_{NaK,|\alpha\rangle}(B = 0) = -416\, a_0$ for $|\alpha\rangle = |1,-1\rangle_{Na}\,|1,-1\rangle_{K}\,|0,0\rangle$, where a_0 is the Bohr radius. This appears to be compatible with the three-body loss coefficients that were extracted at the end of the last chapter.

To provide navigational landmarks for the later experiment, the collisional effects are expressed by the elastic and inelastic two-body scattering rate constants $K^{el.}_{\alpha\alpha}(B)$ and $K^{in.}_{\alpha\alpha'}(B)$, respectively. These are shown in fig. 46 in a magnetic field region from 0 to 1000 G and a collisional energy of 1 μK. At least three different signatures can be identified, which are denotes as A, B and C for convenience: For the incoming spin state combination, Feshbach resonances (A.1 & A.2) are expected at 34.2 G and 248.1 G, as shown by the local maxima of the elastic two-body scattering. Similarly, a zero crossing (B) of the scattering length exists at 117.3 G. Finally, at about 259 G, another channel of the $\mathcal{M} = -2$ space, namely $m_{Na} = 0$ and $m_K = -2$, opens up by crossing the threshold $E_{|\alpha\rangle}$. At magnetic fields larger than 259 G, transitions to the now open channel give rise to the inelastic part of the incident channel, displaying

a peak (C) at 651 G, with a shoulder at 690 G. A more detailed discussion of the last feature is given in section 7.4.3. As all these signatures will evoke or impede losses in the mixture, all of them can be located using atom loss spectroscopy.

7.4 HETERONUCLEAR FESHBACH SPECTROSCOPY OF $|1,-1>_{na} + |1,-1>_{k}$

This section presents the measurements of the previously unknown heteronuclear Feshbach spectrum. In its essence, the experimental sequence is similar to the homonuclear case presented earlier, but preceded by a preparation phase to account for the large three-body losses at zero magnetic field.

Both species are transferred simultaneously into the cODT. To avoid large density-dependent losses, loading takes place at a temperature of about 10 μK. After the coils have been switched over to Helmholtz operation, the bias field is first ramped up in 5 ms to a magnetic field value of $B_0 \approx 100$ G. This magnetic field window serves as a safe spot for the dual-species operation, as neither the inter- nor the intraspecies interactions are disruptive in this region (see also fig. 44 and 46). A rigorous discussion of this region follows in section 7.4.2. The magnetic field value is chosen such that thermalization through elastic collisions is still provided on a reasonable time scale. Following this, the dipole trap beam intensities are subsequently reduced, forcing evaporation of the atomic clouds. After the system has thermalized, time of flight measurements give a typical temperature of $T = 2.3$ μK for both species.

Through their mutual loss increase, the fluctuations of both species atom numbers are coupled with each other. Therefore, the atom numbers are chosen such that this stage of the experiment yields an atom number imbalanced mixture ($N_{major}/N_{minor} \approx 10$). This is achieved through adjustment of the individual MOT loading times. The atom numbers for each species are tuned in a range of 10^4 to 10^6 depending on the atom number imbalance that one wants to prepare.

After this initialization phase, Feshbach spectroscopy is performed similar to the homonuclear case by searching for spectral features as a function of the magnetic

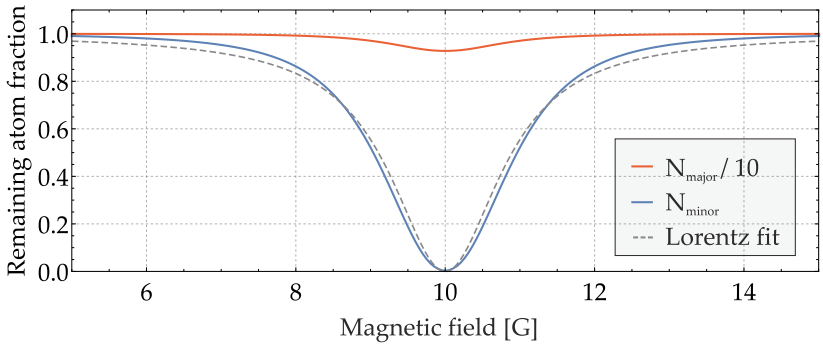

Figure 47: Expected ideal lineshape across a heteronuclear Feshbach resonance at $B_{res} = 10$ G, unit width and atom number ratio $(N_{major}/N_{minor}) = 10$. Solid blue and red line are the solutions to the coupled differential equations governing the interspecies loss dynamics at a constant holding time. The Feshbach resonance is visible in a strong drop in the minority component (blue curve), with the resulting lineshape being similar to a Lorentzian (dashed line). The majority component (red curve) shows only a slight decrease.

bias field strength. Through the atom number imbalance, the minority cloud is used as a probe while the majority component serves as a bath. The lineshape of the minority cloud will be different from the homonuclear case, which is pictured in fig. 47. For a holding time in which the minority component will show sizable losses, the majority atom number will be barely affected by the resonance. By approximating $dN_{Major}/dt \approx 0$ (hence $n_{Major}(r,t) = n_{Major}(r)$), the coupled loss rate equations reduce to minority atom number loss dynamics. It is further assumed that temperature increase is not significant and that background collisions and homonuclear three-body losses appear on much larger timescales. Under all these approximations, the time evolution of the minority atom loss simplifies to

$$\frac{dN_{Min}(t)}{dt} \propto -\frac{1}{3} L_3^{(Maj,Maj,Min)} \xi_{(Maj,Maj,Min)} N_{Maj}^2 N_{Min}(t) \tag{7.17}$$

$$-\frac{2}{3} L_3^{(Maj,Min,Min)} \xi_{(Maj,Min,Min)} N_{Maj} N_{Min}^2(t) \tag{7.18}$$

$$\approx -\frac{1}{\tau_{Min.}} N_{Min}(t) \tag{7.19}$$

where the numerical factors ξ account for the geometric mismatch of the two cloud densities in the trap. The first term can be expected to dominate as it depends quadratically on the majority component. By neglecting the second term, the minority atom number dynamics can be described by a simple exponential decay. In these atom number imbalanced systems, it is therefore sensible to define an effective $1/e$ lifetime $\tau_{Min.}$ of the minority component that gives a general assessment of the loss strength of the spectroscopied loss regions. The resulting loss profile in fig. 47 then resembles more a Lorentzian than a Gaussian distribution, even though both fitting functions will give satisfying results.

Starting from the safe spot B_0, the bias field is ramped in a few milliseconds to a variable value B_f and held there for variable holding times $t_{hold} \geqslant 100\,ms$. At the end of each cycle, all magnetic fields are switched off and the clouds are released from the cODT. Atom numbers are obtained by performing absorption imaging, where the majority is measured *in-situ* and the minority in time of flight. As in the homonuclear measurement, the magnetic field values are sampled in a pseudo-random[6] fashion.

7.4.1 *Heteronuclear Feshbach resonances*

The expected heteronuclear signatures are the ones outlined in the theoretical section 7.3. They are presented piece by piece, with the regular Feshbach resonances first. Figure 48 shows the recorded atom losses corresponding to signature A.1 (a) and A.2 (b). The low-field resonance A.1 around 30 G was found to be strongly interwoven with one of the homonuclear ^{39}K resonances measured earlier. To discern the overlapping resonances, it was used that the homo- and heteronuclear resonance exhibit strongly different widths. The homonuclear resonance is spectrally sharp with a comparatively small width of $\sigma_K = 5.7\,G$, where σ denotes the FWHM value of the loss signal. In the case of heteronuclear collisions, the calculated large negative background scattering length is equivalent to the existence of a virtual state

6 Although a true randomizing option is implemented in the experimental control, the random sampling points are often manually set. Because human entities are rather bad at randomizing samples [209], there will be some sort of Markovianity left, but this is only of academic interest.

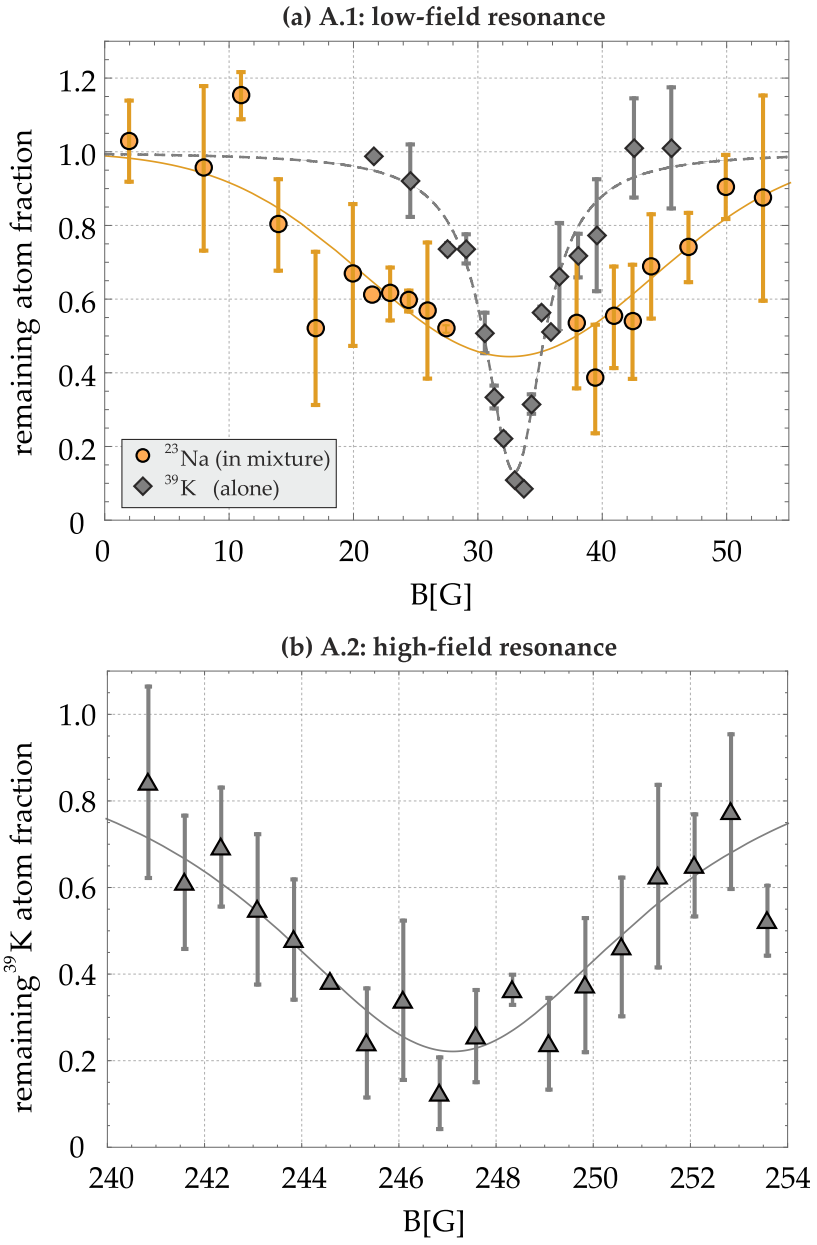

Figure 48: Remaining fraction of atoms as a function of the applied magnetic field strength B. The Feshbach resonances A.1 and A.2. are visible due to drops in the atom number. (a) ^{39}K Atom number loss in single-species operation (gray diamonds) and ^{23}Na losses in dual-species operation (yellow dots) unveil two overlayed resonances. The fitted function (dashed line) determines the homonuclear resonance. A Gaussian fit (solid line) to the wings of the ^{23}Na minority signal determines the heteronuclear resonance location. The absolute atom numbers are 3×10^4 (^{23}Na) and 1.5×10^5 (^{39}K). (b) The high-field resonance A.2, measured using ^{39}K as the minority. The absolute atom number is 2.6×10^5.

right above threshold. Large continuum coupling persists in this channel, which will in turn broaden the resonance strongly ($\sigma_{A.1} = 27.3\,\mathrm{G}$). The heteronuclear signature is recorded using ^{23}Na as the minority probe. By numerically solving the combined loss dynamics using the simple mapping of the magnetically tunable scattering length onto the L_3 coefficient, the following scenario is expected: As the

resonance pair is approached, the heteronuclear resonance is first interacted upon through its larger width, and the line profiles are identical to the ones presented in fig. 47. As the homonuclear resonance region is reached, a steep dip appears in the ^{39}K majority, which in turn strongly diminishes the main loss term for the ^{23}Na minority. This will result in a decrease of minority losses in the vicinity of the resonance pair. The predicted simulation results match the ones obtained in the experiment. In principle it is possible to perform a bimodal fit to the resulting overlapping feature. Inspired by the treatment of bimodal density distributions found in BECs, the data set was instead divided into regions and only the flanks that clearly belonged to the heteronuclear resonance (as they are not visible on the homonuclear ^{39}K signal) were fitted. Out of simulation and measurements, a region spanning $\approx 2\sigma_K$ is determined in which the heteronuclear signature will be significantly affected by the ^{39}K resonance. This region is then filtered out for the fitting procedure of the A.1 resonance location. Even without the central part of the feature, it can be located with a statistical uncertainty of 0.8 G to be at 32.5 G. This is mainly because for a Gaussian fit, amplitude uncertainties are more strongly correlated to uncertainties in the width rather than uncertainties in the location of the extremal point.

No such complication exists for the high-field resonance A.2, which is measured to be at 247.1 G $\pm$ 0.2 G using ^{39}K as the minority probe. Both locations are in excellent agreement with the previous theoretical predictions (see fig. 46), with small deviations on the order of 1 G that reflect both the uncertainty in the potential energy curves and the expected but unknown Efimov detuning.

7.4.2 *The interaction zero crossing*

The value at which the interspecies scattering turns from repulsive to attractive (Zero point crossing, signature B in 46) is of particular interest for the dual-species operation, as it provides the magnetic field region in which atom losses are expected to be low. The naive dimensional analysis would indeed predict the three-body losses to be minimal (even zero) in this region. Yet identifying a minimum of the three-body loss rate with a zero crossing of the scattering length is not necessarily correct. Indeed, several situations where these do not coincide have been reported in the literature, e.g. for Li and Cs systems [210, 211]. Therefore a "normal" three-body loss measurement that was used for the homo- and heteronuclear resonances can give misleading results in this case. To localize the zero point crossing, a mechanism had to be utilized that traces two-body losses directly.

For this, the two-body losses that appear during optical evaporation are exploited. The reasoning is sketched in fig. 49. In standard optical evaporation (a), a certain amount of particles is removed from the trap. For the optical trapping potential U_i, where i denotes the species, one finds $U_K \approx 2.51\ U_{Na}$, i.e. a preferable ejection of ^{23}Na as the cODT intensities are reduced. Sympathetic cooling of ^{39}K by ^{23}Na will lead to an enhancement of ^{23}Na losses during rethermalization (b). In the experiment, a balanced atom number is prepared at $\sim$ 10 μK. After lowering the optical potential depth in 1.5 s to a value which gives 2 μK in single-species ^{23}Na operation, the sodium atom number is recorded after a thermalization time. The loss enhancement will be reduced and ultimately disabled as the interspecies scattering rate approaches zero (c). This behaviour is reproduced in the experiment by observing a signal revival in the sodium atom number as shown in fig. 50.

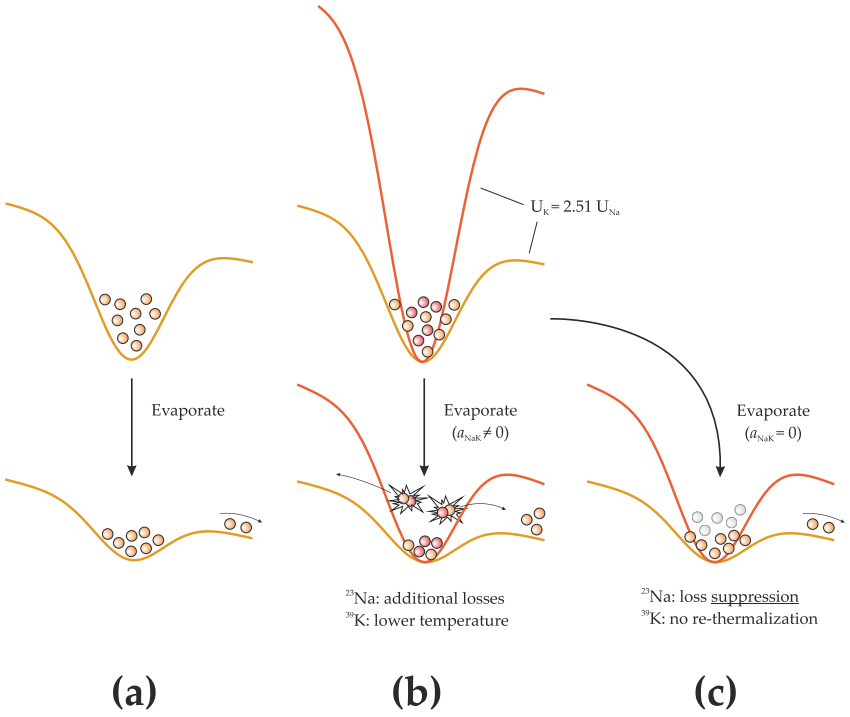

Figure 49: Sketch of the thermalization measurement method. (a) Evaporative cooling of ^{23}Na in an ODT. A certain amount of particles is lost. (b) Evaporative cooling in the mixture and $a_{NaK} \neq 0$. Through the larger trap depth, ^{39}K is barely evaporated. Interspecies collisions that sympathetically cool ^{39}K will lead to an enhancement of losses in the ^{23}Na cloud. (c) Evaporative cooling in the mixture and $a_{NaK} = 0$. As the mixture does not interact, the loss enhancement is suppressed.

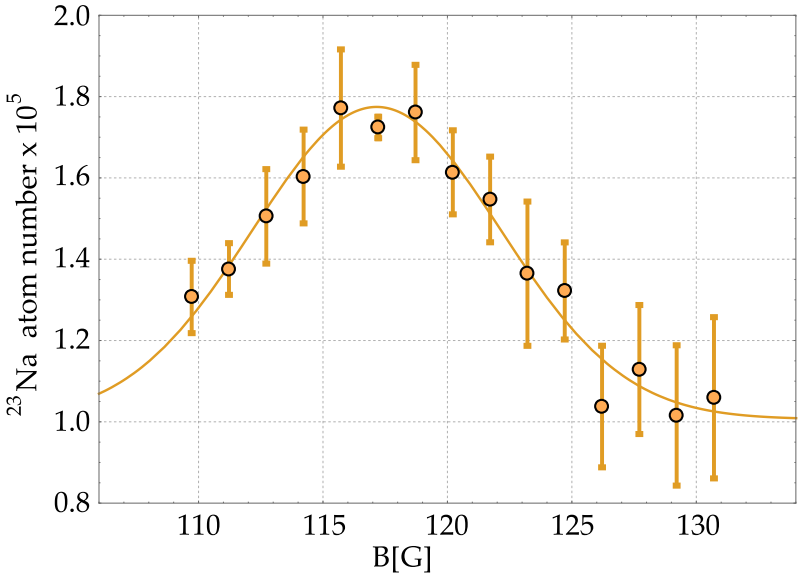

Figure 50: ^{23}Na atom number as a function of the magnetic field strength B in a forced evaporation sequence. A revival of the ^{23}Na signal at ~ 117 G indicates the reduction of this loss enhancement as the interspecies scattering rate goes to zero. A Gaussian fit (solid line) is used to extract its location. [4]

By fitting a phenomenological Gaussian to the observed signal increase, the zero-crossing is determined to be located at $117.2\,G \pm 0.2\,G$, in agreement with the predicted value of 117 G.

7.4.3 *Channel mixing resonance*

The last remaining signature, previously denoted as C in fig. 46, is the result of channel mixing between the states spanning the $\mathcal{M} = -2$ manifold.

Figure 51 depicts the energy levels of the diatomic system for $\mathcal{M} = -2$ as a function of the magnetic field strength B. The atomic asymptote is given by the incident channel α, with its energy dependence through the magnetic moment leveled to zero. For lucidity, all states with the exception of $|\alpha\rangle$ and $|\beta\rangle = |f = 1, m_f = 0\rangle_{Na} + |f = 2, m_f = -2\rangle_K$ have been grayed out. At a magnetic field of 259 G, β becomes an open channel by crossing the collisional threshold of $|\alpha\rangle$. Starting from that field, $|\alpha\rangle$ will be embedded in the continuum of $|\beta\rangle$, and inelastic collisions $|\alpha\rangle \rightarrow |\beta\rangle$ become energetically allowed. This explains the sudden appearance of the inelastic scattering rate constant in fig. 46. Similarly, from this magnetic field on, the scattering length has to be described by a complex number, where the imaginary part reflects again an inelastic contribution. The effect of inelastic losses becomes sizable in the magnetic field region between 650 and 700 G, when two molecular states cross $|\alpha\rangle$ and resonantly enhance the (elastic and inelastic) scattering rate constant. Any collisional decay to $|\beta\rangle$ is accompanied by a kinetic energy gain $E_{\alpha\beta} = E_\alpha(B) - E_\beta(B)$ of the atom pair. In the region $B > 600\,G$, $E_{\alpha\beta} > 9.7\,mK$ strongly exceeds the optical confinement, and the atom pair leaves the trap. The channel mixing process can therefore be directly probed using atom loss spectroscopy.

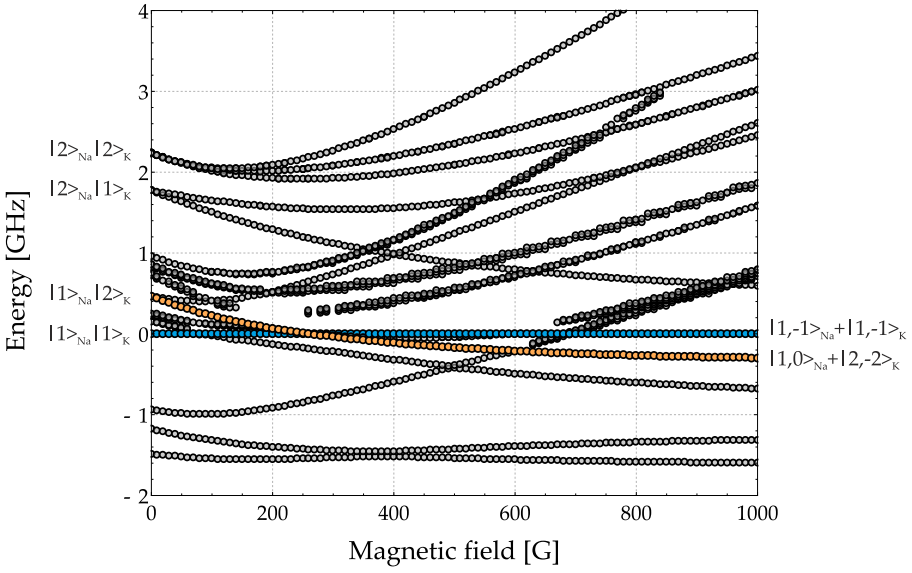

Figure 51: Energy levels of the diatomic system in the collisional space $\mathcal{M} = -2$ as a function of magnetic field strength. At 259 G, the state combination $|1,0\rangle_{Na} + |2,-2\rangle_K$ (orange dots) becomes an open channel by crossing the atomic asymptote (blue dots).

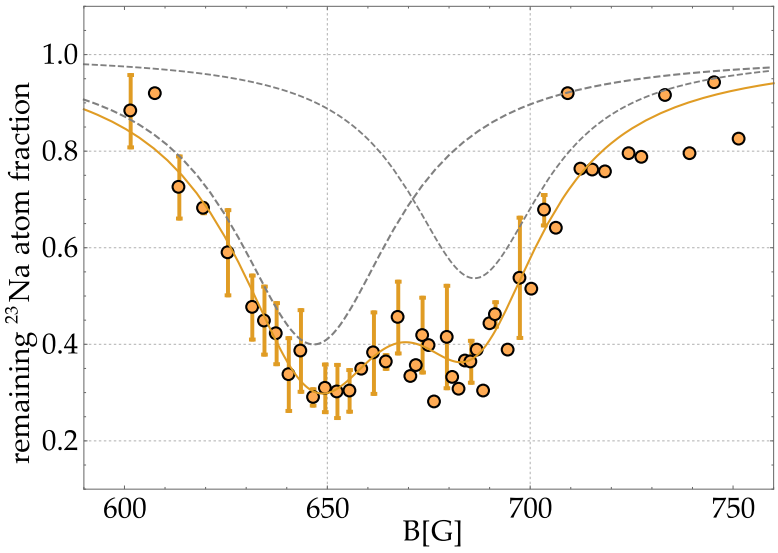

Figure 52: Remaining fraction of ^{23}Na atoms as a function of the applied magnetic field strength B. Two overlapping loss features are discerned, which are identified as signature (C) from fig. 46. A combined fit (straight line) is given together with two individual Lorentzian loss profiles (dashed lines). The absolute atom number is 3.7×10^5 ^{23}Na atoms [4].

As losses in this resonance region will be primarily mediated by two-body instead of three-body collisions, dynamics on faster timescales are expected. The samples are held at a given magnetic field for $t_{hold} \leqslant 10\,\text{ms}$, much shorter than the holding times for signatures A.1 and A.2. Almost complete depletion of the atomic signal is observed, with a 1/e lifetime of 4 ms at 650 G. In unison with the calculations presented in section 7.3, the strongly shortened effective lifetime suggests two-body collisions as the driving loss mechanism. This assumption can be further tested by examining the atom number decay at different densities or temperatures [212], which is not investigated here. The observed double feature corresponds to the predicted overlap of two Feshbach resonances, as can be seen by a secondary structure (or "shoulder") in the inelastic contribution in Fig. 46). Their individual positions are extracted by a joint fit as shown in fig. 52.

In total, the s-wave resonances A.1 and A.2, the zero crossing B and the two closely spaced resonances C have been experimentally located. Their positions and widths, together with the calculations of this work and recent predictions of [187] are summarized in table 5.

7.5 QUANTUM DEGENERATE MIXTURES

Based on the recorded Feshbach spectrum, it is now possible to discuss magnetic field regions suitable for producing quantum degenerate atomic samples of two species. For this purpose, a domain is searched for in which either both species can be individually cooled and display a non-destructive interspecies behaviour, or in which one of the samples can efficiently cool the other one sympathetically.

Feature	$B_{Exp.}$[G]	$\sigma_{Exp.}$[G]	$B_{Th.}$[G]	$B_{Th.}$[G][187]	$\tau_{min.}$ [order of mag.]
A.1	32.5 (0.8)	27.3 (2.9)	34.2	2.0	~ 100 ms
A.2	247.1 (0.2)	9.5 (3.0)	248.1	241.4	
B	117.2 (0.2)	11.7 (1.1)	117.	75.7	~ 10 s
C	646.6 (1.5)	48.6 (5.6)	651.5	-	~ 10 ms
	686.2 (1.5)	40.9 (5.9)	686.7	-	

Table 5: Experimental magnetic field positions $B_{Exp.}$, FWHM widths $\sigma_{Exp.}$ and respective statistical standard errors $(\pm)$ together with the theoretically calculated positions $B_{Th.}$ of this thesis and a comparison with recent work [187] Each type of signature has a different characteristic effective minority lifetime. The order of magnitude (when sampling with the same parameter set) is given.

7.5.1 *Interaction domains*

Figure 53 shows the interspecies scattering length from 0 to 700 G based on the results obtained in the last section, together with the intraspecies scattering taken from [213] for ^{23}Na and [188, 214] for ^{39}K. Due to the magnetic field independent interaction of ^{23}Na in this magnetic field window, it can be condensed at arbitrary bias field values, and its scattering length $a_{Na} = 52\,a_0$ will only contribute to a positive interaction offset on the dual-species operation. For ^{39}K on the other hand, the appearance and relative shape of its Feshbach resonances constrains the magnetic field of operation to a magnetic field valley between 32.6 G and 162.8 G and to the immediate left-side slope of the 562.2 G resonance. Outside of these regions, the ^{39}K interaction will be negative, leading to mean-field collapse of the condensate wave function. The further discussion concentrates on the valley region, where the ^{39}K scattering length is strictly positive and widely tunable between $10\,a_0$ and ∞. Due to the location of A.1 at the valley border and the appearance of the zero point scattering near the valley center, the interspecies scattering monotonically decreases in the discussed region, and can be set to values $-62.1\,a_0 < a_{NaK} \leqslant \infty$. This freedom regarding sign and magnitude of intra- as well as interspecies interaction marks the valley as a rich source for different two-species scenarios, including miscibility, phase separation, collapse and droplet formation. The figure of merit for the identification of different interaction domains is [215, 216, 217]

$$\delta g(B) = \left(g_{NaK}^2(B)/\left(g_{Na} \times g_K(B)\right)\right) - 1, \tag{7.20}$$

where $g_i(B) = ((2\pi\hbar^2 a_i)/\mu_i)$ denotes the interaction parameter for the intra- and interspecies interaction respectively, $\hbar$ being the reduced Planck constant and μ_i the respective reduced mass. A condensed mixture is said to be miscible if $\delta g < 0$, whereas $\delta g > 0$ implies either immiscibility or mean-field collapse, depending on the sign of g_{NaK}.

Figure 54 shows $\delta g(B)$ in the aforementioned magnetic field valley, where four different interaction domains are identified. In the region $B_1 : B < 109.1$ G, the interspecies interaction outweighs the intraspecies one, such that $\delta g > 0$, when the atomic wave functions will be phase separated, rendering sympathetic cooling of ^{39}K inefficient. This changes in the region around the zero point crossing, B_2 :

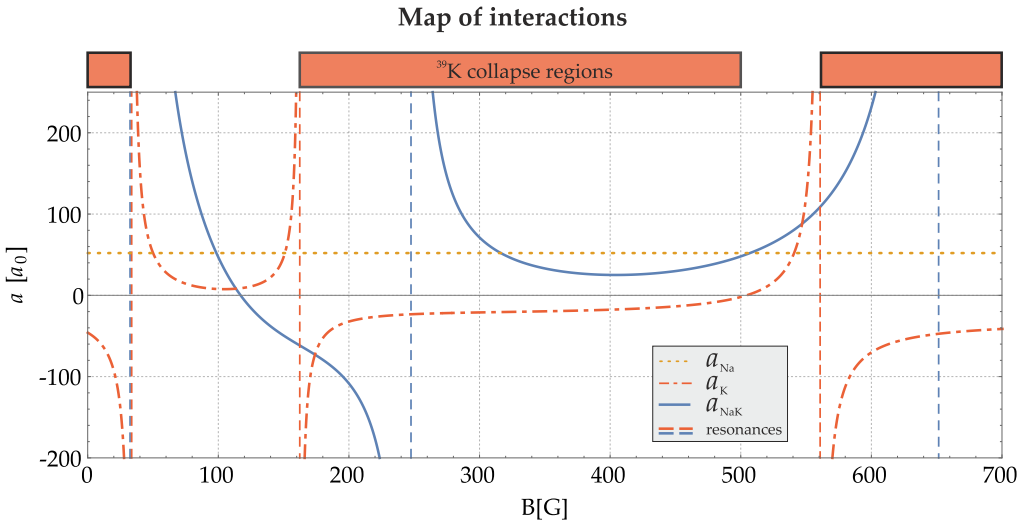

Figure 53: Inter- and intraspecies scattering lengths a_{NaK}, a_{Na} and a_K as a function of magnetic field strength. The positions of ^{39}K and ^{23}Na^{39}K resonances are indicated by dashed vertical lines. The regions in which ^{39}K BECs experience single-species mean-field collapse are marked.

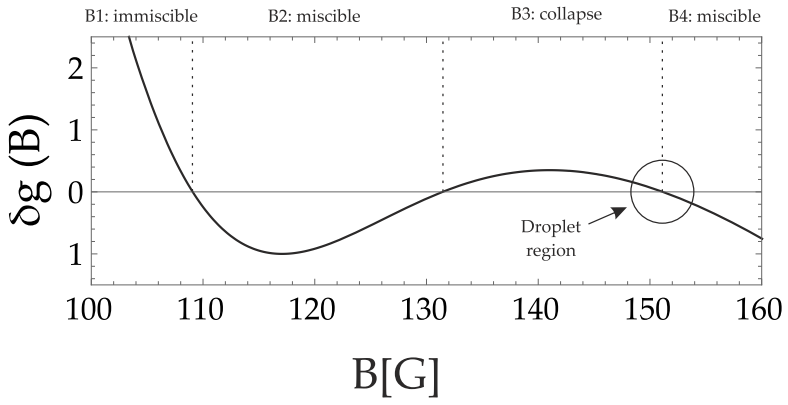

Figure 54: Miscibility parameter δg as a function of magnetic field. Three sign changes exist in the magnetic field valley outlined by the two low-field ^{39}K resonances, that can be assigned to miscible, immiscible and collapse regions, respectively. At the crossover of B_3 and B_4, beyond-mean-field effects will lead to the formation of heteronuclear quantum droplets.

$109.1\,\mathrm{G} < B < 131.5\,\mathrm{G}$. The clouds are miscible in this domain, but due to the small values of a_K and a_{NaK}, ^{39}K displays unfavorable thermalization properties and cannot be efficiently cooled to quantum degeneracy. At $B_3 : 131.5\,\mathrm{G} < B < 151.1\,\mathrm{G}$, both intra- and interspecies interactions are sizable, with $\delta g > 0$. In this region, two clouds with high density overlap will not be mean-field stable, leading to collapse of the mixture. At the borders of the collapse region B_3, the mean-field terms cancel each other out, and beyond mean-field effects can lead to the formation of self-stabilizing droplets [96]. Finally, at $B_4 : 151.1\,\mathrm{G} < B < 162.8\,\mathrm{G}$, δg becomes again negative as ^{39}K is approaching its second resonance. In this region the individual intraspecies scattering lengths are large enough allowing for efficient evaporation, whereas a_{NaK} will be small and negative, ensuring miscibility of the cloud. The

region B_4 can therefore be highlighted as most suited for the purpose of condensing both clouds.

The exactness of eq. (7.20) relies on equal densities, and therefore neither accounts for density imbalances nor includes geometric effects due to the unequal optical trap depths and gravity [218]. The mass imbalance $m_K/m_{Na} \approx 1.7$ partially balances the stronger confinement of ^{39}K, giving relative trap frequencies $\omega_K/\omega_{Na} \approx 1.217$. This leads to a differential gravitational sag of $\delta z_0(\omega_z) = (3.19/\omega_z^2)\,\mathrm{Hz}^2\mathrm{m}$, decreasing the overlap region and shifting the boundaries of the magnetic field domains $B_{1,2,3,4}$. In particular, B_4 will extend to lower magnetic fields, and the $B_3 - B_4$ boundary will smear out.

A note on single-shot imaging processing

To verify that both clouds are condensed in the same experimental cycle, they have to be subsequently imaged in the same time of flight. The CCD sensor architecture uses frame transfer in order to enable the CCD camera to rapidly switch between exposure and readout. In this configuration, only a part of the CCD chip is illuminated and parallel chip arrays are used to store the acquired data. Then a set of four pictures is taken, first two "atomic" pictures that each contains one atomic species, with a delay of 3 ms inbetween. These are followed by two reference pictures that are taken after both clouds have left the acquisition region.

Most critically, condensate signatures such as the bimodal distribution have to be visible in both pictures of a single shot. In this experiment, early attempts to achieve two condensates faced an unfavorable signal-to-noise ratio. The picture storage region of the CCD had been blackened using a custom machined slit aperture, yet the way it was implemented gave rise to diffraction patterns on the illuminated part of the chip. These pattern may change slightly between atomic and reference image, leading to stripes in the calculated density distribution. To separate the desired information from parasitic bias and noise, a wide variety of image processing methods such as Fourier filtering is described in the literature [177, 219, 220, 221]. In this thesis, the additional noise is reduced using a principal-component analysis (PCA). This method is nowadays widely used in the field of data mining and face recognition [222, 223], but has been also applied in cold atom experiments in the past [224, 225]. In these cold atom systems, the PCA was applied onto the obtained density distributions. In this thesis, the PCA operates only on the reference picture, with the intrinsic advantage that the atomic picture and therefore the actual atom distribution will be not altered [226].

The reasoning behind PCA is that for the investigated cold atom system, the dimensionality of the *data* space is much larger than the dimensionality of the *feature* space that one is interested in. Therefore, even though an image acquired on a 100×100 CCD chip spans a vector space of dimension 10^4, a much smaller vector subspace can be defined that is able to describe the whole image up to a small error. This vector subspace is efficiently spanned by the principal components of the system.

Two regions of interest (ROI) are defined: The atom ROI contains the atomic density distribution, whereas the ref. ROI is another illuminated part that does not overlap with the atom ROI. A database of ~ 200 reference images is acquired. This set of reference images is used to build a linear model that can estimate the illumination at the atom ROI out of the illumination of the ref. ROI. A singular value

decomposition on the ref. ROI allows to express the picture data as a superposition of the 200 principal components, which contain all relevant information of the picture. Using the same transformation on the atom ROI results in a constructed estimate of the reference image in the atom ROI. The resulting fringe reduction helped tremendously for the initial verification of simultaneous degeneracy. It can be of similar use when intra-trap structures such as quantum droplets are investigated, such as recently done by the Pfau group [227].

7.5.2 *Dual-species degeneracy*

Two stable condensates are realized in this setup by optical evaporation in the magnetic field region B_4, typically at $B_0 = 153\,\mathrm{G}$. Here, all three scattering lengths are of similar magnitude,

$$a_{\mathrm{Na,K,NaK}} = \{52, 65.4, -52.6\}\ a_0, \tag{7.21}$$

which leads to similar thermalization rates. Following a quick magnetic field ramp to B_0, dual-species evaporation is performed by consecutive linear intensity ramps of the crossed optical dipole trap. Both species are then released from the optical traps and the bias field is subsequently switched off. The whole experimental sequence is depicted in fig. 55.

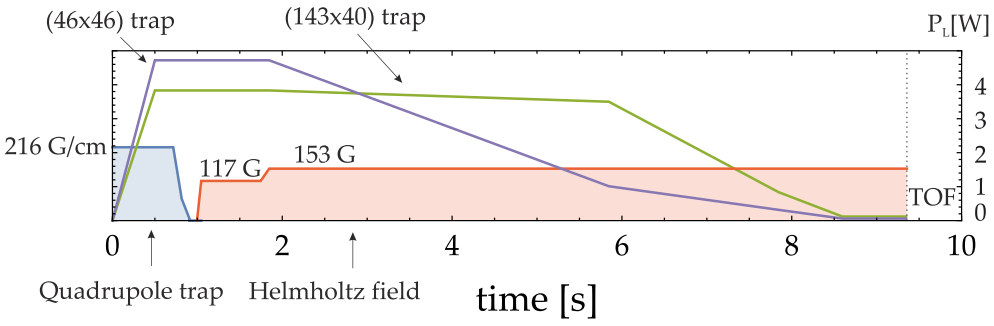

Figure 55: Exemplary experimental sequence to obtain quantum degenerate mixtures.

Interestingly, probing the magnetic field border between the regions B_3 and B_4 showed that stable quantum degenerate mixtures can be created also at magnetic fields $\tilde{B} < B_4$. As an example, this is shown below for $\tilde{B} = 150.4\,\mathrm{G}$. In particular, $\delta g(\tilde{B}) = 0.047$, when eq. (7.20) dictates mean-field collapse as $\tilde{B} \in B_3$. The cooling procedure is operated as depicted in 55. After optical evaporation, the final trap frequencies are $\omega_{x,y,z,(\mathrm{Na})} = 2\pi\,(36, 129, 157)\,\mathrm{Hz}$. Figure 56 shows the resulting density distributions for a typical experimental run as well as the one-dimensional integrated optical densities. A bimodal fit discerns the condensed (N_c) and thermal part (N_T) of the clouds. For the used parameters, condensed fractions of $N_{c,\mathrm{Na}} = 42\,\%$ and $N_{c,K} = 17\,\%$ with a total atom number $N_c + N_T$ of 4×10^4 for ^{23}Na and 7×10^4 for ^{39}K are obtained.

As outlined before, the magnetic field regions B_3 and B_4 given by eq. (7.20) will shift due to the reduced cloud overlap. It is therefore perceivable that depending on the density distribution of both clouds, this geometric effect can ensure stability at the chosen field $\tilde{B}$. Alternatively, it was pointed out that at the border of these regions, beyond-mean-field effects will lead to the formation of quantum droplets.

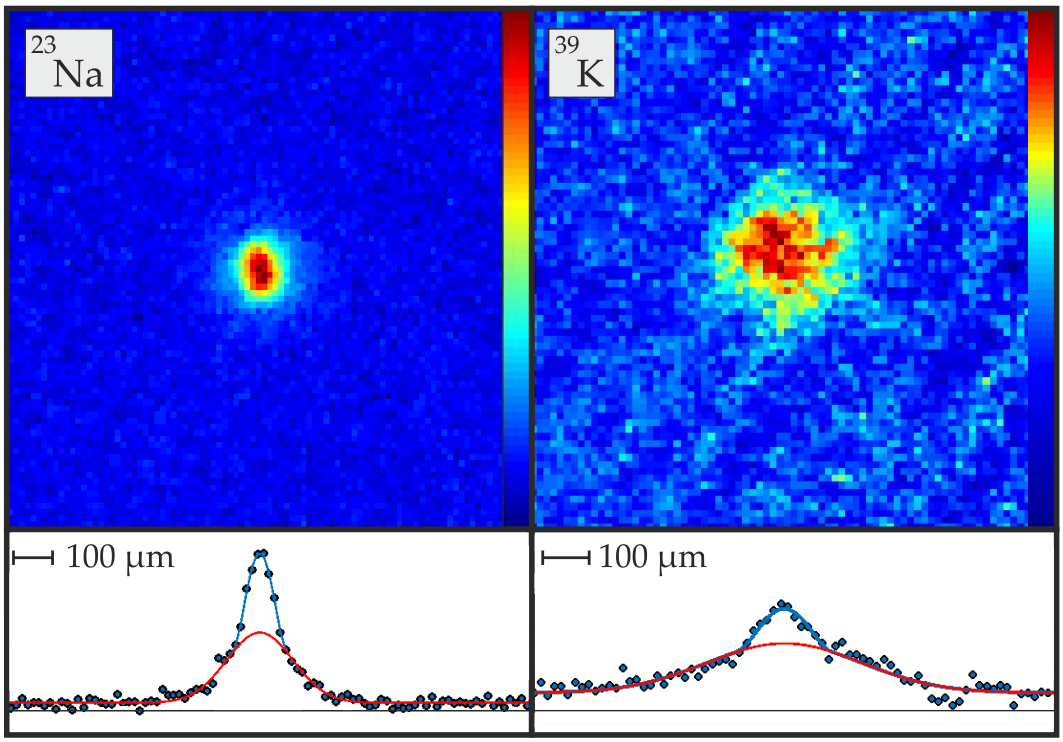

Figure 56: Top: Typical absorption images of ^{23}Na (left) and ^{39}K (right) after a ballistic expansion time of 11.3 ms (^{23}Na) and 14.4 ms (^{23}K), respectively. Optical evaporation was performed at a magnetic field $\tilde{B} = 150.4$ G. Bottom: Integrated column densities of the top pictures (blue dots) together with bimodal fits of the thermal (red line) and condensed parts (blue line), respectively [4].

Both effects have been investigated. The possibility of forming heteronuclear quantum droplets in NaK is currently investigated theoretically in the Santos group. Figure 57 shows the calculated ground state density distribution obtained out of a two-component coupled Gross-Pitaevskii description that includes the Lee-Huang-Yang correction. The simulations have been performed using the identical parameter set (atom number, trap frequency, scattering lengths) that lead to the experimental shot depicted in fig. 56. At the used magnetic field $\tilde{B}$, a droplet solution emerges in the center of the trap. In this region, the mean-field terms cancel each other out, which locks the atom number density ratio

$$\frac{n_K}{n_{Na}} \stackrel{!}{=} \sqrt{\frac{g_{Na}}{g_K}}. \tag{7.22}$$

For the magnetic field $\tilde{B}$, both intraspecies scattering lengths are similar, thus $g_{Na} > g_K$ through the mass dependence. Therefore, $n_{Na} < n_K$ in the droplet region, leading to an ejection of ^{23}Na condensate atoms from the droplet region. These are visible as additional flanks in fig. 57. Thus, the appearance of a droplet may well explain the observed stability. However, up to now the predicted spatial signatures were not observed in the experiment.

The most apt explanation for the stability of both condensed clouds can be given by the details of the trapping geometry. At the final trap frequencies, the differential gravitational sag $\delta z_0 = 3.27\,\mu$m exceeds the individual (i.e. without interspecies interactions) vertical Thomas-Fermi radii of the condensate wave functions, when the condensate wave function overlap of the two clouds is already

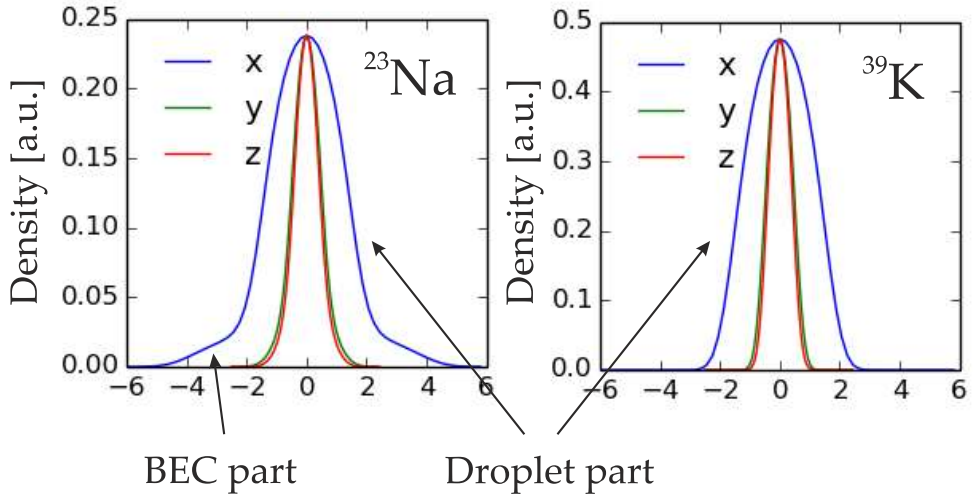

Figure 57: Density distributions for ^{23}Na (left) and ^{39}K calculated using a two-component Gross-Pitaevskii equation where Lee-Huang-Yang beyond mean field corrections are included. Condensate atom numbers, trap frequencies and scattering lengths are chosen to be identical to the experimental realization presented in fig. 56. The effect of gravitational sag is not included. Picture provided with courtesy from Daniel Edler, only labels have been added.

strongly reduced to about 30 %. Hence the impact of the interspecies interaction is reduced, and mean-field stability can be obtained. This was verified by calculating stationary solutions of the coupled Gross-Pitaevskii equations for the mixture in the Thomas-Fermi approximation. For the used experimental parameters and final observed atom numbers, the derived chemical potentials dictate stability of the condensates. The reduced overlap also modifies the thermalization properties of the mixture. In an interacting and overlapping scenario, both clouds have to be in thermal equilibrium after a thermalization time, hence $T_{Na} \equiv T_K$. Yet in a forced evaporation sequence with non-interacting or non-overlapping clouds, in general $T_{Na} \neq T_K$. The intermediate regime, i.e. the effect of reduced interspecies collisions due to decreased spatial overlap, has been studied before [228], where a considerable decrease of the interspecies rethermalization rates was found. In the experimental sequence corresponding to the measurement campaign of fig. 56, the individual cloud temperature are obtained by Gaussian fits to the wings of the thermal cloud fraction. This gives $T_K = 186\,\mathrm{nK}$ and $T_{Na} = 87\,\mathrm{nK}$, respectively. Both values are consistent with the individual extracted condensed fractions and critical temperatures. It can be therefore assumed that in the chosen evaporation sequence, both samples are in thermal equilibrium with themselves, but not with each other. Verifying these findings by numerical simulations demands exact tracing of the evaporation dynamics in presence of the thermal background and are therefore beyond the scope of the stationary Gross-Pitaevskii equation ansatz that was used to support the above explanation of mean-field stability. Both effects, the mean-field stability as well as the thermalization properties, are currently under investigation - their results will be discussed in future work of this group [116].

The main objective, namely the realization of a quantum degenerate mixture, has been achieved. The presented experimental shot at a magnetic field $\tilde{B}$ displayed

about condensate fractions corresponding to about 1×10^4 atoms for each species. Through optimization of the evaporation trajectory and operating at a magnetic field of 153 G $\in B_4$, these numbers could be increased to condensate atom numbers of 4×10^4 each, at comparable temperatures ~ 100 nK.

7.5.3 *Conclusion*

This chapter presented a detailed theoretical and experimental investigation of the ^{23}Na and ^{39}K collisional properties at ultra-cold temperatures. It was focused on the spin state combination $|1,-1\rangle_{Na} + |1,-1\rangle_K$ with the goal to achieve dual-species condensation. The theoretical calculations show three distinct signatures, and it has been shown how all of them can be spectrally resolved using atom loss spectroscopy. The measured features coincide well with the theoretical prediction, highlighting the quality of the recent data on the fermionic isotope pair [204]. The potential energy curves can be further improved by measuring the remaining Feshbach resonances of the bosonic isotope in other collisional channels. It was shown that the interplay of intra- and interspecies scattering lengths gives rise to four different magnetic field regions $B_{1,2,3,4}$, in which different mixture phenomena can be studied. By tuning a_{NaK}, a quantum degenerate mixture was achieved by forced optical evaporation. Quantum degenerate mixtures are found to be stable beyond the mean-field criterion, and the influence of the differential gravitational sag on the miscibility and the thermalization properties of the mixture was discussed. With reduced cloud overlap, the mixture was found to be out of thermal equilibrium as the cODT is switched off, and the ^{23}Na appears colder due to the lower trap depth. Thermalization can be achieved by raising the trap frequencies after the final stage of forced evaporation, which reduces the differential sag. Combined with the miscible interactions, a high spatial overlap of the atomic clouds gives ideal starting conditions for the association of Feshbach molecules and subsequent molecular ground-state spectroscopy. A thorough study of the different interaction regions $B_{1,2,3,4}$ is left for future studies. Of considerable interest is the border between B_3 and B_4 due to the possibility to study higher-order mean-field effects like the Lee-Huang-Yang correction to the Gross-Pitaevskii equation. This correction manifests itself in the formation of quantum droplets. With the condensed clouds at hand, this region can be revisited and quantum droplets studied. Together with the immiscible region B_1 and the miscible region B_4 explored in this article, the magnetic field valley outlined in fig. 54 provides a wealth of possible phase transitions to be studied in future research.

8

TWO-PHOTON PATHWAYS IN MOLECULAR NaK

The preceding chapters showcased the experimentally achieved progress. Using the resonances located in chapter 7, Feshbach molecules can be created either by a magnetic field sweep over the resonance [229] or by radio-frequency association, which is done by matching the binding energy of the molecular state to the frequency of a rf-source [55, 230]. This chapter is devoted to theoretical considerations regarding the transfer from the thereby created Feshbach molecules into the ground state. The main results of this chapter have been published in [1], figures appearing identically in that publication are marked correspondingly.

Compared to the free atom pair, the radial amplitude of the Feshbach molecular wave function is already much stronger ($\approx 100\times$) localized. Still, its mean molecular bond length is very large, as can be seen in fig. 58, in which the Feshbach wave function is represented through the least bound vibrational state of the $a^3\Sigma^+$potential. As its radial extent can be much larger than the characteristic Van der Waals length of the underlying potential, several of the Feshbach molecule properties will be given by the simple sum of the corresponding atomic properties, and some distinct molecular features will appear less pronounced. In particular, the permanent dipole moment of bialkali molecules scales as r^{-7} in the long-range region [231] where r is the internuclear distance, and therefore no sizable dipolar effects can be expected to emerge for this state. Moreover, as transitions between vibrational levels do not obey selection rules, the loosely-bound Feshbach molecule is not a stable configuration as it can decay to lower vibrational states of the potential. Therefore, it is desirable to transfer the molecules via an optical transition into the absolute ground state of the system. Here, their radial wave function will be a Gaussian function localized at the equilibrium distance of the underlying potential energy curve (see also fig. 58), and a large dipole moment can be achieved.

The radically different character of Feshbach and ground state sets constraints to the type of transfer that can be successfully executed. Firstly, the direct wave function overlap between weakly bound Feshbach molecules and deeply bound ground state molecules is vanishingly small. Secondly for alkali dimers, Feshbach molecules and ground state molecules can have very different electronic spin character. While Feshbach molecules often display dominant $a^3\Sigma^+$ character[1], rovibronic ground state molecules are purely $X^1\Sigma^+$ molecules. As the electric dipole operator does not act on the spin wave function, this contribution will also be extremely small.

Both problems can be met by using a two-photon transfer involving a *singlet-triplet bridge* in the excited state manifold. This is also depicted in fig. 58, in which the molecular potential curves corresponding to the ground asymptote K(4s) + Na(3s) and the excited asymptote K(4p) + Na(3s) are shown together with a sketch of a typical two-photon scheme for mapping Feshbach molecules onto the rovibrational ground state. A pump light field couples Feshbach molecules to an appropriate

1 That ultra-cold Feshbach molecules are treated as triplet-dominant is more a rule of thumb than a strict law. Singlet amplitude is generated by superposing states with opposing amplitudes (e.g. $|\uparrow\downarrow\rangle - |\downarrow\uparrow\rangle$), whereas cold systems usually prepare pure spin states ensembles.

electronically excited intermediate state; an overlapping Stokes pulse couples the target $X^1\Sigma^+$ rovibrational ground state to the same excited state level, completing the two-photon transfer. Therefore, an appropriate electronically excited state serves as a bridge for the transfer, both in terms of wave function overlap and electron spin mixing for triplet-to-singlet conversion.

This experimental approach for ultra-cold molecule creation has first been demonstrated in a seminal KRb experiment of the JILA group [232, 233], where second-order spin-orbit coupling has been used to induce the singlet-triplet mixing. Two differences can be noted between the KRb study and the NaK case. First, by comparing the atomic spin-orbit coupling constant $\xi_{Rb,(K),[Na]} = 79.20(19.24)[5.73]\text{cm}^{-1}$ of atomic Rb, K and Na in their lowest p- state, one sees that such a bridge will be expected to be far weaker for NaK than KRb. As one cannot endlessly compensate this weakness by increasing laser power and focusing of light beams, the suitability of such a scheme has to be reevaluated for NaK.

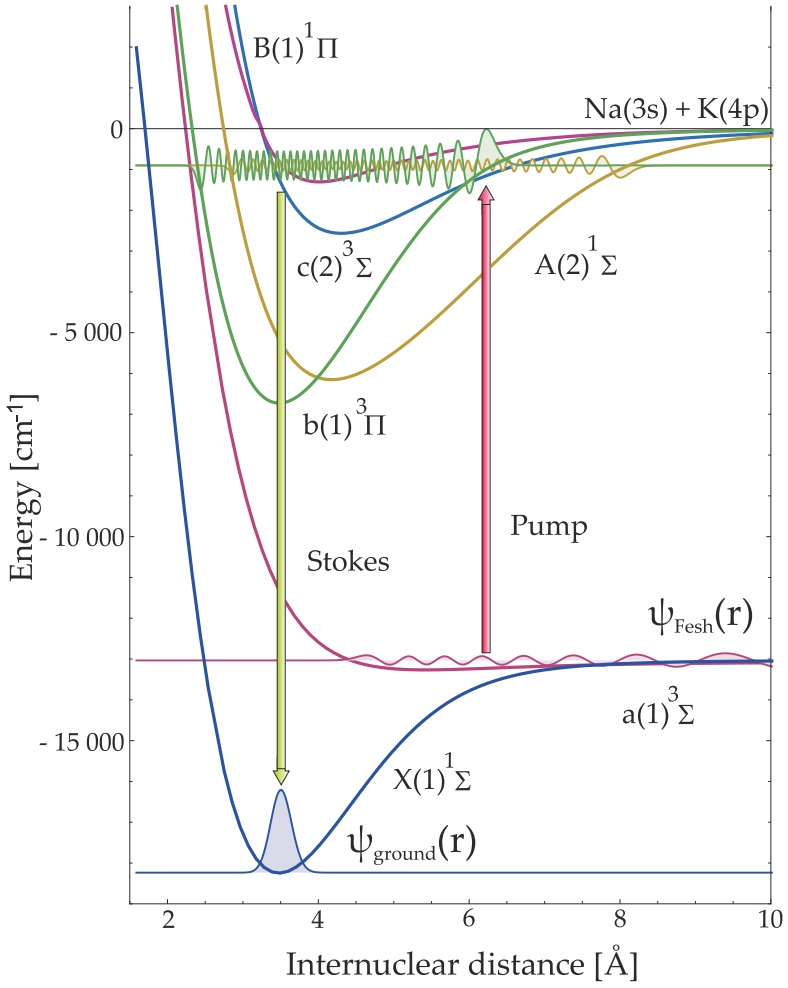

Figure 58: Scheme of the coherent transfer sequence from a Feshbach state to the absolute ground state of the molecule. In this example, the intermediate level is of the resonant type, where $A^1\Sigma \sim b^3\Pi$ are strongly coupled. Green and orange wave function amplitudes reflect the respective singlet and triplet components of this particular level [1].

The second difference between NaK and KRb is hidden in the Feshbach molecular state. The Feshbach resonances obtained in this thesis were shown to be exceptionally broad. In experiments done at the MIT using $^{23}Na^{40}K$, broad resonances have also been reported [65], and it has been argued that this can vastly influence the spin character. For the MIT system, it was stated [74] that the singlet amount in the Feshbach state might allow for direct singlet coupling to an intermediate state, which would render a triplet-singlet bridge unnecessary.

At the time this study was conducted, the bosonic data presented in this thesis had not been acquired yet, and experimental Feshbach molecular data was only availabe for the fermionic molecule $^{23}Na^{40}K$. Therefore, the Feshbach state modeling presented here used the fermionic isotope in order to be able to compare the used model and theoretical results to experimental data. For the fermion, the nuclear spin is $i_K = 4$, hence $7/2 \leqslant f_K \leqslant 9/2$. For the excited state, the dominating contribution to the singlet-triplet admixture will be given by the interaction between orbital angular momentum and spin, therefore the effect of hyperfine coupling was neglected. Without hyperfine coupling, the singlet and triplet potential will be identical for both isotopes, thus the excited state results are directly adaptable to the bosonic case.

Ultimately, the parameter of interest is the product of the two dipole matrix elements, representing the two-photon transition:

$$d_{(F\to X)} = \langle \psi_F | \hat{d} | \psi_{int.} \rangle \langle \psi_{int.} | \hat{d} | \psi_X \rangle. \tag{8.1}$$

Here, $|\psi_F\rangle$ corresponds to the Feshbach molecule, whereas $|\psi_{int.}\rangle$ is the intermediate level selected for an effective two-photon process. The rovibronic ground state is abbreviated as $|\psi_X\rangle \equiv \left|X^1\Sigma^+(v=0, J=0)\right\rangle$, where v and J are the vibrational and rotational quantum numbers of the molecule.

This chapter focuses on a detailed analysis of the involved molecular potentials to identify transition windows in which both the transition amplitude from the Feshbach state to the intermediate state and from the intermediate state to the ground state are sizable. In what follows, the individual components of the resulting two-photon matrix element are piecewise evaluated. For the Feshbach state near a resonance, the influence of the hyperfine interaction on the singlet admixing is shown, and the suitability of a pure singlet bridge is discussed. The intermediate state is studied with particular emphasis on its spin mixing characteristics. Combining the ground and excited state analysis, two-photon transition dipole matrix elements are calculated, which unveils possible two-photon transfer paths. The theoretical framework relies again on coupled-channel calculations. These were first performed using subroutines developed in the Tiemann group. For the excited state manifold, this formalism transforms the problem at hand to Hund's coupling case (e), as the spin-orbit operator acquires diagonal form in this basis. To which extent it will reflect the experimental situation is not clear, and modifications might be in order, similar to the hyperfine operator shown in the last chapter. Later on, the author acquired spin-orbit coupling matrix elements in Hund's coupling case (a) from Andrey Stolyarov (Moscow University) that were obtained out of deperturbation analysis [69]. Using these experimentally obtained matrix elements, another calculation routine was set up independently. Both formalisms gave similar results, and the former approach is presented here.

8.1 THE FESHBACH STATE

The initial state of the two-photon sequence, i.e. the Feshbach level, is investigated first. This already gives insight into the requirements concerning the choice of an intermediate level in order to accomplish an efficient ground state conversion. The crunchpoint of eq. (8.1) lies in the radial variation of the Feshbach molecule's wave function that is obtained out of the coupled-channel Schroedinger equation introduced in chapter 2. Hence, solutions are pursued for the equation

$$\mathcal{H}\,|\psi_F\rangle = E\,|\psi_F\rangle, \tag{8.2}$$

subject to either bound-state or scattering boundary conditions and with the multi-channel Feshbach state vector ψ_F. The Hamiltonian $\mathcal{H}$ for the diatomic collision is again given by

$$\mathcal{H} = T + V + H_{hf} + H_{dd} + H_{Zee}. \tag{8.3}$$

$T = -\hbar^2\nabla^2/(2\mu)$ is the relative kinetic energy operator, whereas $H_{hf,(dd),[Zee]}$ are the hyperfine (magnetic dipole-dipole) [Zeeman] interaction, respectively. The numerical approach to the coupled-channel calculation is identical to the one outlined earlier and not repeated here. Again, the atomic masses, hyperfine parameters as well as electronic and nuclear g factors are taken from [107, 202].

For this analysis, the $X^1\Sigma^+$and $a^3\Sigma^+$potentials obtained in [207] were used, in which both triplet and singlet transitions have been studied together. The whole potential representation is tabulated in their article as a nonlinear power series expansion in the potential minimum regime, as well as a hard-core short-range and Van der Waals long-range extension, which are smoothly matched. The joint description of both the $X^1\Sigma^+$as well as the $a^3\Sigma^+$curves fixes their relative position and therefore serves as a common frequency reference connecting the singlet to the triplet manifold, removing uncertainties in the two-photon detuning between Pump and Stokes lasers. The potential curves are refined by using again the MIT Feshbach data that provides a complementary, ultra-cold dataset probing the long-range region of the potential.

The Feshbach molecule is fully described by the basis set given by the atomic quantum numbers (Hund's coupling case e):

$$|(i, s, f, m)_{Na}; (i, s, f, m)_K, F, m_F\rangle \equiv |f_{Na}, m_{Na}, f_K, m_K, F, m_F\rangle\,, \tag{8.4}$$

where $s_A(i_A)$ is the electron (nuclear) spin, f_A the total angular momentum and m_A its projection onto the space fixed axis of atom A, and F, m_F the total angular momentum and its projection of the system excluding rotation. The number of channels is given by the number of possible projections of the individual angular momenta onto the space fixed axis equating to the same total magnetic quantum number. For a rotational state $\ell = 0$, $M = m_F$. In this study, it is assumed that the diatomic pair has been converted to a molecule possessing a total magnetic quantum number of $M = -3/2$, as this is the combination in which a particularly broad Feshbach resonance has been observed at MIT. For this combination, the total number of channels that constitute the Feshbach scattering wave function is sixteen.

8.1.1 *Feshbach spectrum and spin character*

Having employed the Feshbach resonance locations to improve the long-range description of the potential, the resulting coupled-channel calculations reproduce the s-wave resonance positions measured in [65] with an uncertainty of 100 mG. The calculated binding energies for $\mathcal{M} = -3/2$ are shown in fig. 59 below the asymptote of the atom pair $|1,1\rangle_{Na} + |9/2,-5/2\rangle_K$. Three s-wave resonances situated and observed in [65] between 96 G and 138 G are discernable.

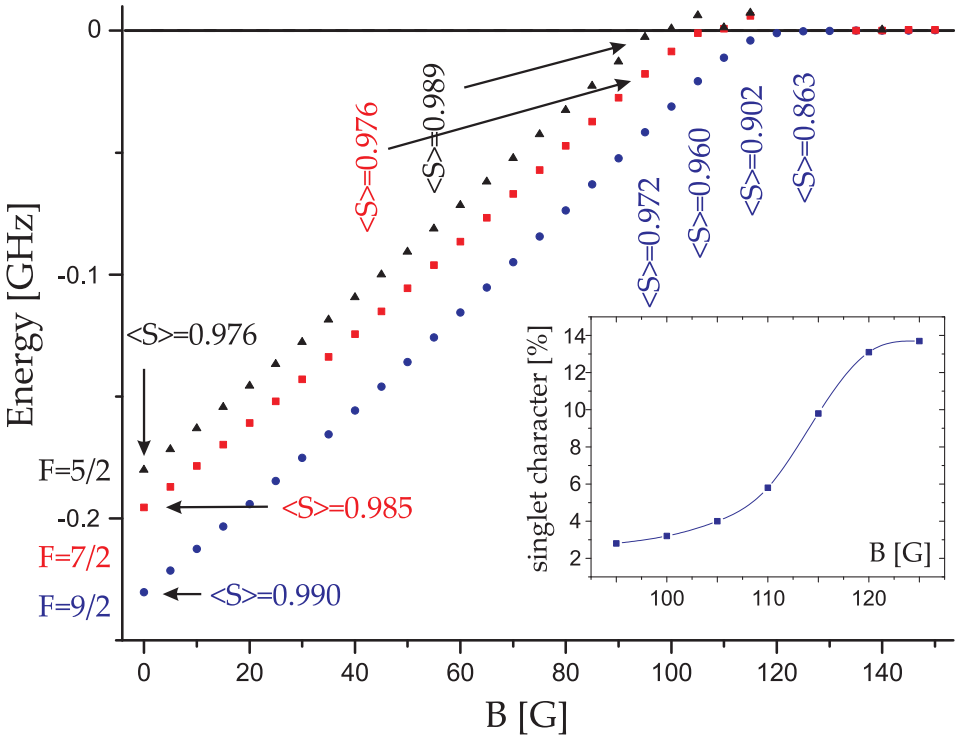

Figure 59: Binding energies of $^{23}Na^{40}K$ for the total quantum number $\mathcal{M} = -3/2$ as a function of magnetic field leading to s-wave resonances. For various magnetic fields the expectation value $\langle S \rangle$ of the electronic spin is given. Inset: Singlet character as a function of B for the $(1,1)_{Na}$ + $(9/2,-5/2)_K$ resonance situated at 136 Gauss. For the sharp resonances at lower fields, only a subtle change in spin character is observed. [1]

Having obtained the scattering multi-channel wave function, its spin composition is inspected as a function of the applied magnetic field. For this, the expectation value of the total spin is calculated, once using the numerically obtained Feshbach wave function (corresponding to full coupling of hyperfine and Zeeman interaction) and once by performing a basis transformation through angular momentum recoupling (where the angular momentum quantum numbers are assumed to be well defined). Denoting $|\phi_i\rangle$ as an eigenvector (e.g. of the atomic spin basis) of an

operator $\hat{\mathcal{K}}$ the expectation value of its quantum numbers for the Feshbach state under consideration can be written as

$$\begin{aligned}\langle\hat{\mathcal{K}}\rangle &= \langle\psi_F|\hat{\mathcal{K}}|\psi_F\rangle \\ &= \langle\psi_F|\hat{\mathcal{K}}\left[\sum_i |\phi_i\rangle\langle\phi_i|\right]|\psi_F\rangle \\ &= \sum_i \kappa_i \langle\psi_F|\phi_i\rangle\langle\phi_i|\psi_F\rangle \\ &= \sum_i \kappa_i |\langle\phi_i|\psi_F\rangle|^2\end{aligned} \tag{8.5}$$

where κ_i are the corresponding eigenvalues to each basis vector. Clearly $\langle S\rangle = 0$ and $\langle S\rangle = 1$ correspond to pure singlet and triplet states, respectively. The closed channel state will be dominantly a bound state of the $a^3\Sigma^+$potential, hence any notable singlet admixture will probably arise out of coupling to open channels. As the resonance width can be linked to the coupling strength between these collision channels, the wide $B = 138$ G Feshbach resonance seems a promising candidate for generating singlet character in the Feshbach state. In [74], it was shown that the singlet admixing increases as the magnetic field approaches the resonance, and a singlet admixture of 14% was stated. This behaviour is confirmed by the numerical calculations shown in fig. 59, where the expectation value of the total spin operator is evaluated. A comparison of the three s-wave resonances shows that the spin character only changes significantly for the broadest resonance at 138 G, saturating also at approx. 14% as the resonance is approached (see inset in 59).

This result can be understood by utilizing a different basis, as the total spin is not appearing as a quantum number in the atomic spin basis. However, the expected spin character can be calculated by performing angular momentum recoupling into a representation in which the total electronic and nuclear spin quantum numbers S and I are defined. The unitary transformation from such basis $|S, I, F, \mathcal{M}\rangle$ to the atomic basis of the entrance channels $|f_{Na}, m_{Na}, f_K, m_K, F, \mathcal{M}\rangle$ then reads

$$|f_{Na}, m_{Na}, f_K, m_K, F, \mathcal{M}\rangle = \sum_{F,S,I} \langle f_{Na}, f_K|S, I\rangle \, \langle m_{Na}, m_K|F, \mathcal{M}\rangle \, |S, I, F, \mathcal{M}\rangle \,,$$

where the transformation coefficient is expressed by the Wigner 9j symbol

$$\langle f_{Na}, f_K|S, I\rangle = \begin{Bmatrix} s_{Na} & i_{Na} & f_{Na} \\ s_K & i_K & f_K \\ S & I & F \end{Bmatrix} \sqrt{(2f_{Na}+1)(2f_K+1)(2I+1)(2S+1)} \tag{8.6}$$

together with Clebsch-Gordan coefficient $\langle m_{Na}, m_K|F, \mathcal{M}\rangle$ that projects onto the magnetic submanifold. Summing over all possible cases for $\mathcal{M} = -3/2$ gives a singlet ($S = 0$) fraction of $\sim 18\%$ at the lowest asymptote, roughly matching the saturation behavior by 14% shown in the inset of fig. 59. The difference is induced by the competition between hyperfine and Zeeman coupling at 125 G, when f_{Na} and f_K will no longer be exact quantum numbers. As one shifts away from the resonance to lower fields, the molecular state converges towards an almost pure triplet state.

8.1.2 *Feshbach molecular wave function and its magnetic field dependence*

The rather high value of more than 10% singlet admixture *suggests* that a pure singlet pathway towards the ground state is possible, in which only Franck-Condon factors to excited singlet states have to be calculated. The following section will discourage this conclusion. For this, the scattering wave function itself is inspected, as it comprises more information than the spin character. Near the Feshbach resonance, one has to distinguish between "atomic" open-closed channel mixing on one side, and "molecular" singlet-triplet mixing on the other side. To provide an intuitive insight into both perspectives, two different representations of the total

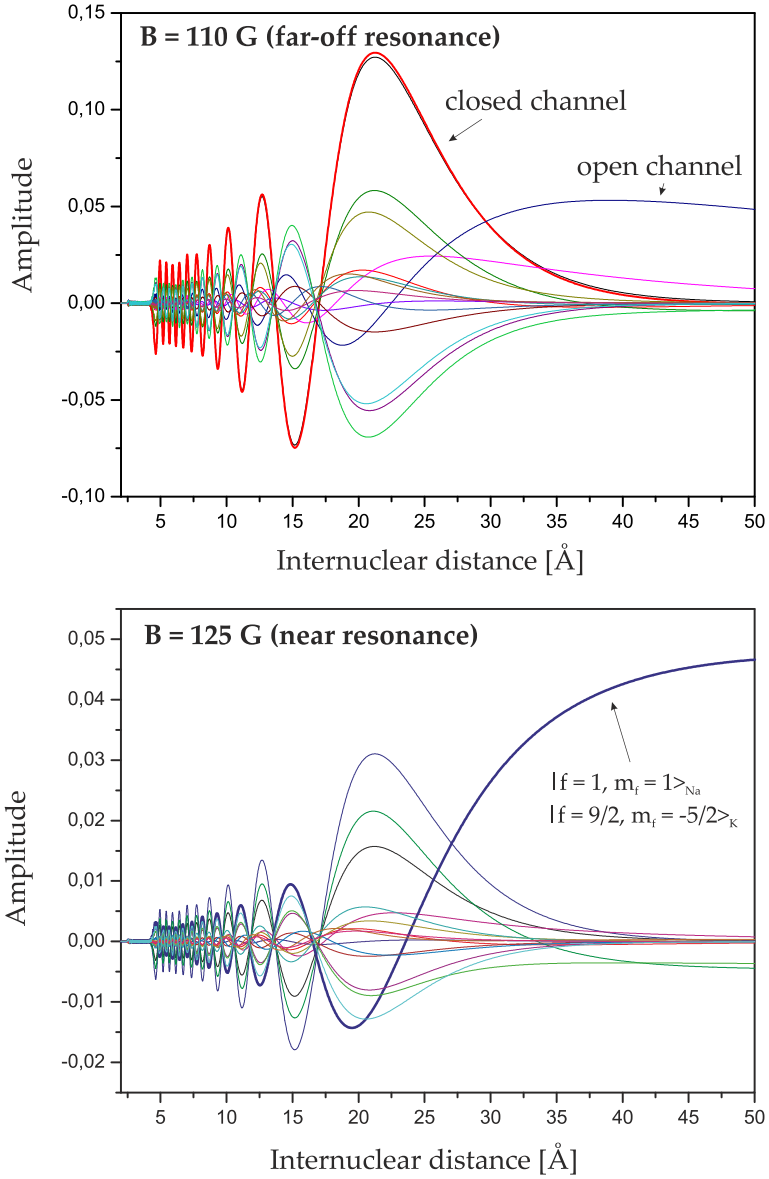

Figure 60: Multi-component wave functions for the bound level at 110 G (upper graph) and 125 G (lower graph), projected onto the Hund's case (e) basis. The 125 G wave function displays a distinct open channel fraction through sizable amplitude at a large internuclear distance $r > 40$ Å. This component has the quantum numbers of the open channel with lowest energy, which are given in the figure. [1]

multi-channel wave function are utilized. At large internuclear distances, Hund's case (e) is a convenient choice of a basis set, as the coupling to the molecular axis plays only a secondary role. By projecting the wave function onto the atomic basis $|f_{Na}, m_{Na}, f_K, m_K, F, \mathcal{M}\rangle$, one obtains direct access to the open and closed channel character of the scattering wave function. This is shown in fig. 60 for two magnetic field values 125 G and 110 G, for which the bound molecular level has a binding energy of $E_{125} = 250\,\text{kHz} \times h$ and $E_{110} = 11\,\text{MHz} \times h$, respectively. Closed and open channels can be distinguished by their long-range behaviour as indicated in the upper graph of fig. 60. At larger internuclear distances, closed channel amplitudes quickly decay to zero, whereas the open channel amplitude remains sizable[2].

At 125 G, the molecular state is only weakly bound and strong coupling to the open channel persists, which is highlighted by the large amplitude of one single basis vector, labeled by quantum numbers. As the open channel contains a considerable fraction of singlet character, this directly translates into an increased singlet-triplet ratio for the Feshbach state. At first glance, one could therefore interpret a high singlet admixing as being beneficial for the desired ground state transfer, because one could directly couple to a more or less pure singlet intermediate state. Yet components going over to open channels possess significant wave function amplitude only at large distances, which will not contribute to the transition dipole matrix element in eq. (8.1) due to vanishing vibrational overlap with the excited state. Hence, the wave function amplitudes and their state character localized at smaller internuclear distances are of great interest.

The Hund's case (e) representation is not suitable for directly identifying the singlet and triplet admixture, as the total spin is not appearing as a quantum number in the basis vector. For that reason, the Feshbach wave function is transformed into a state basis in which the total spin is used, namely Hund's case (b). Here, the angular momentum coupling, neglecting in this case the molecular rotation, gives rise to a set of quantum numbers $|S, G, F, M\rangle$, where the quantum number G is obtained by coupling the total spin S with the nuclear spin of sodium. Afterwards, the nuclear spin of ^{40}K and G are coupled to obtain F. Note that the ^{23}Na hyperfine splitting is larger by a factor of 1.4 compared to ^{40}K, which validates the coupling order. The resulting projections of the wave function onto the basis (b) are shown in fig. 61, again for a magnetic field of 125 G (upper graph) and 110 G (lower graph). For reasons of clarity and comprehensibility, all but the strongest triplet and singlet channel contributions have been removed. From fig. 61 it is evident that one benefits from changing the magnetic field from 125 G to 110 G, as it leads to compacting the Feshbach wave function at internuclear distances $r < 20$ Å, where the maximum amplitude becomes 0.035 for 125G and 0.16 for 110 G already. Both triplet and singlet amplitudes are enhanced in the deeply bound 110 G region. To quantify this in terms of bound states, the single-channel wave functions for the last bound levels of the $X^1\Sigma^+$ and $a^3\Sigma^+$ potentials, v_X=74 and v_a=19, have been calculated. At internuclear distances drawing near the chemical region, the amplitude from the continuum coupling will be damped out and the individual channel wave functions will change over to the corresponding bound state wave functions. Matching their amplitude at internuclear distances $r \lesssim 10$Å (see fig.

2 The open channel wave function still has to decay eventually as it has to be an element of the Hilbert space $\mathcal{L}^2$. To handle the continuum description, an infinitely large box is installed at a large internuclear distance of 5000 a_0 that does not change the overall physical picture.

61), scaling factors $\beta_a(B), \beta_X(B)$ for the unperturbed single-channel wave functions are obtained. These scaling factors can be interpreted as the amplitude gain or loss for the Franck-Condon overlap in the eventual two-photon transfer. For the two magnetic fields shown in fig. 61, this gives a ratio $\beta_X(110)/\beta_X(125) = 5.48$ for the strongest singlet and $\beta_a(110)/\beta_a(125) = 4.33$ for the strongest triplet channel. Evaluating Feshbach transition dipole matrix elements, this gain in $\beta_{a,X}$ directly translates into a transition probability gain of one full magnitude.

Concluding, the rise in singlet character close to the resonance field is accompanied by significant total amplitude loss in the inner part. This behavior cannot

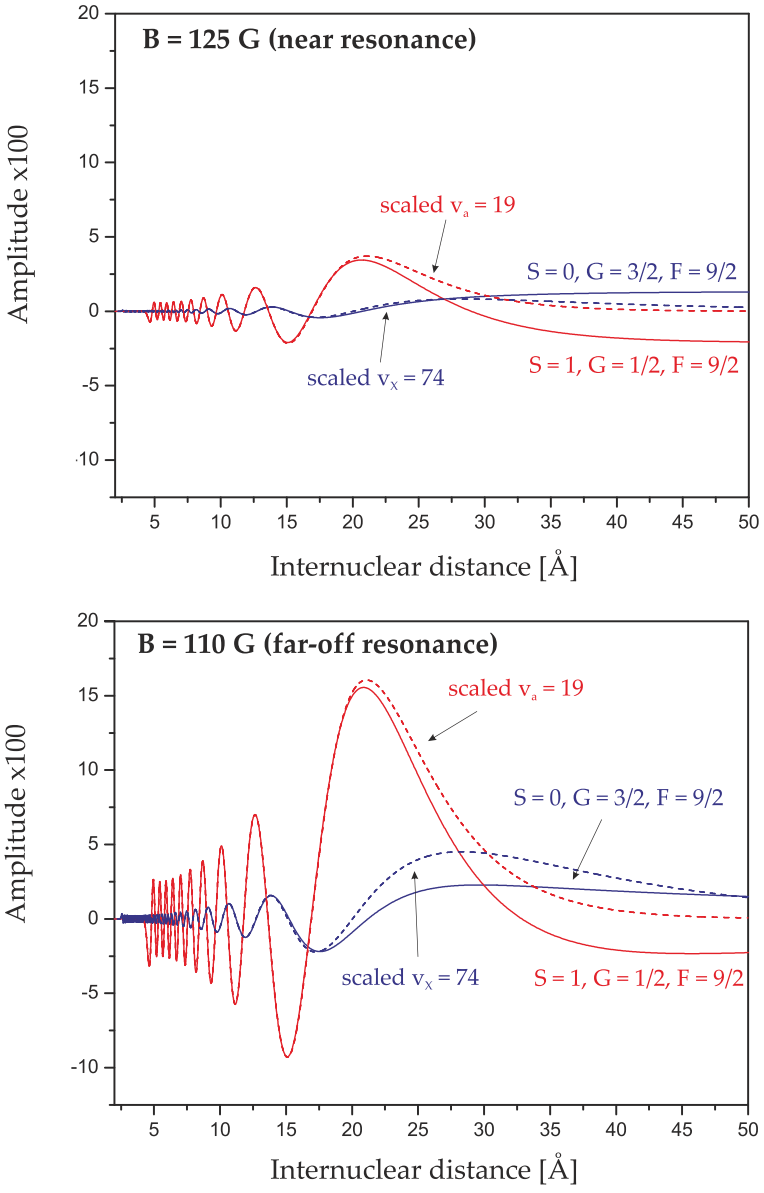

Figure 61: Multi-component wave function of the bound level at 125 G (upper graph) and 110 G (lower graph), projected onto the Hund's case (b) basis. For clarity, all but the strongest triplet and singlet channels were removed. As dashed lines the vibrational wave functions of the pure singlet and triplet states are given for the least bound level, scaled to the amplitude of the appropriate inner parts of the multichannel wave function. [1]

be revealed by inspecting the spin character, as it cloaks such details due to the integration procedure by which expectation values are calculated. Instead, one has to look directly into the multi-channel wave function, which naturally contains a much higher degree of detailed information. Note that this behavior is depending on the resonance that one works with (e.g. the sharp resonance at 96 G displays slightly increasing singlet character as one moves from the resonance). For each resonance, there will be a magnetic field which optimizes the transfer to the molecular ground state via a selected intermediate state. This reflects the competition of singlet amplitude admixed by the open channel coupling and the increase in amplitude of the desired component in the inner region of the wave function.

8.2 INTERMEDIATE STATES

The intermediate state will be one of the eigenstates of the Hamiltonian

$$\mathcal{H} = H_0 + H_{\text{Int.}}. \tag{8.7}$$

Here, H_0 contains the kinetic energy and diabatic potential operators of a specific molecular state manifold. The generally used manifold corresponds to either one of the two lowest electronic excitations Na(3p)+K(4s) or Na(3s)+K(4p), and the spin-orbit coupling will be the dominant interaction in $H_{\text{Int.}}$. Since the atomic spin-orbit coupling constant for the lowest p-state of K is about a factor of 3 larger than the corresponding coupling for the lowest p-state of Na ($\xi_{K,[Na]} = 19.24[5.73]\,\text{cm}^{-1}$), the states asymptotically converging to K(4p) are chosen for this analysis, which is also the energetically lowest one of both sets mentioned above.

Note that the state $|\psi_X\rangle$ will be populated from the intermediate states. $|\psi_X\rangle$ is symmetric under parity inversion for the rotational state $J = 0$, demanding for levels with odd parity for the excited states. For the asymptote under consideration, this then gives five molecular state vectors. For state labeling, the ${}^{2S+1}\Lambda^{\pm}_{\Omega}$ symmetry (Hund's case (a)) is used, where Λ (Ω) gives the projection of the electron orbital (total) angular momentum along the internuclear axis. The manifold under consideration then comprises two states ${}^1\Sigma^+_{0^+}$,${}^3\Pi_{0^+}$ sharing $\Omega = 0^+$ and three states ${}^3\Sigma^+_1$,${}^1\Pi_1$,${}^3\Pi_1$ sharing $\Omega = 1$.

The interaction Hamiltonian H_{Int} can be divided into hyperfine and spin-orbit interaction. Despite playing a pivotal role for the ground states, the hyperfine interaction is neglected in the following ion on excited states, because it is a small perturbation compared to the singlet-triplet coupling by the spin-orbit interaction. For the same reason, by setting $B = 0$, no magnetic field effects are discussed. Whether this simplification will give any shortage to the conclusions drawn here is discussed near the end of the chapter.

An in-depth review of the remaining coupling terms can be found e.g. in [234, 235]. The weakest term is given by the spin-rotation coupling $\gamma\,\mathbf{R}\cdot\mathbf{S}$ with a coupling constant γ [236] that can induce e.g. the coupling between ${}^3\Pi_{0^+}$ and ${}^1\Pi_{1^+}$. Additionally, there is the Coriolis interaction from H_0 coupling states with $\Delta\Omega = \pm 1$. The coupling from $\Omega = 1$ to $\Omega = 2$ does not play any role here because $\Omega = 2$ states do not posses $J' = 1$ levels. The dominating term is given by the spin-orbit interaction which couples states possessing the same value of Ω ($\Delta\Omega = 0$). In the asymptotic limit $r \to \infty$, it acquires diagonal form in the atomic spin basis, where it leads to the well-known fine structure splitting, in this case mediated by potassium's fine structure constant ξ_K. After a basis transformation to Hund's case

(a), it will be in general a radially dependent function. For the excited states under consideration, the corresponding matrix elements have been studied and tabulated by Stolyarov and co-workers [69].

In matrix representation, the multi-channel vector for the excited states $|\psi_{exc.}\rangle$ is written using its five channel components:

$$\mathcal{H}\,|\psi_{exc.}\rangle = \begin{pmatrix} T+V_{1\Sigma} & SO & Cor. & S-R & 0 \\ SO & T+V_{3\Pi} & S-R & Cor. & Cor. \\ Cor. & S-R & T+V_{1\Pi} & SO & 0 \\ S-R & Cor. & SO & T+V_{3\Sigma} & SO \\ 0 & Cor. & 0 & SO & T+V_{3\Pi} \end{pmatrix} \begin{pmatrix} {}^1\Sigma_0^+ \\ {}^3\Pi_{0^+} \\ {}^1\Pi_1 \\ {}^3\Sigma_1^+ \\ {}^3\Pi_1 \end{pmatrix} \tag{8.8}$$

Where SO, Cor. and S-R are spin-orbit, Coriolis and spin-rotation interaction, respectively, T is the kinetic energy operator and V_m denotes the potential energy curve for state m. Note that these are the *diabatic* potential energy curves of the system. Therefore they will cross in radial space and share the same asymptotic dissociation limit. Diagonalization of them in presence of their interaction terms will give the *adiabatic* potential curves[3], displaying avoided crossings and splitting according to the fine structure at the asymptote.

The computational approach to this problem is a bit different from the ones performed in context of Feshbach resonances. Again, the multi-channel radial Schroedinger equation is solved, but here not the scattering wave function but the bound state spectra of the coupled potential energy curves have to be obtained. For bound state calculations, several fast spectral methods are available. Here, the Fourier grid method is utilized, in which the radial dependence of the Hamiltonian is discretized on a grid [86]. The main appeal of this method is that *all* eigenvalues and -functions are deductible by diagonalizing one single matrix. The radial grid is discretized on N grid points with a total length L, hence every matrix element of the Hamiltonian is itself a matrix. In Hund's case (a), the potential energy curves are diagonal $N \times N$ matrices:

$$V_m = \begin{pmatrix} V_{m,1} & & & & 0 \\ & V_{m,2} & & & \\ & & \ddots & & \\ & & & V_{m,N-1} & \\ 0 & & & & V_{m,N} \end{pmatrix} \tag{8.9}$$

The kinetic operator is diagonal in the Fourier k-space. Through an inverse Fourier transform, it can be represented on the radial grid as a non-diagonal $N \times N$ matrix that is equal for each of the channels:

$$T_{ii} = \frac{\hbar^2\left(N^2+2\right)}{24\mu L^2} \tag{8.10}$$

$$T_{ij} = -1^{(i-j)}\frac{\hbar^2}{4\mu L^2 \sin^2\left[(i-j)(\pi/N)\right]}, \quad i \neq j \tag{8.11}$$

For a given grid size N, diagonalization of the Hamiltonian in eq. (8.8) gives the 5N lowest coupled channel eigenvalues and -functions of the system. By projecting the eigenvalues on the individual channels, the individual state admixture is obtained.

3 *adiabatos* (Greek): 'impassable', from *a-* 'not' + *dia* 'through' + *batos* 'passable' (from *bainein* 'go')

8.2.1 *Modeling excited state molecular potentials*

The reliability of the following calculations will be dictated by the accuracy with which the applied PECs and their interaction reflect reality. For NaK, *ab initio* curves provided by quantum chemistry calculations are tabulated in the literature [237]. These give a complete overall description of the PEC, which, however, is accompanied by lower total accuracy. The results obtained by using such potentials can in general not compete with the accuracy provided by spectroscopic studies. The desired states have also been investigated by molecular spectroscopy [69, 70, 71]. The results of such studies are usually represented by a set of spectroscopic constants that reproduce the measured energy levels.

Out of these constants, the potential energy curves were reconstructed using the Rydberg-Klein-Rees (RKR) method [238]. This provides the underlying potential curve by using the energy levels that this curve will produce, and can therefore be seen as an inversion method that constructs the problem out of the solution. For this, one utilizes the semi-classical Sommerfeld quantization rule of the action integral:

$$\sqrt{2\mu}\oint\sqrt{E(v,J)-V_{\text{eff}}(r,J)}\,dr \stackrel{!}{=} h\left(v+\frac{1}{2}\right), \tag{8.12}$$

where the integration is performed for one complete cycle of motion. The effective potential is the sum of potential energy curve $V_0(r)$ and rotation energy:

$$V_{\text{eff}}(r,J) = V_0(r) + \frac{\hbar^2 J(J+1)}{2\mu r^2}. \tag{8.13}$$

The rotation-vibration energy for a level with quantum numbers (v,J) is $E = G(v) + B(v)J(J+1)$ with the vibration energy $G(v)$ and the v-dependent rotational constant $B(v)$. Obtained out of a spectroscopic study, they are parametrized using the Dunham expansion [239]

$$E(v,J) = \sum_i \sum_k Y_{ik}\left(v+\frac{1}{2}\right)^i [J(J+1)]^k \tag{8.14}$$

with the so-called Dunham coefficients Y_{ik}. The potential can be reconstructed out of these energies by noting that for any given energy level, the inner and outer turning points r_- and r_+ mark the points at which the energy is equal to the potential energy. To link V_0, $E(v,J)$ and the turning points, one uses the PEC area for a given $E(v,J)$,

$$A(E,J) = \int_{r_-}^{r_+} [E - V(r)]\,dr, \tag{8.15}$$

and the turning points can be evaluated using

$$\partial_E A = r_+ - r_-, \tag{8.16}$$

$$\partial_J A \propto \frac{1}{r_+} - \frac{1}{r_-}. \tag{8.17}$$

The area function in eq. (8.15) does not look so different from the action integral in (8.12). In fact, using the Sommerfeld quantization rule, it is possible to form

an integrand that only depends on the measured eigenvalues. The derivation is skipped here, but can be found e.g. in [240]. As a result, the turning points for a given vibrational level v_0 can be constructed out of the so-called Klein action integrals f and g:

$$f = \frac{\hbar}{\sqrt{2\mu}} \int_{-1/2}^{v_0} \frac{1}{\sqrt{E_0 - E(v,J)}} dv \tag{8.18}$$

$$g = \left(\frac{\hbar}{\sqrt{2\mu}}\right)^{-1} \int_{-1/2}^{v_0} \frac{\hbar B(v)}{\sqrt{E_0 - E(v,J)}} dv \tag{8.19}$$

$$r_{\pm} = \sqrt{\frac{f}{g} + f^2} \pm f \tag{8.20}$$

Note that J and v are discrete variables in the physical system, they are treated as continuous in this description. The action integrals are solved numerically. This procedure is obtained for a set of selected energy levels, yielding the potential sampled by the corresponding turning points, and spline interpolation gives a continuous form. The spectroscopied energy levels can be usually reproduced by this method with a relative error of 10^{-5} [241]. The reason why the RKR method works so well is that for large vibrational numbers, the semi-classical quantization rule can be considered valid. For small vibrational numbers, the low-lying turning points sample a potential not far from a harmonic oscillator, for which the semi-classical treatment is exact following out of the Ehrenfest theorem [242].

The resulting molecular RKR potentials reproduce the bound molecular states of the chemical region with a quality which considerably exceeds the *ab initio* approach. Yet the RKR treatment is only applicable for the region in which the molecular states have been explored experimentally. For the used states, the valid vibrational level range is:

$$v = \{0 - 75\}\ (A(2)^1\Sigma) \tag{8.21}$$

$$v = \{0 - 63\}\ (b(1)^3\Pi) \tag{8.22}$$

$$v = \{0 - 36\}\ (c^3\Sigma) \tag{8.23}$$

$$v = \{0 - 43\}\ (B(1)^1\Pi) \tag{8.24}$$

If RKR potentials are extrapolated beyond the spectroscopically investigated range, the potential slope errors become large. It is therefore advised to use these RKR potentials only to describe the potential minimum part, and switch to different representations at short- and long-range, respectively. The short range part of the PECs can be modeled by a repulsive wall involving a high inverse power in internuclear distance r. The long-range description is given as an inverse power series involving the individual dispersion coefficients, where high quality theoretical values are tabulated in the literature [243, 244]. However, as pointed out in chapter 2, it is only valid for internuclear distances larger than the LeRoy radius, when the atoms of the dimer can be considered detached. The LeRoy radius for NaK is reported to be 10.8 Å [70]. Yet the only RKR curve fully covering the region until that value is the $B^1\Pi$ one [70]. This it implies that one has to borrow an *ab initio* shape in order to bridge the part between RKR and long-range description. To avoid mixing theoretical and semi-empirical descriptions, it was decided to follow a different path described below, taking the *ab initio* curves of [245] and refine them by using the fully explored ground state potentials. The RKR potentials [69, 70, 71] are then

employed together with spectroscopic data as a cross-check for the spectroscopically covered regions.

Ab initio calculations rely on approximations which in the end will over- or underestimate certain facets of the potentials as for example the well depth of the potentials. It is noted that a lot of these errors are systematic. As an example, r-dependent errors in the theoretical curves are mostly generated out of basis-set superposition errors[4], so they will in general affect all calculated curves in similar fashion. Possessing reliable experimental data on both the ground states, the $a^3\Sigma^+$and $X^1\Sigma^+$can be compared with the *ab initio* ground state PECs. Out of this, some systematic deviations in the *ab initio* calculations can be found and used to correct the corresponding excited states.

This idea has been developed in [246, 247] and is used here in the same fashion. For a given singlet (triplet) state S (T), the first refinement step is given by

$$V_{S,\text{refined}} = V_{X,\text{exp.}} + \left[V_{S,\textit{ab initio}} - V_{X,\textit{ab initio}}\right], \tag{8.25}$$

$$V_{T,\text{refined}} = V_{a,\text{exp.}} + \left[V_{T,\textit{ab initio}} - V_{a,\textit{ab initio}}\right]. \tag{8.26}$$

The potentials are further refined by comparing them to data sets acquired by the Tiemann group [207], as depicted in fig. 62.

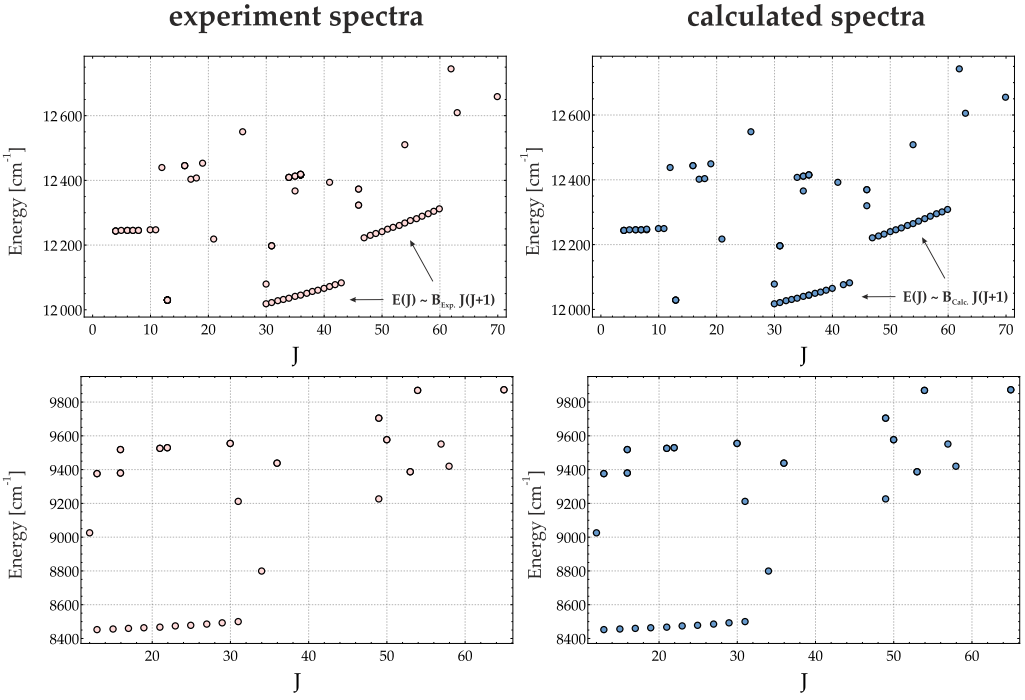

Figure 62: Left: Experimentally acquired spectra as a function of assigned rotational angular momentum J obtained in [207]. Right: Calculated spectra with the refined potential curves for the same values of J. The energy is given with respect to the ground state dissociation threshold. Rotational progressions unveil the difference between real and calculated rotational constant B for that state.

4 In quantum chemistry calculations, interaction energies are usually calculated using a linear combination of atomic orbitals and calculating the energy of the molecule with respect to the asymptotic limit. Both atomic basis sets have to be truncated, giving rise to a uncertainty with which the asymptotic energy can be determined. When the atomic wave functions start to overlap, each atom can borrow basis functions from the other basis set, so the accuracy is increased. The comparison of asymptotic and intertwined distances then produces errors.

In their experiment, all levels are uniquely assigned to a rotational angular momentum quantum number. Coupled channel calculations are performed using the same rotational angular momenta and the curves $V_{S,refined}$, $V_{T,refined}$ for the excited state potentials. A first comparison allows to extract common energetic offsets. Of special interest are measurements of rotational progressions, which are visible in fig. 62 as energetically closely spaced J-chains. In such progressions, the energy of the rotational level is given by $E_{Exp.} = B_{i,Exp}J(J+1)$, where B_i is the rotational constant of the i-th molecular state. Comparing this with calculations of the same progression allows to obtain $\Delta B_i = B_{i,Calc.} - B_{i,Exp.}$. In a rigid rotor model, $B \sim (r_{eq.})^{-2}$, where $r_{eq.}$ is the equilibrium internuclear distance of the corresponding potential curve. Hence, ΔB_i is balanced out by slightly ($\sim 10^{-3} - 10^{-2}$Å) shifting the equilibrium distance of the corresponding excited state potential.

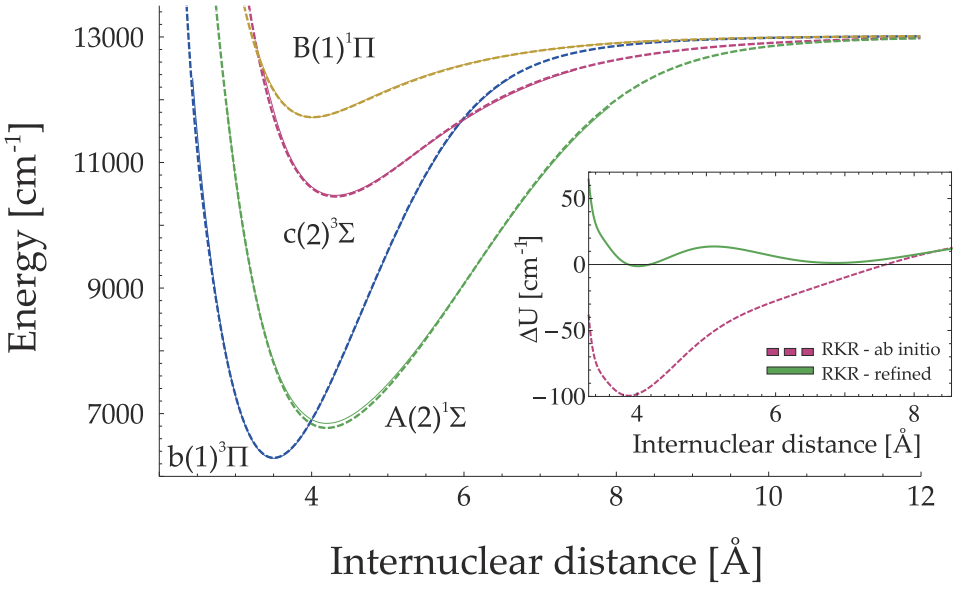

Figure 63: Diabatic PECs of the Na(3s) + K(4p) manifold used in this study. The energy zero is chosen at the atomic ground state asymptote. Shown are the refined diabatic PECs (dashed) as well as RKR curves (solid) for comparison. Inset: Potential difference between the $B^1\Pi$ RKR potential, the raw *ab initio* curve (dashed line) and the refined curve (solid line), respectively.

This whole procedure considerably improves the quality of the curves, as shown exemplary in the inset of fig. 63 for the $B^1\Pi$ potential. It is reliable for the singlet states, as the region, where the ground state refinements are applied, is well covered by the spectroscopic studies. For the triplet states, one has to employ refinements through the corresponding $a^3\Sigma^+$ state, which gives good results for $R > 4.55$ Å up to and beyond the LeRoy radius. For smaller internuclear distances, the short-range description could be used from the ground state, but already small differences in the short-range parameters could lead to massive discrepancies due to the high inverse powers involved, and the refinement procedure would actually worsen the initial potential. To circumvent artifacts arising of such modifications, the refined part is instead smoothly connect to the respective RKR parts at $R = 4.65$Å. The final PECs used for the following calculations are shown in fig. 63 (dashed lines) together with the RKR curves obtained from [69, 70, 71] (solid lines), showing satisfactory agreement.

8.2.2 *Spin character of excited molecular states*

Similar to the ground state discussion, this analysis begins by inspecting the spin character of the individual eigenstates. For finding the eigenstates the molecular state vectors in (a) are unitarily transformed into the Hund's case (e) basis, as the spin-orbit operator is diagonal in this representation. A diagonalization procedure then gives rise to a set of eigenstates and -energies for each total angular momentum J, spanning 7000 cm^{-1} for the full depth of $b^3\Pi$. Projecting the eigenstates onto the Hund's case (a) state vectors and integrating their squared amplitudes yields the fractions of the individual channels. This is shown in fig. 64 for $\Omega = 1$ and a frequency window of 3000 cm^{-1} below the dissociation limit $3^2S_{1/2}$(Na)+$4^2P_{3/2}$(K). Symbolic notations such as $^3\Sigma^+(^3\Pi)$ marks the channel fraction of $^3\Sigma^+$ within a dominant $^3\Pi$ state. In the JILA scheme [56] an eigenstate of the type $^1\Pi \sim^3 \Sigma \sim^3 \Pi$ was used, where the notion $\sim$ implies coupling. Therefore, the focus here lies on the $^1\Pi - ^3\Pi$ and $^1\Pi - ^3\Sigma^+$ coupling because this promises to have a strong Stokes transition from $B^1\Pi$ to $X^1\Sigma^+$. The resulting structure can be briefly divided into two regions, which are naturally split at the energy E_0 of the lowest level of $B^1\Pi$, being indicated in fig. 64 by a black vertical line.

The region lying energetically below E_0 can be classified as a *perturbative* region. The eigenstates display $> 99\%$ character of either the $^3\Sigma^+$ (red squares) or $^3\Pi_1$

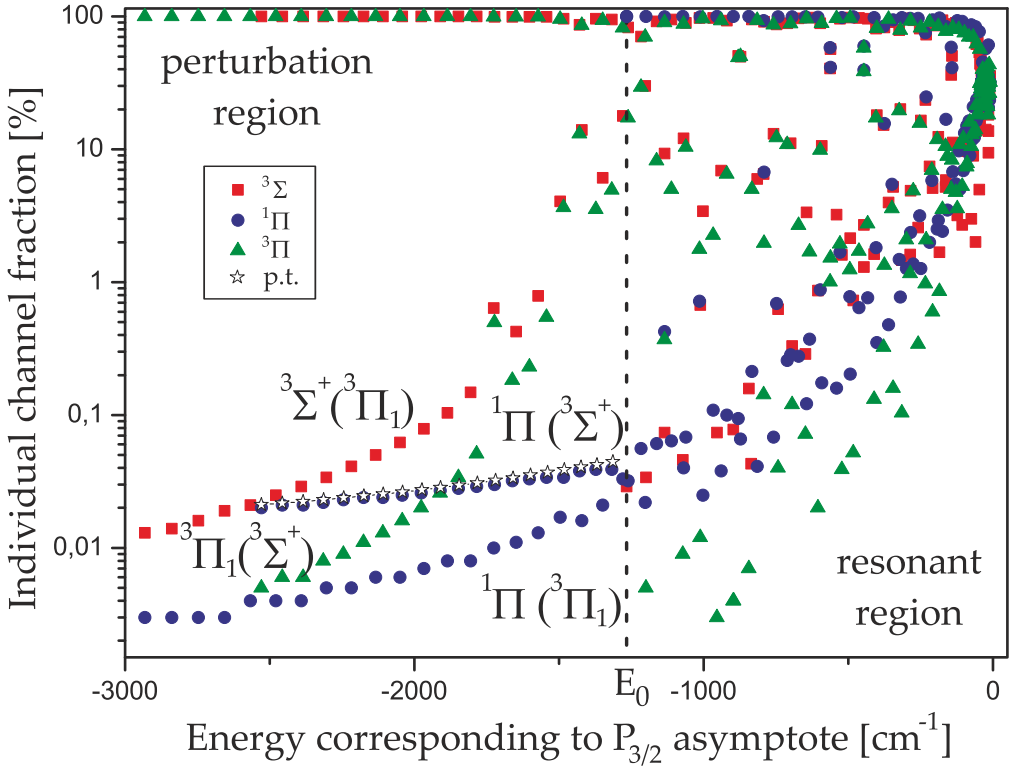

Figure 64: Integrated square of the individual $\Omega = 1$ channel wave functions at each eigenenergy, together with a $J = 1$ perturbative model for the $^1\Pi(^3\Sigma^+)$ case (open stars, p.t. = perturbation theory). A label of the form $^3\Sigma^+(^3\Pi)$ marks the $^3\Sigma^+$ fraction within a dominant $^3\Pi$ state. The vertical line at E_0 is positioned at the first state with dominant $^1\Pi$ character [1].

(green triangles) channel in the upper line of fig. 64. Note that this corresponds to a distinct molecular structure, where the assignment of measured energies to vibrationally bound levels is straightforward. In this area, $^1\Pi$ (blue dots) fraction is generated in almost pure $^3\Sigma^+$ states via spin-orbit coupling and in almost pure $^3\Pi_1$ states via higher order effects, as the direct coupling matrix element between $^1\Pi$ and $^3\Pi_1$ is strictly zero. The spin-orbit induced singlet admixture in $^3\Sigma^+$ states becomes $0.02 - 0.04\%$.

This result can be understood by a simple perturbative approach. The k-th eigenstate of $^1\Pi$ is denoted as $\left|\psi_k^{^1\Pi}\right\rangle$ and its eigenenergy as E_k, similarly the n-th bound $^3\Sigma^+$ level as $\left|\psi_n^{^3\Sigma}\right\rangle$ and E_n. Approximating the spin-orbit operator by its atomic coupling constant ξ_K, the first order state correction of the almost pure triplet manifold becomes

$$\sum_k \frac{\langle\psi_k^{^1\Pi}|\hat{\xi}|\psi_n^{^3\Sigma}\rangle}{E_k - E_n}\left|\psi_k^{^1\Pi}\right\rangle \approx \xi_K \times \sum_k \frac{FCF(k,n)}{\Delta E_{k,n}}\left|\psi_k^{^1\Pi}\right\rangle \tag{8.27}$$

where the problem reduces to a calculation of the vibrational overlap FCF between the states of interest and their respective energy difference $\Delta E_{k,n}$. Summing the squared coefficients of eq. (8.27) results in the singlet fraction of the n-th triplet state, which is also displayed in fig. 64 (open stars), and the good agreement with the simulation emphasizes the perturbative character of the admixing. Note that the absolute amount is slightly overestimated by the perturbative approach. The dominant contribution in eq. (8.27) to the interaction comes from the k-th vibrational $^1\Pi$ level sharing considerable (42% mean) wave function overlap with the $n = k + 2$-th vibrational $^3\Sigma^+$ level, which originates accidentally from the relative forms of the potentials and their relative positions in r.

For completeness, also the $^3\Sigma^+ - ^3\Pi$ interaction is discussed. Far below E_0, the eigenstates have either dominantly $^3\Sigma^+$ or $^3\Pi$ character. However, the interaction features a frequency window of around $400\,cm^{-1}$ below E_0, in which the assignment to an experimental observation becomes difficult because the admixtures of either $^3\Sigma^+$ ($^3\Pi$) character to $^3\Pi$ ($^3\Sigma^+$) exceed 1%. As the eigenenergies approach around $E \approx -1200\,cm^{-1}$, the mixed amount rapidly increases to 30% and decreases subsequently, displaying a resonant behavior. In this energy interval the two potentials $^3\Sigma^+$ and $^3\Pi$ cross each other. The vibrationally averaged interaction parameter then largely exceeds the vanishing frequency difference, and the crossing resonance occurs. The appearance of this structure near E_0 is accidental.

At and above E_0, the assignment of structures in fig. 64 becomes complicated, and work in this area will be accompanied by increased spectroscopic effort. This region is classified as the *resonant* region, because the presence of vibrationally bound $^1\Pi$ states is accompanied by levels of other electronic states. These resonances are qualitatively different from the crossing resonances discussed before. They appear due to energetically nearly degenerate singlet and triplet rovibrational levels ($\Delta E_{n,k} \lesssim 5\,cm^{-1}$), when the interaction parameter will be larger than the energy difference and any perturbative treatment will break down. The resonantly interacting states share no similarities concerning relative vibrational quantum numbers, and no simple pattern can be identified in the spectrum.

Such accidentally resonant structures also appear below the first $^1\Pi$ state and belong to $^1\Sigma^+ - ^3\Pi_0$ states coupling with $\Omega = 0^+$, which have been removed from fig. 64 for clarity. Also a perturbative region admixing $^1\Sigma^+$ character to dominantly

$^3\Pi_0$ states exists just below the potential minimum of the $^1\Sigma^+$ state about 6000 cm^{-1} below the asymptote, and is almost overlayed by the $^1\Sigma^+ - {}^3\Pi_0$ crossing resonance. As the wave functions involved in this low energy region only spread over a small internuclear distance range, the overlap with the Feshbach molecular wave function will be small and two-photon transfer not efficient. The general two-photon process will be quantified in the following section.

Discussion

The suitability of the found structures (second order admixing, crossing resonances and degenerate resonances) are shortly discussed for the two-photon process, commenting on their robustness to changes in the PECs. Shifting the potential curves in terms of total energy or equilibrium distance will shift the crossing resonances accordingly to the new crossing position, but will not alter their fundamental structure. On the other hand, the direct resonances occurring in near-degenerate states will react highly sensitive to any potential change due to their accidental nature. Despite the good agreement of the refined PECs with experimental data, it puts large uncertainties in the actual mixing value of such a resonance. In fact, by changing the PEC parameters slightly, some resonances will vanish completely and others appear. This model is therefore not reliable for giving quantitatively exact predictions of the positions and values of the resonant mixtures.

The second order admixed states in the perturbative region will present the most robust structures. They will be largely unaffected by energetic offsets, as only the energy denominator in eq. 8.27 varies, and a mismatch by 1 cm^{-1} will change $\Delta E_{n,k}$ by less than 0.1 %. Also slight radial mismatches in the turning points will only introduce minor corrections due to the integral nature of the $^3\Sigma^+$ state perturbation by the $^1\Pi$ manifold. Together with the relative spectroscopic ease which awaits one at such a perturbative level, this highlights the perturbative region as being a good candidate for the desired two-photon transfer. Yet the absolute value of the singlet spin character might cast doubt on the suitability of these states for the two-photon process. For the KRb analogue, the used level was reported to possess a singlet character of 0.2% [248]. By just comparing the SO coupling strengths, one would expect the NaK case to have a factor $(\xi_{Rb}/\xi_K)^2 \approx 17$ lower admixture. This is partially compensated for due to the earlier discussed potential shapes, which favor the NaK case. The NaK admixture of around 0.04%, a typical value from fig. 64, is still a factor of 5 lower than the KRb one. For a definite statement, one has again to inspect closely the wave functions and calculate transition matrix elements, which is quantified below.

8.3 TWO-PHOTON PROCESS

In the previous sections, a full understanding of ground and excited state molecular potentials was provided. Everything is now set to quantify the two-photon transition matrix element $d_{(F\to X)}$ given by equation (8.1). For the Feshbach state the broad $F = 9/2$ resonance appearing for $\mathcal{M} = -3/2$ is used. Decomposing the Feshbach molecular state vector yields the individual channel contributions. Because the Hilbert spaces of the ground and excited states do not match (the ground state comprises hyperfine structure), the Feshbach molecular state is presented using

the least bound vibrational states, as depicted in 61: Note that by cutting off the other channels, interference effects of those contributions are ignored, and only interference of the strongest channels with each other is considered. The neglected amplitude would gain importance when evaluating the hyperfine structure for the excited states. Using this approach, the Feshbach molecular state cany be approximated by

$$|\psi_F(B)\rangle \approx \beta_X(B)\left|X^1\Sigma^+(v=74, J=0)\right\rangle + \beta_a(B)\left|a^3\Sigma^+(v=19, J=0)\right\rangle \quad (8.28)$$

where β_i $(i = a, X)$ are the magnetic field dependent scaling factors obtained in the matching procedure of section 8.1.

The transition dipole matrix elements are calculated from the Feshbach molecular state and the $X^1\Sigma^+(v=0, J=0)$ state to all $j = \{1, \ldots, 683\}$ electronically excited bound eigenstates obtained up to 10 cm^{-1} below the atomic asymptote $P_{3/2}$ of potassium. They formally read $|\psi_{int.,j}\rangle = \sum_i c_{i,j}\,|i\rangle$, with $i = \left\{^1\Sigma^+, {}^3\Sigma_1^+, {}^1\Pi, {}^3\Pi_0, {}^3\Pi_1\right\}$, where the sums of the squared coefficients give the channel fractions shown in fig. 64 of section 8.2. The radial dependent singlet and triplet electronic transition dipole moments are taken from [245].

The resulting absolute values $|d_X|$ of the dipole matrix elements from the ground state $X^1\Sigma^+(v=0, J=0)$ to the intermediate states and $|d_a|$ from the Feshbach state to the intermediate states are shown in fig. 65 as a function of the intermediate state eigenenergy for a magnetic field of $B = 110$ G for all states with $\Omega = 0^+$ and $\Omega = 1$. In the upper graph, locally strongest transitions to singlet (triplet) dominant eigenstates have been connected by a red (blue) line, serving as a guide to the eye. In the lower graph, the locally strongest triplet (singlet) transitions are connected by blue (red) lines, representing transitions to triplet (singlet) dominated states.

The one-photon process corresponding to the Stokes pulse is discussed first, which is shown in the upper graph of fig. 65. The rovibronic ground state is localized at the bottom of the $X^1\Sigma^+$ potential, which has its minimum at $R_{eq,X} = 3.499$Å. In the region in which this singlet wave function has significant amplitude, the singlet transition dipole moments do not vary by more than 10%, being 9.7 Debye $(A^1\Sigma^+)$ and 7.5 Debye $(B^1\Pi)$ at the equilibrium distances [245]. The ground state wave function then acts as a Gaussian filter between 3 and 4 Å for the singlet part of the intermediate states. The first eight eigenstates around -7000 cm^{-1} in fig. 65 have dominant triplet character, resulting in modest matrix elements. As soon as the bottom of the $A^1\Sigma^+$ PEC is reached, the matrix element rises steadily due to the increasing Franck-Condon factors. When the inner turning point of the $A^1\Sigma^+$ state approaches $R_{eq,X}$, the matrix element maximizes at 2.92 Debye for the eigenstates around $E \approx -5260\,cm^{-1}$ and decreases rapidly thereafter. Due to the large electronic dipole moment of the $X^1\Sigma^+$ to $A^1\Sigma^+$ molecular transition, its peak value gives the global maximum moment achievable for the Stokes pulse. A similar behavior is observed around E_0, when $B^1\Pi$ contributions enter into the intermediate states and the matrix element peaks with an absolute value of 2.52 Debye at $E \approx -900\,cm^{-1}$. In addition to the two singlet dominant structures, one recognizes the window (blue color in fig. 65) between the potential minima of the $c^3\Sigma^+$ and the $B^1\Pi$ state. In this region, a significant admixture of $B^1\Pi$ character to the dominantly $c^3\Sigma^+$ molecular states leads to significant transition dipole moment from the purely singlet $X^1\Sigma^+(v=0, J=0)$ state to the $c^3\Sigma^+$ dominated

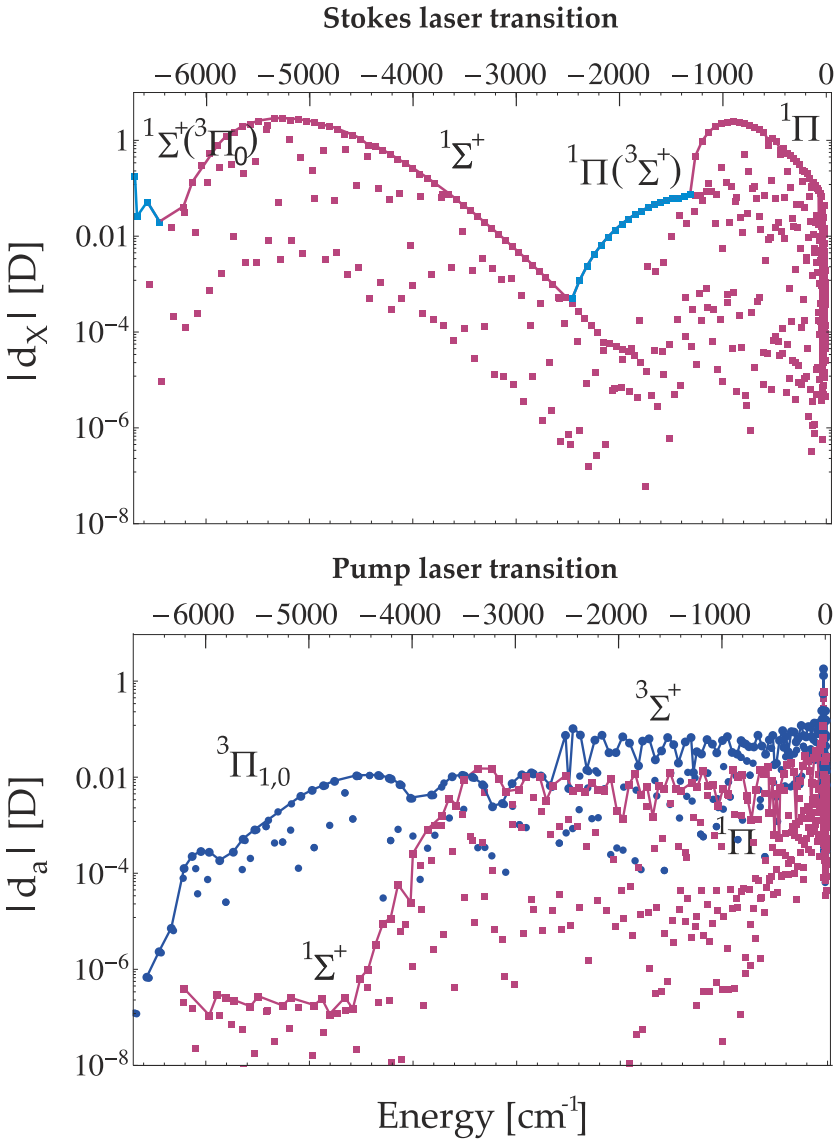

Figure 65: Absolute values of the transition dipole matrix elements for all intermediate states. Upper graph: Stokes laser transitions ($|i\rangle \rightarrow |X\rangle$). Lower graph: Pump laser transitions ($|F\rangle \rightarrow |i\rangle$, decomposed into the singlet (red squares) and triplet (blue circles) part). The energy is given with respect to the $P_{3/2}$ dissociation limit [1].

intermediate states. Note that transition matrix elements to these triplet dominant states largely exceed matrix elements to close lying singlet dominant states.

The lower graph of fig. 65 shows the matrix elements obtained for the Pump pulse. Due to the large extension of the loosely bound Feshbach molecules over considerable internuclear distances, the wave function overlap will in general tend to be larger the closer the intermediate level gets to the dissociation limit. This is strongly noticeable for the singlet fraction, which shows a sharp rise in dipole matrix element around $E \approx -4500\,\mathrm{cm}^{-1}$ due to largely increasing Franck-Condon factors. At lower energies, the singlet dipole matrix elements are below 10^{-6} Debye and the singlet component can be considered negligible. At $E \approx -2530\,\mathrm{cm}^{-1}$, the triplet matrix element rises by one order of magnitude, marking the beginning of the $c^3\Sigma^+$

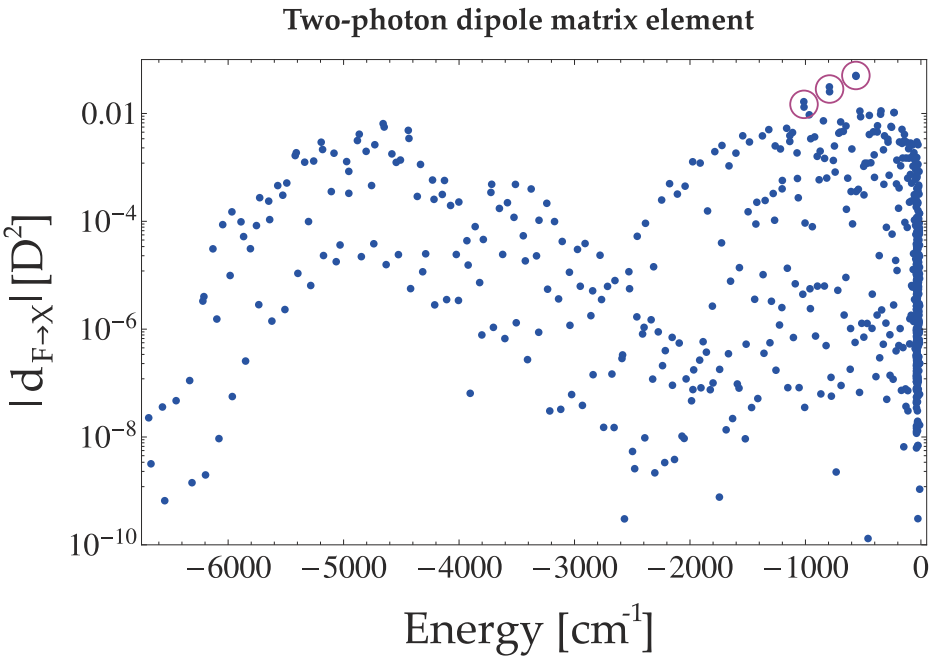

Figure 66: Absolute value of the two-photon dipole matrix element. The circles mark double dots that indicate degeneracy induced resonances [1].

dominated intermediate states. Matrix elements corresponding to these transitions are about one order of magnitude larger than the ones which can be assigned to $^3\Pi$ transitions, owing to the fact that the $^3\Sigma^+$ electronic transition dipole moment is considerably larger in the region of interest, which is further enhanced by a higher Franck-Condon overlap at the outer turning points. The largest values appear for levels at and beyond the $P_{1/2}$ asymptote ($E = -57.72\,\mathrm{cm}^{-1}$). However, the density of states is very large in this area. In addition, phenomena like predissociation have to be taken into account, opening unfavorable decay channels.

Figure 66 shows the two-photon transition dipole matrix element $d_{(F\to X)}$ obtained from the matrix elements shown in fig. 65. Degeneracy induced resonances can be recognized due to the appearance of double dots, examples are encircled in fig. 66. The largest transition dipole matrix elements are obtained at one of these resonances situated in the $^3\Sigma^+ - {}^1\Pi$ regime, where two-photon matrix elements of $0.052\,\mathrm{Debye}^2$ can be reached at $E \approx -560\,\mathrm{cm}^{-1}$ making these resonances highly interesting for two-photon transfer schemes. However, the exact positions and properties of degeneracy induced resonances critically depend on small corrections of excited state molecular potentials and their prediction should be taken with care. Making use of these resonances demands accurate spectroscopic knowledge of the resonance positions as they can only be pinpointed by experiments.

Further possible pathways can be identified by investigating levels in the perturbation region, as their theoretical description is much more robust. Intermediate $c^3\Sigma^+$ levels perturbed by a small admixture of singlet character from the $B^1\Pi$ molecular potential lead to two-photon coupling matrix elements from the Feshbach state to the $X^1\Sigma^+(v = 0, J = 0)$ state of $10^{-5} - 10^{-2}\mathrm{Debye}^2$, coming close to the values obtained for degenerate resonances. It is further noted that in this area, the one-photon dipole moments for the two involved transitions can be of similar

magnitude. In general, a two photon STIRAP sequence benefits from similar peak Rabi frequencies of Pump and Stokes pulse in terms of robustness. Those states are found e.g. at $E \approx -1542\,\mathrm{cm}^{-1}$, when the singlet (triplet) dipole matrix elements read 0.057 (0.069) Debye. For the ground state case, this exceeds the 0.046 Debye reported in a similar analysis for the KRb case [248]. It can therefore be concluded that such states will be highly promising candidates for the two-photon process.

9 OUTLOOK

In this thesis, a novel experimental apparatus was presented and its capabilities to realize quantum degenerate matter successfully demonstrated. The main obstacle in dual species operation for this mixture, namely sizable three-body losses due to strong interspecies interaction, was effectively eliminated. By locating Feshbach resonances, the interspecies interaction became freely adjustable, and for the first time, a Bose condensed mixture of ^{23}Na + ^{39}K was simultaneously created. The experimental achievements were complemented by a theoretical study concerned with the coherent transfer of a triplet-dominated Feshbach molecule to the ground rovibrational singlet state. The necessity of a singlet-triplet bridge was proven, and the excited state manifold was resolved in terms of spin character and dipole matrix elements in order to provide possible two-photon pathways. The conjunction of theoretical and experimental efforts are the NaK molecular potential energy curves, for which profound understanding has been acquired on both the theoretical and experimental level. In the following sections, the next steps planned with the NaK system are presented.

QUANTUM DROPLETS

The experimental achievements of this thesis put this system into the quantum degenerate realm, which enables a wide variety of further phenomena to be studied. In addition to the planned magnetoassociation into quantum degenerate Feshbach molecules, also the investigation of quantum degenerate mixtures is possible. The location of the found Feshbach resonances and the resulting shape of the interspecies scattering length leads to a surprisingly rich playground for studying miscibility phenomena. The key elements here are the coincidental overlap of intra- and interspecies resonance, the interspecies zero crossing in the outlined magnetic field valley and the constant ^{23}Na scattering length. The combination of these three properties dictate the shape of the magnetic field valley, in which *all* common mixture phases can be found. Any experimental studies in these region will benefit from the large width of the corresponding magnetic field regions, when an elaborated magnetic field stabilization is not necessary.

Above all, the investigation of the interaction regions revealed the presence of a *droplet region* in a magnetic field range around 150 G. These droplets have spectacular properties. Most notably they are self-stabilizing objects, i.e. their density distribution shows no expansion even in absence of a trapping potential. This phenomenon can be of great interest also for other research fields such as matter wave interferometry. A topical idea in this research field is to conduct future measurement campaigns in microgravity environments or on satellites, as the leading order phase shift scales quadratically with the available interferometry time [133]. In such systems, the interferometry time is mainly limited by the expansion velocity of the source. As a quantum droplet *does not expand*, the realization of a single macro-droplet could significantly increase the achievable sensitivity.

An investigation of this effect is therefore highly desirable. The theory of droplets is still quite young, and the same holds true for their experimental realization. Droplets have been realized 2016 in dipolar dysprosium [37] followed by the realization 2017 in a potassium spin mixture [99]. In the latter system, the droplets showed low lifetimes on the order of $\sim 10\,\mathrm{ms}$, which was attributed to three-body decay. Realizing it in the $^{23}\mathrm{Na} + {}^{39}\mathrm{K}$ system would be the first demonstration of this effect as a *two-species droplet*. A benefit of the Na + K system is that the individual scattering lengths in the droplet region are $\sim 50\,a_0$ each, which means that rather long lifetimes of the samples are in reach. The temperature and density dependent three-body losses of the relevant magnetic field range are currently under investigation. At the same time a theoretical collaboration with the Santos group in Hannover was started, in which the corresponding beyond-mean-field terms were derived and numerical simulation performed that match the parameters of the Hannover NaK experiment.

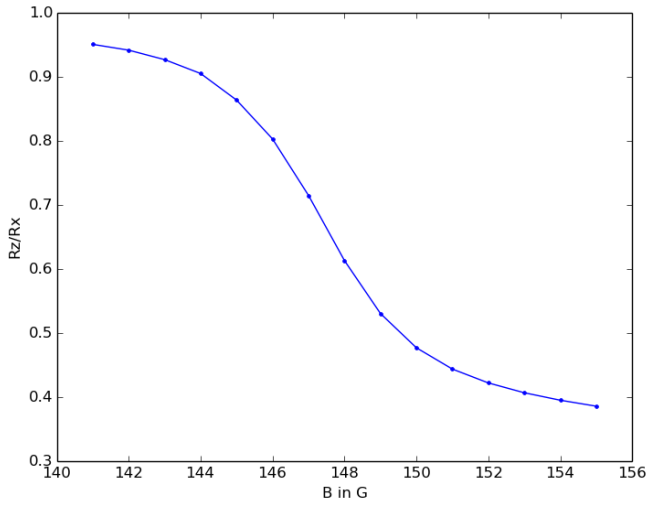

Figure 67: Calculated aspect ratio R_z/R_x for a Gross-Pitaevskii equation including beyond-mean-field effects for the magnetic field region of interest and typical trap parameters of this experiment. The droplet solution enforces a radial symmetric profile. Picture provided with courtesy from Daniel Edler.

Figure 67 shows the radial profile of a typical simulation result in the critical region. As a first experimentally detectable signature, the aspect ratio of the droplet compared to the BEC could be identified. As already described in the fundamental part of this thesis, a BEC is characterized by a density distribution that is largely similar to the inverted trap potential. Initial simulations show that this does not apply to the heteronuclear droplet solution, which instead enforces radial symmetry. Droplets could then be identified by a bimodal structure, with a round droplet in the middle and deformed condensate flanks. This effect can be enhanced by setting a large trap aspect ratio, e.g. by adiabatically ramping down one of the trapping beam intensities. The resulting waveguide-like trap should clearly unveil the corresponding signature. A study of this novel state of matter would be a direct investigation of a quantum many-body system, and thus fits perfectly to the dipolar phenomena that will be investigated in this experiment in the long run.

THE COMPLETE FESHBACH SPECTRUM

In chapter 8, Feshbach resonances were examined with regard to their suitability for the envisaged two-photon transfer. By decomposing the scattering wave function near a Feshbach resonance into its singlet and triplet components, it was shown that a cleverly selected operating point can significantly increase the usable radial part of the wave function. In that chapter, only an exemplary representation was given, since resonances using the fermionic isotope ^{40}K were used. A thorough investigation of this mechanism for bosonic resonances has so far been postponed, simply due to the lack of experimental data for comparison. With the realized experimental apparatus, it is now possible to acquire the complete Feshbach spectrum for the bosonic isotope. In this thesis, Feshbach spectroscopy was performed in the spin state combination $|1,-1\rangle + |1,-1\rangle$. Of special interest is the $|1,1\rangle + |1,1\rangle$ combination, as it constitutes the absolute ground state of the diatomic system. For an overview, the remaining resonances to be expected are listed in table 6. In subsequent measurement campaigns, Feshbach spectra could already be obtained in other collisional channels, where the theoretical and experimental treatment is essentially identical to the one outlined in chapter 7 of this thesis. The current stage of this campaign is the theoretical comparison and further data evaluation, and the results will be presented in a forthcoming thesis [162]. The encompassing knowledge about the collisional spectra, acquired through the bosonic and fermionic isotope, can then be used to further improve the molecular potential energy curves, which in turn further increases the prediction accuracy for the two-photon process.

Feshbach resonance choice for ground state transfer

With all Feshbach resonances being resolved, the theoretical study, which has been presented here for the fermionic isotope, can be extended to the bosonic case. The theoretical study of Viel & Simoni has already taken a similar path [187]. In their article they represent spin expectation values not only as a function of the magnetic field but also by their radial dependence. They concluded that for ^{23}Na^{39}K, Feshbach resonances exist in which the singlet character can be large, but will be *not* delocalized such as the fermionic combination was proven in this thesis to be. However, it is pointed out again that the predictions in [187] are based on a significantly worse model of the singlet potential and should be taken with care. It therefore seems wise to revisit these calculations with the updated potential curves. A comprehensive examination using the approach outlined in chapter 8 can then be readily adapted to the bosonic case. The refined excited state potentials generated in this work are identical for both isotopes, and only the hyperfine terms of the ground state potential have to be replaced.

$\mathcal{M} = m_{Na} + m_K$	$\|f, m_f\rangle_{Na} + \|f, m_f\rangle_K$	B_{res}[G]
2	$\|1,1\rangle + \|1,1\rangle$	410.0
		508.5
1	$\|1,1\rangle + \|1,0\rangle$	6.5
		329.0
		467.0
		580.5
	$\|1,0\rangle + \|1,1\rangle$	8.5
		418.5
0	$\|1,0\rangle + \|1,0\rangle$	5.5
		29.5
	$\|1,1\rangle + \|1,-1\rangle$	15.0
		393.5
		536.5
		>600
	$\|1,-1\rangle + \|1,1\rangle$	10.0
	$\|1,-1\rangle + \|1,1\rangle$	522.5
-1	$\|1,-1\rangle + \|1,0\rangle$	12.5
	$\|1,0\rangle + \|1,-1\rangle$	107.5
		540.5
		138.0
		471.0
		>600
-2	$\|1,-1\rangle + \|1,-1\rangle$	33.3
		247.68
		650
	$\|1,0\rangle + \|2,-2\rangle$	229.5
		260.5
		>600
	$\|2,-2\rangle + \|1,0\rangle$	360
		528

Table 6: Overview of predicted Feshbach resonances for the different spin state combinations. The calculations have been performed on a grid spacing of half a Gauss in a magnetic field region $< 600\,G$. The $|1,-1\rangle + |1,-1\rangle$ structures have been observed in this work. All others will be presented in [162].

TO THE GROUND STATE

Having selected a suitable resonance, atom pairs will be converted into molecules using rf-association. Here, the magnetic field is moved into the vicinity of a resonance, and a radio frequency is matched to the binding energy of the molecular state. This method has been already thoroughly investigated in other systems [55, 230, 74], and with the high knowledge of the underlying molecular potentials, the binding energy can be precisely predicted. Afterwards, the stage is set for molecular spectroscopy using the associated molecules. Through a combined theoretical and experimental effort [1, 203], the wavelength region around 816 nm (for the pump pulse, or "up-leg") and 573 nm (for the Stokes pulse, or "down-leg") has been selected. As a wavelength of 573 nm is difficult to realize without relying on dye lasers, the corresponding laser frequency will be provided by frequency doubling a 1146 nm source.

The two-photon transition will be executed in STIRAP (Stimulated Raman adiabatic passage) configuration [249]. An excellent review on this method can be found in [250]. In a STIRAP sequence, pump and Stokes beam couple the initially populated state $|1\rangle$ and the target state $|2\rangle$ resonantly to an excited state $|e\rangle$. Both beams are operated in pulse mode, and the pulses act in *seemingly counterintuitive* ordering (first Stokes pulse, then pump pulse, with an overlap inbetween). When the Stokes beam is initialized, the initial state $|1\rangle$ does not interact with the given light field - it is the *dark state* $|\mathcal{D}(t=0)\rangle$ of the system as the process starts. As the pump pulse intensity raises, a dark state $|\mathcal{D}(t)\rangle$ can always be found through destructive interference of pump and Stokes beam, and the admixture of $|1\rangle$ and $|2\rangle$ into the dark state is given by the mixing angle, i.e. the local Rabi frequency ratio of both beams. Using the adiabatic theorem, the atoms will always follow the dark state if the pulse shape is chosen accordingly. Quite remarkable, the ensuing adiabatic passage can be crafted such that the excited state is never populated, which suppresses spontaneous emission and allows to work on resonance.

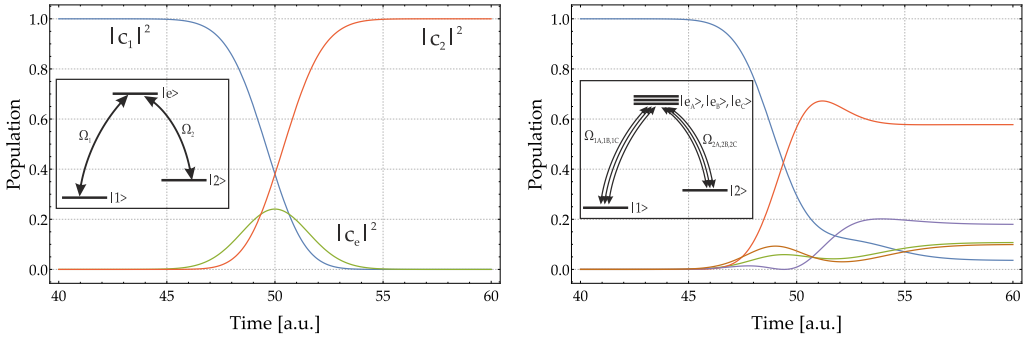

Figure 68: STIRAP population dynamics. Left: In an ideal three-level STIRAP scenario (time-delayed Gaussian pulses with anti-intuitive ordering, not shown here), particles are succesfully transferred with a transfer rate of about 1 from an initial to a target state without significantly populating the intermediate state. The temporal pulse area was deliberately shifted from the "perfect" case (5π) to highlight that small changes lead to an excited state contribution. Right: The presence of non-resolved hyperfine structure gives rise to a set (here: three) of STIRAP transitions with different Rabi frequencies. In this example, typical Clebsch-Gordan coefficients were used for the relative coupling matrix elements. The resulting transfer efficiency is significantly reduced.

This works great in an idealized three-level system as shown in 68. However, recent experimental results in fermionic $^{23}Na^{40}K$ showed that the hyperfine spectrum of the excited state manifold can affect the STIRAP efficiency [135, 251]. For the excited state used in that study, a single hyperfine transition cannot be isolated due to the absence of Fermi contact interaction. The individual excited states are not coupled directly with each other because of selection rules. They do however lead to a fragmentation of the STIRAP process in multiple parts. Therefore instead of one STIRAP with one well-defined dark state, they drive multiple STIRAP transitions simultaneously, all with different Rabi frequencies and dark state conditions. The resulting dephasing destabilizes the intended dark state and considerably worsens the achievable transfer efficiency. An exemplary simulation for this is also shown in 68.

For the Hannover experiment, this implies that the Feshbach resonance has to be selected in terms of possible complications arising in the excited state manifold. The collaboration with the Tiemann group has already investigated hyperfine state resolved spectra in a molecular beam experiment [203], which will strongly help to choose an atomic state combination in which intermediate state complications can be minimized.

On the experimental side, the STIRAP system has been completely setup. A picture of the different parts of the setup is shown in fig. 69. Both the 816 nm and

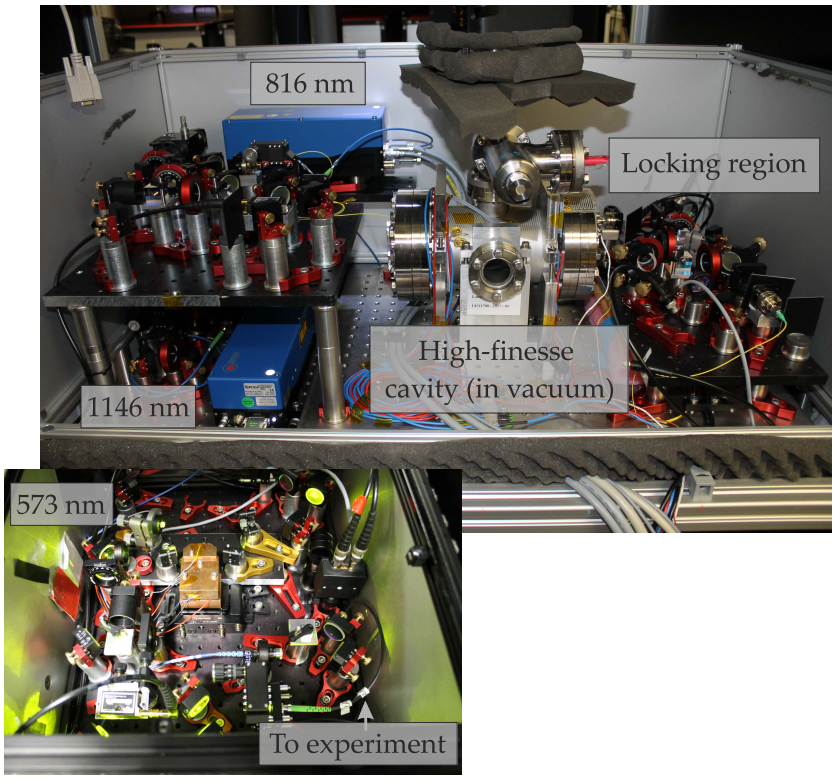

Figure 69: STIRAP lasers and locking region (details see text).

1146 nm laser wavelengths will be provided by tunable TOPTICA DL-pro diode laser systems. As molecular Rabi frequencies are usually small, the relative laser phase of the beams has to be stable over a rather long time, which translates into a desired relative linewidth of the beams of < 1 kHz [252]. In conventional systems, stability is achieved by beating both beams on a photodiode, which is not possible

here owing to the large frequency difference of the beams to each other. A part of both sources are therefore locked onto a high-finesse ($\mathcal{F} \approx 16000$) Fabry-Perot cavity situated in a vacuum environment. To provide tunability of the beams, the light sent to the locking region is traversing fiber-coupled EOMs and the shiftable sideband peaks can be locked onto the cavity modes. At the moment of writing, all beam paths, the frequency doubling stage and locking of both beams onto the cavity has been succesfully realized [116].

Hence molecular spectroscopy can be started as soon as Feshbach molecules have been realized. It is mentioned that molecular spectroscopy can also be done in cold atomic systems which have not been Feshbach associated yet. This gives a tradeoff between the experimental cycle time (faster data acquisition allows faster averaging of noisy spectra), and the smaller Rabi frequency (the free atomic scattering wave function is about a factor 100 weaker localized at low internuclear distances).

Having accomplished the ground state transfer, the last pending question is whether first measurements in this realm will be conducted in an optical dipole trap or an optical lattice. This experiment intends to use a 1064 nm based optical lattice system that has been already set up and whose corresponding beams have been already aligned into the main chamber. Performing experiments in an ODT system will focus more on the chemical reactivity in ultra-cold collisions, and can help to understand the molecular properties of ultra-cold NaK. Quantum chemical effects will be strongly suppressed in an optical lattice, and working in such an environment will emphasize the dipolar properties of the system. In both cases, the number of posable theoretical questions, thinkable physical scenarios and possible experimental measurements will be endless.

BIBLIOGRAPHY

[1] T. A. Schulze, I. I. Temelkov, M. W. Gempel, T. Hartmann, H. Knöckel, S. Ospelkaus, and E. Tiemann. Multichannel modeling and two-photon coherent transfer paths in NaK. *Physical Review A*, 88(2), aug 2013. doi: 10.1103/physreva.88.023401.

[2] Florian Richter, Daniel Becker, Cédric Bény, Torben A Schulze, Silke Ospelkaus, and Tobias J Osborne. Ultracold chemistry and its reaction kinetics. *New Journal of Physics*, 17(5):055005, 2015. URL http://stacks.iop.org/1367-2630/17/i=5/a=055005.

[3] M W Gempel, T Hartmann, T A Schulze, K K Voges, A Zenesini, and S Ospelkaus. Versatile electric fields for the manipulation of ultracold nak molecules. *New Journal of Physics*, 18(4):045017, 2016. URL http://stacks.iop.org/1367-2630/18/i=4/a=045017.

[4] Torben A. Schulze, Torsten Hartmann, Kai K. Voges, Matthias W. Gempel, Eberhard Tiemann, Alessandro Zenesini, and Silke Ospelkaus. Feshbach spectroscopy and dual-species bose-einstein condensation of na23-k39 mixtures. *Physical Review A*, 97(2), feb 2018. doi: 10.1103/physreva.97.023623.

[5] K. B. Davis, M. O. Mewes, M. R. Andrews, N. J. van Druten, D. S. Durfee, D. M. Kurn, and W. Ketterle. Bose-einstein condensation in a gas of sodium atoms. *Physical Review Letters*, 75(22):3969–3973, nov 1995. doi: 10.1103/physrevlett.75.3969.

[6] M. H. Anderson, J. R. Ensher, M. R. Matthews, C. E. Wieman, and E. A. Cornell. Observation of bose-einstein condensation in a dilute atomic vapor. *Science*, 269(5221):198–201, jul 1995. doi: 10.1126/science.269.5221.198.

[7] C. C. Bradley, C. A. Sackett, J. J. Tollett, and R. G. Hulet. Evidence of bose-einstein condensation in an atomic gas with attractive interactions. *Physical Review Letters*, 75(9):1687–1690, aug 1995. doi: 10.1103/physrevlett.75.1687.

[8] Markus Greiner, Cindy A. Regal, and Deborah S. Jin. Emergence of a molecular bose–einstein condensate from a fermi gas. *Nature*, 426(6966):537–540, nov 2003. doi: 10.1038/nature02199.

[9] Maciej Lewenstein, Anna Sanpera, Veronica Ahufinger, Bogdan Damski, Aditi Sen(De), and Ujjwal Sen. Ultracold atomic gases in optical lattices: mimicking condensed matter physics and beyond. *Advances in Physics*, 56(2):243–379, mar 2007. doi: 10.1080/00018730701223200.

[10] Martin T. Bell and Timothy P. Softley. Ultracold molecules and ultracold chemistry. *Molecular Physics*, 107(2):99–132, jan 2009. doi: 10.1080/00268970902724955.

[11] H. Perrin. Ultra cold atoms and bose-einstein condensation for quantum metrology. *The European Physical Journal Special Topics*, 172(1):37–55, jun 2009. doi: 10.1140/epjst/e2009-01040-8.

[12] C. A. Regal, M. Greiner, and D. S. Jin. Observation of resonance condensation of fermionic atom pairs. *Physical Review Letters*, 92(4), jan 2004. doi: 10.1103/physrevlett.92.040403.

[13] M. W. Zwierlein, C. A. Stan, C. H. Schunck, S. M. F. Raupach, A. J. Kerman, and W. Ketterle. Condensation of pairs of fermionic atoms near a feshbach resonance. *Physical Review Letters*, 92(12), mar 2004. doi: 10.1103/physrevlett.92.120403.

[14] Markus Greiner, Olaf Mandel, Tilman Esslinger, Theodor W. Hänsch, and Immanuel Bloch. Quantum phase transition from a superfluid to a mott insulator in a gas of ultracold atoms. *Nature*, 415(6867):39–44, jan 2002. doi: 10.1038/415039a.

[15] Michael L. Wall. *Quantum Many-Body Physics of Ultracold Molecules in Optical Lattices*. Springer International Publishing, 2015. doi: 10.1007/978-3-319-14252-4.

[16] Massimo Boninsegni and Nikolay V. Prokof'ev. Colloquium: Supersolids: What and where are they? *Reviews of Modern Physics*, 84(2):759–776, may 2012. doi: 10.1103/revmodphys.84.759.

[17] G. V. Chester. Speculations on bose-einstein condensation and quantum crystals. *Physical Review A*, 2(1):256–258, jul 1970. doi: 10.1103/physreva.2.256.

[18] E. Kim and M. H. W. Chan. Probable observation of a supersolid helium phase. *Nature*, 427(6971):225–227, jan 2004. doi: 10.1038/nature02220.

[19] E. Kim. Observation of superflow in solid helium. *Science*, 305(5692):1941–1944, sep 2004. doi: 10.1126/science.1101501.

[20] James Day and John Beamish. Low-temperature shear modulus changes in solid 4he and connection to supersolidity. *Nature*, 450(7171):853–856, dec 2007. doi: 10.1038/nature06383.

[21] Duk Y. Kim and Moses H. W. Chan. Absence of supersolidity in solid helium in porous vycor glass. *Physical Review Letters*, 109(15), oct 2012. doi: 10.1103/physrevlett.109.155301.

[22] William Gilbert. *De Magnete*. Dover Publications (New York), 1893.

[23] R. Mottl, F. Brennecke, K. Baumann, R. Landig, T. Donner, and T. Esslinger. Roton-type mode softening in a quantum gas with cavity-mediated long-range interactions. *Science*, 336(6088):1570–1573, may 2012. doi: 10.1126/science.1220314.

[24] M. Saffman, T. G. Walker, and K. Mølmer. Quantum information with rydberg atoms. *Reviews of Modern Physics*, 82(3):2313–2363, aug 2010. doi: 10.1103/revmodphys.82.2313.

[25] H. Haffner, C. Roos, and R. Blatt. Quantum computing with trapped ions. *Physics Reports*, 469(4):155–203, dec 2008. doi: 10.1016/j.physrep.2008.09.003.

[26] Julian Léonard, Andrea Morales, Philip Zupancic, Tilman Esslinger, and Tobias Donner. Supersolid formation in a quantum gas breaking a continuous translational symmetry. *Nature*, 543(7643):87–90, mar 2017. doi: 10.1038/nature21067.

[27] Jun-Ru Li, Jeongwon Lee, Wujie Huang, Sean Burchesky, Boris Shteynas, Furkan Çağrı Top, Alan O. Jamison, and Wolfgang Ketterle. A stripe phase with supersolid properties in spin–orbit-coupled bose–einstein condensates. *Nature*, 543(7643):91–94, mar 2017. doi: 10.1038/nature21431.

[28] Zhen-Kai Lu, Yun Li, D. S. Petrov, and G. V. Shlyapnikov. Stable dilute supersolid of two-dimensional dipolar bosons. *Physical Review Letters*, 115(7), aug 2015. doi: 10.1103/physrevlett.115.075303.

[29] Axel Griesmaier, Jörg Werner, Sven Hensler, Jürgen Stuhler, and Tilman Pfau. Bose-einstein condensation of chromium. *Physical Review Letters*, 94(16), apr 2005. doi: 10.1103/physrevlett.94.160401.

[30] Mingwu Lu, Nathaniel Q. Burdick, Seo Ho Youn, and Benjamin L. Lev. Strongly dipolar bose-einstein condensate of dysprosium. *Physical Review Letters*, 107(19), oct 2011. doi: 10.1103/physrevlett.107.190401.

[31] K. Aikawa, A. Frisch, M. Mark, S. Baier, A. Rietzler, R. Grimm, and F. Ferlaino. Bose-einstein condensation of erbium. *Physical Review Letters*, 108(21), may 2012. doi: 10.1103/physrevlett.108.210401.

[32] J. Stuhler, A. Griesmaier, T. Koch, M. Fattori, T. Pfau, S. Giovanazzi, P. Pedri, and L. Santos. Observation of dipole-dipole interaction in a degenerate quantum gas. *Physical Review Letters*, 95(15), oct 2005. doi: 10.1103/physrevlett.95.150406.

[33] T. Lahaye, J. Metz, B. Fröhlich, T. Koch, M. Meister, A. Griesmaier, T. Pfau, H. Saito, Y. Kawaguchi, and M. Ueda. d-wave collapse and explosion of a dipolar bose-einstein condensate. *Physical Review Letters*, 101(8), aug 2008. doi: 10.1103/physrevlett.101.080401.

[34] Axel Griesmaier, Jürgen Stuhler, Tobias Koch, Marco Fattori, Tilman Pfau, and Stefano Giovanazzi. Comparing contact and dipolar interactions in a bose-einstein condensate. *Physical Review Letters*, 97(25), dec 2006. doi: 10.1103/physrevlett.97.250402.

[35] L. Chomaz, R. M. W. van Bijnen, D. Petter, G. Faraoni, S. Baier, J. H. Becher, M. J. Mark, F. Wächtler, L. Santos, and F. Ferlaino. Observation of roton mode population in a dipolar quantum gas. *Nature Physics*, mar 2018. doi: 10.1038/s41567-018-0054-7.

[36] K. Aikawa, A. Frisch, M. Mark, S. Baier, R. Grimm, and F. Ferlaino. Reaching fermi degeneracy via universal dipolar scattering. *Physical Review Letters*, 112 (1), jan 2014. doi: 10.1103/physrevlett.112.010404.

[37] Igor Ferrier-Barbut, Holger Kadau, Matthias Schmitt, Matthias Wenzel, and Tilman Pfau. Observation of quantum droplets in a strongly dipolar bose gas. *Physical Review Letters*, 116(21), may 2016. doi: 10.1103/physrevlett.116.215301.

[38] Matthias Wenzel, Fabian Böttcher, Tim Langen, Igor Ferrier-Barbut, and Tilman Pfau. Striped states in a many-body system of tilted dipoles. *Physical Review A*, 96(5), nov 2017. doi: 10.1103/physreva.96.053630.

[39] Arthur Schawlow. New Scientist, October . page 225.

[40] Paul S. Julienne, Thomas M. Hanna, and Zbigniew Idziaszek. Universal ultracold collision rates for polar molecules of two alkali-metal atoms. *Physical Chemistry Chemical Physics*, 13(42):19114, 2011. doi: 10.1039/c1cp21270b.

[41] V. S. Prasannaa, S. Sreerekha, M. Abe, V. M. Bannur, and B. P. Das. Permanent electric dipole moments of alkaline-earth-metal monofluorides: Interplay of relativistic and correlation effects. *Physical Review A*, 93(4), apr 2016. doi: 10.1103/physreva.93.042504.

[42] E. S. Shuman, J. F. Barry, and D. DeMille. Laser cooling of a diatomic molecule. *Nature*, 467(7317):820–823, sep 2010. doi: 10.1038/nature09443.

[43] J. F. Barry, D. J. McCarron, E. B. Norrgard, M. H. Steinecker, and D. DeMille. Magneto-optical trapping of a diatomic molecule. *Nature*, 512(7514):286–289, aug 2014. doi: 10.1038/nature13634.

[44] S. Truppe, H. J. Williams, M. Hambach, L. Caldwell, N. J. Fitch, E. A. Hinds, B. E. Sauer, and M. R. Tarbutt. Molecules cooled below the doppler limit. *Nature Physics*, 13(12):1173–1176, aug 2017. doi: 10.1038/nphys4241.

[45] Loïc Anderegg, Benjamin L. Augenbraun, Yicheng Bao, Sean Burchesky, Lawrence W. Cheuk, Wolfgang Ketterle, and John M. Doyle. Laser cooling of optically trapped molecules. *ArXiv 1803.04571v1*, 2018.

[46] Maurice Petzold, Paul Kaebert, Philipp Gersema, Mirco Siercke, and Silke Ospelkaus. A zeeman slower for diatomic molecules. *New Journal of Physics*, 2018.

[47] M. W. Zwierlein, C. A. Stan, C. H. Schunck, S. M. F. Raupach, S. Gupta, Z. Hadzibabic, and W. Ketterle. Observation of bose-einstein condensation of molecules. *Physical Review Letters*, 91(25), dec 2003. doi: 10.1103/physrevlett.91.250401.

[48] S. Ospelkaus, K.-K. Ni, M. H. G. de Miranda, B. Neyenhuis, D. Wang, S. Kotochigova, P. S. Julienne, D. S. Jin, and J. Ye. Ultracold polar molecules near quantum degeneracy. *Faraday Discussions*, 142:351, 2009. doi: 10.1039/b821298h.

[49] N. Balakrishnan and A. Dalgarno. Chemistry at ultracold temperatures. *Chemical Physics Letters*, 341(5-6):652–656, jun 2001. doi: 10.1016/s0009-2614(01)00515-2.

[50] S. Ospelkaus, K.-K. Ni, D. Wang, M. H. G. de Miranda, B. Neyenhuis, G. Quemener, P. S. Julienne, J. L. Bohn, D. S. Jin, and J. Ye. Quantum-state controlled chemical reactions of ultracold potassium-rubidium molecules. *Science*, 327(5967):853–857, feb 2010. doi: 10.1126/science.1184121.

[51] Michael Mayle, Brandon P. Ruzic, and John L. Bohn. Statistical aspects of ultracold resonant scattering. *Physical Review A*, 85(6), jun 2012. doi: 10.1103/physreva.85.062712.

[52] Michael Mayle, Goulven Quéméner, Brandon P. Ruzic, and John L. Bohn. Scattering of ultracold molecules in the highly resonant regime. *Physical Review A*, 87(1), jan 2013. doi: 10.1103/physreva.87.012709.

[53] Bo Yan, Steven A. Moses, Bryce Gadway, Jacob P. Covey, Kaden R. A. Hazzard, Ana Maria Rey, Deborah S. Jin, and Jun Ye. Observation of dipolar spin-exchange interactions with lattice-confined polar molecules. *Nature*, 501(7468): 521–525, sep 2013. doi: 10.1038/nature12483.

[54] Kaden R. A. Hazzard, Bryce Gadway, Michael Foss-Feig, Bo Yan, Steven A. Moses, Jacob P. Covey, Norman Y. Yao, Mikhail D. Lukin, Jun Ye, Deborah S. Jin, and Ana Maria Rey. Many-body dynamics of dipolar molecules in an optical lattice. *Physical Review Letters*, 113(19), nov 2014. doi: 10.1103/physrevlett.113.195302.

[55] J. J. Zirbel, K.-K. Ni, S. Ospelkaus, T. L. Nicholson, M. L. Olsen, P. S. Julienne, C. E. Wieman, J. Ye, and D. S. Jin. Heteronuclear molecules in an optical dipole trap. *Physical Review A*, 78(1), jul 2008. doi: 10.1103/physreva.78.013416.

[56] S. Ospelkaus, A. Pe'er, K.-K. Ni, J. J. Zirbel, B. Neyenhuis, S. Kotochigova, P. S. Julienne, J. Ye, and D. S. Jin. Efficient state transfer in an ultracold dense gas of heteronuclear molecules. *Nature Physics*, 4(8):622–626, jun 2008. doi: 10.1038/nphys997.

[57] S. Ospelkaus, K.-K. Ni, G. Quéméner, B. Neyenhuis, D. Wang, M. H. G. de Miranda, J. L. Bohn, J. Ye, and D. S. Jin. Controlling the hyperfine state of rovibronic ground-state polar molecules. *Physical Review Letters*, 104(3), jan 2010. doi: 10.1103/physrevlett.104.030402.

[58] Piotr S. Żuchowski and Jeremy M. Hutson. Reactions of ultracold alkali-metal dimers. *Physical Review A*, 81(6), jun 2010. doi: 10.1103/physreva.81.060703.

[59] Maykel L. González-Martínez, John L. Bohn, and Goulven Quéméner. Adimensional theory of shielding in ultracold collisions of dipolar rotors. *Physical Review A*, 96(3), sep 2017. doi: 10.1103/physreva.96.032718.

[60] P. Zabawa, A. Wakim, A. Neukirch, C. Haimberger, N. P. Bigelow, A. V. Stolyarov, E. A. Pazyuk, M. Tamanis, and R. Ferber. Near-dissociation photoassociative production of deeply bound NaCs molecules. *Physical Review A*, 82(4), oct 2010. doi: 10.1103/physreva.82.040501.

[61] M. Gröbner, P. Weinmann, F. Meinert, K. Lauber, E. Kirilov, and H.-C. Nägerl. A new quantum gas apparatus for ultracold mixtures of k and cs and KCs ground-state molecules. *Journal of Modern Optics*, 63(18):1829–1839, feb 2016. doi: 10.1080/09500340.2016.1143051.

[62] Fudong Wang, Xiaodong He, Xiaoke Li, Bing Zhu, Jun Chen, and Dajun Wang. Formation of ultracold NaRb feshbach molecules. *New Journal of Physics*, 17(3):035003, mar 2015. doi: 10.1088/1367-2630/17/3/035003.

[63] Tetsu Takekoshi, Lukas Reichsöllner, Andreas Schindewolf, Jeremy M. Hutson, C. Ruth Le Sueur, Olivier Dulieu, Francesca Ferlaino, Rudolf Grimm, and Hanns-Christoph Nägerl. Ultracold dense samples of dipolar RbCs molecules in the rovibrational and hyperfine ground state. *Physical Review Letters*, 113 (20), nov 2014. doi: 10.1103/physrevlett.113.205301.

[64] Peter K. Molony, Philip D. Gregory, Zhonghua Ji, Bo Lu, Michael P. Köppinger, C. Ruth Le Sueur, Caroline L. Blackley, Jeremy M. Hutson, and Simon L. Cornish. Creation of UltracoldRb87cs133molecules in the rovibrational ground state. *Physical Review Letters*, 113(25), dec 2014. doi: 10.1103/physrevlett.113.255301.

[65] Jee Woo Park, Cheng-Hsun Wu, Ibon Santiago, Tobias G. Tiecke, Peyman Ahmadi, and Martin W. Zwierlein. Quantum degenerate bose-fermi mixture of chemically different atomic species with widely tunable interactions. *Phys. Rev. A*, 85:051602, 2012.

[66] S. Barratt. The absorption spectra of mixed metallic vapours. *Proceedings of the Royal Society A: Mathematical, Physical and Engineering Sciences*, 105(730): 221–225, feb 1924. doi: 10.1098/rspa.1924.0015.

[67] I. Russier-Antoine, A.J. Ross, M. Aubert-Frecon, F. Martin, and P. Crozet. An improved potential energy curve for the ground state of nak. *J. Phys. B: At., Mol. Phys.*, 33:2753, 2000.

[68] W.T. Zemke and W.C. Stwalley. Analysis of long range dispersion and exchange interactions between one na atom and one k atom. *J. Chem. Phys.*, 111:4956, 1999.

[69] R. Ferber, E. A. Pazyuk, A. V. Stolyarov, A. Zaitsevskii, P. Kowalczyk, Hongmin Chen, He Wang, and William C. Stwalley. The c3Σ, b3Π and a3Σ states of nak revisited. *J. Chem. Phys.*, 112:5740, 2000.

[70] Shunji Kasahara, Masaaki Baba, and Hajime Katô. High resolution laser spectroscopy up to the dissociation limit of the nak $b^1\Pi$ state and predissociation near the dissociation limit. *J. Chem. Phys.*, 94:7713, 1991.

[71] A. J. Ross, C. Effantin, J. d'Incan, and R. F. Barrow. Laser-induced fluorescence of nak: the b(1) 3Π state. *J. Phys. B: At., Mol. Phys.*, 19:1449, 1986.

[72] M. Tamanis, M. Auzinsh, I. Klincare, O. Nikolayeva, R. Ferber, A. Zaitsevskii, E. A. Pazyuk, and A. V. Stolyarov. Lifetimes and transition dipole moment functions of nak low lying singlet states: Empirical and ab initio approach. *J. Chem. Phys.*, 109:6725, 1998.

[73] Johannes Deiglmayr, Mireille Aymar, Roland Wester, Matthias Weidemüller, and Olivier Dulieu. Calculations of static dipole polarizabilities of alkali dimers. prospects for alignment of ultracold molecules. *J. Chem. Phys.*, 129: 064309, 2008.

[74] Cheng-Hsun Wu, Jee Woo Park, Peyman Ahmadi, Sebastian Will, and Martin W. Zwierlein. Ultracold fermionic feshbach molecules of 23na40k. *Phys. Rev. Lett.*, 109:085301, 2012.

[75] Jee Woo Park, Sebastian A. Will, and Martin W. Zwierlein. Ultracold dipolar gas of fermionic $^{23}Na^{40}K$ molecules in their absolute ground state. *Phys. Rev. Lett.*, 114:205302, May 2015. doi: 10.1103/PhysRevLett.114.205302. URL https://link.aps.org/doi/10.1103/PhysRevLett.114.205302.

[76] Matthias W. Gempel. *Towards Ultracold Polar NaK Molecules and the Investigation of Dipolar Quantum Gases*. PhD thesis, Leibniz Universität Hannover, 2016.

[77] R. Shankar. Scattering theory. In *Principles of Quantum Mechanics*, pages 523–561. Springer US, 1994. doi: 10.1007/978-1-4757-0576-8_19.

[78] Wolfgang Nolting. *Grundkurs Theoretische Physik 6*. Springer Berlin Heidelberg, 2014. doi: 10.1007/978-3-642-25393-5.

[79] Hermann Schulz. *Statistische Physik. Beruhend auf Quantentheorie. Eine Einführung*. Harri Deutsch, 2005.

[80] Torben Schulze. Gauge field simulators with cold atoms. Master's thesis, Leibniz Unversität Hannover, 2010.

[81] Cheng Chin, Rudolf Grimm, Paul Julienne, and Eite Tiesinga. Feshbach resonances in ultracold gases. *Reviews of Modern Physics*, 82(2):1225–1286, apr 2010. doi: 10.1103/revmodphys.82.1225.

[82] W. Ketterle, D.S. Durfee, and D. M. Stamper-Kurn. Making, probing and understanding bose-einstein condensates. In *Bose-Einstein condensation in atomic gases, Proceedings of the International School of Physics "Enrico Fermi"*, 1999.

[83] Jesse L. Silverberg, Matthew Bierbaum, James P. Sethna, and Itai Cohen. Collective motion of humans in mosh and circle pits at heavy metal concerts. *Physical Review Letters*, 110(22), may 2013. doi: 10.1103/physrevlett.110.228701.

[84] Albert Frisch, Michael Mark, Kiyotaka Aikawa, Francesca Ferlaino, John L. Bohn, Constantinos Makrides, Alexander Petrov, and Svetlana Kotochigova. Quantum chaos in ultracold collisions of gas-phase erbium atoms. *Nature*, 507(7493):475–479, mar 2014. doi: 10.1038/nature13137.

[85] Mark R. Hermann and J. A. Fleck. Split-operator spectral method for solving the time-dependent schrödinger equation in spherical coordinates. *Physical Review A*, 38(12):6000–6012, dec 1988. doi: 10.1103/physreva.38.6000.

[86] C. Clay Marston and Gabriel G. Balint-Kurti. The fourier grid hamiltonian method for bound state eigenvalues and eigenfunctions. *The Journal of Chemical Physics*, 91(6):3571–3576, sep 1989. doi: 10.1063/1.456888.

[87] B. R. Johnson. New numerical methods applied to solving the one-dimensional eigenvalue problem. *The Journal of Chemical Physics*, 67(9):4086, 1999. doi: 10.1063/1.435384.

[88] James F. E. Croft, Alisdair O. G. Wallis, Jeremy M. Hutson, and Paul S. Julienne. Multichannel quantum defect theory for cold molecular collisions. *Physical Review A*, 84(4), oct 2011. doi: 10.1103/physreva.84.042703.

[89] R. Pires, M. Repp, J. Ulmanis, E. D. Kuhnle, M. Weidemüller, T. G. Tiecke, Chris H. Greene, Brandon P. Ruzic, John L. Bohn, and E. Tiemann. Analyzing feshbach resonances: ALi6-cs133case study. *Physical Review A*, 90(1), jul 2014. doi: 10.1103/physreva.90.012710.

[90] Physicists create new state of matter at record low temperature. NIST.gov news page. https://goo.gl/bkQcKq.

[91] Wolfgang Ketterle and N. J. van Druten. Bose-einstein condensation of a finite number of particles trapped in one or three dimensions. *Physical Review A*, 54(1):656–660, jul 1996. doi: 10.1103/physreva.54.656.

[92] J. L. Roberts, N. R. Claussen, S. L. Cornish, E. A. Donley, E. A. Cornell, and C. E. Wieman. Controlled collapse of a bose-einstein condensate. *Physical Review Letters*, 86(19):4211–4214, may 2001. doi: 10.1103/physrevlett.86.4211.

[93] C. C. Bradley, C. A. Sackett, and R. G. Hulet. Bose-einstein condensation of lithium: Observation of limited condensate number. *Physical Review Letters*, 78(6):985–989, feb 1997. doi: 10.1103/physrevlett.78.985.

[94] Robert William Pattinson. *Two-Component Bose-Einstein Condensates: Equilibria and Dynamics at Zero Temperature and Beyond*. PhD thesis, University of Newcastle, 2014.

[95] Eleonora Fava. *Static and dynamics properties of a miscible two-component Bose-Einstein Condensate*. PhD thesis, University of Trento, 2018.

[96] D. S. Petrov. Quantum mechanical stabilization of a collapsing bose-bose mixture. *Physical Review Letters*, 115(15), oct 2015. doi: 10.1103/physrevlett.115.155302.

[97] Kean Loon Lee, Nils B. Jørgensen, I-Kang Liu, Lars Wacker, Jan J. Arlt, and Nick P. Proukakis. Phase separation and dynamics of two-component bose-einstein condensates. *Phys. Rev. A*, 94:013602, Jul 2016. doi: 10.1103/PhysRevA.94.013602. URL https://link.aps.org/doi/10.1103/PhysRevA.94.013602.

[98] D. J. McCarron, H. W. Cho, D. L. Jenkin, M. P. Köppinger, and S. L. Cornish. Dual-species bose-einstein condensate ofRb87andcs133. *Physical Review A*, 84 (1), jul 2011. doi: 10.1103/physreva.84.011603.

[99] C. R. Cabrera, L. Tanzi, J. Sanz, B. Naylor, P. Thomas, P. Cheiney, and L. Tarruell. Quantum liquid droplets in a mixture of bose-einstein condensates. *Science*, 359(6373):301–304, dec 2017. doi: 10.1126/science.aao5686.

[100] T. D. Lee, Kerson Huang, and C. N. Yang. Eigenvalues and eigenfunctions of a bose system of hard spheres and its low-temperature properties. *Physical Review*, 106(6):1135–1145, jun 1957. doi: 10.1103/physrev.106.1135.

[101] G. Semeghini, G. Ferioli, L. Masi, C. Mazzinghi, L. Wolswijk, F. Minardi, M. Modugno, G. Modugno, M. Inguscio, and M. Fattori. Self-bound quantum droplets in atomic mixtures.

[102] Michael Gröbner. *A quantum gas apparatus for ultracold mixtures of K and Cs*. PhD thesis, University of Innsbruck, 2017.

[103] Daniel A. Steck. Sodium d line data, December 2010. URL http://steck.us/alkalidata.

[104] Tobias Tiecke. Properties of potassium. URL http://www.tobiastiecke.nl/archive/PotassiumProperties.pdf.

[105] C. J. Pethick and H. Smith. *Bose–Einstein Condensation in Dilute Gases*. Cambridge University Press, 2008. doi: 10.1017/cbo9780511802850.

[106] Erik W. Streed, Ananth P. Chikkatur, Todd L. Gustavson, Micah Boyd, Yoshio Torii, Dominik Schneble, Gretchen K. Campbell, David E. Pritchard, and Wolfgang Ketterle. Large atom number bose-einstein condensate machines. *Review of Scientific Instruments*, 77(2):023106, feb 2006. doi: 10.1063/1.2163977.

[107] E. Arimondo, M. Inguscio, and P. Violino. Experimental determinations of the hyperfine structure in the alkali atoms. *Reviews of Modern Physics*, 49(1): 31–75, jan 1977. doi: 10.1103/revmodphys.49.31.

[108] M. Landini, S. Roy, L. Carcagní, D. Trypogeorgos, M. Fattori, M. Inguscio, and G. Modugno. Sub-doppler laser cooling of potassium atoms. *Physical Review A*, 84(4), oct 2011. doi: 10.1103/physreva.84.043432.

[109] John L. Bohn, James P. Burke, Chris H. Greene, H. Wang, P. L. Gould, and W. C. Stwalley. Collisional properties of ultracold potassium: Consequences for degenerate bose and fermi gases. *Physical Review A*, 59(5):3660–3664, may 1999. doi: 10.1103/physreva.59.3660.

[110] Chiara D'Errico, Matteo Zaccanti, Marco Fattori, Giacomo Roati, Massimo Inguscio, Giovanni Modugno, and Andrea Simoni. Feshbach resonances in ultracold 39 k. *New Journal of Physics*, 9(7):223, 2007. URL http://stacks.iop.org/1367-2630/9/i=7/a=223.

[111] Yan Feng, Luke R. Taylor, and Domenico Bonaccini Calia. 25 w raman-fiber-amplifier-based 589 nm laser for laser guide star. *Optics Express*, 17(21):19021, oct 2009. doi: 10.1364/oe.17.019021.

[112] Gary C. Bjorklund. Frequency-modulation spectroscopy: a new method for measuring weak absorptions and dispersions. *Optics Letters*, 5(1):15, jan 1980. doi: 10.1364/ol.5.000015.

[113] E. A. Donley, T. P. Heavner, F. Levi, M. O. Tataw, and S. R. Jefferts. Double-pass acousto-optic modulator system. *Review of Scientific Instruments*, 76(6): 063112, jun 2005. doi: 10.1063/1.1930095.

[114] Matthias W. Gempel. A laser system for cooling and trapping of ^{40}k. Master's thesis, Technische Universität München, 2010.

[115] X. Baillard, A. Gauguet, S. Bize, P. Lemonde, Ph. Laurent, A. Clairon, and P. Rosenbusch. Interference-filter-stabilized external-cavity diode lasers. *Optics Communications*, 266(2):609–613, oct 2006. doi: 10.1016/j.optcom.2006.05.011.

[116] Kai Konrad Voges. *(Title tba)*. PhD thesis.

[117] K. N. Jarvis, J. A. Devlin, T. E. Wall, B. E. Sauer, and M. R. Tarbutt. Blue-detuned magneto-optical trap. *ArXiv e-prints*, December 2017.

[118] J. Dalibard and C. Cohen-Tannoudji. Laser cooling below the doppler limit by polarization gradients: simple theoretical models. *Journal of the Optical Society of America B*, 6(11):2023, nov 1989. doi: 10.1364/josab.6.002023.

[119] Maurice Petzold. Zeeman slower und magnetischer transport zur präparation einer quantenentarteten mischung aus 23na und 40k. Master's thesis, Leibniz Universität Hannover, 2012.

[120] T. Arpornthip, C. A. Sackett, and K. J. Hughes. Vacuum-pressure measurement using a magneto-optical trap. *Physical Review A*, 85(3), mar 2012. doi: 10.1103/physreva.85.033420.

[121] Daniel Edler. Computer assisted data analysis for a polar molecule experiment. Master's thesis, Leibniz Universität Hannover, 2016.

[122] Robert Sylvester Williamson III. *Magneto-Optical Trapping of Potassium Isotopes*. PhD thesis, University of Wisconsin, 1997.

[123] Jacob F. Sherson, Christof Weitenberg, Manuel Endres, Marc Cheneau, Immanuel Bloch, and Stefan Kuhr. Single-atom-resolved fluorescence imaging of an atomic mott insulator. *Nature*, 467(7311):68–72, aug 2010. doi: 10.1038/nature09378.

[124] Lawrence W. Cheuk, Matthew A. Nichols, Katherine R. Lawrence, Melih Okan, Hao Zhang, and Martin W. Zwierlein. Observation of 2d fermionic mott insulators ofK40with single-site resolution. *Physical Review Letters*, 116 (23), jun 2016. doi: 10.1103/physrevlett.116.235301.

[125] D. B. Hume, I. Stroescu, M. Joos, W. Muessel, H. Strobel, and M. K. Oberthaler. Accurate atom counting in mesoscopic ensembles. *Physical Review Letters*, 111 (25), dec 2013. doi: 10.1103/physrevlett.111.253001.

[126] Andreas Hueper. *(Title tba)*. PhD thesis, Leibniz Universitaet Hannover.

[127] G. Reinaudi, T. Lahaye, Z. Wang, and D. Guéry-Odelin. Strong saturation absorption imaging of dense clouds of ultracold atoms. *Optics Letters*, 32(21): 3143, oct 2007. doi: 10.1364/ol.32.003143.

[128] PTB. local gravity information system.

[129] K. M. R. van der Stam, E. D. van Ooijen, R. Meppelink, J. M. Vogels, and P. van der Straten. Large atom number bose-einstein condensate of sodium. *Review of Scientific Instruments*, 78(1):013102, jan 2007. doi: 10.1063/1.2424439.

[130] H. J. Lewandowski, D. M. Harber, D. L. Whitaker, and E. A. Cornell. Simplified system for creating a bose–einstein condensate. *Journal of Low Temperature Physics*, 132(5):309–367, Sep 2003. ISSN 1573-7357. doi: 10.1023/A:1024800600621. URL https://doi.org/10.1023/A:1024800600621.

[131] Manuele Landini. *A tunable Bose-Einstein condensate for quantum interferometry*. PhD thesis, University of Trento, 2012.

[132] Michael A. Joffe, Wolfgang Ketterle, Alex Martin, and David E. Pritchard. Transverse cooling and deflection of an atomic beam inside a zeeman slower. *Journal of the Optical Society of America B*, 10(12):2257, dec 1993. doi: 10.1364/josab.10.002257.

[133] Dennis Schlippert. *Quantum tests of the universality of free fall*. PhD thesis, Leibniz Universität Hannover, 2014.

[134] J. Stuhler, P. O. Schmidt, S. Hensler, J. Werner, J. Mlynek, and T. Pfau. Continuous loading of a magnetic trap. *Physical Review A*, 64(3), aug 2001. doi: 10.1103/physreva.64.031405.

[135] Nikolaus Buchheim. *Dual-species apparatus for creating a dipolar quantum gas of $^{23}Na^{40}K$ molecules*. PhD thesis, Ludwig-Maximilians-Universität München, 2015.

[136] A. Görlitz, T. L. Gustavson, A. E. Leanhardt, R. Löw, A. P. Chikkatur, S. Gupta, S. Inouye, D. E. Pritchard, and W. Ketterle. Sodium bose-einstein condensates in theF=2state in a large-volume optical trap. *Physical Review Letters*, 90(9), mar 2003. doi: 10.1103/physrevlett.90.090401.

[137] Z. Hadzibabic, S. Gupta, C. A. Stan, C. H. Schunck, M. W. Zwierlein, K. Dieckmann, and W. Ketterle. Fiftyfold improvement in the number of quantum degenerate fermionic atoms. *Physical Review Letters*, 91(16), oct 2003. doi: 10.1103/physrevlett.91.160401.

[138] K. M. R. van der Stam, A. Kuijk, R. Meppelink, J. M. Vogels, and P. van der Straten. Spin-polarizing cold sodium atoms in a strong magnetic field. *Physical Review A*, 73(6), jun 2006. doi: 10.1103/physreva.73.063412.

[139] S. P. Ram, S. R. Mishra, S. K. Tiwari, and H. S. Rawat. Temperature and phase-space density of a cold atom cloud in a quadrupole magnetic trap. *Journal of the Korean Physical Society*, 65(4):462–470, Aug 2014. ISSN 1976-8524. doi: 10.3938/jkps.65.462. URL https://doi.org/10.3938/jkps.65.462.

[140] Dahyun Yum, Jina Park, Wanhee Lee, and Wonho Jhe. Systematic study of the rf-induced evaporation of 87rb atoms in a spherical magnetic quadrupole trap. *Journal of the Korean Physical Society*, 60(1):1–5, Jan 2012. ISSN 1976-8524. doi: 10.3938/jkps.60.1. URL https://doi.org/10.3938/jkps.60.1.

[141] Piet O. Schmidt. *Scattering properties of ultra-cold chromium atoms*. PhD thesis, Universität Stuttgart, 2003.

[142] Joao Magueijo. *A Brilliant Darkness: The Extraordinary Life and Mysterious Disappearance of Ettore Majorana, the Troubled Genius of the Nuclear Age*. Basic Books, 2009.

[143] Salvatore Esposito. *Ettore Majorana: Unveiled Genius and Endless Mysteries*. Springer International Publishing, 2017.

[144] Ettore Majorana. Atomi orientati in campo magnetico variabile. *Il Nuovo Cimento (1924-1942)*, 9(2):43–50, Feb 1932. ISSN 1827-6121. doi: 10.1007/BF02960953. URL https://doi.org/10.1007/BF02960953.

[145] Anton Piccardo-Selg. Degenerate quantum gases: Towards bose-einstein condensation of sodium. Master's thesis, Kirchhoff Institut für Physik, 2008.

[146] R. Dubessy, K. Merloti, L. Longchambon, P.-E. Pottie, T. Liennard, A. Perrin, V. Lorent, and H. Perrin. Rubidium-87 bose-einstein condensate in an optically plugged quadrupole trap. *Physical Review A*, 85(1), jan 2012. doi: 10.1103/physreva.85.013643.

[147] Raphael Scelle. Cooling, plugging, trapping : exploiting optical dipole potentials for polaron experiments. Master's thesis, Ruprecht-Karls-Universitaet Heidelberg, 2009.

[148] Wolfgang Petrich, Michael H. Anderson, Jason R. Ensher, and Eric A. Cornell. Stable, tightly confining magnetic trap for evaporative cooling of neutral atoms. *Physical Review Letters*, 74(17):3352–3355, apr 1995. doi: 10.1103/physrevlett.74.3352.

[149] Myoung-Sun Heo, Jae yoon Choi, and Yong il Shin. Fast production of largeNa23bose-einstein condensates in an optically plugged magnetic quadrupole trap. *Physical Review A*, 83(1), jan 2011. doi: 10.1103/physreva.83.013622.

[150] Mirco Siercke. *Realization of Bose-Einstein Condensation of 87Rb in a Time-orbiting Potential Trap*. PhD thesis, University of Toronto, 2011.

[151] Waldemar Herr. *Eine kompakte Quelle quantenentarteter Gase hohen Flusses für die Atominterferometrie unter Schwerelosigkeit*. PhD thesis, Leibniz Universität Hannover, 2011.

[152] Kevin Diedrich. Entwurf und realisierung einer elektronischen steuerung für einen optischen shutter. Bachelor Thesis, 2017.

[153] J. T. M. Walraven. Atomic hydrogen in magnetostatic traps,. In *Quantum dynamics of simple systems: the Forty-Fourth Scottish Universities Summer School in Physics*, 1996.

[154] O. J. Luiten, M. W. Reynolds, and J. T. M. Walraven. Kinetic theory of the evaporative cooling of a trapped gas. *Physical Review A*, 53(1):381–389, jan 1996. doi: 10.1103/physreva.53.381.

[155] W. Ketterle and N. J. van Druten. Evaporative cooling of atoms. *Advances in Atomic, Molecular, and Optical Physics*, 37:181–236, 1996.

[156] C. R. Monroe, E. A. Cornell, C. A. Sackett, C. J. Myatt, and C. E. Wieman. Measurement of cs-cs elastic scattering atT=30 μk. *Physical Review Letters*, 70 (4):414–417, jan 1993. doi: 10.1103/physrevlett.70.414.

[157] C.J Myatt. *Bose-Einstein Condensation Experiments in a Dilute Vapor of Rubidium*. PhD thesis, University of Colorado, 1997.

[158] Jan Rudolph et al. A high-flux bec source for mobile atom interferometers. *New Journal of Physics*, 17(6):065001, 2015.

[159] K. B. Davis, M. O. Mewes, and W. Ketterle. An analytical model for evaporative cooling of atoms. *Applied Physics B Laser and Optics*, 60(2-3):155–159, 1995. doi: 10.1007/bf01135857.

[160] Alan Corney. *Atomic and laser spectroscopy*. Oxford University Press, 1977.

[161] C. G. Townsend, N. H. Edwards, C. J. Cooper, K. P. Zetie, C. J. Foot, A. M. Steane, P. Szriftgiser, H. Perrin, and J. Dalibard. Phase-space density in the magneto-optical trap. *Physical Review A*, 52(2):1423–1440, aug 1995. doi: 10.1103/physreva.52.1423.

[162] Torsten Hartmann. *(Title tba)*. PhD thesis.

[163] Cheng-Hsun Wu, Ibon Santiago, Jee Woo Park, Peyman Ahmadi, and Martin W. Zwierlein. Strongly interacting isotopic bose-fermi mixture immersed in a fermi sea. *Physical Review A*, 84(1), jul 2011. doi: 10.1103/physreva.84.011601.

[164] B. J. DeSalvo, Krutik Patel, Jacob Johansen, and Cheng Chin. Dual-degeneracy in a bose-fermi mixture with extreme mass imbalance. 2017.

[165] Rudolf Grimm, Matthias Weidemüller, and Yurii B. Ovchinnikov. Optical dipole traps for neutral atoms. In *Advances In Atomic, Molecular, and Optical Physics*, pages 95–170. Elsevier, 2000. doi: 10.1016/s1049-250x(08)60186-x.

[166] Luis Santos. Theory of ultra cold gases. Lecture notes, Leibniz Universität Hannover, 2009.

[167] M. Safronova, Bindiya Arora, and Charles Clark. Frequency-dependent polarizabilities of alkali-metal atoms from ultraviolet through infrared spectral regions. *Physical Review A*, 73(2), feb 2006. doi: 10.1103/physreva.73.022505.

[168] Silke Ospelkaus-Schwarzer. *Quantum Degenerate Fermi-Bose Mixtures of 40K and 87Rb in 3D Optical Lattices*. PhD thesis, University of Hamburg, 2006.

[169] M. Schmitt, M. Wenzel, F. Böttcher, I. Ferrier-Barbut, and T. Pfau. Self-bound droplets of a dilute magnetic quantum liquid. *Nature 539, 259*, 2016.

[170] Erik Schwanke. Hyperfeinstruktur des nak-grundzustandes und intensitätsstabilisierung einer dipolfalle. Master's thesis, Leibniz Universität Hannover, 2014.

[171] Walter Kohn. Cyclotron resonance and de haas-van alphen oscillations of an interacting electron gas. *Physical Review*, 123(4):1242–1244, aug 1961. doi: 10.1103/physrev.123.1242.

[172] Pierre-Alexandre Pantel, Dany Davesne, Silvia Chiacchiera, and Michael Urban. Trap anharmonicity and sloshing mode of a fermi gas. *Physical Review A*, 86(2), aug 2012. doi: 10.1103/physreva.86.023635.

[173] Manuel Scherer. *Nichtklassische Zustände in Spinor-Bose-Einstein-Kondensaten*. PhD thesis, Leibniz Universität Hannover, 2011.

[174] Y. Castin and R. Dum. Bose-einstein condensates in time dependent traps. *Physical Review Letters*, 77(27):5315–5319, dec 1996. doi: 10.1103/physrevlett.77.5315.

[175] Yu. Kagan, E. L. Surkov, and G. V. Shlyapnikov. Evolution of a bose-condensed gas under variations of the confining potential. *Physical Review A*, 54(3):R1753–R1756, sep 1996. doi: 10.1103/physreva.54.r1753.

[176] F Dalfovo, C Minniti, S Stringari, and L Pitaevskii. Nonlinear dynamics of a bose condensed gas. *Physics Letters A*, 227(3-4):259–264, mar 1997. doi: 10.1016/s0375-9601(97)00069-8.

[177] J. Szczepkowski, R. Gartman, M. Witkowski, L. Tracewski, M. Zawada, and W. Gawlik. Analysis and calibration of absorptive images of bose–einstein condensate at nonzero temperatures. *Review of Scientific Instruments*, 80(5): 053103, may 2009. doi: 10.1063/1.3125051.

[178] Ryan Olf, Fang Fang, G. Edward Marti, Andrew MacRae, and Dan M. Stamper-Kurn. Thermometry and cooling of a bose gas to 0.02 times the condensation temperature. *Nature Physics*, 11(9):720–723, jul 2015. doi: 10.1038/nphys3408.

[179] Tino Weber, Jens Herbig, Michael Mark, Hanns-Christoph Nägerl, and Rudolf Grimm. Three-body recombination at large scattering lengths in an ultracold atomic gas. *Physical Review Letters*, 91(12), sep 2003. doi: 10.1103/physrevlett.91.123201.

[180] Juris Ulmanis. *Heteronuclear Efimov Scenario in Ultracold Quantum Gases*. Springer Theses, 2017.

[181] Jacob Johansen, B. J. DeSalvo, Krutik Patel, and Cheng Chin. Testing universality of efimov physics across broad and narrow feshbach resonances. *Nature Physics*, 13(8):731–735, may 2017. doi: 10.1038/nphys4130.

[182] A. J. Moerdijk, H. M. J. M. Boesten, and B. J. Verhaar. Decay of trapped ultracold alkali atoms by recombination. *Physical Review A*, 53(2):916–920, feb 1996. doi: 10.1103/physreva.53.916.

[183] E. A. Burt, R. W. Ghrist, C. J. Myatt, M. J. Holland, E. A. Cornell, and C. E. Wieman. Coherence, correlations, and collisions: What one learns about bose-einstein condensates from their decay. *Physical Review Letters*, 79(3): 337–340, jul 1997. doi: 10.1103/physrevlett.79.337.

[184] L. J. Wacker, N. B. Jørgensen, D. Birkmose, N. Winter, M. Mikkelsen, J. Sherson, N. Zinner, and J. J. Arlt. Universal three-body physics in ultracold krb mixtures. *Phys. Rev. Lett.*, 117:163201, Oct 2016. doi: 10.1103/PhysRevLett.117.163201. URL https://link.aps.org/doi/10.1103/PhysRevLett.117.163201.

[185] Ruth S. Bloom, Ming-Guang Hu, Tyler D. Cumby, and Deborah S. Jin. Tests of universal three-body physics in an ultracold bose-fermi mixture. *Phys. Rev. Lett.*, 111:105301, 2013.

[186] Shih-Kuang Tung, Karina Jiménez-García, Jacob Johansen, Colin V. Parker, and Cheng Chin. Geometric scaling of efimov states in a ^{6}Li–^{133}Cs mixture. *Phys. Rev. Lett.*, 113:240402, 2014.

[187] Alexandra Viel and Andrea Simoni. Feshbach resonances and weakly bound molecular states of boson-boson and boson-fermion nak pairs. *Phys. Rev. A*, 93:042701, Apr 2016. doi: 10.1103/PhysRevA.93.042701. URL https://link.aps.org/doi/10.1103/PhysRevA.93.042701.

[188] Chiara D'Errico, Matteo Zaccanti, Marco Fattori, Giacomo Roati, Massimo Inguscio, Giovanni Modugno, and Andrea Simoni. Feshbach resonances in ultracold 39k. *New Journal of Physics*, 9(7):223–223, jul 2007. doi: 10.1088/1367-2630/9/7/223.

[189] F. Ferlaino, A. Zenesini, M. Berninger, B. Huang, H. C. Nägerl, and R. Grimm. Efimov resonances in ultracold quantum gases. *Few-Body Systems*, 51(2-4):113–133, oct 2011. doi: 10.1007/s00601-011-0260-7.

[190] T. Schuster, R. Scelle, A. Trautmann, S. Knoop, M. K. Oberthaler, M. M. Haverhals, M. R. Goosen, S. J. J. M. F. Kokkelmans, and E. Tiemann. Feshbach spectroscopy and scattering properties of ultracold li + na mixtures. *Physical Review A*, 85(4), apr 2012. doi: 10.1103/physreva.85.042721.

[191] Martin Berninger, Alessandro Zenesini, Bo Huang, Walter Harm, Hanns-Christoph Nägerl, Francesca Ferlaino, Rudolf Grimm, Paul S. Julienne, and Jeremy M. Hutson. Feshbach resonances, weakly bound molecular states, and coupled-channel potentials for cesium at high magnetic fields. *Physical Review A*, 87(3), mar 2013. doi: 10.1103/physreva.87.032517.

[192] C. H. Schunck, M. W. Zwierlein, C. A. Stan, S. M. F. Raupach, W. Ketterle, A. Simoni, E. Tiesinga, C. J. Williams, and P. S. Julienne. Feshbach resonances in fermionicLi6. *Physical Review A*, 71(4), apr 2005. doi: 10.1103/physreva.71.045601.

[193] C. Marzok, B. Deh, C. Zimmermann, Ph. W. Courteille, E. Tiemann, Y. V. Vanne, and A. Saenz. Feshbach resonances in an ultracoldLi7andrb87mixture. *Physical Review A*, 79(1), jan 2009. doi: 10.1103/physreva.79.012717.

[194] Sanjukta Roy, Manuele Landini, Andreas Trenkwalder, Giulia Semeghini, Giacomo Spagnolli, Andrea Simoni, Marco Fattori, Massimo Inguscio, and Giovanni Modugno. Test of the universality of the three-body efimov parameter at narrow feshbach resonances. *Physical Review Letters*, 111(5), aug 2013. doi: 10.1103/physrevlett.111.053202.

[195] Charles Cerjan, editor. *Numerical Grid Methods and Their Application to Schrödinger's Equation*. Springer Netherlands, 1993. doi: 10.1007/978-94-015-8240-7.

[196] B.R Johnson. The multichannel log-derivative method for scattering calculations. *Journal of Computational Physics*, 13(3):445–449, nov 1973. doi: 10.1016/0021-9991(73)90049-1.

[197] Gabriel G. Balint-Kurti, Richard N. Dixon, and C. Clay Marston. Grid methods for solving the schrödinger equation and time dependent quantum dynamics of molecular photofragmentation and reactive scattering processes. *International Reviews in Physical Chemistry*, 11(2):317–344, sep 1992. doi: 10.1080/01442359209353274.

[198] Jeremy M. Hutson. Coupled channel methods for solving the bound-state schrödinger equation. *Computer Physics Communications*, 84(1-3):1–18, nov 1994. doi: 10.1016/0010-4655(94)90200-3.

[199] Olivier Dulieu and Paul S. Julienne. Coupled channel bound states calculations for alkali dimers using the fourier grid method. *The Journal of Chemical Physics*, 103(1):60–66, jul 1995. doi: 10.1063/1.469622.

[200] Olivier Dulieu and Andreas Osterwalder, editors. *Cold Chemistry*. Royal Society of Chemistry, 2017. doi: 10.1039/9781782626800.

[201] *Cold Molecules: Theory, Experiment, Applications*. CRC Press, 2009. ISBN 9781420059038. URL https://www.amazon.com/Cold-Molecules-Theory-Experiment-Applications/dp/1420059033?SubscriptionId=0JYN1NVW651KCA56C102&tag=techkie-20&linkCode=xm2&camp=2025&creative=165953&creativeASIN=1420059033.

[202] G. Audi and A.H. Wapstra. The 1995 update to the atomic mass evaluation. *Nuclear Physics A*, 595(4):409–480, dec 1995. doi: 10.1016/0375-9474(95)00445-9.

[203] I. Temelkov, H. Knöckel, A. Pashov, and E. Tiemann. Molecular beam study of the a $^3\Sigma^+$ state of nak up to the dissociation limit. *Phys. Rev. A*, 91:032512, Mar 2015. doi: 10.1103/PhysRevA.91.032512. URL https://link.aps.org/doi/10.1103/PhysRevA.91.032512.

[204] Min-Jie Zhu, Huan Yang, Lan Liu, De-Chao Zhang, Ya-Xiong Liu, Jue Nan, Jun Rui, Bo Zhao, Jian-Wei Pan, and Eberhard Tiemann. Feshbach loss spectroscopy in an ultracold na23-k40 mixture. *Physical Review A*, 96(6), dec 2017. doi: 10.1103/physreva.96.062705.

[205] Zhang Ji-Cai, Zhu Zun-Lue, Sun Jin-Feng, and Liu Yu-Fang. S-wave scattering properties for na-k cold collisions. *Chinese Physics Letters*, 30(2):023401, 2013. URL http://stacks.iop.org/0256-307X/30/i=2/a=023401.

[206] R. Vexiau, D. Borsalino, M. Lepers, A. Orbán, M. Aymar, O. Dulieu, and N. Bouloufa-Maafa. Dynamic dipole polarizabilities of heteronuclear alkali dimers: optical response, trapping and control of ultracold molecules. *International Reviews in Physical Chemistry*, 36(4):709–750, aug 2017. doi: 10.1080/0144235x.2017.1351821.

[207] A. Gerdes, M. Hobein, H. Knöckel, and E. Tiemann. Ground state potentials of the nak molecule. *Eur. Phys. J. D*, 49:67, 2008.

[208] Krzysztof Jachymski and Paul S. Julienne. Analytical model of overlapping feshbach resonances. *Physical Review A*, 88(5), nov 2013. doi: 10.1103/physreva.88.052701.

[209] Nicolo Cesa-Bianchi and Gabor Lugosi. *Prediction, Learning, and Games*. Cambridge University Press, 2006. doi: 10.1017/cbo9780511546921.

[210] Zav Shotan, Olga Machtey, Servaas Kokkelmans, and Lev Khaykovich. Three-body recombination at vanishing scattering lengths in an ultracold bose gas. *Physical Review Letters*, 113(5), jul 2014. doi: 10.1103/physrevlett.113.053202.

[211] M. Gustavsson, E. Haller, M. J. Mark, J. G. Danzl, G. Rojas-Kopeinig, and H.-C. Nägerl. Control of interaction-induced dephasing of bloch oscillations. *Physical Review Letters*, 100(8), feb 2008. doi: 10.1103/physrevlett.100.080404.

[212] Q. Beaufils, A. Crubellier, T. Zanon, B. Laburthe-Tolra, E. Maréchal, L. Vernac, and O. Gorceix. Feshbach resonance in d-wave collisions. *Physical Review A*, 79:032706, Mar 2009. doi: 10.1103/PhysRevA.79.032706. URL https://link.aps.org/doi/10.1103/PhysRevA.79.032706.

[213] Eite Tiesinga, Carl J. Williams, Paul S. Julienne, Kevin M. Jones, Paul D. Lett, and William D. Phillips. A spectroscopic determination of scattering lengths for sodium atom collisions. *Journal of Research of the National Institute of Standards and Technology*, 1996.

[214] A. Simoni, private communication.

[215] Tin-Lun Ho and V. B. Shenoy. Binary mixtures of bose condensates of alkali atoms. *Phys. Rev. Lett.*, 77:3276–3279, Oct 1996. doi: 10.1103/PhysRevLett.77.3276. URL https://link.aps.org/doi/10.1103/PhysRevLett.77.3276.

[216] C. K. Law, H. Pu, N. P. Bigelow, and J. H. Eberly. "stability signature" in two-species dilute bose-einstein condensates. *Phys. Rev. Lett.*, 79:3105–3108, Oct 1997. doi: 10.1103/PhysRevLett.79.3105. URL https://link.aps.org/doi/10.1103/PhysRevLett.79.3105.

[217] H. Pu and N. P. Bigelow. Properties of two-species bose condensates. *Phys. Rev. Lett.*, 80:1130–1133, Feb 1998. doi: 10.1103/PhysRevLett.80.1130. URL https://link.aps.org/doi/10.1103/PhysRevLett.80.1130.

[218] Kean Loon Lee, Nils B. Jørgensen, I-Kang Liu, Lars Wacker, Jan J. Arlt, and Nick P. Proukakis. Phase separation and dynamics of two-component bose-einstein condensates. *Physical Review A*, 94(1), jul 2016. doi: 10.1103/physreva.94.013602.

[219] David A. Smith, Simon Aigner, Sebastian Hofferberth, Michael Gring, Mauritz Andersson, Stefan Wildermuth, Peter Krüger, Stephan Schneider, Thorsten Schumm, and Jörg Schmiedmayer. Absorption imaging of ultracold atoms on atom chips. *Optics Express*, 19(9):8471, apr 2011. doi: 10.1364/oe.19.008471.

[220] Michael Abramoff, Paulo Magalhães, and S.J. Ram. Image processing with imagej. 11:36–42, 11 2003.

[221] Wenyi Ren, Qizhi Cao, Dan Wu, Jiangang Jiang, Guoan Yang, Yingge Xie, and Sheqi Zhang. Wavelet transform based defringing in interference imaging spectrometer. *Optics Express*, 25(15):17039, jul 2017. doi: 10.1364/oe.25.017039.

[222] Xue Li, Osmar R. Zaïane, and Zhanhuai Li, editors. *Advanced Data Mining and Applications*. Springer Berlin Heidelberg, 2006. doi: 10.1007/11811305.

[223] Arjun Mane and Karbhari Kale. *Face Recognition Using Principal Component Analysis*. LAP LAMBERT Academic Publishing, 2015. ISBN 3659673641. URL https://www.amazon.com/Recognition-Using-Principal-Component-Analysis/dp/3659673641?SubscriptionId=0JYN1NVW651KCA56C102&tag=techkie-20&linkCode=xm2&camp=2025&creative=165953&creativeASIN=3659673641.

[224] Stephen R. Segal, Quentin Diot, Eric A. Cornell, Alex A. Zozulya, and Dana Z. Anderson. Revealing buried information: Statistical processing techniques for ultracold-gas image analysis. *Physical Review A*, 81(5), may 2010. doi: 10.1103/physreva.81.053601.

[225] T. Kovachy, P. Asenbaum, C. Overstreet, C. A. Donnelly, S. M. Dickerson, A. Sugarbaker, J. M. Hogan, and M. A. Kasevich. Quantum superposition at the half-metre scale. *Nature*, 528(7583):530–533, dec 2015. doi: 10.1038/nature16155.

[226] Xiaolin Li, Min Ke, Bo Yan, and Yuzhu Wang. Reduction of interference fringes in absorption imaging of cold atom cloud using eigenface method. *Chin. Opt. Lett.*, 5(3):128–130, Mar 2007. URL http://col.osa.org/abstract.cfm?URI=col-5-3-128.

[227] Igor Ferrier-Barbut, Matthias Wenzel, Matthias Schmitt, Fabian Böttcher, and Tilman Pfau. Onset of a modulational instability in trapped dipolar bose-einstein condensates. *Physical Review A*, 97(1), jan 2018. doi: 10.1103/physreva.97.011604.

[228] G. Delannoy, S. G. Murdoch, V. Boyer, V. Josse, P. Bouyer, and A. Aspect. Understanding the production of dual bose-einstein condensation with sympathetic cooling. *Phys. Rev. A*, 63:051602, Apr 2001. doi: 10.1103/PhysRevA.63.051602. URL https://link.aps.org/doi/10.1103/PhysRevA.63.051602.

[229] Tyler D. Cumby, Ruth A. Shewmon, Ming-Guang Hu, John D. Perreault, and Deborah S. Jin. Feshbach-molecule formation in a bose-fermi mixture. *Physical Review A*, 87(1), jan 2013. doi: 10.1103/physreva.87.012703.

[230] C. Klempt, T. Henninger, O. Topic, M. Scherer, L. Kattner, E. Tiemann, W. Ertmer, and J. J. Arlt. Radio-frequency association of heteronuclear feshbach molecules. *Physical Review A*, 78(6), dec 2008. doi: 10.1103/physreva.78.061602.

[231] S. Kotochigova, P. S. Julienne, and E. Tiesinga. Ab initiocalculation of the KRb dipole moments. *Physical Review A*, 68(2), aug 2003. doi: 10.1103/physreva.68.022501.

[232] K.-K. Ni, S. Ospelkaus, M. H. G. de Miranda, A. Peer, B. Neyenhuis, J. J. Zirbel, S. Kotochigova, P. S. Julienne, D. S. Jin, and J. Ye. A high phase-space-density gas of polar molecules. *Science*, 322(5899):231–235, oct 2008. doi: 10.1126/science.1163861.

[233] S. Ospelkaus, K.-K. Ni, M. H. G. de Miranda, B. Neyenhuis, D. Wang, S. Kotochigova, P. S. Julienne, D. S. Jin, and J. Ye. Ultracold polar molecules near quantum degeneracy. *Faraday Discuss.*, 142:351–359, 2009. doi: 10.1039/B821298H. URL http://dx.doi.org/10.1039/B821298H.

[234] R. E. Moss. The molecular hamiltonian. In *Advanced Molecular Quantum Mechanics*, pages 179–193. Springer Netherlands, 1973. doi: 10.1007/978-94-009-5688-9_10.

[235] Timothy A. Barckholtz. Quantitative insights about molecules exhibiting jahn-teller and related effects. *International Reviews in Physical Chemistry*, 17(4):435–524, oct 1998. doi: 10.1080/014423598230036.

[236] Julia Gerschmann, Erik Schwanke, Asen Pashov, Horst Knöckel, Silke Ospelkaus, and Eberhard Tiemann. Laser and fourier-transform spectroscopy of KCa. *Physical Review A*, 96(3), sep 2017. doi: 10.1103/physreva.96.032505.

[237] S. Magnier and Ph. Millié. Potential curves for the ground and numerous highly excited electronic states of k2 and nak. *Phys. Rev. A*, 54:204, 1996.

[238] R. Rydberg. Graphische darstellung einiger banden spektroskopischer ergebnisse. *Z Physics, 73: 376-385.*, 1931.

[239] J. L. Dunham. The energy levels of a rotating vibrator. *Physical Review*, 41(6): 721–731, sep 1932. doi: 10.1103/physrev.41.721.

[240] Robert Field. 5.80 small-molecule spectroscopy and dynamics. MIT OpenCourseWare, https://ocw.mit.edu. License: Creative Commons BY-NC-SA., Fall 2008.

[241] Eberhard Tiemann. Cold molecules. In *Interactions in Ultracold Gases*, pages 175–214. Wiley-VCH Verlag GmbH & Co. KGaA, jan 2005. doi: 10.1002/3527603417.ch4.

[242] Stephen Gasiorowicz. *Quantenphysik*. Oldenbourg Wissensch.Vlg, 2005. ISBN 3486274899.

[243] M. Marinescu and H. R. Sadeghpour. Long-range potentials for two-species alkali-metal atoms. *Phys. Rev. A*, 59:390, 1999.

[244] Sergey G. Porsev and Andrei Derevianko. Accurate relativistic many-body calculations of van der waals coefficients c8 and c10 for alkali-metal dimers. *J. Chem. Phys.*, 119:844, 2003.

[245] M. Aymar and O. Dulieu. Calculations of transition and permanent dipole moments of heteronuclear alkali dimers nak, narb and nacs. *Mol. Phys.*, 105: 1733, 2007.

[246] W. Jastrzebski, P.Kortyka, P.Kowalczyk, O. Docenko, M.Tamanis, R.Ferber, A.Pashov, H.Knöckel, and E. Tiemann. Accurate characterisation of the c(3)1Σ+ state of the narb molecule. *Eur. Phys. J. D*, 36:57, 2005.

[247] A. Zaitsevskii, S.O. Adamson, E.A. Pazyuk, A.V. Stolyarov, O. Nikolayeva, O. Docenko, I. Klincare, M. Auzinsh, M. Tamanis, R. Ferber, and R. Cimiraglia. Energy and radiative properties of the low-lying narb states. *Phys. Rev. A*, 63: 052504, 2001.

[248] Svetlana Kotochigova, Eite Tiesinga, and Paul Julienne. Multi-channel modelling of the formation of vibrationally cold polar krb molecules. *New J. Phys.*, 11:055043, 2009.

[249] U. Gaubatz, P. Rudecki, M. Becker, S. Schiemann, M. Külz, and K. Bergmann. Population switching between vibrational levels in molecular beams. *Chemical Physics Letters*, 149(5-6):463–468, sep 1988. doi: 10.1016/0009-2614(88)80364-6.

[250] Bruce W. Shore. Picturing stimulated raman adiabatic passage: a STIRAP tutorial. *Advances in Optics and Photonics*, 9(3):563, sep 2017. doi: 10.1364/aop.9.000563.

[251] Frauke Seeßelberg, Nikolaus Buchheim, Zhen-Kai Lu, Tobias Schneider, Xin-Yu Luo, Eberhard Tiemann, Immanuel Bloch, and Christoph Gohle. Modeling the adiabatic creation of ultracold polar 23na40k molecules. *Physical Review A*, 97(1), jan 2018. doi: 10.1103/physreva.97.013405.

[252] Markus Debatin. *Creation of Ultracold RbCs Ground-State Molecules*. PhD thesis, University of Innsbruck, 2013.

At times our own light goes out and is rekindled by a spark from another person. Each of us has cause to think with deep gratitude of those who have lighted the flame within us.

— Albert Schweitzer

ACKNOWLEDGMENTS

Keywords: Schartenkach, Ploffi, Aussenwhirlpool, #zerschellen, ergo: qualvoll sterben, Meilensteintrinken, Jazz!, Wurstquasar, ...noch *ein* Bier.

Many people have contributed to the successful completion of this thesis.

First and foremost, I'd like to thank Silke Ospelkaus, not only for giving me the opportunity to pursue a PhD in her group, but also for supporting me whenever and wherever I needed it. Whether I was in a state of confusion, depression or nervousness, she always had wise advice at hand and conveyed it in her helpful, kind manner. I still remember my first week in the lab very vividly. As I was lacking an experimental background, she took her time to build a diode laser together with me, gave tips and tricks all the time and didn't laugh when I had heat-conducting paste on my face. Her continuous interest in my theoretical and experimental progress, as well as her willingness to discuss any open questions 24/7, are by no means to be taken for granted and deserve great praise. The countless discussions with her about physical phenomena have always been characterized by productivity, constructiveness and a friendly attitude - I couldn't think of a better boss.

Furthermore, I would like to thank my additional thesis surveyors, Carsten Klempt and Jan Arlt, and the examination committee chairman Luis Santos. Jan and Luis don't know it, but their inspiring lectures on quantum optics and the theory of ultra-cold gases were the reason why I chose to pursue a scientific career in this research field. I thank Carsten further for several scientific discussions, on the balcony and elsewhere, and also for helpful advices regarding my PhD project.

The S. Ospelkaus group is characterised by a wonderful working atmosphere in which everyone is interested in the other, whether in the private sphere or in the lab progress. My thanks go out to every single member of them, for remaining thoroughly cheer- and respectful. I am especially grateful to the NaK team, that does a tremendous job to maintain the momentum in this awfully complicated apparatus that we have built together. In particular...

- ⋆ I can't thank Ale[ssandro] Zenesini enough for what he did for the experiment. He never shied away from any issue, whether it was of electronic, theoretical or quantum mechanical nature, and constantly pushed the experiment forwards at every conceivable node. Through the myriad of discussions, I learned a huge number of things, and he never lost his composure which is astonishing as I tend to argue *a lot*. But more importantly, I am grateful for everything he's done for me on the personal-professional interfacing level. When fate struck and I became a mess, he rebuilt me. He put me back on track when I lost focus, sent motivating messages when I lost passion, and always gave me the feeling that we can achieve anything if we truly blaze for it.

- ⋆ You can't look at the apparatus without recognizing Matt[hias] Gempel's work in it. His meticulous planning and rigorous implementation form the foundation for everything we have achieved in the laboratory and still hope to achieve. His unquenchable determination was priceless, especially in the time when we experienced our most severe experimental setbacks.

- ⋆ One of [Tor]sten Hartmann's slogans can actually be put on the laboratory door forever: *Never give up, never surrender!* He was - by far - the person I spent the most lab time with, in which we struggled with the stability of the system and unlocked its secrets together. Every time I look at the first resonance .gif, I think back to all the hard work we put into the experiment. Our different approaches to physical issues complemented each other fantastically over time, and we enjoyed sharing our relative expertise with the other. What I appreciate most is the friendly atmosphere when you work with Torsten. You'd think that at some point, when you're working on the same experiment day after day, year after year, you've told yourself everything, and all that's left is to annoy each other. With Torsten however, it was always tingling, humorous and stimulating. With a smile I remember our evenings in the lab late at night when we told each other about the latest developments in our favorite TV series. I've never seen an episode of 24, but practically know the plot by heart. I wish him all the best for the final spurt in his thesis. You can do it!

- ⋆ Thank's to Junior [Kai] Voges, who immediately threw himself head over heels into work from day one of his PhD. In everything he does, he shows great determination, passion and the constant will to go a mile further. This was also shown by his extremely rigorous correction of both our recent paper and my thesis, for which I am very grateful. With him in charge, the experiment is in good hands. I wish him with all my heart that all plans of the NaK experiment will be fulfilled and that there will never be any reason for pessimism.

- ⋆ I'm glad Vasco [Philipp] Gersema recently joined our experiment. He's a real enrichment to our lab, and operates it already as if he had built it himself. With his cheerful manner and singing habits, he will definitely be a worthy successor of mine.

- ⋆ Kevin [Kevin] Diedrich, whose tirades are always a bliss to listen to, who is a good friend in every situation in life and who was one of the greatest supporters when private problems destabilized me.

There is so much more to say to each and every person found below, but I'll try to restrain myself from now on.

- ⋆ A shout goes out to Florian Richter, with whom I had a numerous of fascinating meetings through the development of our ultracold chemistry paper. I also learned a handful of colloquial speech.

- ⋆ I would also like to thank HALOSTAR for the financial support in the early years, which also enabled me to freely select my doctoral project.

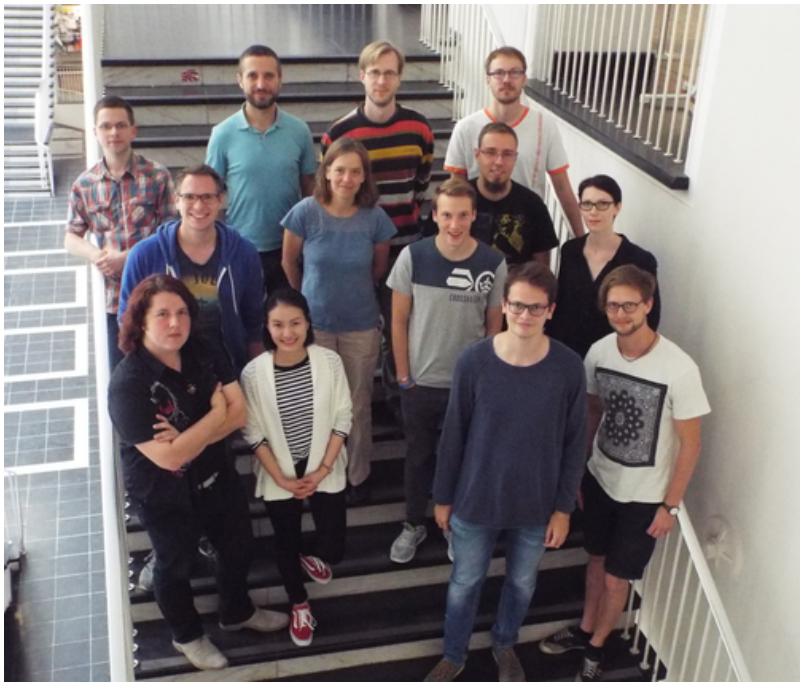

The S. Ospelkaus family in 2017. Thank you, folks.

⋆ I would very much like to express my sincere appreciation to Eberhard Tiemann, who was a fantastic instructor for my first (and second, and third ...) steps regarding molecular physics. I can't help but think of him as a wise man who can provide the solution to literally *all* riddles. He always had time for my everlasting questions, and answered them, never tired, with a clarity and tranquility, which I will take as an inspiration for any future work.

⋆ I would like to thank the NaK spectroscopy team comprising Andreas Gerdes, Horst Knöckel and Ivo Temelkov. From Andreas, I received additional spectroscopic data for the NaK system, which were still on his private computer, and with which the comparison of experiment and theoretical prediction could be very well investigated. Although Andreas was no longer employed at the institute at the beginning of my doctorate, he gladly came by on request, provided the data and gave me a lot of good advice. I would like to thank the *explosive* duo Ivo and Horst for our good and friendly cooperation, especially on the NaK paper. Horst was always on hand with help and advice, and always had a suggestion on how to simplify or otherwise handle a problem. I thank Ivo in general for his humorous way of life and specifically for an email.

⋆ Many thanks and a happy "Juhuuu!" to Anna-Greta Paschke, with whom I shared an office for a long time, and who always made sure that working life can be a place full of entertainment and fun. Thank you for your contagious wit and your unmistakable joy.

⋆ I take this as a quick wave to everyone from Silkes and Christians group, that enrich the daily life with a broad range of attitudes. Out of these, special thanks to Henning Hahn, for being *maybe* the funniest person on earth, to Teresa Feld for the constant dance with words, and once in real, and to Mirco

Siercke, PhD, for being an inexhaustible source of ultracold knowledge and the best neighbour I've ever had. You are brotacular.

⋆ Without the organizational help provided by the administration, everything would quickly spiral out of control. I bow my head in deepest admiration to Elke Huenitzsch and Birgit Ohlendorf, who, even in times of greatest bureaucratic incompetence on my part, never shot me into the stratosphere. Thanks from the bottom of my heart to Birgit for the countless cheerful conversations and the mail she sent me in private when I was truly down. This is not self-evident, but symptomatic of the cordiality in this institute.

⋆ Thanks to all the wonderful people working in this Institute, for you have forged a special place, where one can find colleagues, comrades, friends and family. I owe you some of the most beautiful memories of my life. Coin flicking, wine dining, Schartenkach, pirate sailing, Baileys baking, you name it. My loving greetings go to Holger, Henning, Dennis, Sebastian, Dominika, Kai, Naceur, Waldemar, Felix, Ilka, Kulli, Maike, Bernd Andreas, Baptist, Manuel, Logan, Maral, Steffen, Dennis, Schubi, Gunnar, Temmo and Klaus (ordered alphabetically, so that no one is preferred yet Sebastian is in front of Baptist), who are family to me and enclosed in my heart forever.

⋆ I'd like to express my gratitude to Sina Loriani, Jan-Niclas Siemß und Robin Corgier for giving me shelter in their office in order to complete my thesis. I could have not wished for better working conditions. I further bow my head to their Brofessional approach - they are a highly productive task force, immersed in a friendly atmosphere.

⋆ My dearest thanks are sent out to my family, Martina and Bernd, Hannelore and Joachim, Katharina and Holger, Ju, Kiwi and Frank, Kim, and Tom. I love all of you. I thank my parents for everything they did and do for me, for their continuous support and that they never put any pressure on me. Thanks to Gizmo for showing me what true unconditional love is. I would like to especially thank my brother Kim. When I was marked by exhaustion, he found the right words out of nowhere to fill me with new strength.

⋆ You're supposed to stop when it's best. Therefore, I finish this acknowledgement with the best person known to me - Mareike. Thank you for infusing my life with fun and love of unparalleled dimensions, for supporting me unconditionally in my strenuous times and for commenting on my entire thesis. You spawn the strongest spirit in me, dispel all doubts and make every day special. There is not a single word that can express my feelings for you. Hence, I will now create one on-the-fly: I eternalovabuki you. See? Great word. I will eternalovabuki you. Forever.

.